The compositional variation of small bodies across the Solar System

F. E. Demeo

To cite this version:

F. E. Demeo. The compositional variation of small bodies across the Solar System. Astrophysics [astro-ph]. Observatoire de Paris, 2010. English. NNT : . tel-00514550

Observatoire de Paris

École Doctorale Astronomie et Astrophysique d'Île-de-France

THÈSE DE DOCTORAT

présentée pour obtenir le grade de

DOCTEUR DE L'OBSERVATOIRE DE PARIS

Spécialité: Astronomie & Astrophysique

par

Francesca E. DeMeo

La variation compositionnelle des petits corps à travers le sytème solaire

soutenue le 16 juin 2010 devant le jury:

Dr. Bruno Sicardy	Président
Dr. Hermann Boehnhardt	Rapporteur
Dr. Alberto Cellino	Rapporteur
Dr. Humberto Campins	Examinateur
Dr. Beth Clark	Examinateur
Dr. Daniel Hestroffer	Examinateur
Dr. M. Antonietta Barucci	Co-Directrice de thèse
Dr. Richard P. Binzel	Co-Directeur de thèse

LESIA, Observatoire de Paris-Meudon
francesca.demeo@obspm.fr

The Paris Observatory

Doctoral School of Astronomy and Astrophysics of Île-de-France

DOCTORAL THESIS

presented to obtain the degree of

DOCTOR OF THE PARIS OBSERVATORY

Specialty: Astronomy & Astrophysics

by

Francesca E. DeMeo

The compositional variation of small bodies across the Solar System

defended the 16th of June 2010 before the jury:

Dr. Bruno Sicardy	**President**
Dr. Hermann Boehnhardt	**Reviewer**
Dr. Alberto Cellino	**Reviewer**
Dr. Humberto Campins	**Examiner**
Dr. Beth Clark	**Examiner**
Dr. Daniel Hestroffer	**Examiner**
Dr. M. Antonietta Barucci	**Co-Advisor**
Dr. Richard P. Binzel	**Co-Advisor**

LESIA, Observatoire de Paris-Meudon
francesca.demeo@obspm.fr

Abstract

Small bodies hold keys to our understanding of the Solar System. By studying these populations we seek the information on the conditions and structure of the primordial and current Solar System, its evolution, and the formation process of the planets. Constraining the surface composition of small bodies provides us with the ingredients and proportions for this cosmic recipe. This thesis, comprised of studies of inner and outer Solar System small bodies, is dedicated to understanding the compositional gradient across the Solar System through spectroscopic and photometric measurements.

I present a taxonomy of visible and near-infrared spectral data based on 371 asteroid spectra. The taxonomy consists of 24 classes that best categorize the spectral variation seen among inner Solar System small bodies. From the creation of this taxonomy we learn that with only visible wavelength data there is uncertainty in shape of the 1-μm band. While near-infrared wavelength range is excellent for interpreting data containing diagnostic 1- and 2-μm bands, the more subtly featured C- and X-complexes appear to be largely degenerate in this wavelength regime.

I analyze the photometric colors of 23 Transneptunian Objects and Centaurs, nine of which have never been previously observed, and assign them taxonomic classifications. I discuss objects that either have changed classes from previous data or have significant changes in absolute magnitude. Furthermore, I interpret the surface composition of three outer Solar System small bodies, Jupiter-coupled object (52872) Okyrhoe, and TNOs (90482) Orcus and (73480) 2002 PN$_{34}$, by modeling spectroscopic measurements in the visible and near-infrared wavelength ranges. The spectra reveal varying amounts of H_2O ice among these bodies. For Orcus I provide rough constraints for the presence of materials more volatile than water ice.

I present a search for solid ethane, C_2H_6, on the surfaces of Pluto and Triton, based on near-infrared spectral observations. I model each surface using a radiative transfer model based on Hapke theory (Hapke, 1993) with three basic models: without ethane, with pure ethane, and with ethane diluted in nitrogen. While the presence of less than a few percent of ethane cannot be excluded on both bodies, there is no strong detection on either.

Finally, I review the current knowledge of the compositional distribution of material in our Solar System, providing the global view of small bodies. I particularly focus on the presence of water in all its phases which is especially pertinent our understanding of our own planet, Earth, and the life on it. I briefly compare the general structure of our Solar System to other imaged debris disks to put into perspective the detailed, though narrow, view of our own Solar System with the broad, low resolution view of others.

Keywords: Planetology, Asteroids, Transneptunian Objects, Centaurs, Observations, Spectroscopy, Photometry

Résumé

Les petits corps sont des clés pour comprendre notre système solaire. L'étude de cette population nous donne en effet accès aux informations sur l'état et sur la structure du système solaire primordial et du système solaire actuel, ainsi que sur son évolution et sur les processus de formation des planètes. Connaître la composition de surface des petits corps nous fournit des ingrédients et des proportions pour cette recette cosmique. Cette thèse, qui inclut l'étude des petits corps du système solaire interne et externe, est dédiée à la compréhension de la tendance compositionnelle des corps à travers le système solaire en utilisant des mesures photométriques et spectroscopiques.

Je présente une classification (taxonomie) dans les longueurs d'ondes du visible et du proche infrarouge (de 0.4 2.4 μm), basée sur les donnes spectrales de 371 astéroïdes. Cette taxonomie comprend 24 classes qui chacune caractérise au mieux les variations spectrales observées parmi les petits corps du système solaire interne. De part la création de cette taxonomie, nous apprenons qu'en analysant les données dans les longueurs d'ondes du visible uniquement, il reste des incertitudes sur la forme de la bande d'absorption à 1 micron. Bien que la gamme de longueur d'onde du proche infrarouge soit excellente pour interpréter les données incluant les bandes diagnostiques à 1 et 2 microns, les complexes C et X des spectres sans fortes bandes paraissent plutôt dégénérés dans ce régime.

J'analyse les couleurs photométriques des 23 objets trans-neptuniens (OTN) et Centaures, parmi lesquels neuf n'avaient jamais été observés précédemment, et je leur assigne une classe taxonomique. Je discute des objets qui ont soit changé de classe depuis les données préalables soit changé considérablement de magnitude absolue. De plus, j'interprète la composition de surfaces de trois petits corps du système solaire externe, l'objet couplé avec Jupiter (52872) Okyrhoe et les OTNs (90482) Orcus et (73480) 2002 PN_{34}, en modélisant des mesures spectroscopiques dans les gammes du visible et du proche infrarouge. Les spectres révèlent des variations de quantité de glace d'eau à la surface de ces corps. Pour Orcus j'apporte des contraintes approximatives sur la présence de matériaux plus volatiles que la glace d'eau.

Ensuite, je présente une recherche de l'éthane solide, C_2H_6, sur les surfaces de Pluton et de Triton. Celle-ci est basée sur les observations spectrales dans les longueurs d'ondes du proche infrarouge. Je modélise chaque surface en utilisant un modèle de transfert radiatif fondé sur la théorie de Hapke (Hapke, 1993) de trois manières : sans éthane, avec de l'éthane pur, et avec de l'éthane dilué dans de l'azote. La présence de moins de quelques pourcents d'éthane sur chaque corps ne permet pas d'exclure ce composant de Triton et Pluton, cependant il n'y a pas non plus de forte détection.

Finalement, je reconsidère la connaissance actuelle de la distribution compositionnelle des matériaux de notre système solaire en fournissant une vue globale des petits corps. Je me concentre particulièrement sur la présence de l'eau dans toutes ses phases qui est pertinente surtout pour notre propre planète, la Terre, et la vie. Je compare brièvement la structure générale de notre système solaire aux autres disques d'accrétion, afin de mettre en perspective la vue détaillée mais cependant étroite de notre système solaire avec celle, plus large mais à basse résolution, des autres systèmes planétaires.

Mots-clés: Planétologie, Astéroïdes, Objets Trans néptuniens, Centaures, Observations, Spectroscopie, Photométrie

Contents

Part I

Introduction and Background

Introduction

The study of small bodies began hundreds of years ago with the discovery of Ceres. This rich field has flourished since the advancement of CCDs and new technology and with the discovery of vast new populations, such as Jupiter Trojans and particularly the Transneptunian Objects.

Small bodies span across the entire solar system, experience a gradient of temperatures, exist in widely varying sizes, and also have diverse compositions. Separate populations of bodies, such as the Main Asteroid Belt and the Kuiper Belt, traditionally and justifiably have been studied separately because of the stark differences in composition, temperature, location, and the gap in our relative depth of knowledge of each population. However, comparison between these populations is now crucial to an overarching understanding of the solar system. While we separate these objects into different categories, we must recognize as well that these populations are all linked to some extent, that there is a remnant gradient revealing the Solar System's original structure, and that departures from the trend divulge the history of its evolution. Small bodies are interesting in their own regards as members of our Solar System community, but also for what they represent - as the remnants of the foundation for what created the planets, and as the intermediate link from protoplanetary disks to evolved disks, many with fully developed planetary systems that appear abundant in our universe.

This thesis represents a small attempt to view the small body population in its entirety, presenting research of silicate-rich inner Solar System small bodies side-by-side with ice-rich outer Solar System small bodies. I present a taxonomy of asteroid spectra, that while serves to distinguish different compositions, also provides a tool to search for trends based on heliocentric distance. I analyze spectra of TNOs contributing to our knowledge of the surface compositions in the outer Solar System. Finally, I seek to unify the advancements made from this work as well as from many others to provide a more global view of small body surface compositions and what it teaches us about our Solar System. I present general trends we see among small bodies extended out to the Kuiper Belt, and compare the structure of our Solar System to that of other debris disks.

While reading this thesis it is important to remember what "system" means and to regard our Solar System in such context: a system is "a group of interacting, interrelated, or interdependent elements forming a complex whole." While many small bodies are interesting individually or as distinct populations, it is only when combined together and viewed from a greater distance that we can unify the information each object provides into a global understanding of the system itself.

Chapter 1

Background

To understand any single part of the Solar System it is important to put it into context with the system in its entirety. This chapter provides the basic foundation for the work in this thesis. A general overview of the structure of the Solar System as we understand it today is introduced. Evolution scenarios and likely events that shaped the Solar System are described. Finally, a general characterization of the composition of and processes affecting the surfaces of small bodies are presented.

Contents

1.1 The Current Structure of the Solar System

It is often found with a large enough sample that there are no rigid boundaries between certain classes of objects, but instead there is a somewhat smooth gradient bridging all types of bodies. Creating boundaries and definitions, however, facilitate study and discussion. Outlined here are the main (non-solar) components of which the Solar System is composed. The definitions of a planet, dwarf planet, and small body stated here originate from the recently assigned definitions in Resolution 5A of the IAU 2006 General Assembly (Source: IAU Website).

1.1.1 Planets

A "planet" is a celestial body that: 1) is in orbit around the Sun, 2) has sufficient mass for its self-gravity to overcome rigid body forces so that it assumes a hydrostatic equilibrium (nearly round) shape, and 3) has cleared the neighborhood around its orbit.

The eight planets are thus: Mercury, Venus, Earth, Mars, Jupiter, Saturn, Uranus, and Neptune. They are located roughly at 0.4, 0.7, 1.0, 1.52, 5.2, 9.5, 19.2, and 30.0 Astronomical Unit (AU). Note this official definition excludes extra-solar planets because it restricts the definition to bodies orbiting around our Sun. A planet must have cleared its orbit, meaning any body residing in the Main Asteroid Belt between Mars and Jupiter or the Kuiper Belt belt past Neptune is excluded from planet status.

1.1.2 Dwarf Planets

A "dwarf planet" is a celestial body that: 1) is in orbit around the Sun, 2) has sufficient mass for its self-gravity to overcome rigid body forces so that it assumes a hydrostatic equilibrium (nearly round) shape, 3) has not cleared the neighbourhood around its orbit, and 4) is not a satellite.

Dwarf planets are large bodies in the Main Belt, the Kuiper Belt, or further and currently include (1) Ceres, (134340) Pluto, (136108) Haumea, (136472) Makemake, and (136199) Eris. Ceres is located in the asteroid belt, while all others are located past Neptune.

1.1.3 Comets

All other objects in the Solar System, except satellites, are considered "Small Solar-System Bodies." There is a wealth of small bodies in the Solar System which include asteroids and comets. Dynamic and basic physical constraints that characterize each population are detailed for comets in this subsection and asteroids in the next two.

Comets are ice-rich bodies that sublimate volatiles during close approaches to the Sun. They are characterized by a nucleus, the inner core of the body; a coma, the outer spherical halo of sublimated material surrounding the nucleus; and two tails, a dust tail trailing opposite the comet's trajectory and an ion tail in the anti-Sun direction. A neutral gas tail, was discovered on comet Hale-Bopp, however, it is typically not visible. If the nucleus contains species more volatile than water it can form a coma and tail at large distances. Sublimation of water typically begins at a distance of 2-3 AU from the Sun, although more volatile molecules sublimate at greater distances when exposed.

Comets are often described as "dirty snowballs". Carbon and other dark materials are mixed with the ice substantially lowering the albedo. Comet nuclei are notoriously difficult to observe because the coma obscures it at close distances, but the dark surface is too dim to observe when farther away.

They are often discovered when a previously known asteroid is reobserved and the image appears "fuzzy" or blury because a coma is present. Comets are usually separated into these dynamical categories: 1) Long period comets have periods greater than 200 years and highly eccentric orbits and 2) Short period comets have periods less than 200 years. Among them are Halley Family Comets ($P > 20$ years) and Jupiter Family Comets ($P < 20$ years).

Recently discovered within the Main Asteroid Belt is a set of bodies known as either Activated Asteroids or Main-Belt Comets (MBCs). As their name implies, these objects have qualities attributed to both comets and asteroids: asteroid-like orbits within the Main Belt, but comet-like outgassing has been observed through imaging (Hsieh and Jewitt, 2006). MBCs include 133P/Elst-Pizarro, P/2005 U1 (Read), and 118401 (1999 RE_{70}). These objects had all been discovered in the outer belt and two belong to the Themis asteroid family. P/2010 A2 (P/2008 R1 or P/Garradd) was just discovered in the middle part of the belt (a=2.73 AU) with "cometary" activity (Source: Minor Planet Electronic Circular 2010-A32), although it is unique. Throughout most of this body's orbit, it experiences temperatures greater than the melting point of water, suggesting that this was a very recent impact and dust ejected from the surface is observed and not volatiles.

1.1.4 Asteroids

The term "asteroid" is a broad category including all small bodies that do not exhibit coma (i.e. not comets) and are not satellites of a planet. When an asteroid is discovered it is given a preliminary designation based on the date of discovery and how many objects were discovered in the same time period. The first asteroid discovered in the first half of January 2010 is labeled 2010 AA. The second is labeled 2010 AB. The first asteroid discovered in the second half of the month is labeled 2010 BA. Once the alphabet has been used it restarts with 2010 AA1, 2010 AB1 etc.

While they are all labeled in the same designation scheme, their compositions and size vary enormously. These range from the warm, rock-dominated bodies close to the Sun, even inside Earth's orbit, to the cold, ice-rich bodies in the farthest reaches of the Solar System. Typically, the bodies past Jupiter are not referred to as asteroids, but instead as Centaurs and Transneptunian Objects. In this thesis, they are discussed separately from inner Solar System asteroids.

Main-Belt Asteroids: The Main Belt extends from ∼2.0 to ∼3.3 AU. The largest of these objects have diameters of around 1000 (Ceres, although technically a dwarf planet) and 500 (Pallas, Vesta) kilometers. There are estimated to be about 1 million asteroids with a diameter greater than 1 kilometer in the Main Belt (Tedesco et al., 2002). The structure of the belt is shaped in part by the Kirkwood gaps. These gaps occur at the mean-motion resonances (i.e. 3:1, 5:2, 7:3, and 2:1) with Jupiter. Gravitational perturbations from Jupiter create instabilities in these regions, therefore there is a deficit of bodies in these orbits compared with the rest of the Belt. These resonances are also expected to be a source for small bodies with Mars- and Earth-crossing orbits, because asteroids that fall into these resonances experience orbit excitation, increasing the eccentricity. The 3:1 and 5:2 resonances located near 2.5 and 2.82 AU, respectively create the boundaries defining the inner (2.0-2.5 AU), middle (2.5-2.82 AU), and outer (2.82-3.3 AU) portions of the belt.

Asteroid families (Hirayama, 1918; Zappala et al., 1995) provide important information about the asteroid belt and its formation and evolution. An asteroid family is a group of bodies with similar orbital elements that are thought to have originated from a single parent body that was collisionally disrupted. By integrating the orbits of family members back in time, it is possible to determine the approximate time of the collision, thus providing the opportunity to study the differences of surfaces based on age, as well as the frequency of collisions over time.

Near-Earth Objects (NEOs): NEOs include asteroids and comets that have orbits that are within or that cross near-Earth space ($q \leq 1.3$ AU). There are an estimated 5000 to 6000 kilometer-sized Mars Crossing ($q < 1.67$ AU) and near-Earth objects (Bottke et al., 2002). NEO orbits are unstable for periods longer than 10 My (Gladman et al., 2000) years thus requiring resupply from various sources throughout the Solar System (e.g., Öpik, 1963; Wetherill, 1976, 1979; Wisdom, 1985). While the primary source region is the Main Asteroid Belt (particularly the ν_6 and 3:1 resonances and the outer belt; Bottke et al., 2002), about 8% of NEOs are consistent with a cometary origin (Jupiter Family Comets) based on both dynamical and physical criteria: their orbits, albedos, and spectra (DeMeo and Binzel, 2008).

Some NEOs require less propulsion (and therefore lower cost) to encounter by spacecraft than the moon, making them ideal mission targets. Indeed, numerous National Aeronautics and Space Administration (NASA), European Space Agency (ESA) and Japan Aerospace Exploration Agency (JAXA) missions have been dedicated to exploring NEOs and Mars Crossers (or have passed by en route to more distant targets), including NEAR, Hyabusa, Deep Space and several proposed missions.

In 1998, NASA was given the objective to discover 90% of all NEOs with a diameter greater than 1 km by 2008. One kilometer is the approximate size of a body that could cause global disaster if it struck the Earth. More recently the objective was expanded to discover 90% of all asteroids greater than

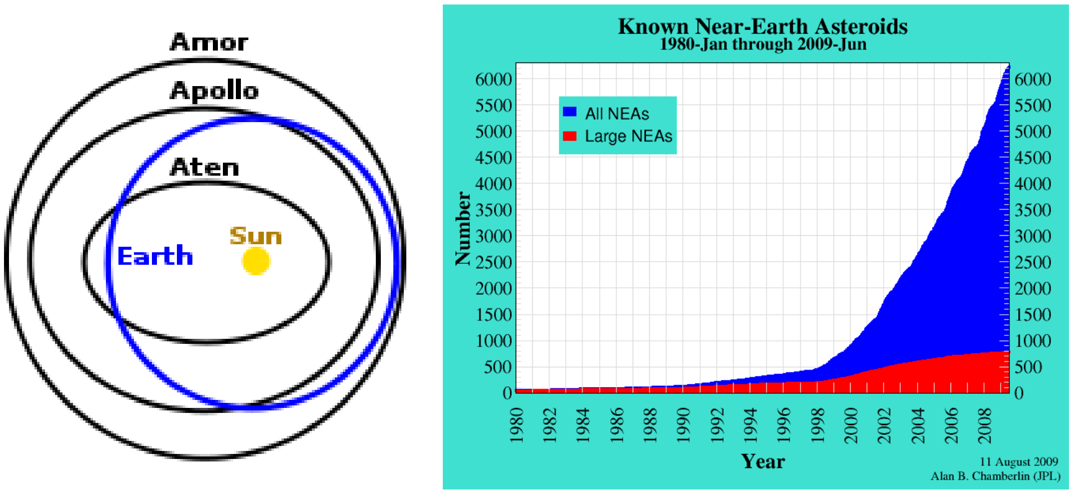

Figure 1.1: **Left:** Typical orbits for Amor, Apollo, and Aten asteroids (Figure Source). **Right:** Discovery rates for NEOs from 1980 to the present. While it appears that most of the largest NEOs have already been discovered, since 1998 the rate of discovery of the smaller bodies been very high. This rate will likely be increased further when Pan-STARRS becomes fully operational in 2012. (Source: NASA)

140 meters in diameter by 2020. While these objects would likely not cause global disaster, they would certainly cause significant local destruction. There are 6792 known NEOs, 803 of which are greater than 1 kilometer (Source: NASA, Feb. 22, 2010). Figure 1.1 shows the rate of discovery of NEOs from 1980 to the present.

NEOs are subdivided into several dynamical categories. Figure 1.1 displays a typical orbit for these objects.

- **Amors**: Objects that satisfy 1.017 $<$ q $<$ 1.3 AU, where q is the perihelion. These objects approach Earth's orbit but do not cross it.
- **Apollos**: Objects that satisfy a $>$ 1 AU and q $\leq$ 1.017 AU, where a is the semi-major axis. These objects cross Earth's orbit.
- **Atens**: Objects that satisfy a $<$ 1 AU and Q $>$ 0.983 AU, where Q is the aphelion. These objects cross Earth's orbit.
- **Atira**: Objects that satisfy Q $<$ 0.983 AU, meaning the orbit lies entirely inside that of Earth's. The class is named after the first object, (163693) Atira, discovered in 2003 (Source: NASA). Some consider these objects part of a subclass of Atens, and have also been called Apoheles.

Potentially Hazardous Asteroids (PHAs): PHAs are a subset of NEOs that are flagged because of their proximity to Earth's orbit. An object is considered a Potentially Hazardous Asteroid (PHA), if its Minimum Orbit Intersection Distance (MOID) with respect to Earth is less than 0.05 AU and it has a diameter of 150 meters or greater. The size condition is satisfied by having an absolute magnitude (H) of 22.0 or less (with an assumed albedo of 0.13). There are 1103 PHAs known today (Source: NASA, Feb. 22, 2010). Continued tracking of these objects increases the accuracy of their orbits which allows us to better quantify the likeliness of impact. These objects are important to characterize because all objects that have impacted the Earth in the past or that will in the future come from this population. The most "famous" of known PHAs is 99942 Apophis which will have a very close approach (about 6 Earth radii, Chesley, 2005) in 2029 and could possibly impact the Earth in 2036 (1:43,000 impact probability, Source: NASA, Sep 8, 2009). Apophis' orbit is shown in Figure 1.2.

Trojan Asteroids: There are almost 4,000 objects in the L4 (2,483 objects) and L5 (1,430 objects) Lagrange points of Jupiter's orbit (Source: Minor Planet Center, Jan. 13, 2010). Jewitt et al. (2000)

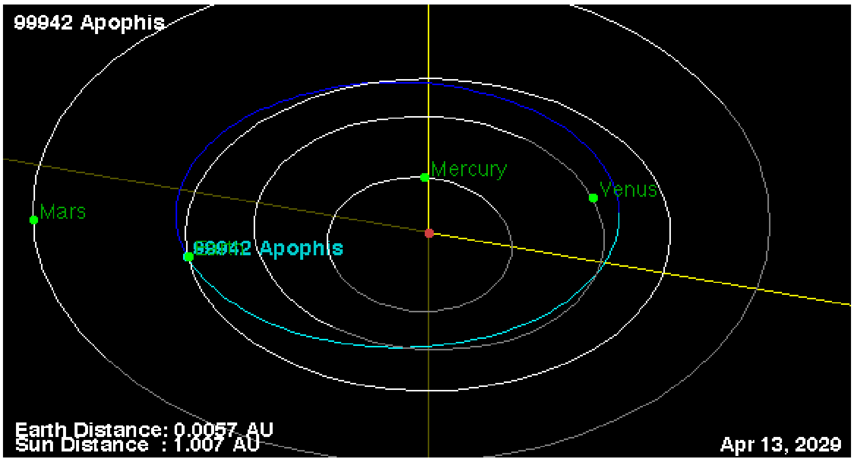

Figure 1.2: Shown here is the orbit of the inner planets and PHA (99942) Apophis. Its orbit closely intersects that of the Earth on April 13, 2029, making it an important object for continued tracking and a great mission target during close approach. (Source: NASA)

estimate that the number of L4 Jupiter Trojans with radius greater than 1 km is estimated to be around 1.6x10^5, which is on the order of the estimated population of the Main Belt. Several Mars and Neptune Trojans have also been discovered.

1.1.5 Centaurs and TNOs

Centaurs: Centaurs are icy bodies in orbit between Jupiter and Neptune. There are 256 known Centaurs (including Scattered Disk Objects) as of May 16, 2010 (Source: Minor Planet Center). Diameters have been derived for over 20 Centaurs, ranging from tens to hundreds of kilometers (Stansberry et al., 2008), although this samples the brightest and therefore mostly likely the largest of the population. Their orbits are not stable over long time periods and are thus thought to have originated in the transneptunian region. (2060) Chiron was the first discovered Centaur in 1977, and it was later learned to have cometary activity and renamed 95P/Chiron. Most Centaurs, however, have been discovered within the past decade. The unique property of the Centaur population is its color bimodality. Their B-R colors divide into gray and red groups with 99.5% confidence (Tegler et al., 2008a). The gray Centaurs also have a lower mean albedo than the red ones, although dynamically, no differences in their orbits have been found (Tegler et al., 2008a).

TNOs: TNOs are objects that reside in and past the Kuiper Belt past Neptune's orbit. The Kuiper belt (see Fig. 1.3) lies roughly between 30 and 55 AU. There are 1130 (as of May 16, 2010) known TNOs including Pluto (which is also a dwarf planet) and excluding Centaurs (Source: Minor Planet Center). Figure 1.3 shows the eight largest known TNOs. The current mass of the Kuiper Belt is estimated to be between 0.01 to 0.1 of Earth's mass (Bernstein et al., 2004; Gladman et al., 2001), and is only 0.1% of the original mass of the Kuiper Belt (Morbidelli et al., 2008, and references therein). Diameters of measured TNOs range from hundreds to thousands of kilometers (Stansberry et al., 2008). The discovery of a serendipitous stellar occultation of a ~500-meter body at 45 AU among archival data supports the current belief that there is a deficit of sub-kilometer TNOs (Schlichting et al., 2009).

Dynamical classifications summarized below are described in detail by Gladman et al. (2008). Figure 1.4 is a plot of the dynamical regions of these classes from Gladman et al. (2008).

- **Resonant:** Resonant objects are in mean motion resonances with Neptune, meaning they complete a fixed number of orbits per orbit of Neptune. The 3:2 resonance is the most populous, and includes Pluto. These objects complete three orbits for every two Neptune orbits. Other prominent resonances include 5:3, 7:4, 2:1, and 5:2.

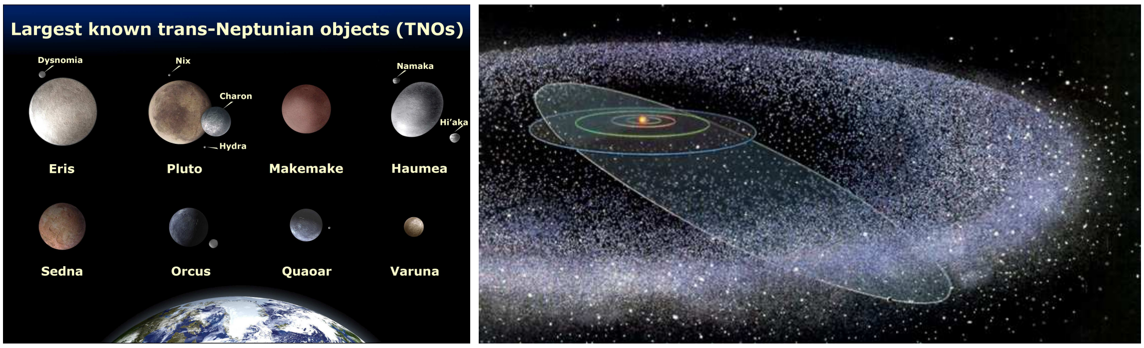

Figure 1.3: **Left:** An artists depiction of the eight largest known TNOs and their satellites relative to the Earth (modified from: Hubble Website). **Right:** An artists depiction of the Kuiper Belt, with the the orbits of Pluto and the giant planets marked (Source: J. Schombert).

- **Scattered Disk Objects:** These objects are in unstable orbits. They have perihelions near Neptune and high eccentricities. Theories that would allow objects to reside in this region include a passing star, a rogue planet, or sweeping resonance, all of which are discussed further in Section 1.2.
- **Detached Objects:** These objects have perihelia decoupled from Neptune and include objects with large semi-major axes.
- **Classical:** Any object not within these outlier groups makes up part of the classical population, whose typical members have relatively circular orbits and low eccentricities. The densest region of objects is between about 42 to 48 AU. The classical objects have been proposed to be split into two populations, the hot and cold populations. The cold population has an inclination of less than 5 degrees and either formed in situ or was pushed outward during the planet migration phase, whereas the hot population has more excited orbits, with inclinations greater than 5 degrees. These bodies were thought to have originally been closer to the Sun and were then perturbed by Neptune and Uranus into their current orbits.

This distinction between the hot and cold populations is made based on both dynamical and physical characteristics. Both Brown (2001) and Elliot et al. (2005) found evidence of two inclination distributions among classical objects. Brown (2001) found that the sum of two Gaussians with sigma of 2.2 and 17 degrees could be fit to the inclinations of around 250 objects, while Elliot et al. (2005) found a cold population core with a full width at half maximum of 4.6 degrees, while the hot population is more disperse. Levison and Stern (2001) found that at low inclinations there were many smaller objects, but there is a deficit of larger objects.

Objects in the cold, low-i population tend to be red, while the high-i population displays a large range of colors from neutral to red (Tegler and Romanishin, 2000; Trujillo and Brown, 2002; Doressoundiram et al., 2002; Tegler and Romanishin, 2003; Peixinho et al., 2004; Gulbis et al., 2006). Recent studies, however, support a break in color differences nearer to 12 degrees inclination (Peixinho et al., 2008). Further support for two populations was provided by Noll et al. (2008) who found that 29% of all low-inclination classical TNOs ($i \leq 5.5$ deg) are binaries, while only 9% of high-inclination objects are binaries.

1.2 Solar System Evolution

The Solar System today does not look like it did shortly after formation. There has been significant mixing of material and an excitation of orbits seen in the current Main Belt. In the Kuiper Belt there are a few main attributes of the current structure that make formation in its present location without significant disruption very unlikely. First, is the existence of the hot population of excited objects that vary widely in composition. Second, is the apparent edge of the Kuiper Belt near 50 AU (Allen et al.,

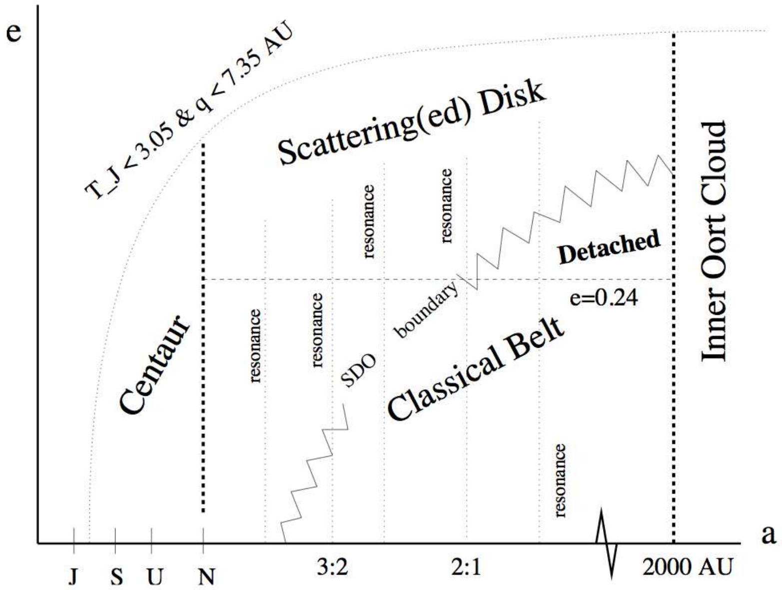

Figure 1.4: Plot of semi-major axis versus eccentricity defining regions of dynamical classes of TNOs. The boundaries defining the classical belt, scattered disk, detached objects, and Centaurs are shown as well as well as the major resonances with Neptune (Source: (Gladman et al., 2008))

2001), after which the flux of objects within the limits of discovery drop rapidly, as opposed to a smooth, constant dropoff in flux. Third, is the total mass of the current Kuiper Belt is much smaller (0.1%) than the expected initial mass. In most models, explained below, the Kuiper Belt was originally much more massive, denser, and closer to the Sun (with an outer edge at approximately 30 AU) than in its present state (Morbidelli et al., 2008).

The most prominent model, the Nice model, includes migration of the giant planets from their original locations in the early Solar System, and is capable of explaining much of the structure of both the Main Belt and the Kuiper Belt. The rogue planet and companion or passing star theories could also bring about the structure of the Kuiper Belt.

In this section we briefly describe the formation of the Solar System and the bodies contained within it. We then summarize the main theories that explain the evolution of the Solar System. Also presented within this section is a period affecting the inner Solar System known as the Late Heavy Bombardment, a violent period where a spike in the flux of impactors caused significant cratering of bodies in the inner Solar System.

1.2.1 Solar System Formation

The Nebula Theory was first proposed in the 1700s, and has been improved (known as the Solar Nebula Disk Model, see Weidenschilling, 2000; Kenyon and Bromley, 2006, for reviews) over time as we've learned more about our own neighborhood and other star systems. The Solar System began as a large nebula (a molecular gas and dust cloud) which eventually accumulated sufficient mass and density for gravitational collapse, this event is expected to be typically triggered by random turbulences which locally increase the density within the cloud. The gas and dust cloud condensed to form a central mass and a flat dust disk, a protoplanetary disk, that surrounded it. The rate of rotation of the disk and central mass increased as it collapsed, conserving angular momentum. The central mass continued to gain mass and a protosun is formed; when enough mass accumulated for fusion to occur it became the Sun. At this point a strong temperature gradient across the disk dictated the distance at which certain materials condensed. The inner disk was too hot for water and more volatile species to form, so it was dominated by rocky material, while the outer disk had a mixture of rocky material and ices.

Within the protoplanetary disk, small, micron-size dust grains collided at velocities low enough because of the gas drag to coalesce to form bodies up to a kilometer in size (although the sticking mechanism for centimeter to kilometer size planetesimals is not well-constrained, Weidenschilling and Cuzzi, 1993). At kilometer sizes, gravity becomes the dominant force during this “runaway growth” stage, and gravitational focusing caused kilometer-size bodies to accrete much faster than smaller planetesimals. During oligarchic growth these bodies cleared their orbits of smaller bodies and debris. Many of these large bodies collided and merged or ejected other bodies and eventually grew to planetary sizes.

The planetary formation process occurred over a very short time period (< 10 My) (Yin et al., 2002) because at this point strong solar winds begin to clear the residual dust from the Solar System, leaving the minor bodies and planets with a paucity of new material to accumulate. At this point destructive collisions become a more significant factor in shaping the Solar System.

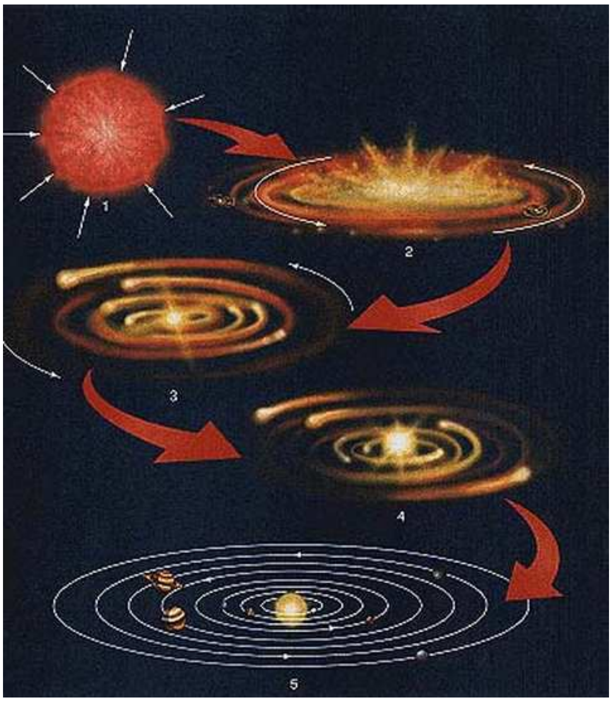

Figure 1.5: A simple scheme of Solar System formation. (1) The Solar System starts as a molecular gas and dust cloud, (2) collapses into a flattened disk with a central mass, (3) small planetesimals form, (4) larger planetesimals then dominate the accretion process and the Sun forms as fusion begins, (5) finally dust is cleared halting planetesimal formation, collisions combine and eject material leaving the 8 planets a Main Belt, Kuiper Belt, and Oort Cloud (Figure Source).

1.2.2 Planet Migration: The Nice Model

In the Nice Model, a model of Solar System evolution created primarily by a group of researchers in Nice, France, Jupiter is originally further from the Sun than its current location, and Saturn, Uranus, and Neptune are closer to the Sun. The Kuiper Belt is also originally much closer to the Sun, with its outer edge around 30 AU (Tsiganis et al., 2005). Over time, Jupiter would move inward as Saturn, Uranus, and Neptune would migrate outward. As Neptune’s orbit crept further from the Sun, it would “drag” the bodies in 3:2 mean motion resonance with it, pushing them outward and preserving the resonance. The result of this outward motion is shown in Figure 1.6.

The first to suggest the idea of planet migration was Fernandez and Ip (1984). The idea that Pluto’s orbit could be explained by planet migration and how that migration would affect the structure of the Kuiper Belt was first presented by Malhotra (1993) and Malhotra (1995). With the help of increased

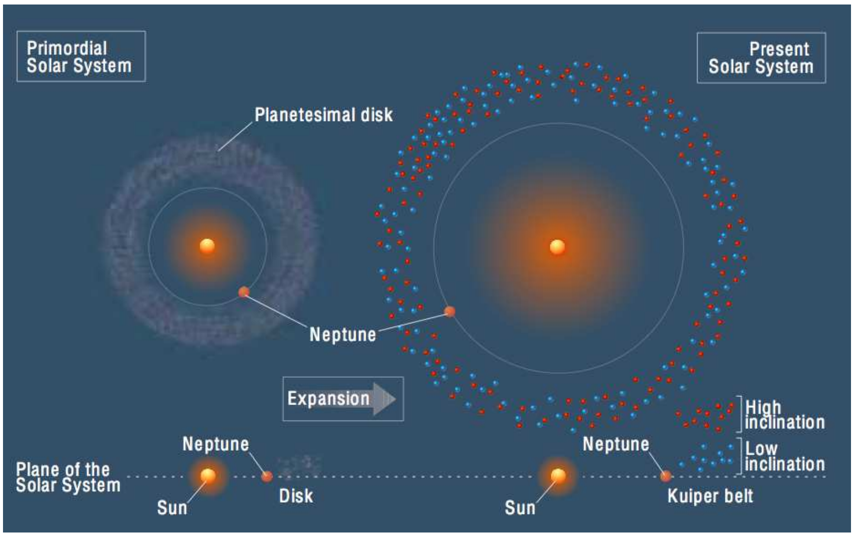

Figure 1.6: The primordial Solar System was thought to be much more compact than its current structure. As Saturn, Uranus, and Neptune migrated outward, the smaller bodies past Neptune were pushed outward expanding the Kuiper Belt to its current location. (Source: Gomes, 2003a)

computing capabilities which allowed solving more complicated numerical integrations, exploration of planet migration was further expanded by Gomes (2003b) and Gomes et al. (2004). Gomes (2003b) introduced objets with mass into the planet migration models and showed that as Neptune moves outward it pushes the belt outward, and also scatters many objects in the process to create the hot population. This scattering is inefficient, with only 0.1% of the original scattered bodies surviving in the Kuiper Belt today (Gomes, 2003b). A simple diagram of the motion of the outer planets and the effect it had on the smaller bodies is shown in Figure 1.7.

Some problems in the work of Gomes (2003b) and Gomes et al. (2004) include the too small eccentricities and positions of the giant planets: Neptune would not proceed past the 1:2 resonance with Uranus (Gomes, 2009). In the Nice Model, after about 600 My Jupiter and Saturn cross their 1:2 resonance which maintains their high eccentricities, which are later dampened by dynamical friction (Tsiganis et al., 2005; Gomes, 2009). This crossing can also create a Jupiter Trojan population although any objects originally in the Trojan regions would be kicked out (Morbidelli et al., 2005; Gomes, 2009). The model has become increasingly refined and can explain many of the intricacies of the structure of the Solar System, such as the detail of the Kuiper Belt (Levison et al., 2008) and the existence of the Late Heavy Bombardment (Gomes et al., 2005; Morbidelli et al., 2009b). Gomes et al. (2005) show that as Jupiter and Saturn cross the 1:2 resonance and their orbits change the ν_6 resonance is displaced. As it sweeps across the Main Belt it ejects many bodies into the inner Solar System. They predict that this instability in the inner Solar System occurred around 3.9 Gy, consistent with current evidence for the Late Heavy Bombardment (see Section 1.2.4).

1.2.3 Passing Star, Companion Star, and Rogue Planet Theories

Ida et al. (2000) proposed that a star passing by the Solar System could create the sharp cutoff in the Kuiper Belt past 50 AU. This suggests that the Solar System was formed in a relatively dense region of stars, and that a star passed within 80 - 200 AU of the Sun after the first 100 My after planetesimal accretion. For this theory to be valid, the timing for the passage is particularly sensitive because a late passage would destroy the 3:2 resonance of objects with Neptune (Gladman et al., 2001; Morbidelli and Brown, 2004). Weaknesses in the theory described in Gomes (2009) include its inability to explain the presence of the hot and cold populations and the deficit of detached objects compared to what would be expected in this scenario.

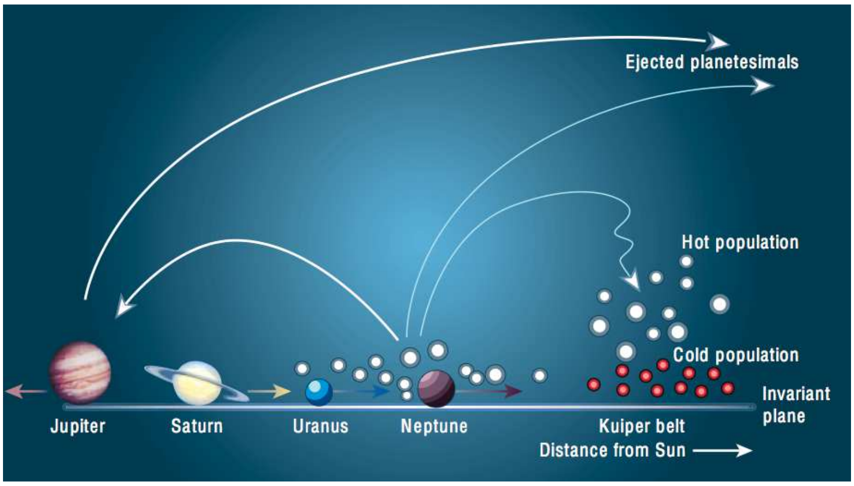

Figure 1.7: In the model by Gomes (2003b), as Jupiter moved inward and the three other giant planets moved outward, most small bodies in the region were ejected from the Solar System. Some bodies that were scattered by Neptune, however, were excited into orbits that are expected to now make up the "hot" population. (Source: Morbidelli and Levison, 2003)

Similarly, the existence of a companion star to the Sun has been proposed by many authors (e.g., Murray and Dermott, 1999; Collander-Brown et al., 2000; Matese et al., 2005; Gomes et al., 2006). This companion could be up to hundreds of Earth masses at a distance of 10^4 to 10^6 AU. The latter two models demonstrate that this companion star could create detached objects, such as Sedna.

Another theory states that a Mars-sized planet could have helped shape the Kuiper Belt. The edge of the Kuiper Belt could have been created by a Mars-sized object at 60 AU, which was proposed by Brunini and Melita (2002). A similar theory by Lykawka and Mukai (2008) stated that a Mars-sized object could have been scattered by Neptune, which would then shape the outer edge of the belt. However, a wide-field survey searching 12000 deg^2 up to a Magnitude of 21 that was sensitive to Mars-size objects out to $\sim$300 AU and Jupiter-size objects to $\sim$1000 AU did not detect any bodies (Schwamb et al., 2009).

1.2.4 The Late Heavy Bombardment

On the Moon, the Nectarian and early-Imbrium basins were formed around 3.8 to 4.1 billion years ago. Additionally, nearly all lunar impact melt breccia samples have ages between 3.8 and 4.0 Gy old (e.g., Cohen et al., 2000; Norman et al., 2006). During this time it is suspected that a spike in impacts occurred throughout the inner Solar System, potentially caused by orbital excitation due to sweeping resonances in the Main Belt resulting from planet migration. Evidence for the Late Heavy Bombardment (LHB) has also been suggested for Mercury, Mars, and Earth.

It has also been argued that the LHB was simply the end of a monotonically decreasing flux of impacts from 4.5 to 4.0 Ga. They purport that the sample of lunar impact melts is highly biased and that we find no material older than 4.0 because the younger impacts erased the underlying older ones (Chapman et al., 2007). Models of the young small body population, though limited, show that the declining bombardment scenario is extremely unlikely (Bottke et al., 2007).

1.2.5 Effects currently shaping the Solar System

The four processes predominantly shaping the current structure of the Solar System are gravity, collisions, and the Yarkovsky and YORP effects.

- **Gravity** is the most important force shaping our Solar System. It was responsible for forming the minor bodies and planets through accretion, and acts as the "glue" keeping them in their solid form.

It is the force keeping all bodies in orbit around the Sun and maintains the distribution present in the Solar System. Gravitional interactions are also responsible for displacing much of the mass in the original asteroid belt and Transneptunian population.

- **Collisions** link the original asteroid and Kuiper belts to the current one. Asteroids are thought to have originally accreted to very large sizes, from $\sim$100 to 1000 kilometers in diameter (Johansen et al., 2007; Cuzzi et al., 2008; Morbidelli et al., 2009a). Throughout the age of the Solar System, most bodies collided creating smaller fragments which eventually resulted in the current size distribution. Collisions affect the surfaces of all bodies in the Solar System, evidenced by the existence of impact craters on all bodies, even ones with young surfaces such as the Earth.

- **The Yarkovsky Effect** is a thermal radiation force that changes the semi-major axis of a small body's orbit. The force can cause small asteroids to migrate over time into resonances which eventually excite their orbits into Mars-crossing or near-Earth orbits, thus resupplying these unstable populations. It is also responsible for the gradual dispersion of asteroid collisional families in orbital element space over time. The Yarkovsky and YORP effects are discussed in Bottke et al. (2006).

  Diurnal Effect: Sunlight reaching the asteroid on the "day" side is absorbed, heating the surface, and is later reradiated as thermal energy in a different direction (the "night" side), after the body has already rotated. As the photons are radiated from the surface they take angular momentum with them, causing an uneven push to the object. For prograde rotators this pushes the body outward, increasing the semi-major axis, and the opposite is true for retrograde rotators. This effect is more important for larger bodies ($100\ \text{m} \lesssim D \lesssim 40\ \text{km}$)

  Seasonal Effect: Throughout an asteroids orbit, the "night" side that radiates more energy than the "day" side faces the direction of the orbital motion. The radiation emitted acts as a breaking force, slowing the motion and causing the body to drift inward (lowering the semi-major axis). This effect is more important for smaller bodies ($1\ \text{m} \lesssim D \lesssim 100\ \text{m}$)

- **YORP:** The Yarkovsky-O'Keefe-Radzievskii-Paddack (YORP) effect, similar to Yarkovsky, is driven by reflection and re-emission of sunlight. YORP controls the asteroid spin vector, rotation rate, and the rate of Yarkovsky drift. It is driven by the asymmetric shape of the body that creates a "windmill" effect. It is particularly effective for objects with diameters less than $\sim$10 km over 10^8 years and faster for smaller bodies (Rubincam, 2000).

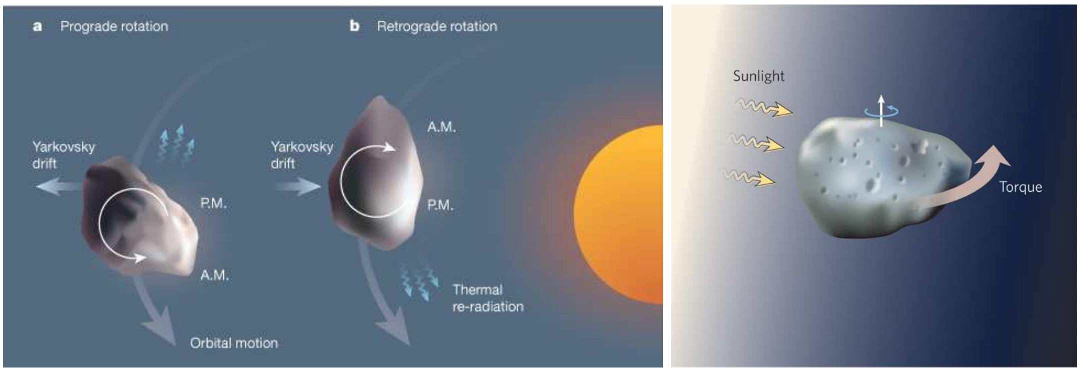

Figure 1.8: **Left:** Diagram of Yarkovsky effect. Asteroid surfaces are heated preferentially on the areas facing the Sun. As they rotate thermal radiation is emitted in a different direction causing the asteroid to change its orbit slowly over time. (Source: Binzel, 2003) **Right:** Diagram of YORP effect. Sunlight hits the uneven surface of an asteroid causing a torque which changes the spin vector and rotation rate. (Source: Bottke, 2007)

1.3 The surfaces of small bodies

1.3.1 Composition

Inner Solar System: The composition of bodies throughout the Solar System varies roughly according to their distance from the Sun. Temperature plays a large role in the compositional gradient throughout the Solar System. Particularly, bodies within the "ice line" cannot retain frozen volatile material. The ice line is the distance from the Sun at which H_2O freezes to its solid form. In the present Solar System the line is located in the main asteroid belt at about 2.7 AU, although it was originally presumed to be near 5 AU earlier in time (Kennedy and Kenyon, 2008).

An asteroid's composition is primarily determined through spectroscopic observations, explained further in Section 2.1. Asteroids are classified into different taxonomic categories that are expected to roughly correlate with surface composition. Taxonomy evolves as technology improves and the resolution and wavelength range of the data increases. A brief introduction to previous classification systems and a presentation of the most recent taxonomy, part of this thesis, is detailed in Chapter 4.

Asteroids located in the inner Solar System are primarily comprised of silicates, which are minerals that contain the component SiO_4. The objects in the inner part of the Main Belt are considered more altered, and the outer belt more primitive, however, radial mixing perhaps caused by sweeping resonances have blurred boundaries.

The three very broad categories that describe asteroids are: primitive, partially melted, and differentiated. Primitive material include C-, X- (although only a subset of X-types, the low albedo P-types), T- and D- types and are mainly made of silicates, carbon, and organics and some are similar to CI and CM meteorites. Partially melted, or at least thermally altered, include the S-complex asteroids and are made primarily of olivine, pyroxene and metal. Their meteorite-analoges are ordinary chondrites and other chondrites. Remnants of disrupted differentiated bodies include basaltic V-types, nearly-pure olivine A-types, and metallic bodies (some M-types), that represent pieces of the crust, mantle, and core.

Much of what we know about the composition of asteroids come from the samples we have on Earth: meteorites. For meteorites, in depth compositional analyses in laboratories can be performed with much higher signal-to-noise ratios than can be achieved through telescope observations. Meteorites are characterized as being either "falls" or "finds", meaning it was either discovered as it fell to the ground, or that it was found on the surface presumably long after it arrived. There is an inherent bias in the sample of "finds" because many meteorites are indistinguishable from ordinary earth rocks, while others, such as iron meteorites, are easily detectable.

Meteorites are broken up into three main classes: stones, stony-irons, and irons. Stones, which make up the large majority of meteorites in our sample, include chondrites (ordinary and carbonaceous), and achondrites. Chondrites are defined by having small grains, or chondrules, that accreted within the asteroid during formation and have remained intact throughout the life of the body. Ordinary chondrites are separated into H, L, and LL classes depending on their iron content (high, low, and very low). Carbonaceous chondrites are divided among classes CI, CM, CV, CR, CO, CK, CH, and CB depending on their composition and have additional notations according to the amount of aqueous and thermal alteration they have undergone. Stony-irons are partially differentiated material and include pallasites and mesosiderites.

Linking meteorites to their asteroid analogues is fundamental to our understanding of asteroid composition. The clearest connection is between the HED meteorites and Vesta (McCord and Johnson, 1970; Consulmagno and Drake, 1977), reviewed in Drake (2001). Binzel and Xu (1993) discovered small asteroids in Vesta's vicinity of similar composition that created a trail to the 3:1 resonance, which is capable of transporting material into near-Earth space (Wisdom, 1985), thus strengthening the case that Vesta is the HED parent body. Many other asteroid-meteorite links have been suggested based on spectral similarity, although no firm conclusions can be reached without more clear mineralogic evidence. These comparisons include olivine-rich A-types to Bracchinites or R-chondrites, subtly featured, low albedo C-types to Carbonaceous Chondrites, K-types to CO and CV chondrites, red D- and T- types to the only sample resembling them, Tagish Lake, and olivine and pyroxene S-types to ordinary chondrites (Burbine, 2000; Burbine et al., 2001; Hiroi et al., 2001; Sunshine et al., 2007; Clark et al., 2009).

Spectral discrepancies between the most common fall, ordinary chondrites, and the most common near-Earth asteroid type, S-type, suggest that some process is affecting the surfaces of asteroids and altering the spectra. This process, called space weathering, is discussed further in section 1.3.2. Most ordinary chondrites are delivered to Earth via the ν_6 resonance, although 3:1 resonance is also a preferential source for H chondrites (Thomas and Binzel, 2010). Curiously, the composition (specifically the percent olivine versus pyroxene) of the most common meteorites, H and L chondrites, do not match the most common near-Earth asteroids which have compositions equivalent to LL chondrites (Vernazza et al., 2008). Asteroid 2008 TC_3 was observed just days before it fell to the Earth and was recovered as meteorite Almahata Sitta (Jenniskens et al., 2009). This event provided an extraordinary opportunity to compare telescopic observations to laboratory measurements, and was the first occasion since the return of lunar samples decades ago.

Outer Solar System: TNOs are located beyond 30 AU from the Sun and therefore have much lower temperatures than asteroids. Their surfaces are dominated by ice and dark materials such as carbon, and most have low albedos, typically from 3 to 10% (Stansberry et al., 2008). In the visible and near-infrared wavelengths, Trans-Neptunian Object (TNO) spectra range from featureless to dominated by ice signatures.

The featureless spectra differ widely in slope from nearly neutral to very highly sloped. TNOs and Centaurs have the highest spectral slopes in the visible wavelength range of all bodies in the Solar System. One hypothesis is that the increased redness, such as that seen in outer belt D-type asteroids, is due to organic material (Gradie and Veverka, 1980; Vilas and Smith, 1985), although it has also been proposed that the reflectance properties of ice may contribute to the uniquely high slopes of TNOs that are not seen elsewhere in the Solar System (Grundy, 2009).

Many TNO spectra have distinct signatures of H_2O ice at 1.5 and 2.0 microns (Barkume et al., 2008; Guilbert et al., 2009a). H_2O ice can be in crystalline or amorphous form and they are easily distinguishable by the additional feature at 1.65 microns for crystalline ice. Crystalline H_2O ice was originally expected to be amorphized by space weathering processes over time scales shorter than the age of the Solar System (Kouchi and Kuroda, 1990). Recent experiments, however, have shown that when crystalline water ice is irradiated, the 1.65-μm band strength decreases when irradiated, but is still present, and that thermal recrystallization is the dominant process at temperatures greater than about 40K (Mastrapa et al., 2006; Zheng et al., 2008). There is one set of TNOs all closely linked in dynamical space that have very unique spectra with very strong solid H_2O bands; these objects are all part of the Haumea family that is believed to have been created by a collision with Haumea over a billion year ago (Brown et al., 2007b; Ragozzine and Brown, 2007).

Only the largest TNOs are massive enough to have retained their volatiles throughout their lifetime. Figure 1.10 shows the loss of volatiles due to Jean's escape on bodies throughout the outer Solar System based on size and temperature. Levi and Podolak (2009) perform a similar calculation, but they include the effects of hydrodynamic escape. Methane has been detected on the surfaces of Pluto, Triton, (136199) Eris (Brown et al., 2005b), (136472) Makemake (Licandro et al., 2006b), (90377) Sedna (Barucci et al., 2005a), and (50000) Quaoar (Schaller and Brown, 2007a; Dalle Ore et al., 2009). Triton is the largest moon of Neptune, but due to its composition and retrograde orbit it is believed to be a captured TNO (McCord, 1966; McKinnon, 1984; Agnor and Hamilton, 2006). Nitrogen is present on the surfaces of Pluto, Triton, Eris, and Makemake; CO has been found on Pluto and Triton, with H_2O and CO_2 ices being present on Triton as well. An analysis of the surfaces of Pluto and Triton is presented in Chapter 7. Only two objects have been discovered to have methanol: (5145) Pholus (Cruikshank et al., 1998) and (55638) 2002 VE_5 (Barucci et al., 2006). NH_3 is present on Pluto's satellite Charon (Buie and Grundy, 2000; Brown and Calvin, 2000) and is suspected on (90482) Orcus (de Bergh et al., 2005; Barucci et al., 2008b). Figure 1.9 shows the spectra of some of the bodies rich in either crystalline H_2O or methane.

1.3.2 Surface Evolution

There are many processes that can cause physical and chemical changes on the surfaces of small bodies. These include collisions, aqueous alteration, thermal alteration, and space weathering. Evidence of aqueous alteration, caused by water interacting with anhydrous rock, is often detected on low albedo asteroids seen as a weak feature at 0.7 μm (Vilas and Gaffey, 1989). Bodies that reside in the inner solar system or that have highly elliptic orbits experience thermal effects due to high temperatures or large temperature

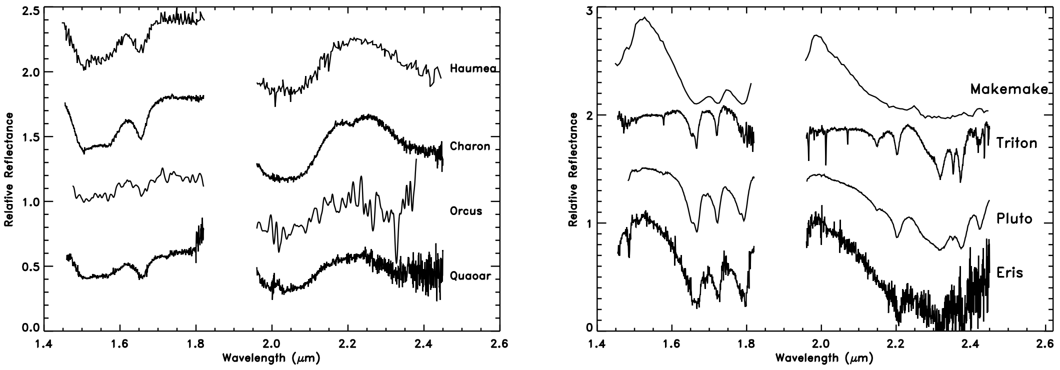

Figure 1.9: **Left:** Spectra of a sample of water-rich TNOs and Pluto's moon Charon. These large minor bodies display the distinct wide absorption bands of water ice at 1.5 and 2 μm as well as at 1.65 μm indicative of the crystalline form of ice. All data are from the Large Program except for Haumea which is from Pinilla-Alonso et al. (2009). There is a large variation in the depths of water absorption bands among TNOs, and water is found in both the crystalline and amorphous form. The strongest bands are seen among the Haumea family. **Right:** Spectra of methane-rich large TNOs, Pluto, Eris, Makemake, and Neptune's largest satellite Triton. These are the largest of TNOs, dwarf planets in fact, and have retained their volatile species throughout their lifetime. The differences between the spectra indicate different compositions and grain sizes. All data are from the Large Program except for Makemake which is from Barkume et al. (2008).

variation throughout their orbits. Comets show the most drastic changes due to temperature differences: sublimation of large amounts of volatiles creating a coma and a tail. Finally, the processes that change the spectrum of airless bodies (bodies with no atmosphere to shield the surface from the space environment) over time are referred to collectively as "space weathering." These effects include bombardment by micrometeorites, solar wind ions, and cosmic ions. The strength of these processes depend on porosity, grain size, composition, and the amount of time a surface has been exposed to space. Also, as distance from the Sun increases the importance of solar wind decreases and of cosmic rays increases. A simple cartoon, Figure 1.11, illustrates space weathering processes acting on the surface of an airless body. Our understanding of and evidence for space weathering is detailed throughout the rest of the section.

Space weathering on the Moon: With the return of Apollo lunar samples, lunar regolith could be compared to fresh lunar rock pulvarized in the laboratory. They were found to have differing spectral signatures, the lunar soil being darker and redder than the fresh sample (McCord and Johnson, 1970; McCord and Adams, 1973). Originally, it was proposed that the darkening and reddening of the spectrum seen in lunar soils was caused by the creation of dark glass agglutinates by meteoritic bombardment of the lunar regolith (Conel and Nash, 1970; Adams and McCord, 1971a,b). Because this glass formation was specific to the Moon, it was not expected to affect the surfaces of asteroids.

Through continued experiments, reviewed in Pieters et al. (2000) and Hapke (2001), it was found that these spectral effects were caused not by the glass, but instead by the production of nanophase iron particles (npFe^0, also referred to as submicroscopic metallic iron, or SMFe, because the particles typically range from tens to hundreds of nanometers in size; Hapke, 2001). FeO reduction in minerals is caused by vapor deposition and irradiation effects from micrometeorite bombardment and solar wind sputtering (Pieters et al., 2000; Hapke, 2001).

Space weathering on asteroids: Ordinary chondrites make up about 80% of all meteorite falls. One would expect that majority of Earth-crossing asteroids would have similar spectra. On the contrary, Q-type asteroids, the type most spectrally similar to ordinary chondrites, are a minority among NEOs. Not a single Q-type asteroid has yet been indisputably discovered in the Main Belt. Thus many questions

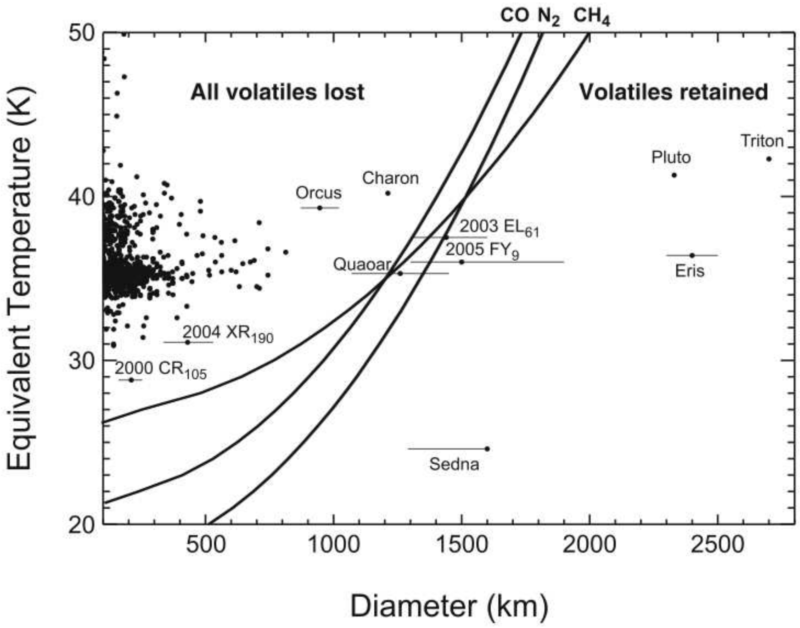

Figure 1.10: Minimum volatile loss in the outer Solar System as a function of temperature and radius. The lines show the temperatures as a function of radius at which the initial inventories of CH_4, N_2, and CO must be lost over the age of the Solar System. (Source and text: Schaller and Brown, 2007b)

arise: is there a delivery bias? Is there a size bias, that only smaller asteroids are ordinary chondrite-like (NEOs can be observed down to smaller sizes than the Main-Belt asteroids because they are closer to Earth and thus brighter)?

One of the most common spectral types among both Main-Belt asteroids and NEOs is the S-type. While similar to the ordinary chondrite spectrum, it is significantly redder and its bands are weaker. Could these asteroids be “disguised” ordinary chondrites? Furthermore, Binzel et al. (2004) show for S-type NEOs that as size decreases (from 5 to 0.1 km) the average spectral slope of the objects decrease. Binzel et al. (2004) suggest this trend is either due to a difference in particle size on the surface, or to the age, since smaller asteroids have shorter collisional lifetimes.

Vernazza et al. (2008) measured the spectral signatures of very young families in the Main Belt and found that they had already been reddened. They prove that this reddening process must occur over very short time scales, less than one million years, implying that any fresh Q-type surface observed in the Solar System must have been rejuvenated very recently.

Evidence for space weathering has been seen by in situ observations of near-Earth asteroids (for a review see Clark et al., 2002). Asteroid 433 Eros was visited by the NEAR Shoemaker spacecraft and images and spectra of the wall of crater Psyche show that dark regolith appears to move downslope and brighter material is then exposed (Veverka et al., 1999; Murchie et al., 2002). On asteroid Itokawa, visited by the Hyabusa spacecraft, the brighter fresher regions are also seen at inclined areas of the Little Woomera region (Saito et al., 2006).

Laboratory simulations of space weathering: Recent laboratory experiments have made significant process toward understanding the effects space weathering could have on the surface of an asteroid. Laboratory simulation of solar wind and cosmic ion can be achieved by keV-MeV ion irradiation. Micrometeorite bombardment can be simulated by impacting meteorites with quartz micro-spheres.

Simulation of micrometeroid and cosmic ray impacts was achieved through nanopulse lasers on olivines and pyroxenes (e.g., Sasaki et al., 2001; Brunetto et al., 2006b)). They showed that laser ablation caused lowering of the albedo, dampening of absorption bands, and reddening of slope, all effects that could ex-

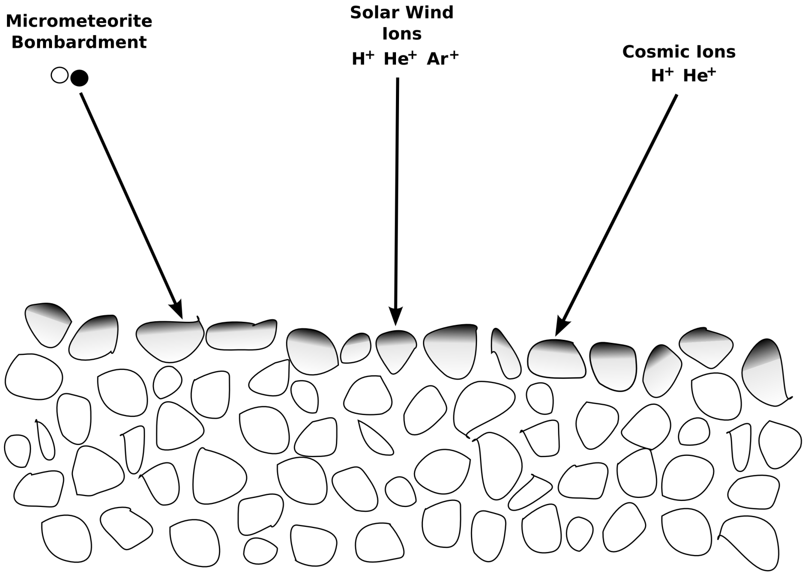

Figure 1.11: This diagram shows the types of processes, including micrometeorite bombardment, solar wind ions, and cosmic ions, that affect the surface of airless bodies. Only the exposed part of the topmost grains are affected. Heavier ions from the Sun such as argon are significant contributors to weathering. In the inner Solar System solar wind is a more important factor than cosmic rays, although farther out in the Solar System, the relative effects of cosmic rays are expected to be more considerable. The different black and white colors represent grains of different compositions. The effect of space weathering is best understood on silicates, for which the grains are darkened and reddened.

plain the transition from "fresh" ordinary chondrite meteorite material to the observed asteroid spectra. It has also been demonstrated that pyroxene is less sensitive to the effects of space weathering than olivine (Hiroi et al., 1999; Hiroi and Sasaki, 2001). Figure 1.12 present the spectra of olivine and orthopyroxene before and after irradiation in a laboratory by nanopulse lasers.

Space weathering in the outer Solar System: Although there is a much lower flux of solar ions at greater distances, space weathering effects are not isolated to the inner Solar System. Laboratory experiments have been performed on ices such as methane (CH_4), methanol (CH_3OH) and benzene (C_6H_6) (Brunetto et al., 2006a). They show that an organic refractory residue forms which darkens and reddens the spectra. When red material such as asphaltite and kerite is irradiated, however, the visible spectrum tends to become more neutral (Moroz et al., 2004). Crystalline H_2O ice is amorphized and NH_3 is destroyed by irradiation (Kouchi and Kuroda, 1990; Mastrapa et al., 2006; Strazzulla and Palumbo, 1998; Cooper et al., 2003). Significant work remains to be realized to advance our understanding of the effects of space weathering in the distant regions of the Solar System.

Surface freshening: While space weathering ages a surface, there are processes which rejuvenate and "freshen" it by shifting regolith, thus surfacing unaltered material just below the top layer. Impacts, if large enough, can cause seismic activity that mobilizes regolith (Richardson et al., 2005). Additionally, YORP (see Section 1.2.5) spin-up is thought to be significant for NEOs, because the uneven radiation distributed throughout the surface increases the rotation rate of the body. Achieving thus fast rotation rates could disturb the regolith layer, and perhaps even cause small grains to escape the surface of these low-gravity bodies (Walsh et al., 2008). Another mechanism occurs when asteroids pass close to a planet and experience large gravitational (tidal) forces that cause "shaking" which surfaces fresher material from just below. A study has shown (Binzel et al., 2010) that there is statistical significance to the freshness

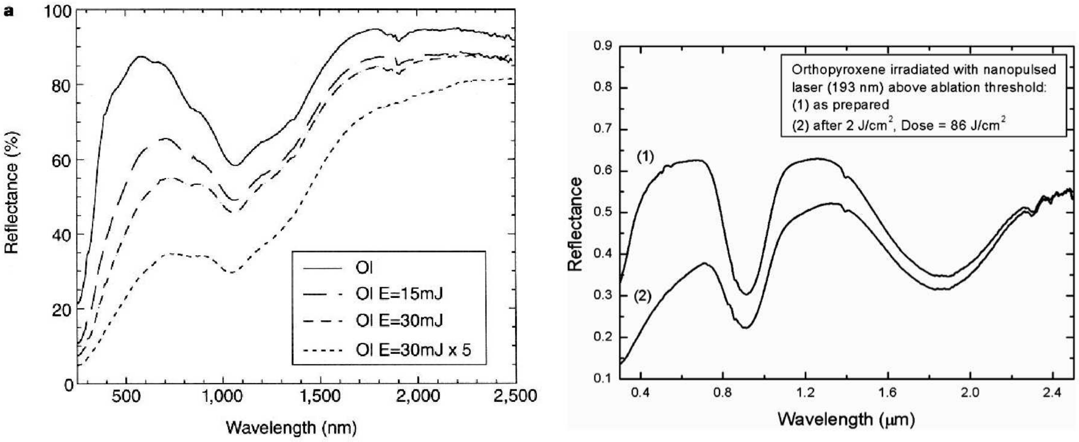

Figure 1.12: Laboratory experiments simulating space weathering through nanophase pulses. **Left:** Olivine before and after specified irradiation doses by Sasaki et al. (2001). After irradiation the reflectance in the visible regime is significantly decreased causing an apparent reddening of the spectrum and decrease in absorption. **Right:** Orthopyroxene before and after irradiation by Brunetto et al. (2006b). As for olivine the reflectance at shorter wavelengths is decreased at shorter wavelengths although the effect is not as pronounced for pyroxene as for olivine.

of an NEOs surface and the value of its Earth Minimum Orbit Intersection Distance (MOID), the closest distance a body should pass by a certain planet by integrating the orbit back a specified number of years.

Chapter 2

Observational Data

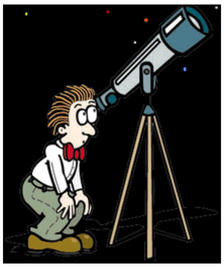

Observations from Earth can provide important information about small bodies, and at a much lower cost than in-situ spacecraft missions. Information such as rotational period, size, shape, density, albedo, and composition can be determined. In this chapter I overview the main observational techniques used for the analysis in this work which include photometry and spectroscopy, describe the telescopes and instruments used to conduct this research, and explain the process of reducing the data to its final, analyzable form. Finally, I describe the two principal observing programs I have been involved in during this thesis.

Contents

2.1 Methods of investigating surface composition

Photometry and Spectroscopy are the primary techniques used to determine the composition of a body's surface. By looking at the changes in reflectance over wavelength, absorption features can be identified that indicate the presence of a material that absorbs light at that particular wavelength. For this work, observations were carried out in the visible and near-infrared from 0.45 to 2.45 microns.

When studying small bodies one is typically interested in the relative reflectance, that is, the reflectance off the surface of the body with respect to the reflectance of the Sun. Since these small bodies don't emit any light at these wavelengths, all light measured from its surface is reflected sunlight. To find the relative reflectance we divide the asteroid spectrum by the solar spectrum. Asteroids are only observable at night, meaning near-simultaneous measurements of the Sun and target body are not possible. A solar-like star (e.g., Landolt, 1992; Persson et al., 1998) is observed instead.

A second and important reason for measuring a standard star is to correct for absorptions due to the Earth's atmosphere. Atmospheric transmission depends on the wavelength as well as the atmospheric conditions (temperature, cloudiness, wind). The regions in the visible and near-infrared that are particularly opaque are 1.4-1.5 microns and 1.8-2.0 microns. See Figure 2.1 for the atmospheric transmission in the visible and near-infrared wavelength region. Because of the effects of the atmosphere, observations with telescopes in space, such as the Hubble and Spitzer telescopes, are particularly valuable.

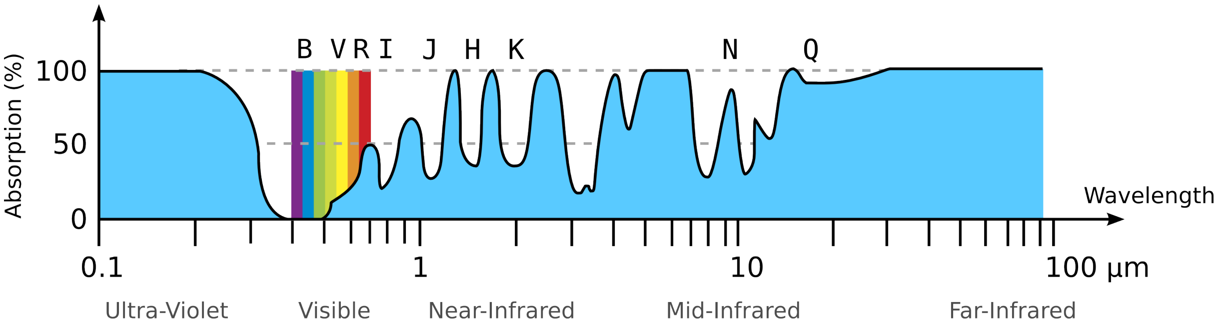

Figure 2.1: Plot representing Earth's atmospheric absorption as a function of wavelength. Interpreting data in regions of strong telluric absorption is difficult and must involve very careful corrections. This plot is reproduced and translated from Carry (2009).

It was previously mentioned that all light measured from a small body is reflected sunlight, however, some NEOs pass so close to the Sun that they are extremely hot and emit thermal radiation even in the near-infrared with a spike in reflectance beginning around 2.3-2.4 microns. Measurements of this "thermal tail" can provide constraints on the surface albedo (Lebofsky et al., 1986; Rivkin et al., 2005). The darker the body, the more light is absorbed at a particular distance from the Sun, and therefore the warmer the body becomes and the more thermal energy it emits.

2.1.1 Photometry

Photometry is an observational imagery technique that measures the flux of incoming light from an object. The total flux in a specific band-filter is measured and is converted into a magnitude.

Photometric measurements in a single band over a few hours are used to measure the lightcurve of an object. By calculating the periodicity of the magnitude with time, the rotation rate of a small body can be determined. This change in magnitude is due either to the shape irregularity of an object where more light is reflected when more surface is exposed in the direction of measurement, or it could be due to heterogeneity on the surface and light and dark patches are exposed during rotation.

Transits, eclipses and occultations are observed using photometry. By measuring the change in magnitude, the rapidity of the change, and the length of time of the transit, constraints can be made on the radius and magnitude of the body as well as the presence or absence of an atmosphere.

Photometric measurements in multiple bands are used to determine the color of an object, for example how blue, red, or neutral it is compared to the colors of the sun. For observing dim objects, particularly for sampling a large portion of TNOs, photometry is the preferred method as opposed to spectroscopy because better signal-to-noise ratios can be achieved since the light is less dispersed than for spectroscopy.

2.1.2 Spectroscopy

Spectroscopy is a measure of emission or reflectance of a source. The incoming light is dispersed according to wavelength. For non-cometary Solar System bodies, the light reflecting off the surface of the body is divided by a spectrum of a solar-like star to determine the reflectance relative to that of the original light source, the Sun. If the resulting spectrum is flat, the light is reflected equally across all measured wavelengths. If the spectrum has a positive slope, more light is reflected at longer wavelengths. Localized dips in the spectrum indicate a particular material is absorbing light at that wavelength. Analyzing these absorption features provides crucial information about the composition on the surfaces of these bodies. For asteroids, signatures at 1 and 2 microns are indicative of olivine and pyroxene. For TNOs, features at 1.5 and 2 microns are indicative of H_2O. A feature at 2.15 microns reveals nitrogen, and a large array of strong absorptions in the visible and near-infrared represent methane. Reflected light penetrates only a few microns below the surface, so spectroscopy probes only the utmost surface layer. Any information about the interior can only be inferred by density measurements.

2.2 Telescopes and Instruments

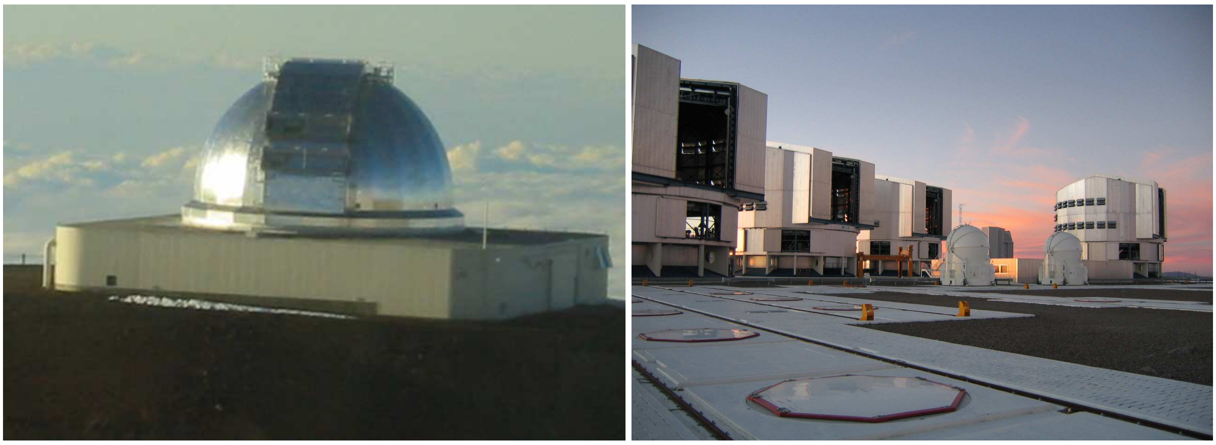

Figure 2.2: **Left:** The NASA InfraRed Telescope Facility at the Mauna Kea Observatory on the Big Island in Hawaii. **Right:** The Very Large Telescope at the Paranal Observatory in the Atacama desert in Chile.

2.2.1 IRTF

The NASA InfraRed Telescope Facility (IRTF) is a 3.0-meter telescope located at the Mauna Kea Observatory summit of Mauna Kea, Hawaii. It is equipped with 4 instruments, SpeX, NSFCAM2, CSHELL and MIRSI, that allow imaging, polarimetry, and low and high resolution spectroscopy in the near to mid infrared. For the work in this thesis we use the instrument SpeX for low resolution spectroscopy. The IRTF is an ideal size for observing MBAs down to diameters of tens of kilometers and NEOs hundreds of meters (and even tens of meters for very close approaches). An image of the IRTF is shown in Figure 2.2.

SpeX: SpeX is a medium-resolution spectrograph and imager that operates in the 0.8 - 5.5 micron range (Rayner et al., 2003), on the 3-meter NASA IRTF located on Mauna Kea, Hawaii. SpeX can be operated in a number of science modes which include, single prism, single order, and cross-dispersed. The resolution ranges from 250 to 2500 depending on the mode and wavelength range. SpeX is a grating spectrograph; the grating is used to disperse the incoming light (the function that a prism could similarly perform).

Observations on the IRTF can be performed anywhere in the world provided the user has a solid internet connection and VNC. Most IRTF observations for this work were performed remotely either at the MIT campus in Cambridge, Massachusetts or at the Centre d'Observation à Distance en Astronomie à Meudon (CODAM) at the Meudon Observatory in Meudon, France.

2.2.2 VLT

The European Southern Observatory (ESO) Very Large Telescope (VLT) (see Fig. 2.2) is located at the Paranal Observatory in the Atacama desert in Chile. It is comprised of four 8.2-meter telescopes. These four units are named Antu, Kueyen, Melipal, and Yepun. For the research presented in this work we used the instruments Focal Reducer Spectrograph 2 (FORS2) and Infrared Spectrometer and Array Camera (ISAAC) on unit 1 (Antu), Focal Reducer Spectrograph 1 (FORS1) on unit 2 (Kueyen), and Spectrograph for INtegral Field Observations in the Near Infrared (SINFONI) on unit 4 (Yepun). The results for TNOs in this thesis come from VLT observations performed either in visitor or service mode. While TNOs are hundreds to thousands of kilometers in diameter, they are far from the Sun and often have dark surfaces. Thus their visible magnitudes are often greater than 20 even in the most ideal conditions. The VLT and other large telescopes are crucial for the study of the surfaces of TNOs because spectroscopic observations are not possible on smaller telescopes.

FORS: FORS, a visible (0.33 - 1.1 μm) imager and spectrograph, is installed on both Unit 1 (FORS2) and Unit 2 (FORS1) of the VLT. After a Charge-Coupled Device (CCD) change in 2007, FORS1 was optimized to the blue range (less than 0.6 μm), so observations were then taken using FORS2 which is optimized to the red range. FORS1 is equipped with two 2k x 4k E2V CCDs, while FORS2 has two 2k x 4k MIT CCDs, each with 15 μm pixels. The field of view is $6.8'$ x $6.8'$. Photometry observations were performed in IMA (imaging) mode and spectroscopy in LSS (long slit spectroscopy; resolution 200) mode. The BVRI filters used for photometry are centered at 0.429 μm, 0.554 μm, 0.657 μm and 0.768 μm.

ISAAC: ISAAC (Infrared Spectrometer and Array Camera, Moorwood et al., 1998) is an infrared (1 - 5 μm) imager and spectrograph. For work presented here we use the the short wavelength arm in imaging and low resolution spectroscopy (resolution 500) modes with the 1024 x 1024 Hawaii Rockwell array with a pixel size of 18.5 μm. The pixel scale is 0.148"/pixel and the field of view is $2.5'$ x $2.5'$. For photometry, the J, H, and K_s filters were used with central wavelengths of 1.25, 1.65, and 2.16 μm, respectively, each with widths of about 0.3 μm.

SINFONI: SINFONI (Eisenhauer et al., 2003; Bonnet et al., 2004) is a near-infrared (1.1 - 2.4 μm) echelle spectrograph mounted on the Cassegrain focus of Unit 4 of the VLT. The spectrograph has 4 gratings, J, H, K, and H+K each with a spectral resolution of 2000, 3000, 4000, and 1500, respectively. There are three spatial resolutions to choose from, 0.25", 0.1" and 0.025" per image slice, which correspond to a field-of-view of 8"x8", 3"x3", or 0.8"x0.8", respectively.

The echelle grating is used for high resolution and a cross disperser is used to separate orders which are projected on a 2D CCD array. Its field of view is split into 32 image-slitlets which reflect onto small plane mirrors before being re-directed toward the grating. The 32 spectra are then re-imaged on a 2048 x 2048 pixel Hawaii 2RG μm near-infrared detector. A diagram of this process is shown in Figure 2.3.

SINFONI may be used with or without Adaptive Optics. The AO module of SINFONI can be fed by an artificial sodium laser guide star (LGS) for high-order AO corrections. A natural guide star is also required to correct for the tip-tilt motions, which are not sensed by the LGS. Figure 2.4 depicts how AO operates.

2.3 Data Reduction

Here we describe the reduction process of the observational data to its final form. We first introduce the calibration files needed for reduction and then describe the basic process for photometry and spectroscopy. More information on CCDs and the reduction process can be found in the book "Handbook of CCD Astronomy" (Howell, 2006).

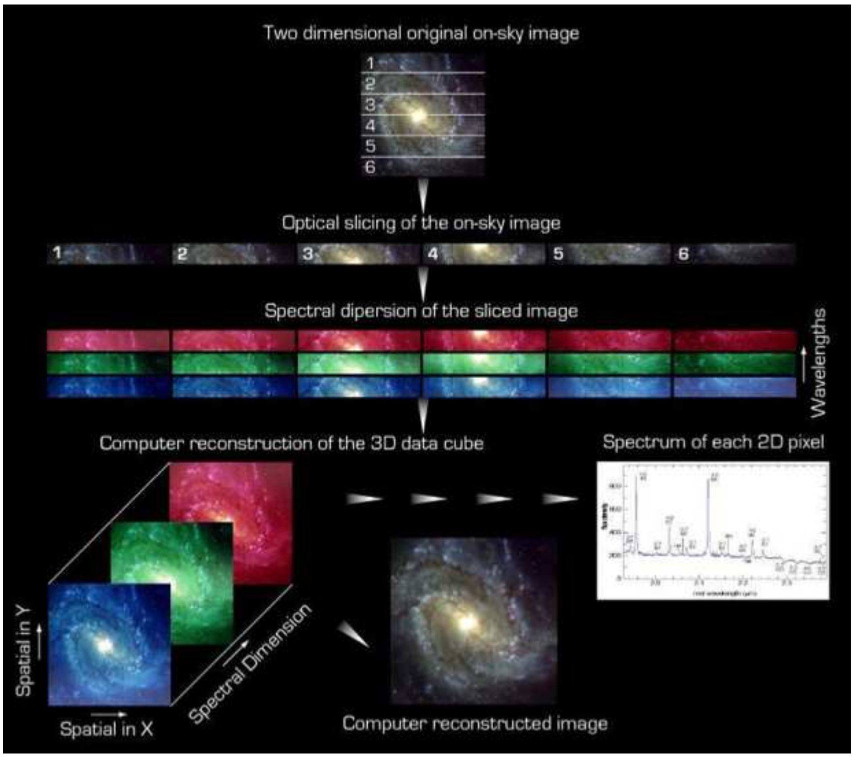

Figure 2.3: Diagram demonstrating how the image field is split into separate segments, each segment is dispersed separating the light per wavelength and finally a 3D image cube is reconstructed with the X and Y spatial dimensions on each slice with 2048 slices which represent the spectral dimensions (each slice represents a certain wavelength). (Source: SINFONI User Manual)

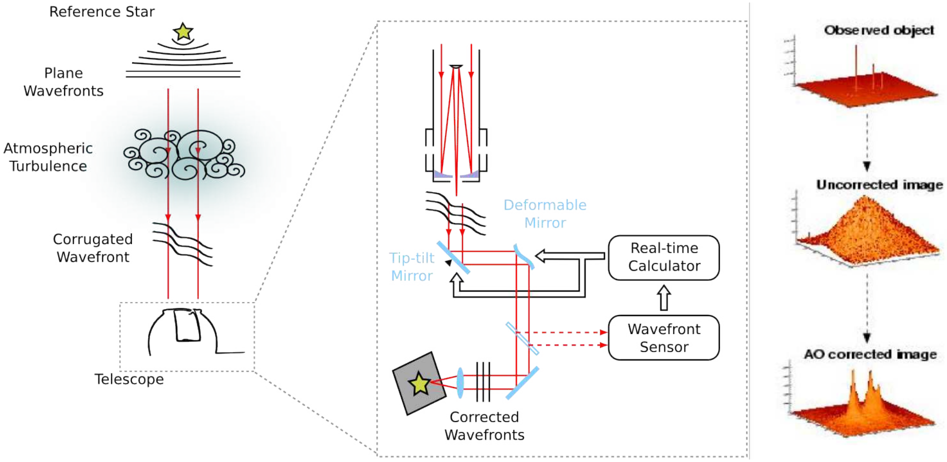

Figure 2.4: This diagram depicts how images are corrected using AO. The left side of the diagram shows that light is affected by the atmosphere before entering the telescope. Wavefront distortions are measured by a real-time computer. A deformable mirror then performs low and high order corrections to compensate. The goal of AO is to achieve diffraction-limited images. The right side of the image shows the observed object, the resulting image uncorrected by Adaptive Optics where the three sources are not distinguishable, and finally the AO corrected image where the three sources are resolved (Source: Carry (2009) and SINFONI User Manual).

2.3.1 Calibration files

- **Bias:** A CCD's zero-level is a positive value. In other words, an unexposed pixel may have a signal. To measure this underlying noise called the bias, an image of a zero second exposure time is taken to determine this value to correct for it.
- **Dark:** Any material at a temperature above absolute zero will be affected by thermal noise. On a CCD, electrons can be excited and freed from the valence and are subsequently collected within the potential well of a pixel. It is not possible to distinguish between the signal from these electrons and that of the measured astronomical light (photons). To minimize this effect CCDs are generally cooled to low temperatures.

  To correct for this extra signal, an exposure is taken of similar length as the target data, however, in this case, the dome and shutter are closed and no light can enter. Any measurement recorded is thus the thermal noise and this signal can be subtracted from the target data. These dark images can also be used to find dead or hot pixels. When dark frames are used, the CCD bias is contained within them and separate bias corrections are not necessary. Typically, multiple dark exposures are taken and the mean or median is calculated to create a "master dark" file.
- **Flat:** Each pixel on a detector has a slightly different efficiency. A flat field image to correct for this effect is usually obtained by illuminating the dome with a light source (a projector lamp), and taking a number of short exposures. Ideally, each pixel should be uniformly illuminated, however, this is never the case. To flatten the response of each pixel, removing the variation among pixels, the target data is divided by a flat field image. As for dark frames, multiple flat field frames are taken and a "master flat" field file is created from the mean or median of all frames.
- **Arc lamp:** Standard or "arc" lamps are used create a pixel to wavelength correspondence to calibrate the data. Arc lamps are typically helium, neon, xenon, argon or a combination. The emission lines from the spectrum of the arc lamp are at known wavelengths and can be identified.
- **Standard star:** For spectroscopy, a solar-like standard star taken at similar airmass as the target is required to correct for atmospheric effects and to remove the signature of the Sun's spectrum from the data to leave only the signature of the target's surface. For photometry, photometric standard stars of well known magnitudes that are not variable are taken to calibrate the relative flux of the target and star to the actual magnitude. Multiple stars throughout the night are needed to correct for atmospheric extinction.

2.3.2 Photometry Reduction

For photometry reduction, the master dark frame is subtracted and the master flat is divided. In the near-infrared, the target is observed in a "jitter" pattern meaning it is moved to a different part of the field for each exposure for optimum sky background correction. The individual frames must thus be shifted and combined into one final file. The flux of the target is then determined by summing the flux within an aperture determined by the seeing and growth curves of the objects. The growth curve is the flux increase per increase in radius. The ideal aperture size maximizes the flux from the target while minimizing background flux from the sky or other objects. The radius is typically 3-5 times the full width at half maximum (FWHM). A flux to magnitude correspondence is calculated by relating the flux of the standard star to its known magnitude. The zero point, extinction coefficient and color term for that night is also calculated for that night of observing. The flux of the target can then be calculated from the star flux to magnitude relation.

2.3.3 Spectroscopy Reduction

To reduce asteroid spectroscopy data, the relevant callibration files include standard star spectra, dark spectra, and flat fields. Once the dark files have been subtracted and the flat fields divided, the two dimensional spectrum is collapsed to one dimension. To find the correspondence between pixel and

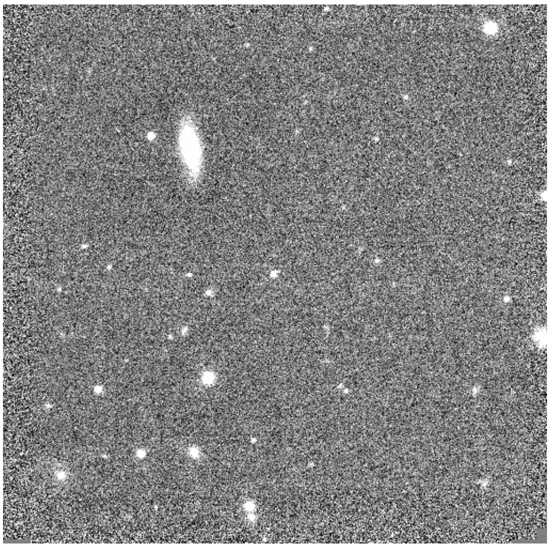

Figure 2.5: Example of an ISAAC image field. The target is typically centered and can be identified by finding its expected location at the time of observation with respect to the background field.

wavelength, the emission features of the lamp must be identified and labeled according to their known wavelength. The target spectra can thus be calibrated using this dispersion relation.

Because we study bodies that do not emit their own light, they reflect sunlight, we want to account for the properties of the Sun's spectrum. Since the Sun cannot be observed during these night time observations, solar-like standard stars are chosen. The target spectrum is divided by that of the standard star. If 100% of the light over every wavelength was reflected, the result would be a flat line of constant value. Since material on the surface scatters and absorbs the light, the division often results in departures from linearity. The spectra can then be normalized to unity at a given wavelength. Visible data is typically normalized at 0.55 μm.

2.4 Observational Programs

The data for this thesis comes primarily from two long-term programs I have been involved with. Here I describe each of these observing campaigns.

Asteroids: In collaboration with researchers at MIT, and as an extension of work I started as an undergraduate student, I contribute to the Small Main-Belt Asteroid Spectroscopic Survey (SMASS, smass.mit.edu). Originally, the goal of this program was to spectroscopically investigate Main-Belt asteroids. In visible wavlengths, over 1,000 spectra were published (Bus and Binzel, 2002b) and are publicly available on the website. The program was extended to survey near-Earth objects under the "MIT-UH-IRTF Joint Campaign for NEO Reconnaissance" which aims to publicly release near-infrared spectral data shortly after observation (e.g., Binzel et al., 2006b). I have been involved in observing, reducing, and analyzing the SpeX IRTF data that we have acquired during this program.

TNOs and Centaurs: As part of the TNO team in Laboratoire d'Étude Spatial et d'Instrumentation en Astrophysique (LESIA) at the Paris Observatory, I have been involved in the Large Program lead by Dr. M. A. Barucci. Based on observations carried out between 2006 and 2008 using the ESO VLT and the NTT (New Technology Telescope), this program is dedicated to investigating the surface properties of Centaurs and Transneptunian objects. Observational methods included spectroscopy, photometry (colors and lightcurves), and polarimetry. During this campaign 45 objects were observed, a significant fraction of which had never previously had photometric or spectroscopic measurements, allowing us for the first time the gain an understanding of the TNO population by analyzing full visible to near-infrared spectra.

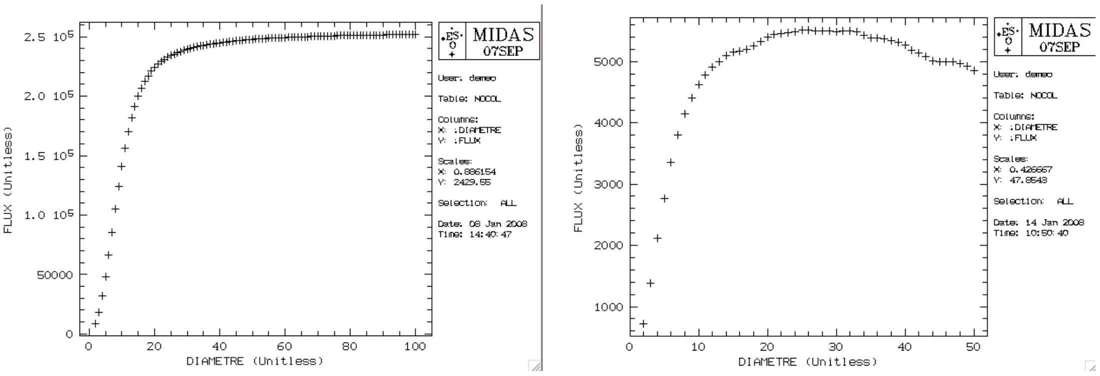

Figure 2.6: **Left:** Example of a growth curve for a star. This plots the flux within the circular aperture as a function of the aperture's radius. The curve shown here is ideal for measuring total flux because the radii which contain nearly 100% of the flux of the target can easily be determined. **Right:** Example of good TNO growth curve. While not as ideal as seen with the star, it adequate to find a flux estimate.

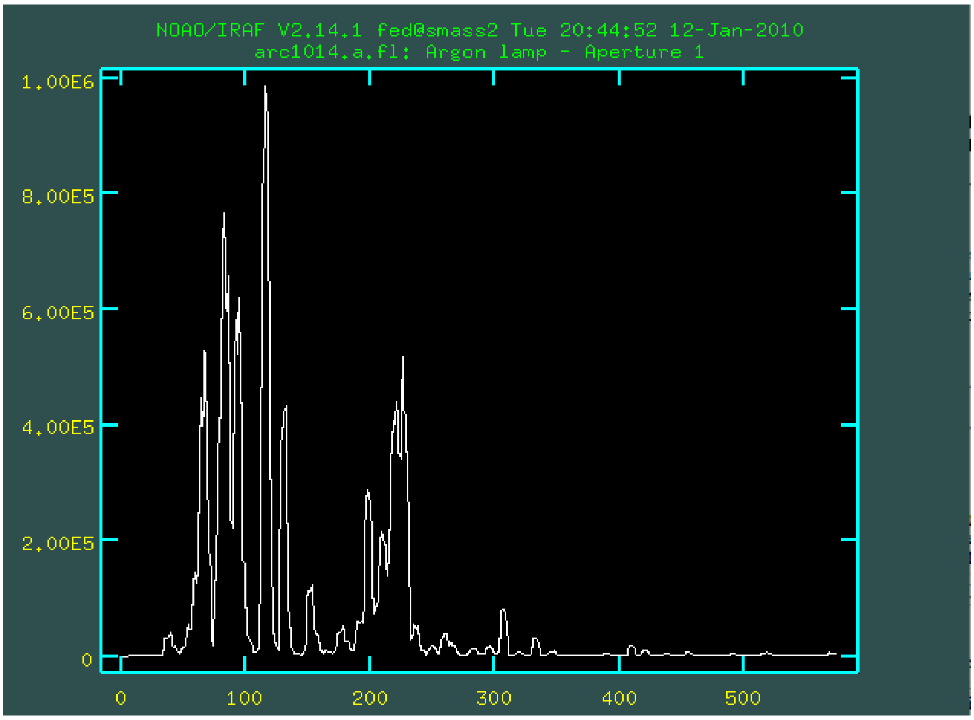

Figure 2.7: This image shows an arc file from an IRTF observation. To calibrate it, each peak must be identified and assigned a wavelength.

Chapter 3

Methods of Analysis

Here I summarize the principal methods of analysis used for the work in this thesis. Principal Component Analysis was used to define boundaries for spectral taxonomic classes in the Bus-DeMeo system described in Chapter 4. G-mode analysis was used to classify TNO colors in Chapter 5. The Hapke model of bidirectional reflectance was crucial in modeling spectral features of icy TNOs to determine composition in Chapters 6 and 7. An alternative reflectance model, the Shkuratov model is also described. Finally, I briefly introduce the space weathering models of Hapke and Brunetto used in ongoing research during this thesis.

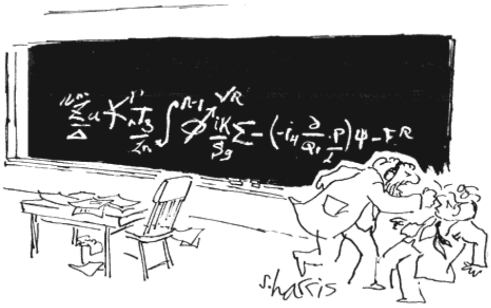

"You want proof? I'll give you proof!"

Contents

3.1 Classification Methods

3.1.1 G-mode analysis

G-mode analysis, developed by Coradini et al. (1977), is an analytical technique that can be used for assignment to a taxonomic class. The method was first introduced to asteroid taxonomy by Barucci et al. (1987). An important advantage to this method is that even if only a subset of variables are available for an object (i.e. only part of a spectrum, or an incomplete set of photometric colors), a preliminary classification can still be achieved.

G-mode takes an initial data array of $N \times M$ where N is the total number of objects each with M variables. Equations 3.1 through 3.4 are the main components of the tool, presented in the notation from Fulchignoni et al. (2000).

$$z_j^2 = \sum_{i=1}^{M} z_{ij}^2 = \sum_{i=1}^{M} \frac{(x_{ij} - \bar{x}_{ij})^2}{\sigma^2} \tag{3.1}$$

z_j^2 is a variable describing the sample, x_{ij} is the ith variable of the jth sample and $\bar{x}_i$ and σ_i are the mean value and standard deviation for the ith variable. Each sample is then tested for its proximity to a “zero class” for class identification. The center of the “zero class” is defined by the following equation, the sum of the three closest samples:

$$z_{p,q,t} = \sum_{i=1}^{3} [(z_{pi} - z_{qi})^2 + (z_{pi} - z_{ti})^2 + (z_{qi} - z_{ii})^2] \tag{3.2}$$

where z_{pi}, z_{qi}, z_{ti} are the normalized values of the ith variable of the pth, qth and tth variables, respectively. The mean (x_*) and standard deviation (σ_*) for each of these variables is then computed:

$$x_* = \frac{1}{3} \sum_{j=1}^{3} x_{ij} \tag{3.3}$$

$$\sigma_* = [\frac{1}{2} \sum_{j=1}^{3} (x_{ij} - x_*)^2]^{1/2} \tag{3.4}$$

The user must then decide the size of the class by choosing a value that defines the boundary. An object is assigned to a class if it falls within that boundary. The statistical distance of a sample from a taxonomic class calculated to determine how good of a fit an object is to a certain class.

For the work presented in Chapter 5, we use the statistical distance value defined by Barucci et al. (2005a) corresponding to a classification confidence of $\pm 3\sigma$. A simple description summarizing the G-mode method can be found in Tosi et al. (2005) and Barucci et al. (1987).

3.1.2 Principal Component Analysis

Shlens (2009) and Smith (2002) are two useful Principal Component Analysis tutorials on which this description is based. Principal Component Analysis was used for the work described in Chapter 4, also presented in DeMeo (2007) and DeMeo et al. (2009a).

Principal Component Analysis (PCA) is a method of reducing the dimensionality of a data set, involving linear coordinate transformations to minimize the variance. The first transformation rotates the data to maximize variance along the first axis, known as Principal Component 1 (PC1$'$), the second axis is the second Principal Component (PC2$'$). The first few principal components contain the majority of the information contained within the data set. An illustration of how PCA works on a sample is shown in Fig. 3.1.

Discovering the relationship between two dimensions is usually relatively straightforward. The data could be fit by a line, polynomial, gaussian, or other fitting equation that minimizes the residual of the data. As the number of dimensions increases, finding relationships among all dimensions becomes increasingly difficult. This is where PCA is useful, because it seeks to minimize the greatest amount of variance with each component. Thus ordering the components in order of importance. The first few being the most important. Higher order principal components are often noise.

The variance (σ_A^2) of a vector A (where $A = \{a_1, a_2, ...a_n\}$) is

$$\sigma_A^2 = \frac{1}{n}\sum_i a_i^2 \tag{3.5}$$

The covariance between A and B (B is another vector) measures the degree of the linear relationship between two variables. The greater the absolute value of the covariance, the stronger the correlation. Positive covariance values signify positively correlated data and large negative values signify negatively correlated data. The covariance between A and B is calculated as:

$$\sigma_{AB}^2 = \frac{1}{n}\sum_i a_i b_i \tag{3.6}$$

When more than two dimensions are involved a covariance matrix C$_X$ of a matrix X can be calculated. In the case for this work each column of matrix X corresponds to a certain wavelength and each row contains the measurements at each wavelength for a certain asteroid.

$$C_X = \frac{1}{n}XX^T \tag{3.7}$$

where X^T is the transpose of matrix X. C$_X$ is thus a square symmetric matrix where the diagonal terms are the variance and the non-diagonal terms are the covariance. The greater the variance between two values the more important they are because they each contain different information (they maximize the signal). On the other hand, the greater the covariance between two values are the more related these values are; combined they do not provide much more information than each does individually and thus they are redundant.

An optimized matrix would minimize all non-diagonal terms (that measure how related values are) and maximize the variance, the information, contained within it. PCA does this by multiplying the covariance matrix by basis vectors (p$_1$,...p$_m$) that are all orthonormal. So, PCA finds the normalized direction, p$_1$, along which the variance is maximized. Next, a direction p$_2$ is computed that maximizes the remaining variance and is orthonormal to p$_1$. This is repeated for all vectors within the set.

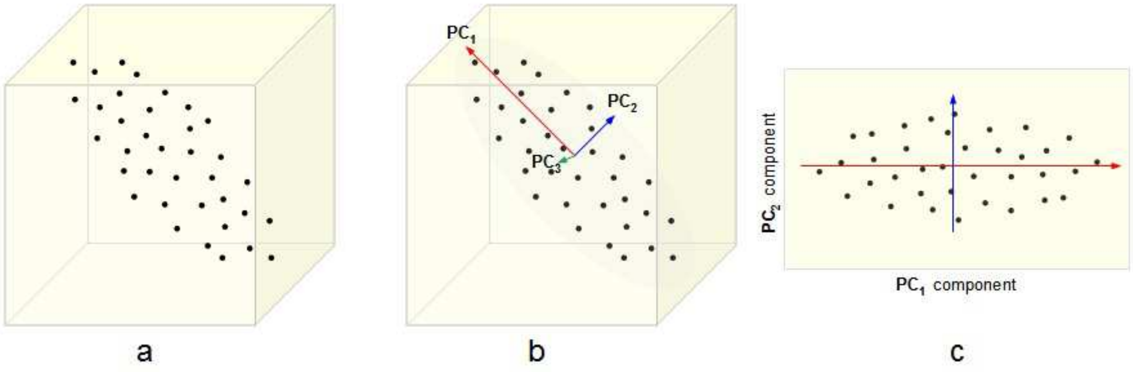

Figure 3.1: An illustration of PCA. a) A data set given as 3-dimensional points. b) The three orthogonal Principal Components (PCs) for the data, ordered by variance. c) The projection of the data set into the first two PCs, discarding the third one. (Figure and Caption source: Dimensionality Reduction Methods for Molecular Motion)

There are three important assumptions to Principal Component Analysis:

1. All transformation are created by *linear* fits to minimize variance. If the data is non-linearly related, PCA may not be the most efficient data analysis method.

2. Larger variances are more significant. The method assumes that greater variance between values provides more important information. If data has low signal to noise and the noise add significant variance to the data set, the noise will be contained within the first, and most important, principal components. Similarly, if greater variance does not necessarily correlate with greater importance this ordering of components is not ideal.

For example, if spectra have large, broad features as well as small, subtle features, PCA will be biased toward recognizing the large features as the most interesting, and thus these features will dominate the first principal components. If the presence of either the large or small features is considered of equal importance regardless of their size or strength, one must recognize this inherent bias in PCA. This was particularly important for this work, where the presence of a more minor feature can be as equally distinguishing and unique as a larger feature, and this must be considered carefully when creating class boundaries and understanding the limits of PCA.

3. The principal components are orthogonal which allows a simple solution.

To compute the principal components of a data set, the transpose of the eigenvector is multiplied by the transpose of the mean-subtracted data set as described in Eq. 3.8:

$$PC_x = [E_x^T][D^T] \tag{3.8}$$

where PC_x is principal component x and E_x is eigenvector x. D is the column vector containing, in the case for this work, an individual reflectance spectrum, normalized to unity at 0.55 μm, from which the mean channel value has been subtracted at each wavelength.

3.2 Bidirectional Reflectance Models

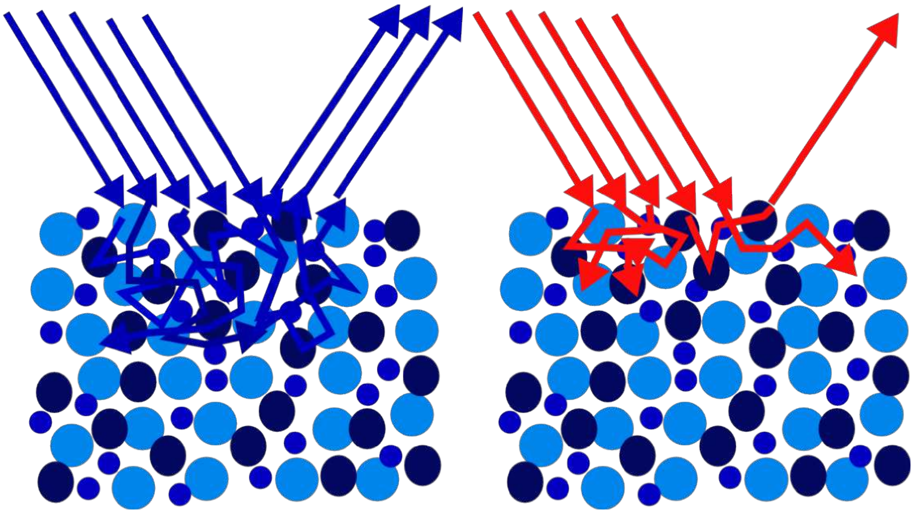

Figure 3.2: For this blue surface, more blue light is reflected than red light. Different colors, and thus different wavelengths, probe different depths of the surface. (This figure is modified from a similar figure by W. Grundy)

Interpreting a spectrum is not necessarily straightforward. Many factors need to be taken into account. The viewing geometry can affect overall reflectance levels and the overall slope. The depth probed is dependent on many factors, such as the opacity of the material, the wavelength of the light, and the grain size. As grain size increases, albedo levels decrease and absorption features widen and deepen. The relative abundances of each material is significant since some molecules are more optically active (and therefore dominate a spectrum's signature) than others. Intimate mixtures of materials are also not necessarily linear combinations of their individual components. Temperatures affect spectra and often cause phase changes in materials such as ices. Therefore linearly combining laboratory spectra of samples taken under limited conditions cannot adequately reproduce a spectrum of a small body in space. Luckily, there are models that take into account these factors by approximating radiative transfer equations. The most commonly used spectral models include the Hapke (Hapke, 1981, 1993) and Shkuratov (Shkuratov et al., 1999) models. In this work only Hapke modeling is applied, and it is described in this section. For a full description of the theory see Hapke (1993).

Hapke theory provides an approximate solution to the radiative transfer equation that describes the emission, absorption, and scattering of light on a nonuniform particulate surface. Exact solutions have been derived (i.e., Chandrasekhar, 1960), but other theories have either required too much computation or were too general. Hapke theory has few free parameters and is comparable with exact solutions within the accuracy of the observational measurements.

Shkuratov et al. (1999) created a one-dimentional model intended particularly for understanding lunar regolith. The approximations and assumptions simplify the model making it depend on fewer variables than for Hapke (1981, 1993). Poulet et al. (2002) perform a comparison of the Hapke and Shkuratov models and find the main differences is the treatment of the phase function, which is a free parameter Hapke model but is fixed in the Shkuratov model. Also, because of the manner in which the materials are mixed, the Hapke model is a valid approximation for a wider variety of situations. For example, the Shkuratov model ignores the angle dependence of reflectance so it is not appropriate for analysis of resolved surfaces.

These models combine optical constants derived from laboratory spectra of different materials under conditions expected to be on the surfaces of small bodies to recreate the telescopic spectral data by calculating the geometric albedo. Optical constants are comprised of the real and imaginary refractive index, as shown in Eq. 3.9

$$m = n + ik \tag{3.9}$$

where m is the complex refractive index, n is the real refractive index and k is the extinction coefficient of the material.

There are two types of mixtures that can be modeled, geographic (areal) and intimate (homogenous). For geographic mixtures, the reflectance of each material is calculated separately and each reflectance is linearly combined based on the total fraction of the surface it represents. It is often referred to as a "checkerboard" mixing of material because each component is spatially separated from the others and incoming light reflects off only grains of one composition. Intimate mixtures, also described as "salt and pepper" mixtures, are where light scatters off multiple types of particles before finally being reflected. The single scattering albedo, w, is calculated for each type grain and a final average is calculated. A third type involves the mixing of components at the molecular level, such as methane diluted in nitrogen in the case for Pluto and Triton. The spectra of molecular mixtures of some materials, particularly ices, are not necessarily equal to the sum of the pure solid components. In this case, the optical constants of the mixture are necessary, and the mixture is created as a single input for the modeling. Figure 3.3 shows the different ways that components can be mixed on a surface.

3.2.1 Hapke Model

The reflectance, the fraction of incident light scattered or reflected by a material, is affected by absorption, scattering, and emission. Different types of emission include single scattering, thermal emission, fluorescence and luminescence, and stimulated emission, although only the first two are relevant to particulate surfaces for this work. For planetary regoliths, we assume a particulate surface of irregularly shaped particles.

The type of reflectance is described by two adjectives, the first being the collimation (how parallel the rays are) of the source, and the second of the detector. The collimation can be directional, conical, or hemispherical. For this work, bi-directional (both the source and detector have directional collimation) and bi-hemispherical reflectance are applicable.

To calculate the geometric albedo using the Hapke model, several parameters need to be defined. α is the volume absorption coefficient inside a particle (Eq. 3.10), where k is the extinction coefficient and λ

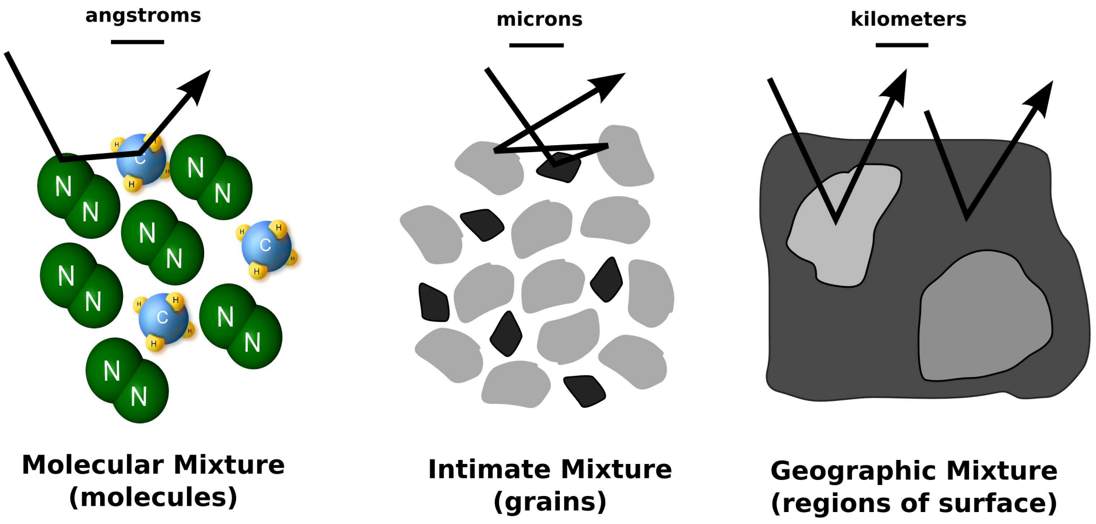

Figure 3.3: This figure shows the different types of mixtures that can be found on a surface. For a molecular mixture, with molecules of sizes typically on the order of angstroms, individual molecules of different species are mixed. A photon may interact with different molecules before finally being reflected. For an intimate mixture, with grains typically tens to hundreds of microns, different types of grains are mixed. A photon may interact with multiple different types of grains before finally being reflected. For a geographic mixture there are patches of a single component that may span for hundreds of meters to hundreds of kilometers. A photon will interact only with grains of a single component. The molecules are not to scale. (Molecule image sources: N_2, CH_4)

is the wavelength. It represents the power scattered relative to the total power removed, or the decrease in power due to absorption of the beam's energy as it propagates.

$$\alpha = \frac{4\pi k}{\lambda} \tag{3.10}$$

μ and μ_0 describe the geometry of the system where e and i are the angle of emergence and incidence, respectively.

$$\mu = cose \tag{3.11}$$

$$\mu_0 = cosi \tag{3.12}$$

The surface scattering coefficient of a particle for diffuse light incident externally (S_e) is defined in Eq. 3.13 (Eq. 6.20 of Hapke, 1993).

$$S_e = \frac{(n-1)^2 + k^2}{(n+1)^2 + k^2} + 0.05 \tag{3.13}$$

The surface scattering coefficient of a particle for diffuse light incident internally (S_i) is defined in Eq. 3.14 (Eq. 6.23 of Hapke, 1993).

$$S_i = 1 - \frac{4}{n(n+1)^2} \tag{3.14}$$

The average single-scattering albedo (w) is defined in Eq. 3.15 (Eq. 11.14 of Hapke, 1993). The single-scattering albedo describes the albedo when light is scattered only once off a single regolith particle.

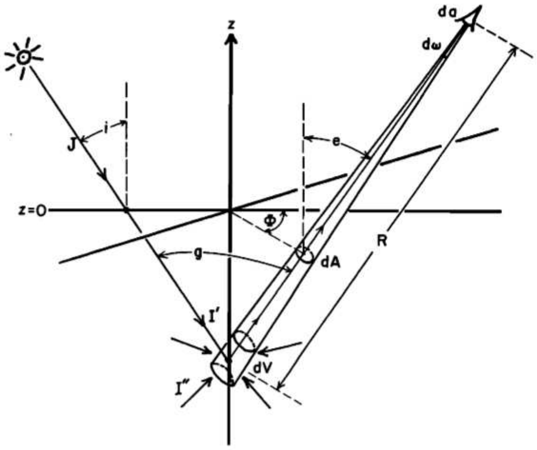

Figure 3.4: This is a diagram of Hapke geometry from Hapke (1981). The incident light J makes an angle i with the z-axis, and the reflected light makes an angle e with the z-axis. The detector has an area *da* and receives light within the solid angle $d\omega$. (Source: Hapke, 1981)

It averages the single scattering albedos of the individual particles weighted by their extinction cross-sectional areas. For the following equation D is the average path length, generally considered on the order of the grain size.

$$w = S_e + \frac{(1 - S_e)(1 - S_i)e^{-\alpha D}}{(1 - S_i e^{-\alpha D})} \tag{3.15}$$

The Chandrasekhar H function for isotropic scatterers is simplified for the reflectance equation and is given in Eq. 8.55 in Hapke defined here in Eq. 3.16.

$$H_\mu = \frac{(1 + 2\mu)}{1 + 2\mu(1 - w)^{\frac{1}{2}}} \tag{3.16}$$

The bihemispherical reflectance (Eq. 3.17) for isotropic scatterers is described by Hapke (1981) as “the brightness of a surface viewed at arbitrary angles compared to a Lambert surface illuminated normally.” A Lambert surface scatters light equally in all directions.

$$r = \frac{w}{4}\frac{\mu_0}{\mu_0 + \mu}([1 + B(g)]P(g) + H(\mu_0)H(\mu) - 1) \tag{3.17}$$

$B(g)$ (Eq. 3.18) in the above equation characterizes the opposition effect, also known as the shadow-hiding effect. At small phase angles the reflectance follows a nonlinear trend. As the phase angle approaches zero there is a sharp surge in brightness. It affects surfaces on which the particles are large compared to the wavelength of the incident light, particularly for fine grain powders less than about 20 μm. The particles on the surface cast shadows on grains deeper down. These shadows are visible at large phase angles, but at very low phase angles the shadows are hidden by the objects that cast them.

$$B(g) = \frac{B_0}{1 + \frac{1}{h}tan(\frac{g}{2})} \tag{3.18}$$

Above, h is the angular-width parameter, also called the compaction parameter, and characterizes the width of the opposition effect peak. “g” is the phase angle, the angle between the Sun, object, and the Earth. B_0 is the value of $B(g)$ at a phase ange of zero.

P(g) from Eq. 3.17 represents the average phase function of particles on the surface. Also called the scattering profile, it describes the amount of incident light scattered in a certain direction. It is often approximated by a series of Legendre polynomials or by the Henyey Greenstein function (Henyey and Greenstein, 1941). The single Henyey Greenstein function is given in Eq. 3.19.

$$P(g) = \frac{1-\xi^2}{(1+2\xi cos(g)+\xi^2)^{\frac{3}{2}}} \tag{3.19}$$

where ξ is the cosine asymmetry factor, which defines whether a surface is forward- ($\xi > 0$), back- ($\xi < 0$), or isotropically- ($\xi = 0$) scattering.

In the case of most planetary regoliths, there is roughness on scales much larger than the particle size, geological features on the order of meters to kilometers. There are three main effects of macroscopic roughness as described by Hapke (1993): 1) Light is scattered from one facet to another which increases the reflectance, 2) Unresolved shadows cast on one part of the surface decreases the reflectance, and 3) As the zenith angle increases, the facets tilted away from the observer will be in shadow while those tilted toward the observer are illuminated and visible. The macroscopic roughness of the surface is accounted for by Eq. 3.20 and is dependent on $\bar{\theta}$, the mean slope angle.

$$S(i,e,\psi) \simeq \frac{\mu_e}{\mu_e(0)} \frac{\mu_0}{\mu_{0e}(0)} \frac{\chi(\bar{\theta})}{1 - f(\psi) + f(\psi)\chi(\bar{\theta})\frac{\mu}{\mu_e(0)}} \tag{3.20}$$

where

$$f(\psi) = e^{-2tan\frac{\psi}{2}} \tag{3.21}$$

Finally the geometric albedo can be calculated by including all the above equations.

$$A_r = \frac{w}{4\pi} \frac{\mu_0}{\mu_0 + \mu}([1 + B(g)]P(g) + H(\mu_0)H(\mu) - 1)S(i,e,\psi) \tag{3.22}$$

3.2.2 Shkuratov Model

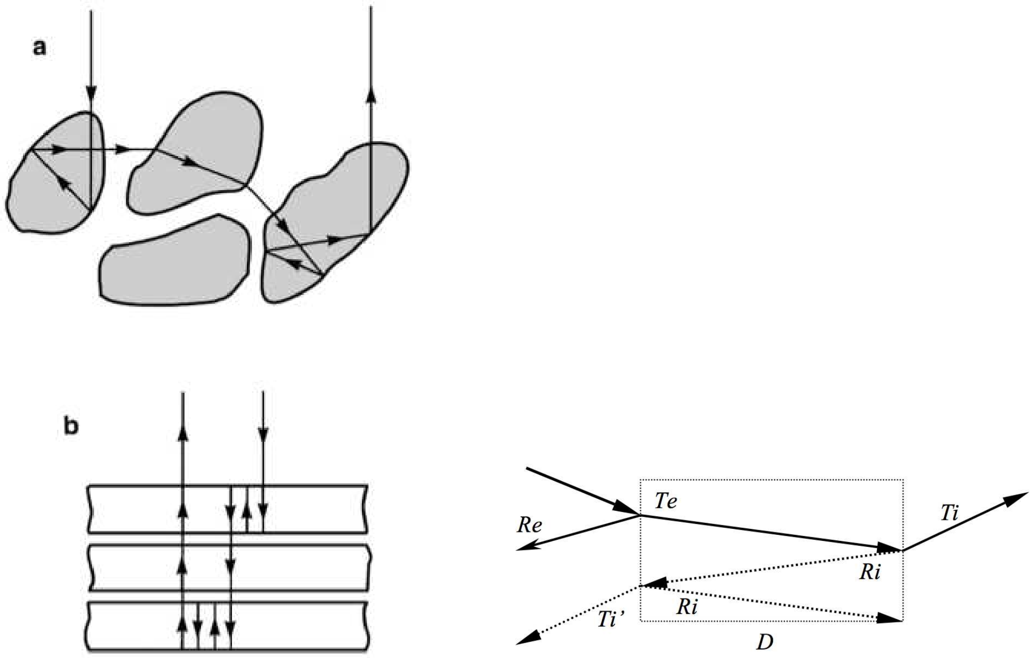

Figure 3.5: **Left:** Part "a" of this diagram shows the behavior of light scattering randomly on irregular particles. Part "b" demonstrates the assumed geometry for the Shkuratov model which approximates the grains as planar slabs (figure from Shkuratov et al., 1999). **Right:** Diagram of the light in the Shkuratov model with labels for the different components (from Barucci et al., 2008a).

The reflectance is calculated by assuming light passes through a half-infinite stack of layers. The Shkuratov model begins by calculating the albedo of a particle approximated by light reflecting on a planar slab. Multiple reflections are accounted for as scattering within this slab. The fraction of light scattered backward (r_b) and forward (r_f) are then found based on the average external and internal reflection coefficients (R_e and R_i) and the optical density, τ.

For intimate mixtures for the Shkuratov model, r_b and r_f are linearly combined for each grain type and then an average for all types according to their abundance is calculated to find the average single scattering albedo.

As light propagates through a medium it is characterized by the reflection, R, and transmission, T, coefficients which depend on the complex index of refraction and the angle of incidence. Each of these coefficients is separated into incidence and emergence terms, for incoming and outgoing light, respectively, subscripted with i and e. A few key equations and approximations are listed below.

$$r_o = (n-1)^2/(n+1)^2 \tag{3.23}$$

$$R_e \approx (r_o + 0.05) \tag{3.24}$$

$$R_b \approx (0.28 \cdot n - 0.2) R_e \tag{3.25}$$

$$R_i \approx 1.04 - 1/n^2 \tag{3.26}$$

r_o is the Fresnel coefficient at the normal incidence, R_b and R_f are the average backward and forward reflectance coefficients and R_e is the sum of the two, and R_i is the average coefficient of internal reflection inside a particle.

The fractions of light scattered by a particle backward and forward are then calculated r_b and r_f. These equations are dependent on the optical density, τ.

$$\tau = \frac{4\pi k D}{\lambda} \tag{3.27}$$

where k is the imaginary part of the complex index of refraction (the extinction coefficient) and D is the average path length of the light. The fraction of light scattered backward and forward is given below.

$$r_b = R_b + \frac{\frac{1}{2} T_e T_i R_i e^{-2\tau}}{1 - R_i e^{-\tau}} \tag{3.28}$$

$$r_f = R_f + T_e T_i e^{-\tau} + \frac{\frac{1}{2} T_e T_i R_i e^{-2\tau}}{1 - R_i e^{-\tau}} \tag{3.29}$$

$$p_b = q \cdot r_b \tag{3.30}$$

$$p_f = q \cdot r_f + 1 - q \tag{3.31}$$

Here, q is the volume fraction filled by particles.

Finally, the albedo of a half-infinite stack of the layers can be calculated.

$$A = \frac{1 + p_b^2 - p_f^2}{2p_b} - \sqrt{\frac{1 + p_b^2 - p_f^2}{2p_b} - 1} \tag{3.32}$$

3.3 Space Weathering Models

Space weathering affects the continuum of a silicate-rich spectrum, but does not greatly affect the positions or relative intensities of the bands (Brunetto et al., 2006b). Weathering causes a greater slope increase at visible wavelengths than near-infrared and decreases the overall albedo (Hapke, 2001; Pieters et al., 2000). There are two space weathering models, a more sophisticated model by Hapke (2001) and a simpler model by Brunetto et al. (2006b). I briefly explain each model in this section.

3.3.1 Hapke Model

The Hapke space weathering model is closely tied to the properties of nanophase iron (nFe0 or submicroscopic iron, SMFe) because these particles are formed in lunar soil by surface weathering. They use Maxwell-Garnett effective medium theory to calculate the absorption coefficient of a silicate host medium with inclusions of small Fe metal spheres (Hapke, 2001). Using approximations it is shown that the absorption coefficient is equal to the sum of the absorption coefficients of the host material and the Fe inclusions ($\alpha = \alpha_h + \alpha_{Fe}$).

$$\alpha_{Fe} = \frac{36\pi}{\lambda}\phi z \tag{3.33}$$

where,

$$z = \frac{n_h^3 n_{Fe} k_{Fe}}{(n_{Fe}^2 - k_{Fe}^2 + 2n_h^2)^2 + (2n_{Fe}k_{Fe})^2} \tag{3.34}$$

α_{Fe} is the absorption coefficient of nanophase iron, ϕ is the volume fraction of Fe particles, n_h and k_h are the real and imaginary refractive index of the host material and likewise for nanophase iron is n_{Fe} and k_{Fe}.

3.3.2 Brunetto Model

Brunetto et al. (2006b) find that the spectral alteration due to weathering can be simply recreated by an exponential function.

The space weathering model created by Brunetto et al. (2006c) is shown in Eq. 3.35

$$W(\lambda) = Ke^{\frac{C_S}{\lambda}} \tag{3.35}$$

where W(λ) is the ‘weathering function’, λ is the wavelength, K is a scale factor and C$_S$ is the strength of the exponential curve, measuring the amount of weathering.

Part II

The Inner Solar System

Chapter 4

Taxonomy of Asteroids

This chapter describes the Bus-DeMeo taxonomy which began as a Masters thesis (DeMeo, 2007), but was expanded and solidified into published form as part of this PhD thesis. Much of the text in Sections 4.1 to 4.3 has been taken directly from DeMeo et al. (2009a). In this chapter I focus on describing the taxonomy and analyzing what has been learned about the usefulness of visible and near-infrared data in spectral analysis. For more discussion of the principal component boundaries for the classes, the reader is referred to DeMeo (2007) and DeMeo et al. (2009a).

Contents

4.1 Need for a new taxonomy

Taxonomic classification systems for asteroids have existed since there were enough data to distinguish meaningful groups. The first taxonomies were based on asteroid broad band filter colors such as Wood and Kuiper (1963) and Chapman et al. (1971) where they noted two separate types of objects denoted as "S"and "C". Figure 4.1 shows the separation of the C and S classes using U-B and B-V colors from Bowell et al. (1978). Taxonomies and their nomenclature grew and evolved as later taxonomies became based on higher resolution spectral data which reveal features offering clues to surface composition, age, and alteration. The most widely used taxonomies for asteroids currently are the Tholen taxonomy (1984) based on the Eight-Color Asteroid Survey data (ECAS, Zellner et al., 1985) and SMASSII spectral taxonomy (Bus, 1999; Bus and Binzel, 2002b,a) based on the SMASSII spectral dataset. The average spectra for each of their classes are shown in Figures 4.1 and 4.2. For a review of the evolution of asteroid taxonomies see Bus (1999).

Both the Tholen and Bus taxonomies were based on Principal Component Analysis, a dimension-reducing technique first applied to the field of asteroid classification by Tholen (1984). Most previous asteroid taxonomies were based on visible data because only in the current decade has spectral data collection become widely available in the near-infrared for asteroids down to relatively faint (V=17) limiting magnitudes. The instrument SpeX on the NASA Infrared Telescope Facility (IRTF) has been crucial to increasing the library of near-IR asteroid spectra. (Rayner et al., 2003)

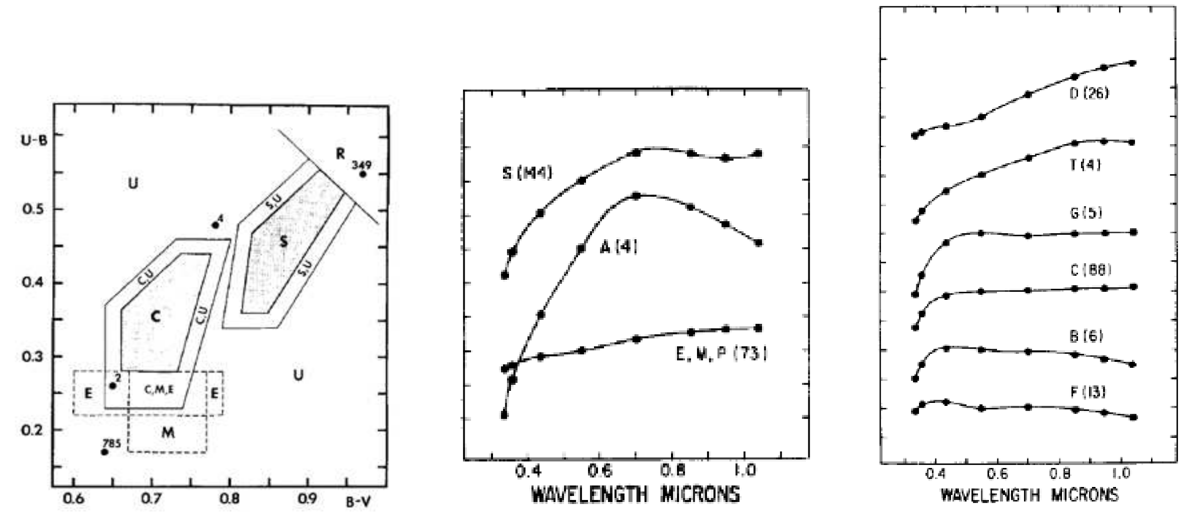

Figure 4.1: **Left:** Separation of classes in Bowell Taxonomy using U-B and B-V colors Bowell et al. (1978). **Middle and Right:** Example spectra for each class in the Tholen taxonomy (Zellner et al., 1985; Tholen, 1984)

The near-IR data range reveals diagnostic compositional information because of the presence of features at one and two microns primarily due to the presence of olivine and pyroxene. Other classification systems created using near-IR data include Howell et al. (1994) who created a neural network taxonomy. Gaffey et al. (1993) created an S-complex taxonomy of olivine- and pyroxene-rich asteroids based on near-infrared data. Our goal was to create a taxonomy extending from visible to near-infrared wavelengths for the entire suite of asteroid characteristics with a method that can be easily reproduced by future users to classify new data. We also strove to keep the notation consistent with past taxonomies, specifically the Bus taxonomy, to facilitate the transition to this new system. The Bus taxonomy, in turn, strove to keep its notation consistent with the Tholen taxonomy.

The taxonomy was created using Principal Component Analysis which is described in detail in Section 3.1.2. It is comprised of 24 classes compared to 26 in the Bus system with three Bus classes eliminated (Sl, Sk, Ld) and one (Sv) created, as well as the addition of a "w" notation, a mark meant to flag objects

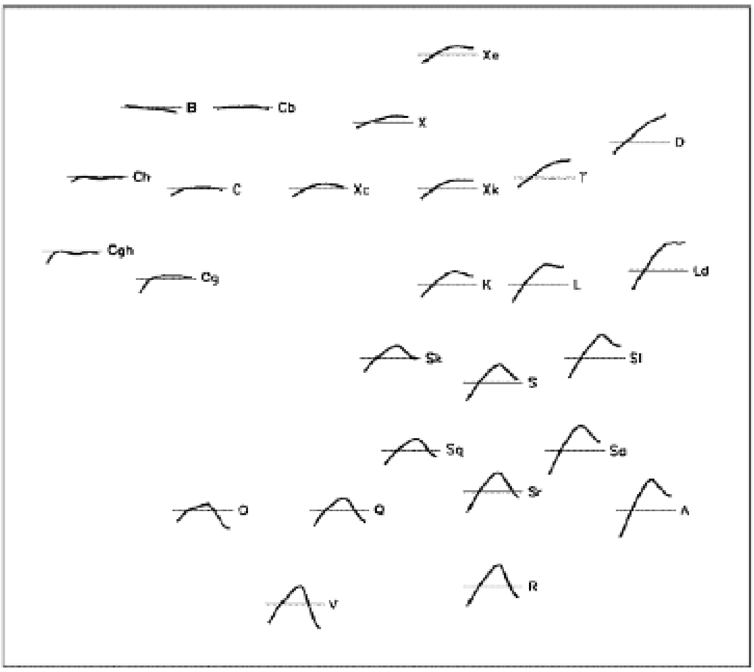

Figure 4.2: A key of the 26 spectral classes of the Bus taxonomy mapped out by their locations in principal component space (Bus and Binzel, 2002a)

having similar spectral features but differing only by having a higher spectral slope.

The taxonomy classes are formally defined by data spanning the wavelength range 0.45 to 2.45 microns as compared with 0.34 to 1.04 microns for Tholen (1984) using eight points, and 0.435 to 0.925 microns for Bus (1999) using 48 points. A method of interpreting near-infrared data from 0.85 to 2.45 microns is also described but for many classes IR-only data do not yield a unique outcome in Principal Component Analysis (PCA) and the data cannot formally be classified.

4.2 The Data

The new data used for creating this taxonomy are near-infrared spectral measurements from 0.8 to 2.5 microns obtained using SpeX in single prism mode (R=250) with a slit width of 0.8 arcseconds.

As described in DeMeo and Binzel (2008), objects and standard stars were observed near the meridian to minimize their differences in airmass and match their parallactic angle to the fixed N/S alignment of the slit. Frames were taken so that the object was alternated between two different positions (usually noted as the A and B positions) on a 0.8 x 15 arcsecond slit aligned north-south. The asteroid spectrum was divided by the spectrum of a solar-type star, giving relative reflectance. Our primary solar analog standard stars were 16 Cyg B and Hyades 64. Additional solar analog stars with comparable spectral characteristics were utilized around the sky. Two to three sets of eight spectra per set were taken for each object, with each with exposures typically being 120 seconds. The total integration time for each of these objects therefore ranged from 30 to 120 minutes.

Reduction was performed using a combination of routines within the Image Reduction and Analysis Facility (IRAF), provided by the National Optical Astronomy Observatories (NOAO) (Tody, 1993), and Interactive Data Language (IDL). We use a software tool called “Autospex” to streamline reduction procedures. Autospex writes macros containing a set of IRAF (or IDL) command files that are then executed by the image processing package. Autospex procedures operate on a single night at a time, with the opportunity for the user to inspect and verify the results at each stage. Briefly, autospex writes macros that: trim the images down to their useful area, create a bad pixel map from flat field images, flat field correct all images, perform the sky subtraction between AB image pairs, register the spectra in both the wavelength and spatial dimensions, co-add the spectral images for individual objects, extract the 2-D spectra from co-added images, and then apply the final wavelength calibration.

Using IDL, an absorption coefficient based on the atmospheric transmission (Atmospheric Transmission Model (ATRAN)) model by Lord (1992) is determined for each object and star pair that best minimizes atmospheric water absorption effects for that pair. This coefficient correction is most important near 1.4 and 2.0 microns, locations of major absorption bands due to telluric H_2O. The final IDL step averages all the object and standard pairs to create the final reflectance spectrum for each object.

Most (321) visible wavelength spectra (usually 0.4 to 0.9 microns) were taken from the Small Main-Belt Asteroid Spectroscopic Survey (SMASS) data set (Bus and Binzel, 2002b). Our sample was comprised of 371 objects with both visible and near-IR data.

4.3 The Taxonomy

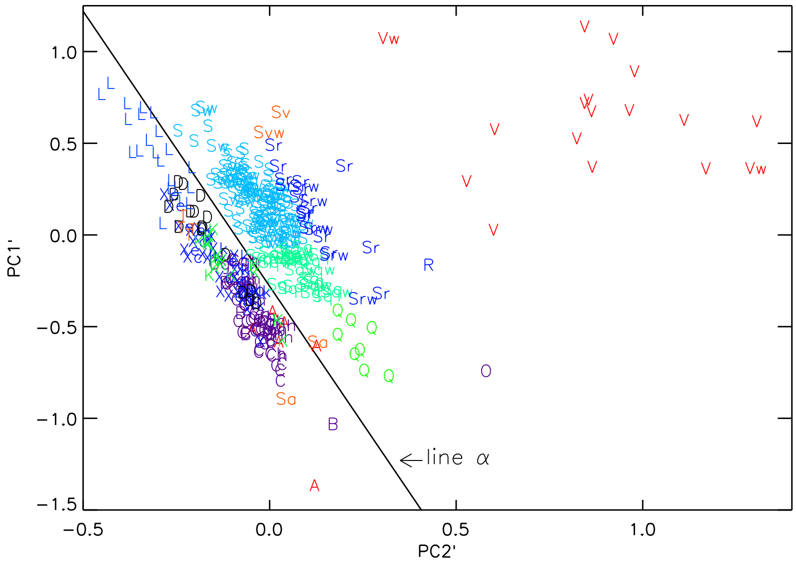

Figure 4.3: Results for PC2′ versus PC1′. All objects plotted are labeled with their taxonomic classification in this system. Notice the "grand divide" between the S-complex and the C- and X-complexes. Line α separates objects with and without 2-μm absorption bands. The direction orthogonal to line α (increasing PC2′ values) indicates deeper 2-μm and narrower 1-μm absorption bands. The direction parallel to line α (increasing PC1′ values) indicates wider 1-μm absorption bands. The notation "PC1′", "PC2′", etc. denotes that these principal components are computed after removal of the slope.

The guiding principle for the classification rules of this taxonomy was to define regions of principal component space that most consistently envelop objects within each of the original Bus (1999) classes. With this principle as a guide, we subjectively define boundaries so that the most similar spectra consistently fall into the same taxonomic classes. The over-riding criterion of similarity of spectral properties in a class, as examined over the full 0.45 - 2.45 μm range, led to some objects in the Bus (Bus, 1999; Bus and Binzel, 2002a) classification receiving new class designations.

Of the 371 objects in our sample, 321 were previously assigned labels within the Bus taxonomy. We used this set of 321 objects to guide the class boundaries. Details of the process and descriptions of the boundaries created are explained thoroughly in DeMeo et al. (2009a) and the flow charts outlining each step to classification are listed Appendces B and C of that work. In Figs. 4.3 and 4.4, the main

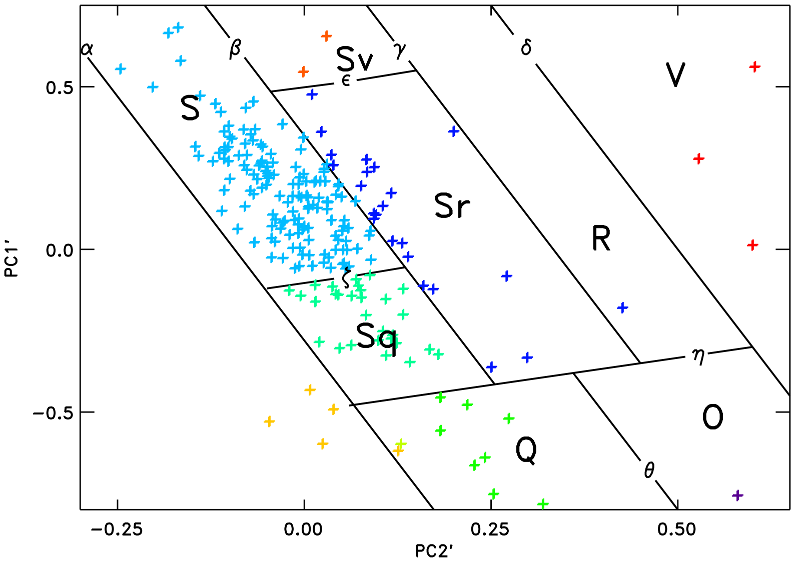

Figure 4.4: PC2′ versus PC1′ plotted for the S-complex plus A-, Q-, O-, R-, and V-types. Boundaries chosen for each class are shown and lines are labeled with greek letters. All boundaries are perpendicular or parallel to line α. A- and Sa- types are the only classes which can lie on either side of line α.

results of the principal component analysis are shown in principal component space. Particularly, Fig. 4.3 displays the "grand divide" (labeled as line α) that separates the featured and subtly featured spectra, and Fig. 4.4 shows the break up of the S-complex.

It is important to note that throughout this chapter on taxonomy, the most basic division among spectra is between "featured" and "subtly featured" spectra. By "featured" we mean the spectrum contains a prominent 1 or 2 micron band. By "subtly featured" we mean there may or may not be shallow absorption features particularly in the visible wavelength range, however, there are no prominent one or two-micron absorption bands.

The taxonomy is comprised of 24 classes (compared to the 26 in Bus and 8 in Tholen). Some argue that too many classes make taxonomy and classification confusing, however, without the proper level of detail compared to the quality of the data, a taxonomy is of little use. For those who are not spectroscopists and seek a "simpler" system, the taxonomy has a hierarchy that suits their needs. The taxonomy, consistent with previous work, has three main "complexes" that encompass the large majority of all spectral types. These include the S-complex, C-complex, and X-complex. This notation has existed nearly since the invention of asteroid taxonomies and puts classification into its most simple form. Within those complexes are classes which subdivide the spectra in further detail. In addition to the complexes, there are the "end members." Those classes represent fairly unique spectra for which there is not a very large sample. Thus this taxonomy can suit the needs of those who seek simplicity as well as those who need more of the detail contained within a spectrum. Here we present the results of the analysis by describing the characteristics of each class over the visible and near-IR wavelengths (and largely overlook the details of PCA). For a table of observations and references for all data included in this work as well as the final taxonomic designations for all objects see Appendix A.1. The spectra are plotted in Appendix A.2.

4.3.1 The end members: A, V, R, O, Q

Spectrally, the A-class has a deep and extremely broad absorption band with a minimum near 1 μm and may or may not have shallow 2-μm absorption band; it is also steeply sloped. It is spectrally very unique and therefore easily identifiable. Figure 4.5 shows the spectral progression from S to A (the S-and Sa-types are described in section 4.3.2).

The V-class, based on the asteroid 4 Vesta (Tholen 1984), is characterized by its strong and very narrow 1-μm absorption band, as well as a strong and wider 2-μm absorption feature. Most V-class asteroids that have been discovered are among the Vesta family and are known as Vestoids, although a few other objects have been identified throughout the main belt, such as 1459 Magnya (Lazzaro et al., 2000) and objects from the basaltic asteroid survey by Moskovitz et al. (2008).

The R-class, created for its sole member 349 Demboska by Tholen (1984), is similar to the V-class in that it displays deep 1- and 2-μm features, however the one-micron feature is broader than the V-type feature and has a shape more similar to an S-type except with deeper features. Bus (Bus and Binzel, 2002a) included three other members in the R-class, two of which are included in our sample. These two objects (1904 Massevitch and 5111 Jacliff) were reassigned to the V-class after discovering that in the near-infrared their one-micron bands remain very narrow. Moskovitz et al. (2008) list 5111 Jacliff as an "R-type interloper" within the Vesta family, but it appears to be an object more confidently linked to Vesta. 1904 Massevitch, however, has a semi-major axis of 2.74 AU. The unusual spectrum and outer belt location for asteroid 1904 has been noted previously (e.g. Burbine and Binzel (2002)). In the sample we present here, asteroids 1904 Massevitch and 1459 Magnya (Lazzaro et al., 2000) are the only two V-types beyond 2.5 AU, a region where V-type asteroids are rare (Binzel et al., 2006a, 2007; Moskovitz et al., 2008).

The O-class also has only one member, 3628 Boznemcova, defined by Binzel et al. (1993). Boznemcova is unique with a very rounded and deep, bowl shape absorption feature at 1 micron as well as a significant absorption feature at 2 μm. Even though the class is separated in the flow chart, more data on R-type and O-type objects may help establish more rigorously their region boundaries. Bus (Bus and Binzel, 2002a) designated three other asteroids as O-type, 4341 Poseiden, 5143 Heracles, and 1997 RT. Only 5143 was included in our sample. Asteroid 5143 is reclassified here as a Q-type because with near-infrared data it is clear the object did not have the distinct "bowl" shape of the one-micron feature of Boznemcova. This adds 5143 Heracles as a Q-type to those known within near-Earth space (e.g., Binzel et al., 2004).

The Q-class, whose boundaries are labeled in Fig. 4.4 was first defined by Tholen (1984) for near-Earth asteroid 1862 Apollo. The class is characterized by a deep and distinct 1-μm absorption feature with evidence of another feature near 1.3 μm as well as a 2-μm feature with varying depths among objects. The spectral differences between the end member classes A, V, R, Q, and O are displayed in Figure 4.5.

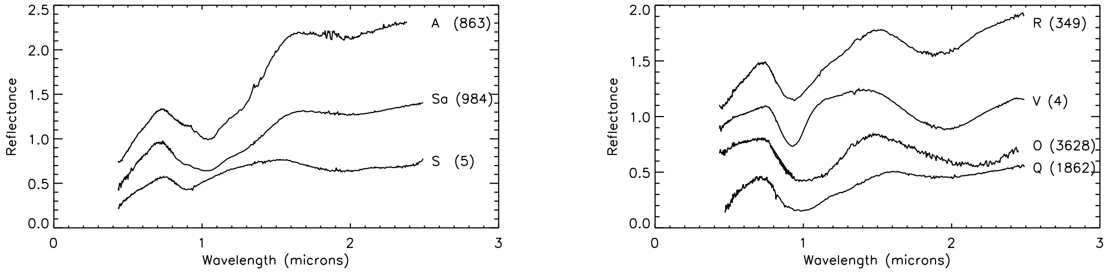

Figure 4.5: **Left:** Examples of S-, Sa-, and A-classes. There is a clear progression from S-types with a shallow one-micron band and low slope to A-types with a deep one-micron band and high slope. Sa- and A-types show similar 1-μm band absorptions, but Sa-types are much less red than A-types. The class and the asteroid number are labeled next to each spectrum. **Right:** Comparison of prototypes for the V-, O-, Q-, and R-classes. Note the O-class has a very wide 1-micron band and the V-class has a very narrow band. The V-types with the deepest 2-micron bands plot farthest from line α. For this and all subsequent spectral plots: We present relative reflectances normalized to unity at 0.55 microns; the spectra are offset vertically for clarity of comparison. The class and asteroid number are labeled next to each spectrum.

4.3.2 The S-complex: S, Sa, Sq, Sr, Sv

Just as in the case of the Bus taxonomy, the S-complex was by far the most difficult to subdivide. Most Bus classes within the S-complex seemed to blend together or scatter randomly in all combinations of PCA components. For example, many objects labeled as “Sa”, “Sl”, and “Sk” in the Bus (Bus, 1999; Bus and Binzel, 2002a) taxonomy no longer form distinct groups when their spectra are extended into the near-IR. Most original Bus class objects of these types merged into the S-class. The Sl and Sk classes were excluded from this new system. The Sa-class was kept, however, it was redefined and no longer contains any of the objects previous designated by the Bus system. Similarly, many Bus S, Sq, and Sk objects become less clearly separated when their spectra extend to the near-infrared. Within PCA space, the Bus S, Sq, and Sk objects were initially impossible to define clearly because the boundaries blur and overlap. Because spectrally the main difference between the classes of the S-complex appears to be the width of the 1-micron absorption band we used the wavelength range 0.8 to 1.35 microns and performed PCA on only S-complex objects to gain insight on their differences. This S-class PCA served as a guide to separate S- complex classes in a meaningful way based on the near-infrared spectral features.

The Sa-class, the most distinct among all S-complex types, has the same characteristic 1-μm absorption band as the A-class, but is less red. A figure showing the spectral progression from S to Sa to A is shown in Fig. 4.5. The current Sa-class was redefined from the Bus system because the two Sa objects (main belt object 984 Gretia and Mars crosser 5261 Eureka) in this system were both Sr-types in the Bus system. Since these objects prove to be intermediate between S and A we change the classification of these two (Bus) Sr-types to Sa in this taxonomy.

The S-class has moderate 1- and 2-μm features. The Sq-class has a 1-μm absorption band that is wider than that of an S-type with evidence of a feature near 1.3 μm like the Q-type, except the 1-μm feature is more shallow for the Sq. Many objects that were previously designated as Sa-, Sl-, or Sq- types in the Bus taxonomy were designated as S- or Sq-types in this extended taxonomy.

The Sr-class typically has a fairly narrow 1-μm feature similar to but more shallow than an R-type as well as a 2-μm feature. One object (5379 Abehiroshi) was a V-type under the Bus (Bus and Binzel, 2002a) system and is now labeled an Sr. While the visible data have a “moderate to very steep UV slope shortward of 0.7 μm with a sharp, extremely deep absorption band longward of 0.75 μm” (Bus and Binzel, 2002a), it is clear with the inclusion of near-infrared data that the one-micron absorption band is too wide to be a V-type.

The Sv-class has a very narrow 1-μm absorption band similar to but more shallow than a V-type as well as a 2-μm feature. Two objects (2965 Surikov and 4451 Grieve) are considered spectrally unique from Sr because they exhibit very narrow 1-μm absorption bands. The objects in this region spectrally appear to be in transition between S- and V-classes. They are not included in the Bus dataset, and Bus and Binzel (2002a) did not report any cases of objects with these characteristics. Because of their intermediate properties between S and V that are clearly displayed over the 0.45- to 2.45-micron range, we define a new class with the label Sv. Figure 4.3.2 displays the spectra of typical S-, Sq-, Sr-, and Sv-class spectra.

4.3.3 The w-notation

The objects in the S-complex had widely varying spectral slopes. To have some taxonomic distinction in spectral characteristics arising from slope, we made an arbitrary cutoff at Slope = 0.25 dividing high slope objects from other objects. These objects are not relabeled in a class of their own. Instead the S, Sq, Sr, and Sv objects with high slopes receive a notation of w added to their name as a moniker for what is commonly discussed as an increase in slope arising from space weathering (Clark et al., 2002). [We make no pretense of knowing whether or not their surfaces are actually weathered.] The high slope S objects are labeled Sw, Sqw, Srw and Svw. We extended this flag to the V- types for which there were two objects with slopes greater than 0.25, which we label as Vw. Sa-types do not receive a w notation because, as an intermediate class between S and A, they are by definition highly sloped. Figure 4.3.2 displays the differences between low- and high-slope objects, S and Sw.

The choice of 0.25 for the “w” notation is arbitrary. When plotting Bus labeled S, Sa, and Sl objects, there is a mixing around the 0.23 to 0.27 slope range. The goal was to keep the “w” notation more selective without setting the boundary too high where objects with unusual slope features (such as deeper UV

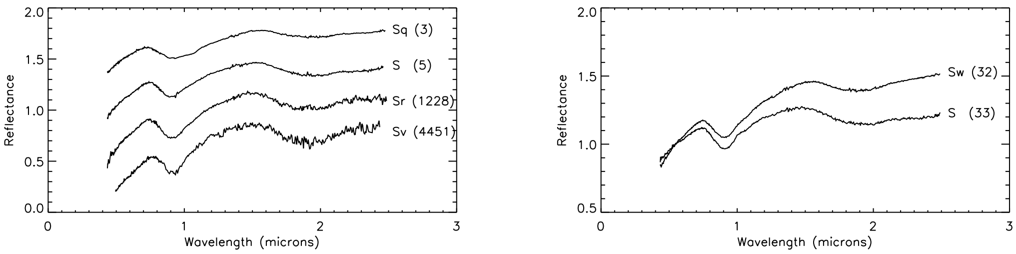

Figure 4.6: **Left:** Comparison of spectra within the S-complex (S, Sq, Sr, Sv) showing the variation in the one-micron absorption band among these types. Sq-types have the widest one-micron feature, similar to the Q-class. Sv-types have the narrowest feature, similar to the V-class. **Right:** Illustration of S and Sw reflectance spectra. The absorption features for both are very similar. Slope is the most significant distinction between the two, where the "w" is a notation to denote the slope difference, but does not describe a distinct class. These two spectra are not offset vertically, showing their differences relative to their common normalization at 0.55 μm.

dropoffs) were preferentially selected rather than focusing on the significant slope range between one and two microns for the S-Complex.

4.3.4 The end members: D, K, L, T

The D-class spectra are linear with a very steep slope, and some show slight curvature or a gentle kink around 1.5 μm. The T-class is linear with moderate to high slope and often gently concaving down, It is preserved from the Bus system, although it is very similar to the X-class in the near-infrared.

The Bus (Bus and Binzel, 2002a) L- and K-classes were part of the S-class in the Tholen (1984) taxonomy. While the L-class may show 1- and 2-μm features, it is distinct from the S-class because the steep slope in visible region levels out abruptly around 0.7 μm, but does not show a distinct absorption band like the S. There is often a gentle concave down curvature in the near-infrared with a maximum around 1.5 μm, and there may or may not be a 2-micron absorption feature. A typical K-class object displays a wide absorption band centered just longward of 1 μm. This feature is unique because the left maximum and the minimum are sharply pointed and the walls of the absorption are linear with very little curvature. Figure 4.7 shows examples of typical spectra in the D-, K-, L- and T- classes.

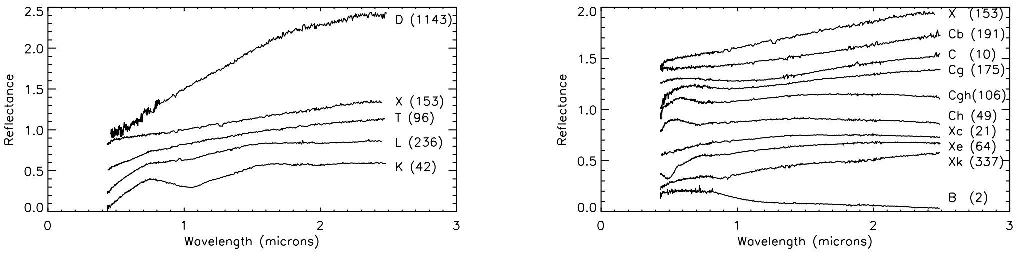

Figure 4.7: **Left:** Prototype examples of D-, L-, K-, T-, and X-class spectra. **Right:** Prototype examples for C- and X-complex spectra.

4.3.5 C- and X- Complexes: B, C, Cb, Cg, Cgh, Ch, X, Xc, Xe, Xk

Over the wavelength range used for this work, PCA is not particularly sensitive to the subtle features that define the C and X complexes. This taxonomy generally strives to follow the definitions created by Bus and Binzel (2002a) because most features exist in the visible wavelength range. Significant analysis was performed to distinguish these classes in the near-IR, which is discussed further in Section 4.6. Figure 4.3.4 shows typical spectra for classes within the C- and X-complexes.

The B-types are easily distinguished by their negative slope. Their spectra are linear and negatively sloping often with a slight round bump around 0.6 μm preceding a slight feature longward of 1 micron and/or a slightly concave up curvature in the 1- to 2-μm region.

Cb-types are linear with a small positive slope that begins around 1.1 μm. Cb objects were intermediate objects between the B- and C-classes in the Bus system (Bus and Binzel, 2002a). We keep the same notation, however, the near-infrared data shows, that Cb objects have low to moderate near-infrared slopes, while the visible slopes are low or negative.

C-types are linear with neutral visible slopes and often have a slight rough bump around 0.6 μm and low but positive slope after 1.3 μm. They also may exhibit slight feature longward of 1 μm. Ch spectra have a small positive slope that begins around 1.1 microns and slightly pronounced UV dropoff, and a broad, shallow absorption band centered near 0.7 μm. The Cgh-class is similar to the Ch showing a 0.7-micron feature, but also has a more pronounced UV dropoff like the Cg-type.

There is only one object (175 Andromache) in the Cg-class carrying over from the Bus (Bus, 1999; Bus and Binzel, 2002a) taxonomy. The Cg-class is characterized by a pronounced UV dropoff similar to the Cgh, but does not show the 0.7-micron feature that define Ch and Cgh.

The X-class is identified based on medium to high slope values and its linear spectrum. Xc-types have low to medium slope and are slightly curved and concave downward. The Xe-class exhibits low to medium slope similar to either Xc- or Xk-type, but with an absorption band feature shortward of 0.55 μm. The Xk-class is slightly curved and concave downward similar to Xc-type but with a faint to feature between 0.8 to 1 μm. The spectral slope after this feature varies widely among spectra.

A summary of the descriptions of each spectral class is provided in Table 4.1. A key of the taxonomy is plotted as the average spectrum for each class in Figs. 4.8 and 4.9.

Table 4.1: Spectral Class Descriptions

Class	**Description**	**Prototypes**
A	Deep and extremely broad absorption band with a minimum near 1 μm, may or may not have shallow 2-μm absorption band; very highly sloped.	246, 289, 863
B	Linear, negatively sloping often with a slight round bump around 0.6 μm and/or a slightly concave up curvature in the 1- to 2-μm region.	2, 3200
C	Linear, neutral visible slope often a slight rough bump around 0.6 μm and low but positive slope after 1.3. May exhibit slight feature longward of 1 μm.	1, 10, 52
Cb	Linear with a small positive slope that begins around 1.1 μm.	191, 210, 785
Cg	Small positive slope that begins around 1.3 microns and pronounced UV dropoff.	175
Cgh	Small positive slope that begins around 1 micron and pronounced UV dropoff similar to Cg also includes a broad, shallow absorption band centered near 0.7 μm similar to Ch.	106, 706, 776
Ch	Small positive slope that begins around 1.1 microns and slightly pronounced UV dropoff also includes a broad, shallow absorption band centered near 0.7 μm.	19, 48, 49
D	Linear with very steep slope, some show slight curvature or gentle kink around 1.5 μm.	1143, 1542, 3248
K	Wide absorption band centered just longward of 1 μm, the left maximum and the minimum are sharply pointed and the walls of the absorption are linear with very little curvature.	42, 579, 742
L	Steep slope in visible region leveling out abruptly around 0.7 μm. There is often a gentle concave down curvature in the infrared with a maximum around 1.5 μm. There may or may not be a 2-micron absorption feature.	236, 402, 606
O	Very rounded and deep, bowl shape absorption feature at 1 micron as well as a significant absorption feature at 2 μm.	3628
Q	Distinct 1-μm absorption feature with evidence of another feature near 1.3 μm; a 2-μm feature exists with varying depths between objects.	1862, 3753, 5660
R	Deep 1- and 2-μm features; the one-micron feature is much narrower than a Q-type, but slightly broader than a V-type.	349
S	Moderate 1- and 2-μm features. The 2-micron feature may vary in depth between objects.	5, 14, 20
Sa	Has a deep and extremely broad absorption band at 1 μm; has similar features to A-types but is less red.	984, 5261
Sq	Has a wide 1-μm absorption band with evidence of a feature near 1.3 μm like the Q-type, except the 1-μm feature is more shallow for the Sq.	3, 11, 43
Sr	Has a fairly narrow 1-μm feature similar to but more shallow than an R-type as well as a 2-μm feature.	237, 808, 1228
Sv	Has a very narrow 1-μm absorption band similar to but more shallow than a V-type as well as a 2-μm feature.	2965, 4451
T	Linear with moderate to high slope and often gently concaving down.	96, 308, 773
V	Very strong and very narrow 1-μm absorption and as well as a strong 2-μm absorption feature.	4, 1929, 2851
X	Linear with medium to high slope.	22, 87, 153
Xc	Low to medium slope and slightly curved and concave downward.	21, 97, 739
Xe	Low to medium slope similar to either Xc- or Xk-type, but with an absorption band feature shortward of 0.55 μm.	64, 77, 3103
Xk	Slightly curved and concave downward similar to Xc-type but with a faint to feature between 0.8 to 1 μm.	56, 110, 337
Bus-Ld	Diverged to L- and D-classes.	279 (D), 3734 (L)
Bus-Sk	Diverged to the S- and Sq-classes.	6585 (S), 3 (Sq)
Bus-Sl	Merged with the S-class.	17 (S), 30 (S)

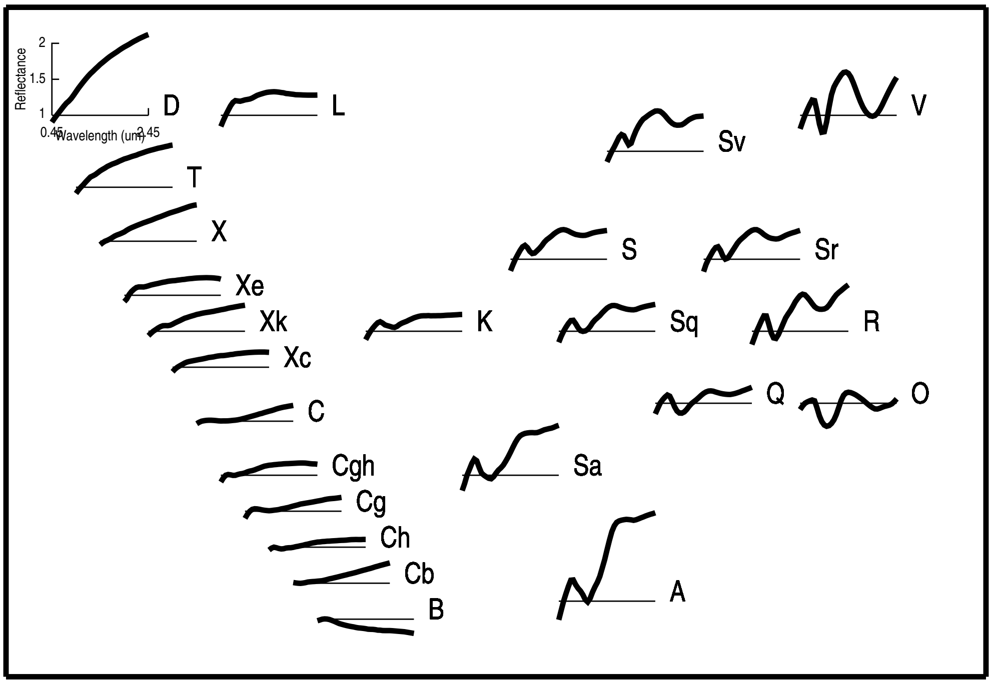

Figure 4.8: A “key” showing all 24 taxonomic classes defined over 0.45 - 2.45 μm. The average spectra are plotted with constant horizontal and vertical scaling and are arranged in a way that approximates the relative position of each class in the primary spectral component space defined by slope, PC1′, and PC2′. Thus the depth and width of the 2-μm band generally increases lower left to upper right, and the depth and width of the 1-μm band increase moving downward and toward the right. For subtly featured objets slope increases from bottom to top. Due to the spectral complexity of the C- and X-complexes, the locations of some of these classes do not strictly follow the pattern. The horizontal lines to which each spectrum is referenced has a reflectance value of unity. This figure and description follows the style of Bus and Binzel (2002a, Fig. 15).

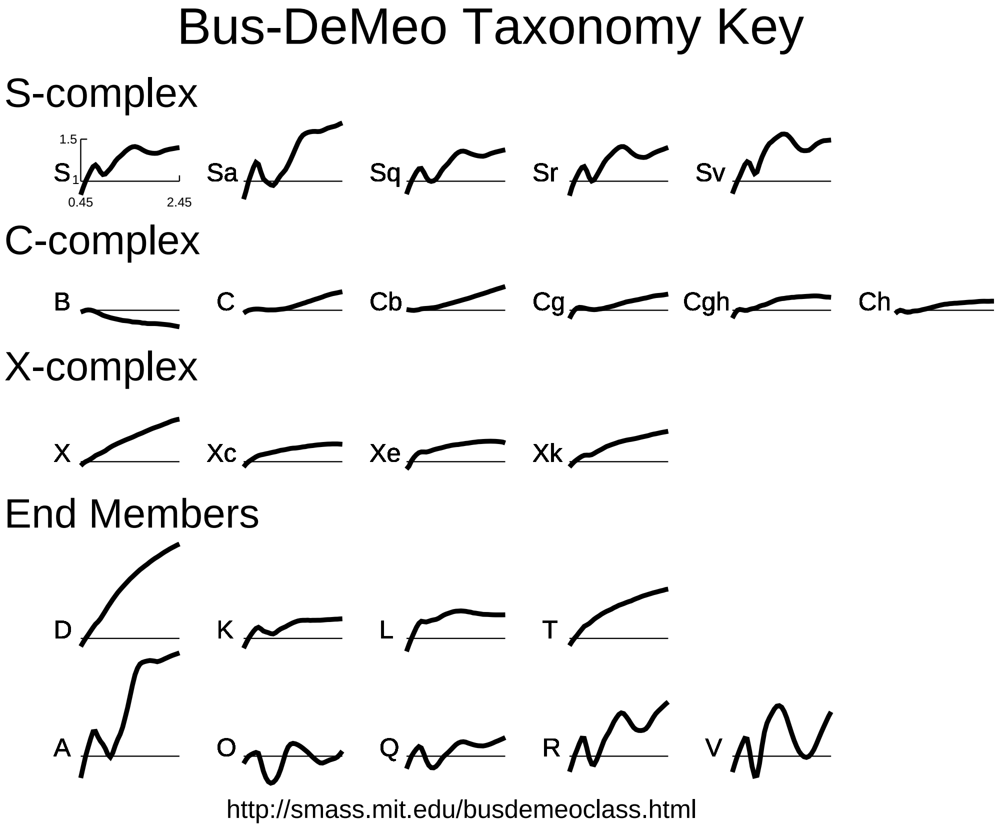

Figure 4.9: Re-arranged key to Bus-DeMeo taxonomy showing average spectra for each of the 24 classes, grouped according to their complex.

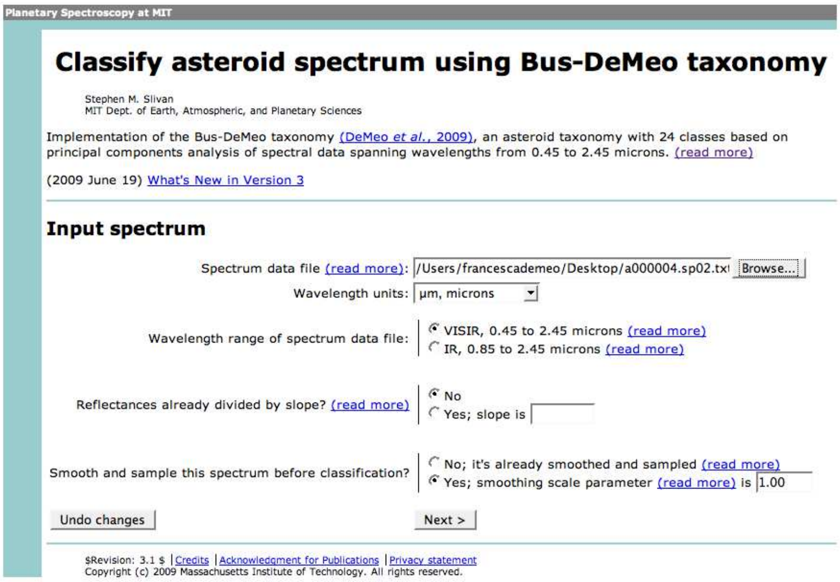

Planetary Spectroscopy at MIT

Classify asteroid spectrum using Bus-DeMeo taxonomy

Stephen M. Slivan
MIT Dept. of Earth, Atmospheric, and Planetary Sciences

Implementation of the Bus-DeMeo taxonomy (DeMeo *et al.*, 2009), an asteroid taxonomy with 24 classes based on principal components analysis of spectral data spanning wavelengths from 0.45 to 2.45 microns. (read more)

(2009 June 19) What's New in Version 3

Input spectrum

Spectrum data file (read more): /Users/francescademeo/Desktop/a000004.sp02.txt
Wavelength units: µm, microns
Wavelength range of spectrum data file: ● VISIR, 0.45 to 2.45 microns (read more) ○ IR, 0.85 to 2.45 microns (read more)
Reflectances already divided by slope? (read more) ● No ○ Yes; slope is
Smooth and sample this spectrum before classification? ○ No; it's already smoothed and sampled (read more) ● Yes; smoothing scale parameter (read more) is 1.00

$Revision: 3.1 $ | Credits | Acknowledgment for Publications | Privacy statement
Copyright (c) 2009 Massachusetts Institute of Technology. All rights reserved.

Figure 4.10: Taxonomy Web Tool Application Step 1: Input Spectrum. Here the user specifies the wavelength units, the wavelength range, and whether or not the slope has been removed and sample has been smoothed.

4.4 Taxonomy Web Application

A web application (constructed by Dr. Stephen Slivan) was created that determines taxonomic types for visible plus near-infrared data or near-infrared-only data based on this extended taxonomy (smass.mit.edu). This tool takes an input spectrum and creates a spline fit with the appropriate data values. It then calculates the principal component values, and classifies the spectrum using the appropriate (visible+near-IR or near-IR-only) flow chart. The final output displays the classification, the principal component values, a definition of the class (or classes if there are multiple possibilities), and plots the spectrum with the average spectrum from each possible class along with the residual to give an quantitative estimate of how good the fit is. The main user interface for the web tool is shown in Figs. 4.10, 4.11, and 4.12.

4.5 IR-only taxonomy

After defining each class using visible and near-infrared data, the next step was to create a system of classification using only near-infrared data. The goals here are twofold: first, it allows classification of data sets in the near-infrared where important mineralogical information lies, second, it acts as a test for the limits of information we can extract with this incomplete wavelength range. We discuss the limits of incomplete data ranges further in Section 4.6.

For many objects, data exist in either the visible or near-infrared wavelength ranges but not both. While taxonomies such as the Bus system (Bus, 1999; Bus and Binzel, 2002a) are available for visible data, no system has been widely accepted for assigning classes to data existing only in the near-infrared. We have adapted our present taxonomy to interpret spectral data available only in the near-infrared range. This adaptive taxonomy is not meant to determine a definite class, but instead is an intermediate tool to indicate classes. We especially note that several classes in section 4.3.5 are carried over unchanged from the Bus taxonomy and are based exclusively on features present at visible wavelengths. Assignment to these classes (Cg, Cgh, Xc, Xe, Xk) requires visible wavelength data, therefore objects in these classes cannot be recognized by near-infrared-only data. Further discussion is provided in Section 4.6.

To study the ability to classify objects having only near-infrared spectral data we took the same 371 objects used in the original taxonomy but included only data longward of 0.85 microns, again splining

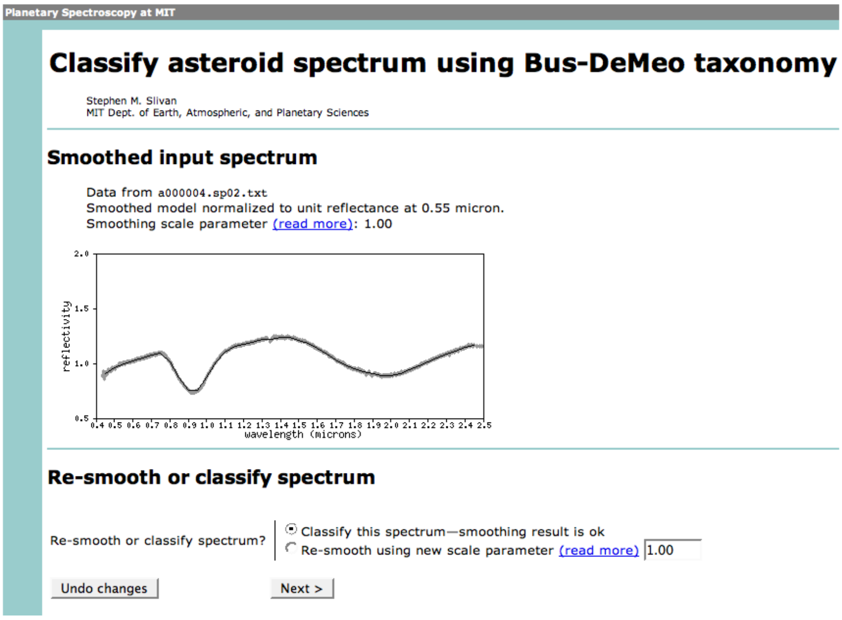

Planetary Spectroscopy at MIT

Classify asteroid spectrum using Bus-DeMeo taxonomy

Stephen M. Slivan
MIT Dept. of Earth, Atmospheric, and Planetary Sciences

Smoothed input spectrum

Data from `a000004.sp02.txt`
Smoothed model normalized to unit reflectance at 0.55 micron.
Smoothing scale parameter (read more): 1.00

Re-smooth or classify spectrum

Re-smooth or classify spectrum?
● Classify this spectrum—smoothing result is ok
○ Re-smooth using new scale parameter (read more) 1.00

Figure 4.11: Taxonomy Web Tool Application Step 2: Smooth Spectrum. The user may increase or decrease the smoothing parameter (default = 1) to change the strength of smoothing. When the user is satisfied, s/he chooses “Classify this spectrum” and then “Next”.

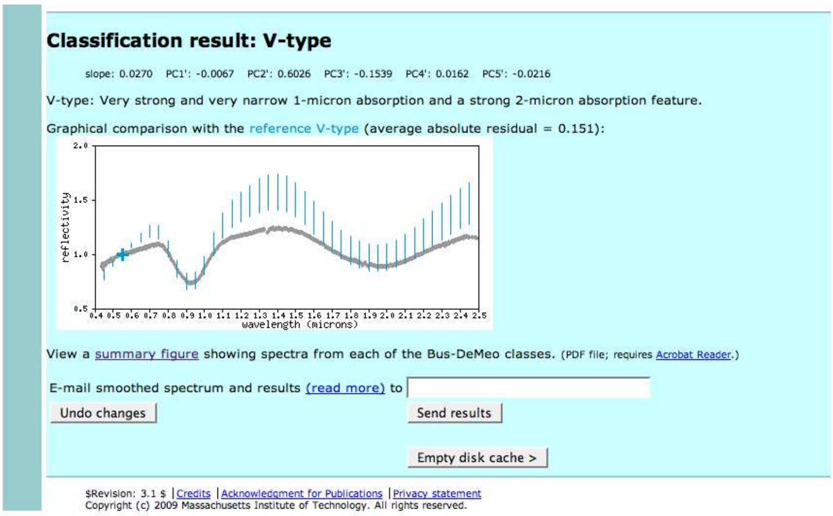

Classification result: V-type

slope: 0.0270 PC1': -0.0067 PC2': 0.6026 PC3': -0.1539 PC4': 0.0162 PC5': -0.0216

V-type: Very strong and very narrow 1-micron absorption and a strong 2-micron absorption feature.

Graphical comparison with the reference V-type (average absolute residual = 0.151):

View a summary figure showing spectra from each of the Bus-DeMeo classes. (PDF file; requires Acrobat Reader.)

E-mail smoothed spectrum and results (read more) to

$Revision: 3.1 $ | Credits | Acknowledgment for Publications | Privacy statement
Copyright (c) 2009 Massachusetts Institute of Technology. All rights reserved.

Figure 4.12: Taxonomy Web Tool Application Step 3: Classify Spectrum. Here the classification result is displayed along with principal component values and a plot of the spectrum compared to the average spectrum for that class. If more than one class is given, the user must inspect each plot and the average absolute residual of the input spectrum compared to the average for each class to determine the best classification for the object.

the data to smooth out noise. Our spline increments remained 0.05 μm covering the range of 0.85 to 2.45 microns resulting in 33 datapoints. We chose to normalize to unity at 1.2 microns, the closest splinefit wavelength value to 1.215 μm which is the isophotal wavelength for the J band based on the UKIRT filter set (Cohen et al., 1992). Next, we removed the slope from the data. As in the case with visible and near-infrared data we calculated the slope function without constraints, and then translate it in the y-direction to a value of unity at 1.2 microns. We then divide each spectrum by the slope function to remove the slope from the data set.

4.6 Limits of only visible or near-IR coverage

It is clear that both the visible and near-infrared wavelengths give important clues to the composition and alteration of asteroid surfaces, but what are the advantages of having both pieces of information? Does the visible wavelength range tell us everything we need to know? Can the near-infrared tell us everything we need to know?

4.6.1 Visible: The 1-micron band uncertainty

For S-complex and other olivine-rich asteroids, the visible wavelength is limiting because we cannot characterize the olivine and pyroxene content without the 1- and 2-micron bands. We find that the "very steep to extremely steep UV slope shortward of 0.75 μm, and a moderately deep absorption feature, longward of 0.75 μm" (Bus and Binzel, 2002a) that defines the Bus A-type surprisingly is not necessarily indicative of the very large 1-micron band seen in olivine-rich ($> 80\%$) spectra. Out of the 10 Bus A-types in our sample, half of them are not A-types in the Bus-DeMeo taxonomy (4 Sw-types, 1 L-type). An example of the divergence of Bus A-types in the near-infrared is shown in Fig. 4.13. When inspecting spectra classified as Bus Sa-types which are in the intermediate class between S and A because of the steep UV slope, we find that their near-infrared information excludes them from this status. All 12 Bus Sa-types within this sample were reclassified as Sw-, Sqw-, and S-types. While all of these objects had steep UV slopes, their 1-micron bands did not appear any more A-like than any other average S-complex spectrum. We find instead, that two objects previously classified as Sr-types under the Bus system do have the characteristic A-type wide and deep 1 micron absorption band, with very low overall slopes compared to A-types. Interestingly, these olivine-rich ($>\sim 80\%$) asteroids are hidden from identification in the visible-only wavelength range because their UV slopes are not nearly as steep and unique as Bus A-types.

Of the 16 Bus K-types in our sample, 5 of them were reclassified as L-types when greater spectral coverage is added. K-types differ slightly from L-types in the visible wavelength range, L-types having steeper UV slopes and a generally flatter spectrum past 0.75 μm, but in the near-infrared the K-types have a distinct 1 micron band, similar to an S-type although often slightly wider and more V-shaped rather than U-shaped, while L-types have much more subtle 1-micron bands.

We do find many strong consistencies between visible and near-ir data as well, which is very useful. Overall, we find that S-complex objects, remain S-complex with added near-ir data, even if the exact shape of the 1 micron band or depth of the 2 micron band cannot be entirely predicted by visible data. All three Bus Q-types in our sample remain unequivocally Q-types. All but one of the Bus V-types remain V-types. These classes are robust whether visible or the combination of visible and near-IR are used for classification.

4.6.2 Near-IR: S-complex and Q-types

The process of creating a decision tree to classify near-infrared-only asteroid data within the same system as the visible and near-IR data provided a rigorous test for the amount of information contained within the near-IR only data.

We started by performing Principal Component Analysis on the same 371 objects used in the original taxonomy, including only the data past 0.85 microns. The data were normalized to unity at 1.2 microns. We find that principal component space nicely separates featured from subtly featured classes in PCir2′ and PCir3′ space. Figure 4.14 shows this division in PC space. We learn that further subdivisions become

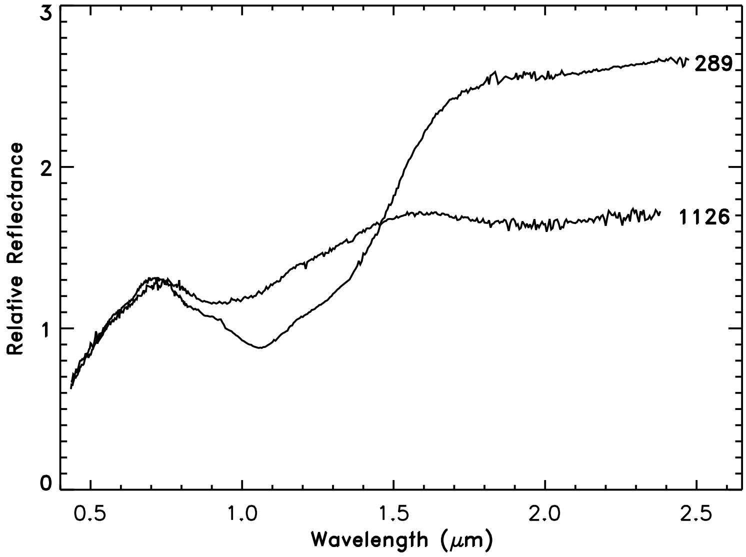

Figure 4.13: Shown here are two Bus A-types, asteroids 289 and 1126. While they have nearly identical behavior in the visible region, their spectra in the near-infrared region are significantly different. Asteroid 289 remains an A-type, but asteroid 1126 becomes and Sw-type.

much more difficult. PCir1′ and PCir2′ space is shown in Fig. 4.15. While some general boundaries can be constrained, the level of detail attained by using the visible plus near-infrared is not possible.

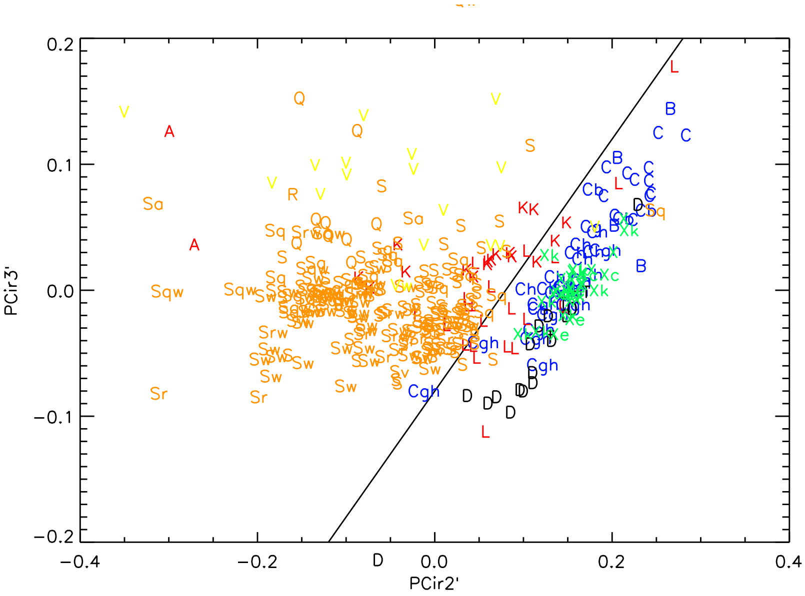

Figure 4.14: Plot of PCir2′ v. PCir3′. Here "featured" versus "subtly featured" objects are separated by the line.

Without the peak at the beginning of the 1-micron absorption feature, we lose important information about the depth and to a lesser extent the width of this feature making separation between S-, Sr-, Sq-, and

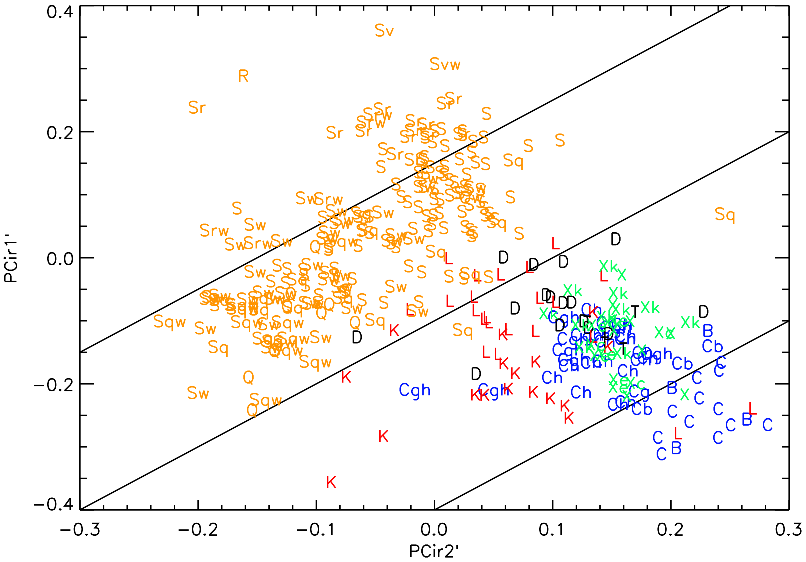

Figure 4.15: Plot of PCir1′ v. PCir2′. Here we create four segments separated by the three lines to help determine to which class an object belongs. Without the visible information, we cannot determine definite class boundaries in many cases.

even Q-types impossible. Principal component analysis cannot separate between these classes. Visual inspection of the overall band shape and width, however, usually allows a more definite classification than PCA could provide. For example, an Sv- and an Sq-type should never be confused even without the entire wavelength range, because Sv-types have extremely narrow bands, while Sq-types are much broader. Distinguishing between the S and Sq classes is often not clear with visual inspection because the differences between their bands are not always so great. We subsequently attempted to find a simple measure of band width to quantitatively separate classes.

By comparing the average spectrum of the S, Sr, Sq, Sv, and Q classes we find that the band minimum for Q is located at 1.0 micron, while for the others it is at 0.9 microns. We created a simple test by comparing the difference between the normalized reflectance value at 0.95 and 0.90 μm (f(0.95)-f(0.90)). We expected that all objects with negative values would be Q-types, because the reflectance values are still decreasing between 0.90 and 0.95 and the minimum has not yet been reached. We found that in general this could separate between Q-types and the others, but not definitively because the average spectra on which we based this method do not represent the entire range of spectra within that class. There were still S- and Sq-types that had minima at longer wavelengths. We attempted many other tests by comparing values and ratios of reflectance values at different points throughout the band. No test or combination of tests could adequately separate among classes.

We also found that many high-sloped S-types (Sw-types) were indistinguishable from lower-sloped objects in the sample with near-IR-only data. As stated in DeMeo et al. (2009a), because the entire 1-micron absorption band is not sampled, some depth versus slope information is lost, making it difficult, if not impossible, to distinguish between a steeply sloped spectrum with a shallow 1-micron feature and a spectrum with a lower slope, but a deep 1-micron feature. Figure 4.16 plots all S-complex, Q-type and R-type spectra in the sample normalized at 0.55 microns (right) and 1.2 microns (left). It is clear that the depth and width of the 1-micron band can be determined because the left peak is present. Figure 4.17 shows only the near-infrared wavelength region. Classification of these spectra is more difficult.

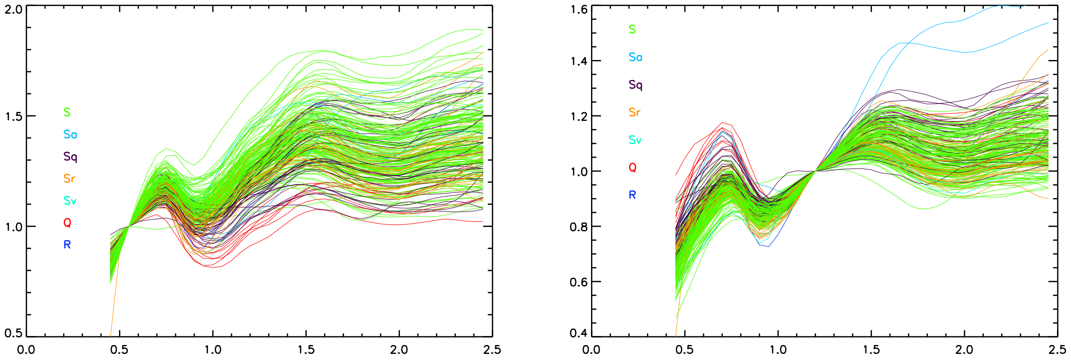

Figure 4.16: **Left:** Here we plot all S-complex, Q-type, and R-type spectra from our sample over the 0.45 - 2.45 micron wavelength range normalized to unity at 0.55 microns. The peak near 0.75 microns before the absorption band allows a clear determination of band depth, band width and overall slope of the spectrum. **Right:** Data here are normalized to unity at 1.2 microns to compare data over the entire range to near-IR-only data normalized at the same wavelength.

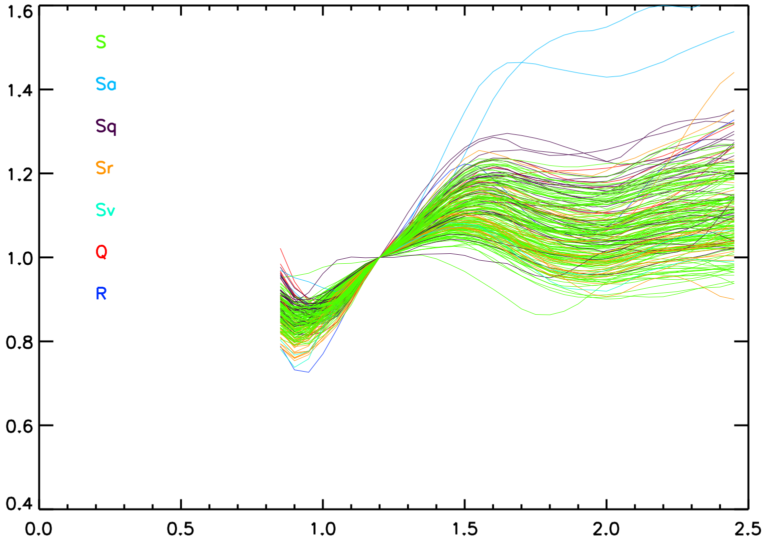

Figure 4.17: Here we plot all S-complex, Q-type, and R-type spectra from our sample over the 0.85 - 2.45 micron wavelength range normalized to unity at 1.2 microns. Without the peak near 0.75 microns before the absorption band, one cannot distinguish between a spectrum with a deep absorption and a low slope, or a shallow absorption and a high slope.

4.6.3 Near-IR: C- and X- complexes

While some information could still be salvaged about the 1-micron band by inspecting its shape and its width in the near-IR range, we learn about the degeneracy of subtly featured objects in the near-infrared. C- and X- complex objects do not have any strong distinguishing features in the near-infraread, with the exception of Xk-types which show a small feature near 1 micron, and C-types which tend to have a shallow, broad feature near 1-1.3 microns. Without the important visible wavelength information is it possible to separate these classes? Is there some slope information still retained? For example, do

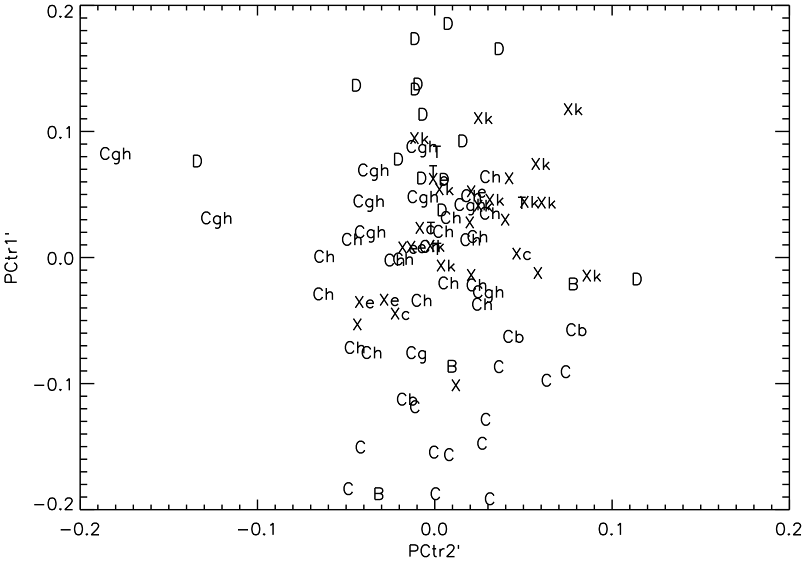

Figure 4.18: Plot of PC values from principal component analysis of *exclusively* C- and X-complex plus D- and T-type objects in near-infrared. Here the first two principal components are plotted.

C-complex objects have lower slopes than do X-complex objects in the near-infrared as is true in the visible?

We started with a comparison of slopes among classes. By comparing the average slope for each class and the range of slopes we find that there is a significant range of near-ir slopes within each class, much more than is seen in the well-contained visible wavelength region. There does not seem to be any clear slope boundaries, except for the exceptionally high-sloped D class.

Since no immediate answer could be found in our near-infrared PCA, we performed another principal component analysis on only subtly featured objects (including all C- and X-complex objects as well as D and T types). The advantage of isolating these objects is that PCA becomes more sensitive to subtle differences between these classes rather than the significant 1 and 2 micron features of S-complex objects.

We find by comparing the first principal component in this subtly-featured-only PCA that C-types tend to have the lowest PC values, while D-types tend to have the highest. These two classes, however, can already be separated by their slope for the D class and by visual confirmation of a subtle 1.3 micron feature for the C class. Unfortunately, no other clear separation between the B, Cb, Cg, Cgh, Ch, X, Xc, Xe, Xk, and T classes are evident. From this we can conclude that the C- and X- complexes can be defined exclusively with visible wavelength data and are entirely degenerate in the near-infrared. Figures 4.18, 4.19, and 4.20 plot the these objects in the various principal component spaces created in this analysis.

4.7 Albedo Distributions among Taxonomic Classes

The next step to refining taxonomy and ultimately our understanding of asteroid surfaces based on remote sensing is to include albedo information. Albedo tells us how dark or bright a surface is, helping constrain composition and age. It is generally found that the S-complex has higher albedos than the C-complex. Table 4.2 reports the average geometric albedo and the standard deviation for each class. The table also reports the debiased average albedos for NEOs calculated in Stuart and Binzel (2004), to compare to the primarily Main Belt sample in this taxonomy. Their objects were classified in the system of Bus and Binzel (2002a) and were grouped into complexes. The average C-type albedo for our sample is lower than for their C-complex. This is likely because we report separately the Cgh-types that have a higher average

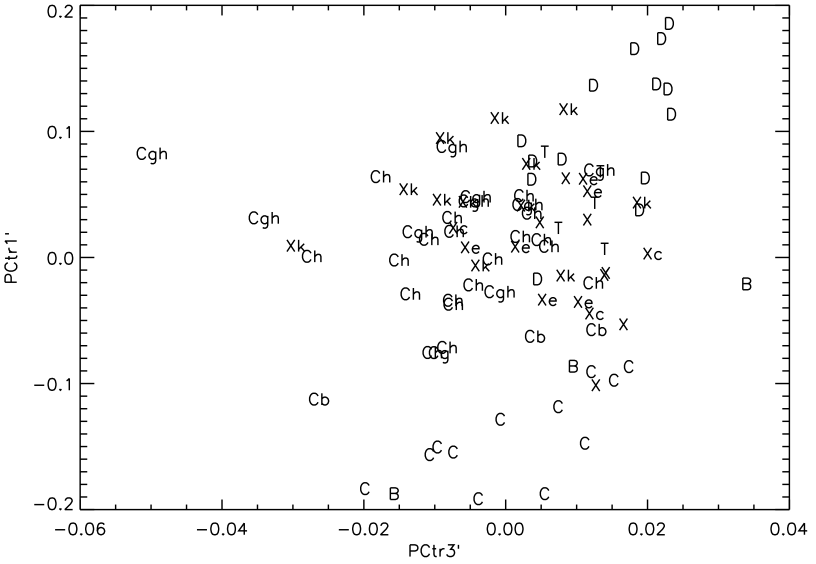

Figure 4.19: Plot of PC values from principal component analysis of *exclusively* C- and X-complex plus D- and T-type objects in near-infrared. Here the first and third principal components are plotted.

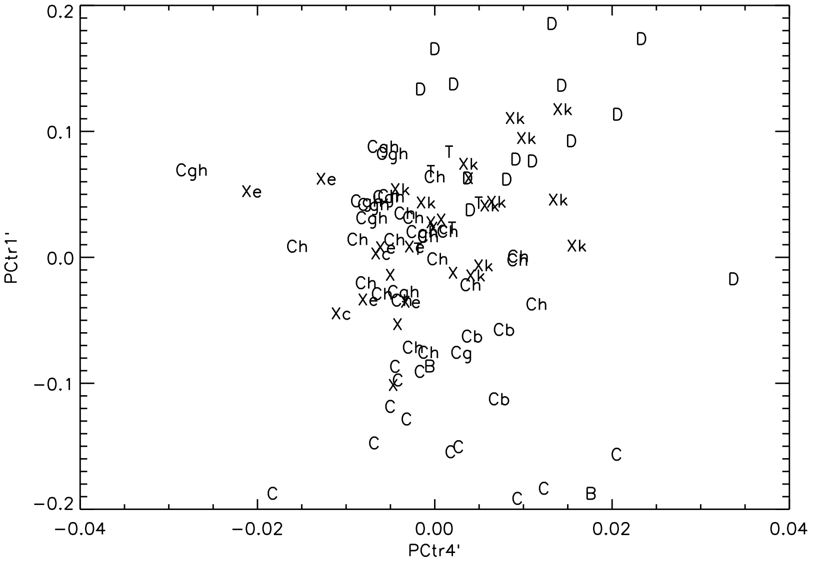

Figure 4.20: Plot of PC values from principal component analysis of *exclusively* C- and X-complex plus D- and T-type objects in near-infrared. Here the first and fourth principal components are plotted.

Table 4.2: Average Albedos for each Taxonomic Class

Class	Albedo[a]	Standard Dev	N[b]	NEO debiased albedo[c]
A	0.29	0.17	5	0.200±0.020
C	0.06	0.02	12	0.101±0.027
Cb	0.07	0.05	3	
Cgh	0.13	0.14	10	
Ch	0.06	0.01	16	
D	0.09	0.06	12	0.042±0.013
K	0.15	0.05	13	
L	0.15	0.05	14	
S	0.21	0.05	63	0.239±0.044
Sw	0.20	0.08	7	
V	0.27	0.14	3	0.417±0.147
X,T[d]	0.06	0.03	7	0.072±0.025
Xc	0.17	0.10	3	
Xe	0.14	0.03	3	
Xk	0.15	0.08	16	

[a] Average geometric albedo per class. Albedo values are from Tedesco et al. (2002)

[b] Number of objects used for average

[c] NEO debiased average albedos are from Stuart and Binzel (2004). They group the classes differently then we have here.

[d] Because the X and T classes are spectrally very similar we combine them for albedo averages to increase the sample size.

albedo. The average NEO albedo for D-types is lower than this sample, however it is based only on one albedo measurement. The V-types also have very different average albedos, although each of our samples only contains 3 objects. Vesta has a high albedo (0.42) matching those of the NEOs, which presumably came from Vesta. The two other Main Belt V-types with albedo measurements (1904 Massevitch and 1459 Magnya) are not in the Vesta family.

Figure 4.21 plots the distribution of geometric albedos for each taxonomic class for which there are at least three objects with albedo values. The albedo data is from Tedesco et al. (2002). While many classes have a small sample size, there are a few trends that can be noted. Many classes (C, Cb, Ch, S, X, T, and Xc) have reasonably well constrained albedos that vary by less than 0.15. The S-type has a broader overall range because of its large sample size, but the large majority of objects do not vary more than the other classes. Some classes (K, L, Sq, and Xk) have wide distribution of albedos among objects. Other classes have "albedo anomalies" in their class, with just one or two outliers with a significantly high albedo. While most Cgh-types have albedos less than 0.1, there is one object with an albedo greater than 0.4. Vesta is the high albedo outlier among V-types; however, the sample size is very small. Among D-types there are also two high albedo outliers. D-types are traditionally thought of as very dark, with very low albedos. The existence of two higher albedo objects forces us to recognize that this class of very red objects likely has a variety of different surfaces.

Larger samples, including objects classified under the Bus or Tholen systems, or simple classifications from SDSS colors, should provide much more insight on the albedo distributions of asteroid populations. The information provided by albedos of objects classified in this system, however, have the advantage of knowledge of spectral behavior in the near-infrared. With a larger sample, it would be worth reexamining the albedo distributions particularly among S-complex objects for which near-infrared data is critical.

4.8 Conclusion

An extended taxonomy was presented here using Principal Component Analysis and visible features to characterize visible and near-infrared wavelength spectra. The system, based on the Bus visible taxonomy from Bus (1999); Bus and Binzel (2002a), has 24 classes compared to 26 in the Bus system. We eliminated three classes: Ld, Sl, and Sk. All the Bus S subclasses (Sa, Sl, Sk, Sq, Sr) had objects that merged back

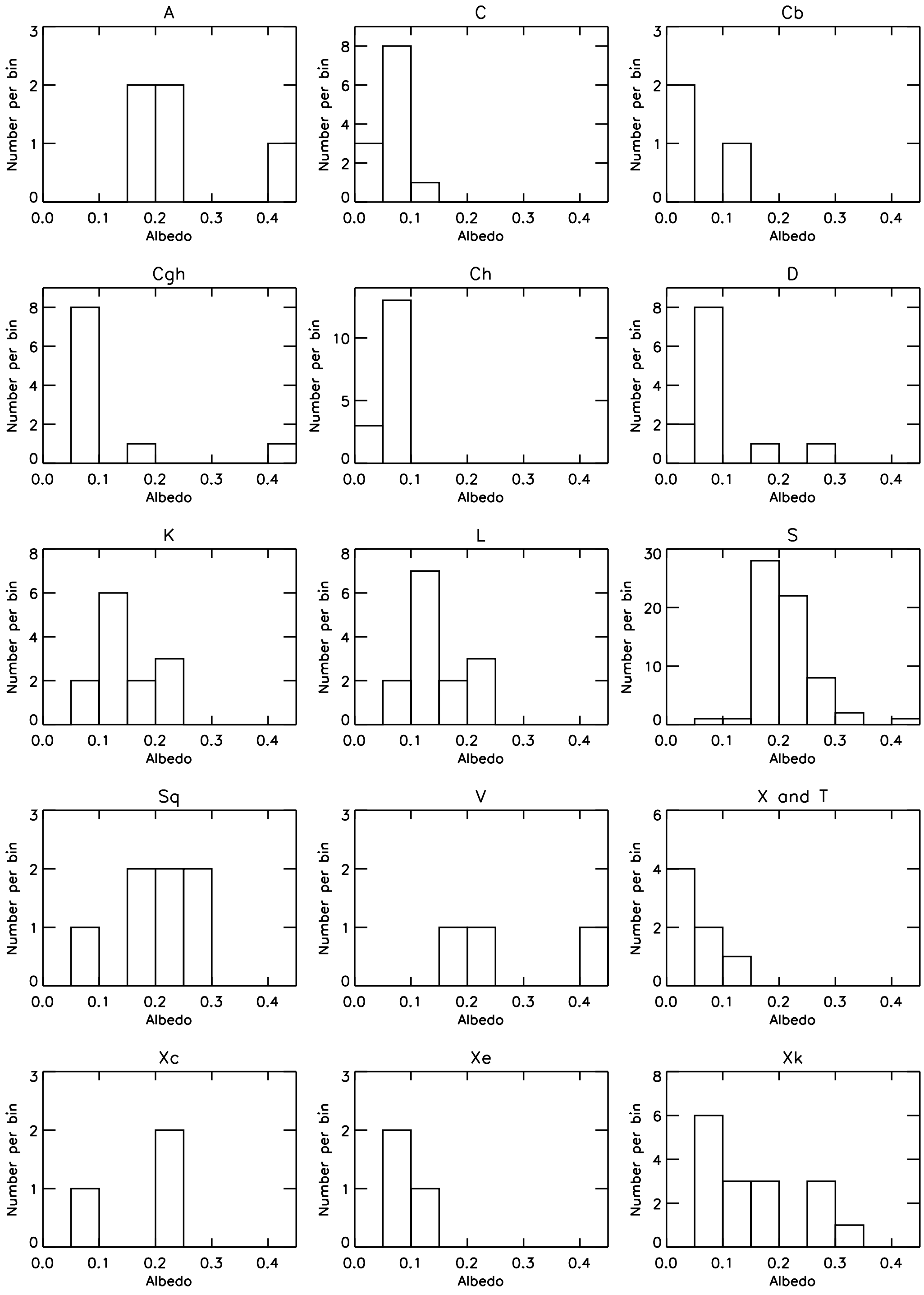

Figure 4.21: The distribution of object geometric albedos per class. Albedos are from Tedesco et al. (2002). Only classes with at least 3 objects with albedo measurements are presented. The bin width is 0.05, and the last bin represents any albedo value greater than 0.4. The mean and median albedo error for the sample are 0.02 and 0.01, respectively. The largest error by far is for a single S-type with a measured albedo of 0.43±0.15.

into the S-class, although many Sq objects remained Sq and two Sr objects were relabeled Sa. A new intermediate class, the Sv-class, was created as a link between the S- and V-classes. High-sloped S, Sq, Sr, Sv, and V objects were given a w notation to indicate possible weathering, but this notation does not constitute a new class. Many of the classes that lie left of line α in PC2$'$ versus PC1$'$ space are either featureless or exhibit only small features at visible wavelengths identified by Bus (1999); Bus and Binzel (2002a). It is still necessary to use these visible features to distinguish the classes because there are no other corresponding features at near-infrared wavelengths. We have also devised a method to categorize data when solely the near-infrared wavelength range is available, however, without visible wavelength information, the near-infrared taxonomy supplement cannot definitively classify many types especially those in the C- and X-complex, as many of those classes are defined only by visible wavelength features.

By attempting to create a supplementary method of classifying near-infrared-only data, we simultaneously provided a test for the limits of having only visible or only near-infrared wavelength data. We find that visible wavelength data is strongly indicative of near-infrared behavior. Spectra classified as A-types however, often do not have the expected strong 1-μm absorption band. We learn that the strength of the dip seen toward the end of the visible regime that indicates the presence of a 1-μm feature, does not necessarily indicate the shape and depth of that feature. This prompted the change of designation among some objects labeled L and K, as well as among some S-, Sq, and Sr- types.

Additionally, we have found the limits of PCA. When near-infrared data are added, PCA is overwhelmed by the 1- and 2- micron features and does not do an adequate job of identifying more subtle features such as those found in the visible region in the C- and X- complex spectra. Even though a more quantitative approach is preferred for distinguishing groups, being able to visually identify and define characteristic features of a spectrum has proven valuable.

The ultimate goal of a taxonomy is to lead toward a better understanding of the mineralogic composition of asteroids. While grouping asteroids is a useful tool, without mineralogic insight behind it, taxonomy is “just a letter”. Many methods of analysis are used to interpret the mineralogy of asteroid spectra. Band depths and widths are used to interpret olivine and pyroxene contents (e.g. Gaffey1993). Modeling, such as that described in section 3.2.1, are also used to estimate abundances by reproducing a spectrum using optical constants created from laboratory spectra. Meteorites, which are actual asteroid samples that can be measured in the lab, are also enormously important for understanding the composition of asteroids. Linking meteorite types with asteroid classes can provide important mineralogic constraints.

There is much future work to be accomplished for asteroid taxonomy. More complete systems in the future should include more than spectral information. Including visible albedo, radar albedo, densities, polarimetric measurements, longer wavelength data, and dynamical families could more thoroughly separate types of objects. At the same time, a taxonomy must always strive to be user-friendly, for if it is overcomplicated or not easily accessible and understandable to the community, it is not providing its intended service.

Part III

The Outer Solar System

Chapter 5

Photometric Analysis of TNOs and Centaurs

This chapter analyzes the photometric colors of 23 TNOs and Centaurs, nine of which have never been previously observed. Taxonomic classifications are assigned to the data and a search for possible variation is performed. The five objects that differ from previous data are discussed in further detail. This chapter is directly from DeMeo et al. (2009b) except for Section 5.6 which is from DeMeo et al. (2010a).

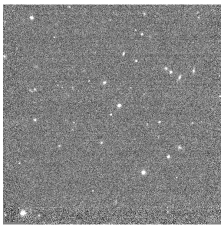

Contents

5.1 State of Understanding

By studying the colors of distant, minor bodies in our solar system, we learn about the initial conditions and evolution of the outer solar system, as well as the characteristics of the building blocks of planets. Because Transneptunian Objects (TNOs) are particularly faint and long integration times are essential for good quality data, photometry currently provides the best method of surveying a significant population of these objects. From these initial data, we can target specific objects of interest for follow-up observations. Although spectroscopy is a more useful tool for determining surface compositions, we are limited to the brightest of the TNO population to achieve acceptable signal-to-noise ratios from even the largest ground based telescopes. TNOs display a wide range of colors ranging from neutral or slightly blue to very red. The goal of surveying a large number of these objects is to identify color characteristics that relate independent populations of TNOs. A review of Transneptunian Object compositions and surface properties is provided by Barucci et al. (2008a).

The first ESO (European Southern Observatory) Large Program at Paranal, Chile, which occurred between 2001 to 2003, provided excellent photometric data (Boehnhardt et al., 2002; Peixinho et al., 2004; Delsanti et al., 2006). Relevant statistical analyses were performed and all possible correlations between colors and orbital parameters were analyzed (for a complete review see Doressoundiram et al., 2008). The main result was that different colors could be identified with the cold classical objects (low inclination, red color and small size diameters), supposed to be more primitive, and the hot classical objects (with higher inclinations and diverse colors and sizes) (Doressoundiram et al., 2002).

In analyzing a significant number of objects, it is important to identify groups of objects with similar characteristics. There are two means of characterizing TNOs, according to either their dynamics or surface properties. Their dynamical orbital groups are defined by Gladman et al. (2008). Our sample includes objects from each of the following Gladman categories: resonant (objects in mean motion resonances with Neptune), detached (pericenters decoupled from Neptune), scattered (unstable orbits and high eccentricities), and classical (circular orbits and low eccentricities).

Taxonomies used to differentiate between a range of surface compositions have been used for small body populations since the 1970s (Chapman et al., 1975) when they were first applied to main belt asteroids. More advanced systems were developed for inner solar system small bodies such as the Tholen taxonomy based on 8 colors (Tholen, 1984) and SMASSII (Small Main-Belt Asteroid Spectroscopic Survey II) spectral taxonomy (Bus and Binzel, 2002a). Classification systems are extremely useful for organizing surface characteristics, which may suggest age, composition, and surface alteration. By applying the same methods used for asteroids (multivariate statistical analysis and principal components), the first TNO taxonomy was created using 22 objects with data for four colors (B-V, V-R, V-I, and V-J) by Barucci et al. (2001). The Barucci taxonomy is a four-class system ranging from a neutral color, BB, to intermediate red colors, BR and IR, to very red, RR.

In this paper we present the visible and near-infrared photometric results for data acquired between October 2006 and September 2007 for 23 objects, 9 of which have never been previously observed, obtained in the framework of a second ESO Large Program (PI=M.A. Barucci) devoted to observing TNOs and Centaurs with different techniques. The corresponding spectra of these objects are presented in Alvarez-Candal et al. (2008) and Guilbert et al. (2009a). While we strive to observe any objects available that have never been observed photometrically, it is also important to continue to study previously observed objects and asses whether results are consistent or if there are changes occur in these objects that could reflect inhomogeneous surface properties. The visible and near-infrared observations were carried out simultaneously when possible. See Appendix B.1 for observational circumstances. We calculate colors for all objects, determine taxonomic types when sufficient data are available, and verify the types for previously observed objects. Classification was performed by G-mode analysis developed in Fulchignoni et al. (2000) for the Barucci classification system (Barucci et al., 2005a) using between two and five color data per object.

5.2 Taxonomy of TNOs

Barucci et al. (2005a) created a new taxonomy for TNOs and Centaurs based on a sample of 51 objects using the same method as asteroid taxonomies (Barucci et al., 1987; Tholen and Barucci, 1989): Principal

Component Analysis (PCA) and multivariate G-mode analysis. Using 5 colors (B-V, V-R, V-I, V-J, V-H), four groups based on photometric colors were defined, each with capitalized two-letter designations to distinguish this TNO taxonomy notation from those for asteroids. Objects having neutral colors with respect to the Sun are classified as BB (blue objects), and those having very high slope are classified RR (very red objects). The BR group contains objects with an intermediate blue-red color, while the IR group includes moderately red objects. These classes are expected to represent objects with different surfaces. Some objects could differ in their initial compositions, which distinguish their colors, while others may have different colors and slopes because their surfaces have been affected by processes such as bombardment by energetic particles over time. Fig. 1 highlights the differences between classes among our sample. It is evident that there is also wide variation in slope among the BB class objects due to the broad boundary defining the class.

Fulchignoni et al. (2000) published an extension of the G-mode analysis method, which enables the new classification of objects within the Barucci taxonomic system. The G-mode analysis calculates how different an object's colors are compared to the mean for that class. A variance value is found for each object for each taxonomic class and any class within three sigma is designated to the object.

Even if only a subset of the colors used in the initial taxonomy exists for an object, the algorithm provides at least a preliminary indication of its class. Of course, the fewer colors (and thus less information) decreases the confidence of the classification. Objects that do not have a full set of colors for classification may be assigned two taxonomic types since there is insufficient information to differentiate to which of the two classes the object belongs. We applied this algorithm to each object with more than one color data, and the resulting classes along with the colors are reported in Appendix B.3.

5.3 Results

We report colors and magnitudes for the 23 observed objects. Magnitudes in the V, J, H, and K_s filters are reported in Appendix B.2. In Appendix B.2, we also provide absolute H magnitudes, labeled $H_v(1,1,0)$, the visible magnitude of an object if it were placed 1 AU from the sun and 1 AU from the Earth with a phase angle of zero. The equation used to calculate the absolute magnitude is expressed in Eq. 1:

$$H_v(1,1,0) = V(1,1,0) = V - 5log(r\Delta) - \alpha\beta \tag{5.1}$$

where V is the visible magnitude reported in Col. 5 of Appendix B.2, and r, Δ, and α are the heliocentric and topocentric distances and the phase angle, respectively, given in Appendix B.1. β is the phase curve slope (mag/deg). For TNOs, we used a β value of 0.14±0.03 mag/deg, the modal value of the measurements from Sheppard and Jewitt (2002). For Centaurs and Jupiter Family Comets (JFC), we used a β value of 0.11±0.01 mag/deg, the result of a least squares fit by Doressoundiram et al. (2005) of the linear phase function $\phi(\alpha) = 10^{-\alpha\beta}$ of data from Bauer et al. (2003).

Mean colors with respect to the V magnitude are shown in Appendix B.3. The errors for the colors were calculated as the square root of the sum of each magnitude error squared, $\sqrt{err_1^2 + err_2^2}$. When more than one observation was taken for an object, and hence more than one magnitude measurement in a certain filter existed, the weighted mean magnitude was calculated and one single color was reported. From these colors, we calculated reflectance values at each wavelength using Eq. 2:

$$R(\lambda) = 10^{-0.4[(M_F - M_V) - (M_F - M_V)_\odot]} \tag{5.2}$$

where (M_F) and $(M_{F\odot})$ are the magnitudes of the object and sun, respectively, at the central wavelength of filter F (specified to be BVRIJHK$_s$). The equation is normalized to unity at the central wavelength of filter V using M_V and $M_{V\odot}$, the V magnitudes of the object and sun, respectively. Solar colors listed in the first row of Appendix B.3 are taken from Campins et al. (1985) and Hardorp (1980). In Fig. 1, a plot is shown of normalized reflectance values for all classified objects with more than three data points; a large slope variation is evident.

Some color values differ significantly from the literature, and even some previously published results disagree significantly from each other (for a summary of TNO photometry values, see Fulchignoni et al., 2008). These color differences could be attributed to inhomogeneous surface compositions or irregular shapes for objects that were not observed simultaneously in the visible and near-infrared wavelengths.

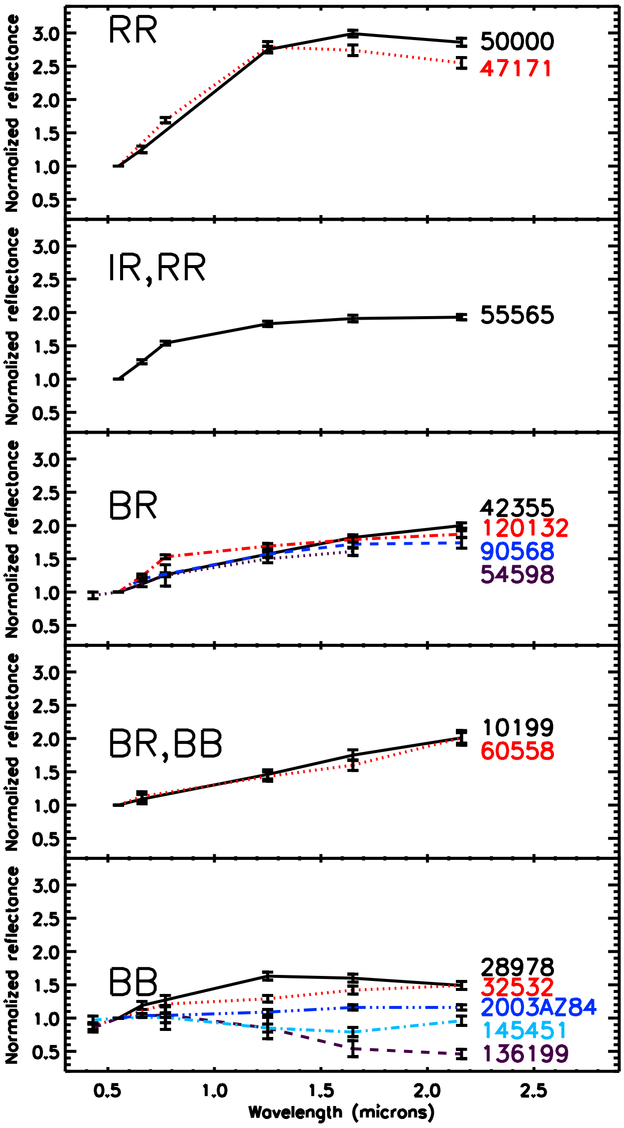

Figure 5.1: Normalized Reflectance Values for 14 TNOs and Centaurs. This figure plots reflectivity values for classified objects with more than two data points. The spectra are normalized to unity at the center of the V-band (0.554 μm). Reflectivities are calculated using Eq. 2. BB objects include 28978, 32532, 136199, 145451, and 2003 AZ84. BR,BB objects are 10199 and 60558. BR objects are 42355, 54598, 90568, and 120132. The IR, RR object is 55565, and the two RR objects are 47171 and 50000.

Table 5.1: Known Lightcurve Data for TNOs

Object	**Δ Magnitude**[a]	**Period (h)**[b]	**Ref**[c]
26375	<0.10		1
28978	<0.05		2,3
32532	0.16 ±0.02,0.18	4.1546±0.0001(s)	4
		8.34(d)	5
42355	<0.05		2,3
47171	<0.05		2,3,6
47932	0.61 ± 0.03	8.329±0.005(d)	1
50000	0.13 ± 0.03	17.6788±0.0004(d)	7
54598	0.75 ± 0.09	4.57±0.02(s)	4
55565	0.08 ± 0.07, <0.03	8.86±0.01(s)	8,9
55637	<0.06, 0.21±0.06	7.2 or 8.4(s)	2,10
60558	0.24 ± 0.06	13.401(s)	10
83982	0.14 ± 0.04	6.97 or 9.67(s)	3
90568	<0.08		9
120132	<0.08		9
136199	<0.01		9

[a] The peak to peak range of the lightcurve.

[b] Lightcurve periods in hours noted as single (s) or double (d) if the period has one or two maxima.

[c] Data is referenced from: 1. Sheppard and Jewitt (2002), 2. Sheppard and Jewitt (2003), 3. Ortiz et al. (2003a), 4. Ortiz et al. (2002), 5. Farnham and Davies (2003) 6. Lacerda and Luu (2006), 7. Ortiz et al. (2003b), 8. Ortiz et al. (2006), 9. Sheppard (2007), 10. Rousselot et al. (2005). For a complete listing see Sheppard et al. (2008).

Some of these objects have known lightcurves that can provide insight into the expected magnitude changes during a rotational period. These lightcurve magnitude amplitudes are listed in Table 5.1. A complete list of all known TNO lightcurves can be found in Sheppard et al. (2008). Objects in our sample with the most striking magnitude changes include 47932 and 54598 with magnitude changes throughout their rotational periods of 0.61 ± 0.03 and 0.75 ± 0.09, respectively.

5.4 Discussion

Using between two and five color data for each object, we classified 18 of the 23 objects, and their classes are reported in Appendix B.3. There were six BB, four BR, two RR and six designated two or more categories due to insufficient data. Three objects (83982, 119951, 2003 UZ117) had only one color and were therefore unclassifiable. Two objects (26375, 145452) did not fall within the range of the 4 taxonomic groups: objects 26375 was previously classified as IR (Fulchignoni et al., 2008), while 145452 had never been previously observed. These two objects did not fall within any particular class because their visible colors matched those of the redder IR and RR classes while their infrared colors were more consistent with the bluer BB and BR classes.

Of the nine newly observed objects, we classified six. Objects 145451 and 145453 are in class BB, 90568 and 120132 are class BR, object 50000 was classified as RR, and the sixth object, 2003 QW90 had only two colors allowing us only to exclude it from the BB class because the object is redder than BB types. Objects 119951 and 2003 UZ117 had insufficient color data to complete the analysis, while the third object 145452 had five colors but did not correspond to any of the four categories.

Fourteen objects in our sample had been previously labeled. Ten objects remained in the same class or at least one of the two designations agreed if an object had been given two types. One (83982) had only one color data and could not be classified. Three objects changed from their previous classes: 26375 (1999 DE9), 28978 (Ixion), and 32532 (Thereus).

Seven objects have known periods from their lightcurves (see Table 5.1 for a summary of lightcurve publications). Object 47171 is a binary Two of the objects, 47932 and 54598 (Bienor) have extreme lightcurve amplitudes (0.61 and 0.75 magnitude changes, see Table 5.1). Their calculated absolute mag-

Table 5.2: Comparison of infrared colors with previous work for selected TNOs

Obj	**J-H**	**J-K**	**Ref** [a]
26375	0.29±0.09	0.35±0.09	4
	0.40±0.09	0.41±0.13	1
	0.32±0.11	0.28±0.11	2
	0.29±0.06	0.36±0.06	3
28978	0.26±0.06	0.25±0.06	4
	0.30±0.07	0.09±0.07	1
32532	0.39±0.07	0.51±0.07	4
	0.34±0.07	0.62±0.07	1
	0.51±0.04	0.62±0.06	5
47932	0.37±0.07	0.44±0.09	4
	0.37±0.11	0.54±0.11	1
54598	0.36±0.06		4
	0.36±0.06		1
	0.35±0.06		6
	0.51±0.07		7

---

[a] References 1: Doressoundiram et al. (2007), 2: Delsanti et al. (2006), 3: Doressoundiram et al. (2003), 4: This work, 5: Barucci et al. (2002), 6: Dotto et al. (2003), 7: Delsanti et al. (2004).

nitudes $H_v(1,1,0)$ are significantly different from previous results, but still inside the Δ magnitude value of their lightcurves. We discuss these objects and others that changed classes in further detail.

5.4.1 26375 (1999 DE9)

Seven measurements combined in Fulchignoni et al. (2008) produced the previous classification (IR) of 26375. Combined with lightcurve data indicating no significant magnitude variations (see Table 5.1) it appears that previous measurements were robust and stable. While our visible colors agree with published results, the infrared colors with respect to V are approximately 0.3 magnitudes lower. Our J-H and J-K colors, however, are in good agreement with previous work (see Table 5.2 and Table 5.3). Jewitt and Luu (2001) noted a feature attributed to H_2O ice (abundance around 10%), which was also detected by Barkume et al. (2008). This feature was not seen by Doressoundiram et al. (2003), suggesting that there may be heterogeneity on the surface.

5.4.2 Ixion (29878)

Ixion (28978) had been previously classified as an IR, but is a BB according to our data, which represents a significant change. The previous classification was based on one set of observations of six colors (data from Doressoundiram et al., 2007). Ixion does not have a significant lightcurve amplitude (see Table 5.1), although, while our J-H color agrees with previous work, the J-K is higher. This may correspond to surface heterogeneity. Our V-J and V-H colors were each almost 0.3 magnitudes lower than seen by Doressoundiram et al. (2007), which produced a significant classification change. Slight H_2O ice features were detected in the infrared spectra by both Licandro et al. (2002) and Barkume et al. (2008).

5.4.3 Thereus (32532)

Thereus (32532) was previously a BR, but our data classifies it as a BB. While our optical data agree with published results, our V-J value is more than 0.3 magnitudes lower, V-H is almost 0.4, and V-K_s is around 0.45 magnitudes lower than averages published by Fulchignoni et al. (2008). These differences are striking. Thereus has a double peak lightcurve of amplitude 0.18 magnitudes (see Table 5.1), and has a period of over eight hours (see Table 5.1). Our measurements were nearly simultaneous with only an 11 minute separation between visible and near-infrared data, so the difference cannot be attributed to observing different parts of the surface. Merlin et al. (2007), however, report spectral variation across the surface, which could account for differences between our data and previous work.

5.4.4 47932 (2000 GN171)

For object 47932, visible and near-infrared observations were taken between 20 and 45 minutes apart. Although this object has a fairly long rotation period of 8.329±0.005 hours (see Table 5.1) with respect to the time difference between our visible and near-infrared observations, double maxima were detected implying that within 45 minutes, the object's surface shape or composition that we measured, changed significantly. It is probable that, during our exposures in J, the surface changed as well. 47932 previously classified as an IR type, by our analysis is placed in either the BR or IR classes, consistent with previous results.

We calculate an absolute magnitude $H_v(1,1,0)$ for 47932, ranging from 6.20 to 6.31±0.04 depending on the night of observation (see Table B.1). Doressoundiram et al. (2007) reports a magnitude of 6.71±0.05, and McBride et al. (2003) report a similar value of 6.71±0.04. The difference between our value and that reported by previous work is well within the 0.61±0.03 magnitude lightcurve amplitude.

5.4.5 Bienor (54598)

Bienor (54598) has a single peak lightcurve with a period of 4.57±0.02 hours (see Table 5.1). Visible and near-infrared observations for Bienor were taken approximately 45 minutes apart, a time period during which the object rotated significantly. Our visible versus near-infrared observations were then acquired on different parts of the surface, which could significantly change the magnitude. The absolute magnitude $H_v(1,1,0)$ calculated from our results is 7.46±0.03 compared to 8.04±0.02 from Doressoundiram et al. (2007). This large difference in magnitude is still smaller than the lightcurve amplitude of 0.75±0.09 (Table 5.1). A weak detection of H_2O ice features was noted by Barkume et al. (2008).

The visible colors B-V, V-R, and V-I, as well as the near infrared colors J-H and J-K, are consistent with past published results. The V-J, V-H, and V-K colors for several objects, however, appear to differ from the published averages (see Table 5.2 and Table 5.3). Some color values are lower than in previous work, while others, such as those for Eris are higher compared to values published by Brown et al. (2005b). While this difference could easily be attributed to surface heterogeneity or large lightcurve amplitudes for some objects, for objects without known variation the reason is less clear. It is important to note, however, that behavior in the optical range (such as small or large lightcurve amplitudes) may indicate but not necessarily constrain behavior in the near-infrared. The difference of colors, spans over different nights, both service and visitor mode, and several people reducing the same data independently, therefore the difference in values when compared to the literature cannot be due to weather, calibration, or reduction of a specific night. The ISAAC instrument broadband filters used for infrared observation differ from the filters that measured magnitudes for UKIRT standard stars, which we used for calibration. A color transformation between ISAAC and other systems is not yet available and could account for part of the difference, although probably not more than a few hundredths of a magnitude.

While objects that were classified in the BB class range did not change classes due to the lower infrared colors, it is important to note that the ranges of possible parameter values are far wider for BB compared with those of the BR and IR classes, implying that for equal magnitude changes an object in the BB class may not change classes, while those within the BR and IR groups may.

5.5 Conclusion

We report photometric observations from the ESO VLT system for 23 objects, nine of which have never been previously observed. Eighteen of these objects were given taxonomic classifications: six BB, four BR, two RR and six in two or more categories due to insufficient data.

Three objects that had been previously observed and classified, were assigned different classes: 26375 (1999 DE9), 28978 (Ixion), and 32532 (Thereus). While there is no significant lightcurve amplitude measured for 26375, H_2O ice features were noted by Jewitt and Luu (2001) and Barkume et al. (2008), but were not detected by Doressoundiram et al. (2003), suggesting that there may be heterogeneity on the surface. Ixion does not have a significant magnitude change during one rotation either, but the

Table 5.3: Comparison of colors with previous work for selected TNOs.

Object	**B-V**	**V-R**	**V-I**	**V-J**	**V-H**	**V-K**	**Ref**
26375		0.62 ± 0.02	1.12 ± 0.02	1.53 ± 0.07	1.82 ± 0.08	1.88 ± 0.08	This work
	0.97 ± 0.03	0.58 ± 0.01	1.15 ± 0.01	1.84 ± 0.04	2.17 ± 0.05	2.19 ± 0.05	Fulchignoni et al. (2008)[a]
28978		0.55 ± 0.06		1.59 ± 0.06	1.85 ± 0.07	1.84 ± 0.07	This work
	1.03 ± 0.03	0.61 ± 0.03	1.19 ± 0.04	1.88 ± 0.09	2.18 ± 0.11	1.97 ± 0.09	Doressoundiram et al. (2007)
32532	0.81 ± 0.05		0.90 ± 0.13	1.35 ± 0.05	1.75 ± 0.06	1.86 ± 0.06	This work
	0.75 ± 0.01	0.49 ± 0.02	0.94 ± 0.01	1.69 ± 0.05	2.14 ± 0.07	2.3 ± -0.05	Fulchignoni et al. (2008)
47932		0.59 ± 0.09	1.12 ± 0.04	1.65 ± 0.05	2.01 ± 0.06	2.08 ± 0.07	This work
	0.92 ± 0.01	0.62 ± 0.01	1.22 ± 0.02	1.84 ± 0.08	2.21 ± 0.14	2.38 ± 0.14	Fulchignoni et al. (2008)
	0.92 ± 0.01	0.62 ± 0.01	1.22 ± 0.02	1.84 ± 0.08	2.21 ± 0.14	2.38 ± 0.14	Fulchignoni et al. (2008)
54598	0.73 ± 0.05		0.93 ± 0.16	1.52 ± 0.06	1.89 ± 0.06		This work
	0.69 ± 0.02	0.47 ± 0.02	0.92 ± 0.05	1.74 ± 0.03	2.14 ± 0.05	2.27 ± 0.11	Fulchignoni et al. (2008)

[a] The values from Fulchignoni et al. (2008) correspond to averages of several measurements. For 26375 and 54598 it includes 7 sources each (3 and 4 for near-ir, respectively). For 32532 and 47932 there are 4 sources each (3 and 2 for near-ir, respectively).

differences between our infrared colors and those reported by Doressoundiram et al. (2007) suggest that there is variation over the surface. We conclude that for Thereus (32532) the change is due to surface variation reported by Merlin et al. (2007), which is also evident in its lightcurve which has significant magnitude changes (∼0.16) measured by Ortiz et al. (2002).

In most of our near-infrared observations, including those of Ixion and Thereus, we report lower color values than previously published results. We measure a wide range of spectral reflectivities among the sample, which covers all four taxonomic classes. Two objects, 47932 (2000 GN171) and 54598 (Bienor), had absolute magnitude values $H_v(1,1,0)$ that were significantly different from previously published results. For both objects, extreme lightcurve amplitudes have been measured, which explain the variable $H_v(1,1,0)$ magnitude and the classification change of 47932 between different observations.

5.6 Final Color Results from the second ESO Large Program

The results presented above represent the first half of the second ESO Large Program. By combining all results from the Large Program and data from the literature Perna et al. (2010) present new statistics on TNO colors. They find among our sample that our measurements of three objects could not be classified in this system (26375, 145452, and 2007 UK_{126}), because their visible colors were red, matching best the IR and RR classes, while the near-infrared colors were bluer, consistent with the BB and BR classes. This suggests greater color diversity than what was found in the original sample used to create the taxonomy. In analysis of the distribution of taxonomic classes among dynamical classes and orbital elements, it was found that 8 of the 13 Centaurs in the sample were in the neutral to moderately red BB and BR classes while the other 5 were in the RR class, confirming the bimodality of the population (Peixinho et al., 2003). All IR class objects in our sample are classical objects, which is consistent with Fulchignoni et al. (2008) where they found the IR class confined to the resonant and classical population.

Chapter 6

A spectroscopic analysis of Jupiter-coupled object (52872) Okyrhoe, and TNOs (90482) Orcus and (73480) 2002 PN$_{34}$

We analyze the surface composition of three outer Solar System small bodies, Jupiter-coupled object (52872) Okyrhoe, and TNOs (90482) Orcus and (73480) 2002 PN$_{34}$, by modeling spectroscopic measurements in the visible and near-infrared wavelength ranges. We find varying amounts of H_2O ice among these bodies, Okyrhoe has no traces in our spectrum, 73480 has small amounts, and Orcus has large quantities. Furthermore, we discuss possible surface variation on Okyrhoe and Orcus, and place constraints on volatile ices on Orcus. This work is directly from the submitted article DeMeo et al. (2010b).

Contents

Table 6.1: Target Information

Parameter	**(52872)** **Okyrhoe**	**(73480)** **2002 PN$_{34}$**	**(90482)** **Orcus**
Orbit	Jupiter-Coupled[a]	Scattered Disk	Resonant (3:2)
Albedo (%)[b]	$2.49^{+0.81}_{-0.55}$	$4.25^{+0.83}_{-0.65}$	$19.72^{+3.40}_{-2.76}$
Diam. (km)	$52.1^{+6.9}_{-6.9}$	$119.5^{+10.3}_{-10.2}$	$946.3^{+74.1}_{-72.3}$
a (AU)[c]	8.4	31.2	39.2
e	0.31	0.57	0.23
i (deg)	15.7	16.6	20.6
Taxonomy[d]	BR	BR, BB	BB

---

[a] Some classify object 52872 as a Centaur, but because its Tisserand parameter T_J is less than 3.05 (T_J=2.95) it is "rapidly perturbed by Jupiter" according to Gladman et al. (2008)

[b] From Stansberry et al. (2008)

[c] a, e, and i are the orbital elements semi-major axis, eccentricity and inclination, respectively.

[d] Classifications are performed using the taxonomic system designed by Barucci et al. (2005a). The designation comes from Fulchignoni et al. (2008) for Okyrhoe and Orcus and from Perna et al. (2010) for (73480) 2002 PN$_{34}$

6.1 Introduction

Transneptunian Object (TNO) spectral signatures provide important constraints on surface composition. While most visible spectra are featureless (Lazzarin et al., 2003; Fornasier et al., 2009), many of the TNO surfaces are ice-rich and have clear spectral signatures in the near-infrared. Some TNO near-infrared spectra are largely featureless and only variations in spectral slope allow us to distinguish one from another (Guilbert et al., 2009a). Only for the largest and brightest TNOs can spectra be measured with a sufficiently high signal-to-noise ratio necessary for a detailed analysis. For dimmer bodies, a taxonomy of photometric colors of TNOs helps categorize objects with similar characteristics (Barucci et al., 2005a). The four classes are BB, BR, IR, and RR, spanning from neutral colors to very red with respect to the Sun.

The spectra of small bodies in the outer Solar System have been divided into a few compositional groups. The largest bodies contain a significant fraction of volatiles on their surfaces. The signatures of methane are particularly apparent on these bodies: Pluto, Eris, Makemake, Quaoar, and Sedna, (e.g., Cruikshank et al., 1976; Brown et al., 2005b; Licandro et al., 2006b; Schaller and Brown, 2007a; Barucci et al., 2005b). Many TNOs and Centaurs show signatures of H_2O ice (Barkume et al., 2008; Guilbert et al., 2009a). Rare signatures of NH_3 (on Charon and Orcus; Buie and Grundy, 2000; Brown and Calvin, 2000; Barucci et al., 2008b) and methanol ((5145) Pholus and 2002 VE$_{95}$; Cruikshank et al., 1998; Barucci et al., 2006) have also been detected. Featureless spectra have a wide range of slopes but no distinct absorption bands, thus leaving the surface composition largely unknown.

Further complicating our understanding of these bodies is a process called space weathering, which includes solar wind, cosmic ray, and micrometeorite bombardment which alter the chemical and physical properties of surfaces. Laboratory studies have provided insight into how these processes affect material expected to be on the surfaces (Strazzulla and Palumbo, 2001; Strazzulla et al., 2003; Brunetto et al., 2006c). The effects of space weathering certainly differ on larger, volatile-rich bodies versus the smaller ones. Rejuvenation processes such as collisions and for larger bodies sublimation and recondensation of ices and possibly cryovolcanism are in constant competition with the space weathering aging process.

Here we present new visible and near-infrared photometric measurements and near-infrared wavelength spectra for the Jupiter-coupled object (52872) Okyrhoe, the Resonant object (90482) Orcus, and Scattered Disk object (73480) 2002 PN$_{34}$. Their physical and orbital properties are listed in Table 6.1. These observations are part of a second Large Program (PI M. A. Barucci) dedicated to investigating the surface properties of Centaurs and Transneptunian objects. The program was carried out between 2006 and 2008 using the European Southern Observatory (ESO) Very Large Telescope (VLT). Observational methods for this program included spectroscopy, photometry (colors and lightcurves), and polarimetry to characterize TNOs with the most information available from ground-based studies. For a summary of previously published results see DeMeo et al. (2010a). In this work we present the observational

Table 6.2: Circumstances of Spectroscopic Observations

Object	**Instr**[a]	**Date**	**UT$_{start}$ (hh:mm)**	**T$_{exp}$ (sec)**	**Airm**	**Standard Star (Airm)**
(52872) Okyrhoe	FORS2	Feb 04, 2008	06:33	1800	1.14	SA102 1081 (1.13)
(52872) Okyrhoe	ISAAC	Feb 03, 2008	07:02	1080	1.155 - 1.176	HIP045953 (1.166)
(52872) Okyrhoe	SINFONI	Feb 03, 2008	05:28	7800	1.128 - 1.204	SA102 1081 (1.140)
(73480) 2002 PN$_{34}$	FORS2	Nov 10, 2007	00:51	2800	1.22	SA115 271 (1.13)
(73480) 2002 PN$_{34}$	SINFONI	Nov 10, 2007	00:32	6000	1.161 - 1.384	SA115 271 (1.167)
(73480) 2002 PN$_{34}$	SINFONI	Nov 12, 2007	01:25	3600	1.247 - 1.678	SA115 271 (1.296)
(90482) Orcus	FORS2	Feb 04, 2008	05:25	2400	1.07	SA102 1081 (1.11)
(90482) Orcus	ISAAC	Feb 03, 2008	05:36	2880	1.058 - 1.087	HIP045953 (1.060)
(90482) Orcus	SINFONI	Feb 04, 2008	03:54	12600	1.058 - 1.252	SA102 1081 (1.135)

[a] FORS2 measures visible wavelength (0.4-0.8 μm), visible spectroscopy is from Fornasier et al. (2009), ISAAC measures J band wavelengths (1-1.4 μm), SINFONI measures H+K band wavelengths (1.4-2.4 μm)

Table 6.3: Circumstances of and Magnitudes from Photometric Observations

Obj	(52872) Okyrhoe	(52872) Okyrhoe	(73480) 2002 PN$_{34}$	(73480) 2002 PN$_{34}$	(90482) Orcus	(90482) Orcus
Date	3 Feb. 2008	4 Feb. 2008	10 Nov. 2007	10 Nov. 2007	3 Feb 2008	4 Feb 2008
UT$_{start}$	06:41	06:18	00:36	02:23	04:46	05:04
V		18.63 ± 0.02	20.68 ± 0.03			19.12 ± 0.02
R		18.14 ± 0.02	20.25 ± 0.05			18.73 ± 0.02
I		17.64 ± 0.02				18.37 ± 0.02
J	16.84 ± 0.06			19.00 ± 0.05	17.91 ± 0.05	
H	16.39 ± 0.07			18.49 ± 0.06	17.72 ± 0.07	
K$_s$	16.28 ± 0.05			18.29 ± 0.05	17.89 ± 0.05	
Δ (AU)[a]	4.883	4.877	14.894	14.894	46.904	46.9
r (AU)	5.800	5.800	15.344	15.344	47.807	47.807
α (deg)	3.9	3.7	3.3	3.3	0.5	0.5

[a] Δ, r, and α are the topocentric distance, heliocentric distance, and phase angle, respectively

circumstances and the photometric results in Tables 6.2 and 6.3, we describe the modeling procedure in Section 6.2, and we suggest surface compositions for each object in Section 6.3 based on bi-directional reflectance models, and compare the data to previously measured spectra to search for heterogeneity.

6.2 Modeling

We apply a radiative transfer model introduced by Hapke (1981). We calculate the geometric albedo A_r using Eq. 6.1 (Eq. 44 from Hapke, 1981) which is a function of the bihemispherical reflectance for isotropic scatterers, r_0, (Eq. 34 of Hapke, 1981) and the average single-scattering albedo, w. Because TNOs are observed at small phase angles we set the phase angle to zero, a good approximation. We use a Henyey-Greenstein function (Henyey and Greenstein, 1941) for the phase function, P_0. For Orcus and 73480, we set the asymmetry parameter to 0.3 for the purposes of this model which corresponds to a forward-scattering surface. Because Okyrhoe's albedo is so low, we had to set the asymmetry parameter to 0.35 to adequately reproduce its spectrum. We set the backscattering function to a fixed value, $B_0 = 0.67$, a value proposed by Verbiscer and Helfenstein (1998) for icy surfaces. We use the albedo as a constraint when modeling our spectra by normalizing the spectra at 0.55 μm to the visible albedo reported in Stansberry et al. (2008). To model their surfaces we use optical constants derived from laboratory spectra taken under similar conditions as those found in the outer Solar System. The best-fit model for each object is determined by minimizing the χ^2 value which quantifies the difference between the data and the model. In the case for these models, the χ^2 value is calculated based on a weighting of the spectrum, so that the fit near important features is considered much more important than the fit in the telluric regions for example.

$$A_r = \frac{1}{2}r_0(1 + \frac{1}{3}r_0) + \frac{w}{8}((1 + B_0)P_0 - 1) \tag{6.1}$$

Table 6.4: Best-fit Models

Object Model	**Amount (%)**	**Grain Size (μm)**	**Material**
(52872)	71	10	Amorphous Carbon
Okyrhoe	26	10	Triton Tholin
χ^2=2.03	3	10	Titan Tholin
(73480)	55	10	Amorphous Carbon
2002 PN_{34}	34	10	Triton Tholin
χ^2=181.21	11	40	Amorphous H_2O
(90482)	50	15	Crystalline H_2O
Orcus	23	15	Amorphous H_2O
Model 1	19	10	Amorphous Carbon
χ^2=200.06	8	10	Triton Tholin
(90482)	50	15	Crystalline H_2O
Orcus	22.5[a]	15	Amorphous H_2O
Model 2	20.5	10	“Blue” component
χ^2=136.49	5	10	Triton Tholin
	2	10	Titan Tholin
	35.5	10	Amorphous H_2O
(90482)	30	10	Crystalline H_2O
Orcus	20.5	10	“Blue” component
Model 3	7	100	Ammonia Hydrate
χ^2=137.56	5	10	Triton Tholin
	2	10	Titan Tholin

---

[a] Some of the concentrations in the models presented here are presented to a decimal place, however, it is important to note that the errors on the concentrations are at least a few percent.

We use an intimate mixture of materials, meaning that a photon interacts with grains of more than one composition before being reflected off the surface. Surfaces are likely, however, to have some combination of horizontally separated “patches”, vertical layers, and intimate mixtures of grains. We use optical constants of H_2O ice in both crystalline and amorphous form (at 40 K and 38 K from Grundy and Schmitt 1998 and Schmitt et al. 1998, respectively), amorphous carbon (Zubko et al., 1996), and Titan and Triton Tholin (Khare et al., 1984, 1993). Carbon and Tholins do not have unique, identifiable absorption bands, and thus their presence on these surfaces is not definite. They are used as representative material that aid in fitting the low albedo and red slope of the spectra, because optical constants are available for these materials. However they could be replaced with different dark or red materials, such as other organics.

For Orcus, we model the spectrum with ammonia hydrate (Roush, personal communication), as well as CH_4 and CO_2 (both from Quirico and Schmitt, 1997b) to place constraints on their abundance. We also artificially create a near-infrared-absorbing “blue” material, similar to that added in the models of Barucci et al. (2008b), to reproduce the spectral behavior. The need for this component is demonstrated in Section 7.4. The quantities and grain sizes for each component in each model are given in Table 6.4, and the best model for each object is plotted in Figs. 6.1, 6.3, and 6.4.

6.3 Discussion

Physical and dynamical properties of these three outer Solar System objects are given in Table 6.1. We discuss each spectrum and the models in detail in the following subsections and compare our data for both Okyrhoe and Orcus to previously published work.

6.3.1 (52872) Okyrhoe

Okyrhoe, discovered in 1998, is often considered a Centaur because of its low semi-major axis and perihelion (with respect to TNOs), but is dynamically classified as a Jupiter-Coupled object by Gladman

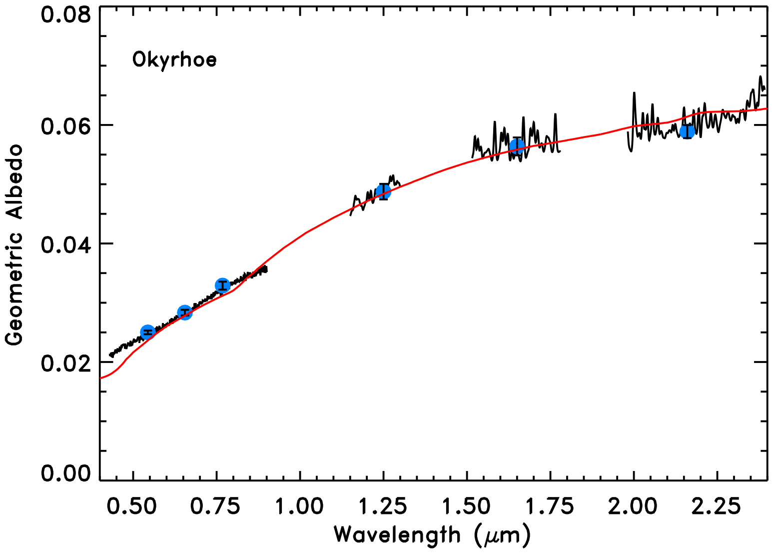

Figure 6.1: The spectrum of Okyrhoe and the best model. Blue circles mark reflectance values converted from photometric colors, and the errors are marked in black (but are smaller than the size of the circle). The best fit model (red) includes amorphous carbon, Triton Tholin and Titan Tholin.

et al. (2008) because it has a Jupiter-Tisserand parameter (T_J) less than 3.05. It has a diameter of around 50 kilometers and a very low albedo near 2.5% (Stansberry et al., 2008).

Okyrhoe was first observed in visible wavelengths by Lazzarin et al. (2003). The spectrum had no absorption features and a slope of 11.8±0.2 (%/10^3 Å). The visible spectrum used for modeling in this work, presented by Fornasier et al. (2009), is also featureless, but has a slightly higher slope of 13.4±0.6 (%/10^3 Å), however, they are still similar within a 2 sigma level of the uncertainties. Furthermore, Lazzarin et al. (2003) did not consider systematic uncertainties due to the solar analogue stars in the determination of the slope uncertainties as was done by Fornasier et al. (2009).

The first near-infrared spectrum of Okyrhoe was modeled by Dotto et al. (2003). They find that including a small amount of H_2O ice improves the fit to the data. Their best model was a spatially segregated combination of kerogen (97%), olivine (1%) and H_2O ice (2%). The high percentage of kerogen was used to reproduce the slope of the visible spectrum while maintaining the flatness in the near-infrared. Albedo was not used as a constraint in their models, although their model did result in a low albedo of 3%. Barkume et al. (2008) detected H_2O ice between the 1 and 3 sigma level on Okyrhoe with a total fraction of 0.11 with an error of almost the same value.

Our best model of Okyrhoe's spectrum includes 71% amorphous carbon, 26% Triton Tholin, and 3% Titan Tholin, all at grain sizes of 10 μm. The carbon lowered the albedo, the Triton Tholin reddened the spectrum, and small amounts of Titan Tholin were useful to reproduce the general shape of the visible spectrum. While the data from Dotto et al. (2003) and Barkume et al. (2008) suggest the possible presence of very small amounts of H_2O, our data does not. This suggests that either there is no H_2O on the surface of Okyrhoe, or possibly there is a trace amount of H_2O ice that is unevenly distributed across the surface. Further observations are necessary to constrain the possible presence of H_2O on parts of the surface.

In Fig. 6.2 we compare our spectra and models to those of previous work. The bottom panel shows the ratio of these spectra to investigate potential differences. The relative reflectance in the near-infrared with respect to the visible (not shown in the figure) is significantly lower for the Dotto et al. (2003) data compared to ours. While there are many possible explanations for this difference, it is likely a problem with the photometric calibration in previous work, but could represent differences in the location on the surface. We calculate the near-infrared slope (%/1000$\AA$) over the range of 1.45 to 2.35 microns excluding the telluric region near 1.8 microns, and include 0.5 to the error for uncertainties of the standard stars.

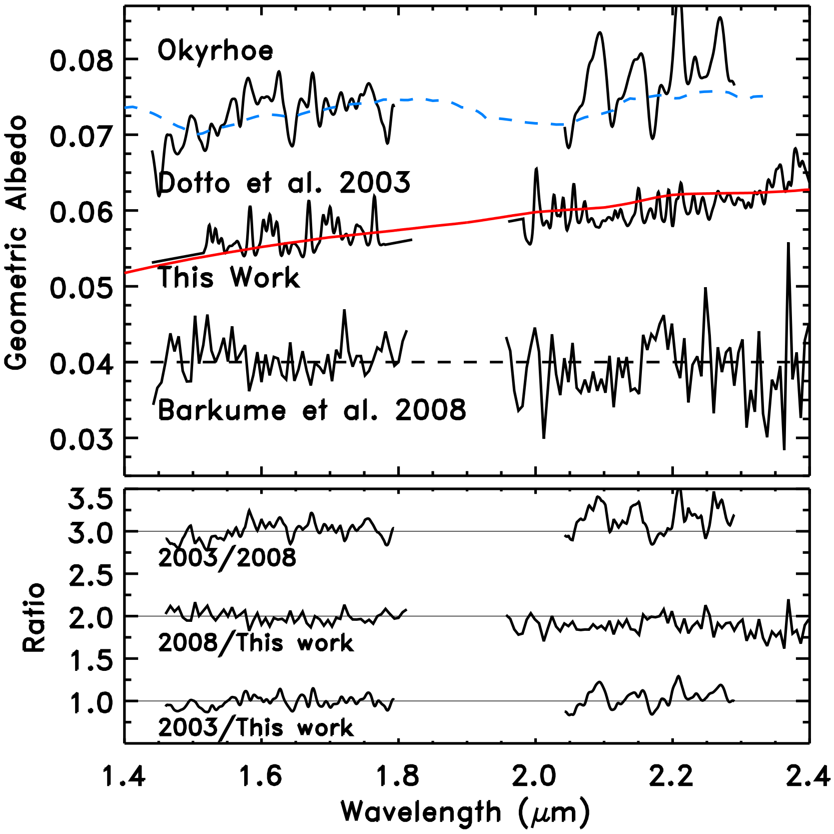

Figure 6.2: The spectra of Okyrhoe from Barkume et al. (2008), this work, and Dotto et al. (2003) (solid black) from bottom to top. We plot our model (solid red) and the model of Dotto et al. (dashed blue). Both data and the model from Dotto et al. have been normalized to 0.025 at 0.55 microns and were shifted vertically by 0.035 for clarity. The data from Barkume et al. has been arbitrarily normalized to 0.04 around 1.5 μm, a horizontal line (dashed black) at 0.04 is drawn to highlight the flatness of the Barkume et al. spectrum.

The slope values we find are 4.1±1.0, -0.6±1.0, and 2.9±0.6 for the data from Dotto et al., Barkume et al., and this work, respectively. However, the real error is likely larger than the formal error as was found for the model fits from Barkume et al. (2008). Also, there is an additional error due to the non-simultaneous (H and K spectra were taken on different nights) observations for the Dotto et al. data. When considering all the sources of error in the measurements, we cannot detect a significant difference in the slopes of these spectra.

6.3.2 (73480) 2002 PN_{34}

73480 is a Scattered Disk object with a diameter of ~120 kilometers and a low albedo of about 4.25% (Stansberry et al., 2008). We present here the first near-infrared spectrum of (73480) 2002 PN_{34}. The visible slope, published by Fornasier et al. (2009), has a moderately red slope of 15.8±0.7 (%/10^3 Å). Because these observations were done in service mode, the schedule did not allow us to obtain a spectrum in the J-band.

Our best fit model of the spectrum (shown in Fig. 6.3) includes 55% (10 μm) amorphous carbon to match the low albedo, 34% (10 μm) Triton Tholin to create the overall red slope of the spectrum, and 11% (40 μm) amorphous H_2O ice to reproduce the 2-μm feature seen as the drop in albedo before and after the telluric interference between 1.8 and 2 microns. While the body is dark, it does appear to have a measurable amount of H_2O on the surface. The model generally provides a good fit, but it overestimates

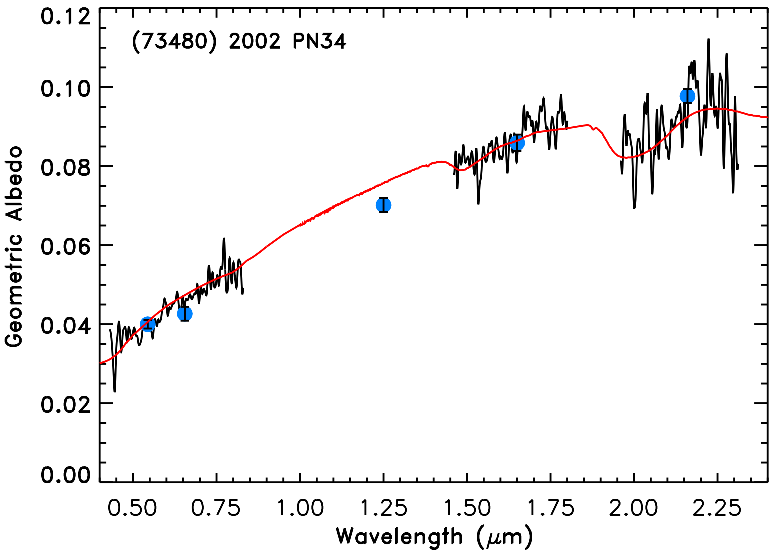

Figure 6.3: The spectrum of 73480 (black) with photometric points and errors (blue and black) and the model (red) overlaid. The model includes amorphous carbon, Triton Tholin, and amorphous H_2O.

the albedo in the J band compared to the single data point from photometric measurements.

6.3.3 (90482) Orcus

Orcus is a Plutino, in the 3:2 resonance with Neptune, discovered in 2004. It is one of the largest bodies, with a diameter of ~950 kilometers and is one of the brighter minor bodies in the distant Solar System with an albedo of ~19.7% Stansberry et al. (2008). Fornasier et al. (2004) reported the first visible and near-infrared spectrum of Orcus taken just days after its discovery. Because no albedo measurements were available at the time, they created a low albedo (4%) and a high albedo (10%) model. Their low albedo model was created from a geographic mixture of 38% kerogen, 60% amorphous carbon and 2% H_2O ice. The high albedo model was created from 4% Titan Tholin, 85% amorphous carbon, and 11% H_2O ice. The visible slope they calculated is same as for the spectrum modeled in this work within the errors (1.8% ± 0.2% and 1.6% ± 0.6%, respectively, from Fornasier et al. (2004, 2009)).

Orcus' spectrum was revisited by de Bergh et al. (2005). They note the uniqueness of the spectrum due to its nearly neutral-sloped visible spectrum and its relatively strong H_2O absorptions reminiscent of Charon. Trujillo et al. (2005) modeled a spectrum of Orcus with H_2O and then calculated the residual by subtracting the model and compared it with CH_4 and found a detection within a 3σ limit. They found the maximum best-fit surface fraction of H_2O ice is 50% ± 16%.

A feature near 2.2 microns with a depth of 10±3% was first detected by Barucci et al. (2008b) in very good signal-to-noise data which could be attributed to either hydrated NH_3 or methane. They detected the 1.65-micron feature indicating the presence of H_2O ice in the crystalline form, and modeled the spectrum with 32% H_2O ice (including both crystalline and amorphous), 5% ammonia diluted in H_2O ice, and 63% of a neutrally absorbing blue component to reproduce the overall blue trend in the near-infrared wavelengths. They found that NH_3 is likely the main component creating the absorption at 2.2 microns, although small amounts of methane cannot be excluded. This feature was also tentatively reported at 2.23 μm in an abstract by Cook et al. (2007a). They suggested it could be due to a mixture of pure ammonia ice and ammonia hydrate.

Orcus has a spectrum quite similar to those of Charon and Quaoar in the near-infrared because of the strong signatures of H_2O crystalline ice and the 2.21 μm feature. On Quaoar, the feature at 2.21 microns is expected to be due to methane (Schaller and Brown, 2007a; Dalle Ore et al., 2009) because of other weak features detected in the spectrum. On Charon, however, the lack of other detectable features

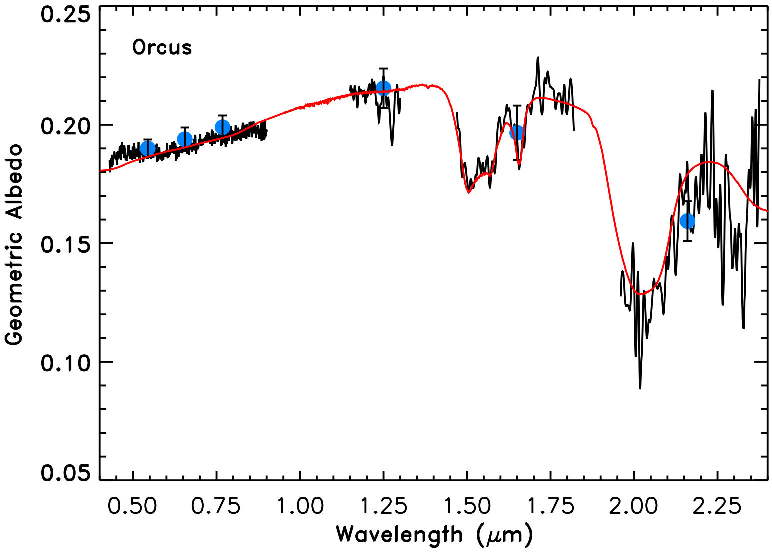

Figure 6.4: The spectrum of Orcus (black) with photometric points and errors (blue and black) and the model (red) overlaid. The model includes an artificially created absorbing blue component (see text), Tholin (Titan and Triton), and pure H_2O ice (amorphous and crystalline).

rules out methane as the primary source of the 2.21-micron band (Cook et al., 2007b).

Both the presence of H_2O ice in the crystalline form as well as NH_3 merit explanation. Crystalline H_2O ice was previously expected to be amorphized by space weathering processes over the age of the Solar System (Kouchi and Kuroda, 1990), but recent experiments (Mastrapa et al., 2006; Zheng et al., 2008), have shown that the 1.65-μm band strength decreases when irradiated, but is still present, and that thermal recrystallization is the dominant process at temperatures greater than about 40K. The amorphization and crystallization processes are discussed in detail in Gil-Hutton et al. (2009). NH_3 is expected to be quickly destroyed by irradiation as well (Strazzulla and Palumbo, 1998; Cooper et al., 2003). Proposed mechanisms to maintain H_2O in crystalline form and resupply NH_3 to the surface include cryovolcanism, impact gardening, and solid-state greenhouse or convection, with cryovolcanism being the favored mechanism (Cook et al., 2007b). Another possibility is that irradiation is not as efficient as we expect for NH_3, as was found for crystalline H_2O.

In Fig. 6.5 we plot the near-infrared spectra of Orcus from this work and from de Bergh et al. (2005), and Barucci et al. (2008b). The spectrum by de Bergh et al. (2005) has a higher (median percent difference between the ratioed spectra of 18 ± 10%) overall reflectance in the K band than more recent data. Their H and K spectra, however, were not taken simultaneously with the same instrument creating an additional calibration error. Furthermore, the spectra were taken during different nights and so they could have observed different parts of the surface and had different observing conditions. Because the difference in reflectance between our data and the de Bergh et al. data is consistent over the entire K range, the most likely explanation is the photometric calibration, which emphasizes the importance of observing simultaneously over an entire wavelength range. Our spectrum is of lower quality than that presented in Barucci et al. (2008b), and we do not detect a clear feature at ∼2.2 μm. To be consistent with the models performed by Barucci et al. (2008b), we also present a model of the data with ammonia hydrate, shown in Fig. 6.6. In our data, any detection is masked by a stronger absorption at wavelengths slightly smaller than 2.2 microns that does not match the location of ammonia, methane or any other known material expected to be on the surface. We suspect this feature is due to noise.

We create three models of Orcus' spectrum shown in Fig. 6.6. Table 6.4 lists the concentration of each component used for each model, as well as the χ^2 value indicating how well the model fits the data. Model 1 uses amorphous carbon as the absorbing component. It is clear that there is some material on the surface not included in the model that absorbs heavily past 1.7 microns as seen by the large mismatch

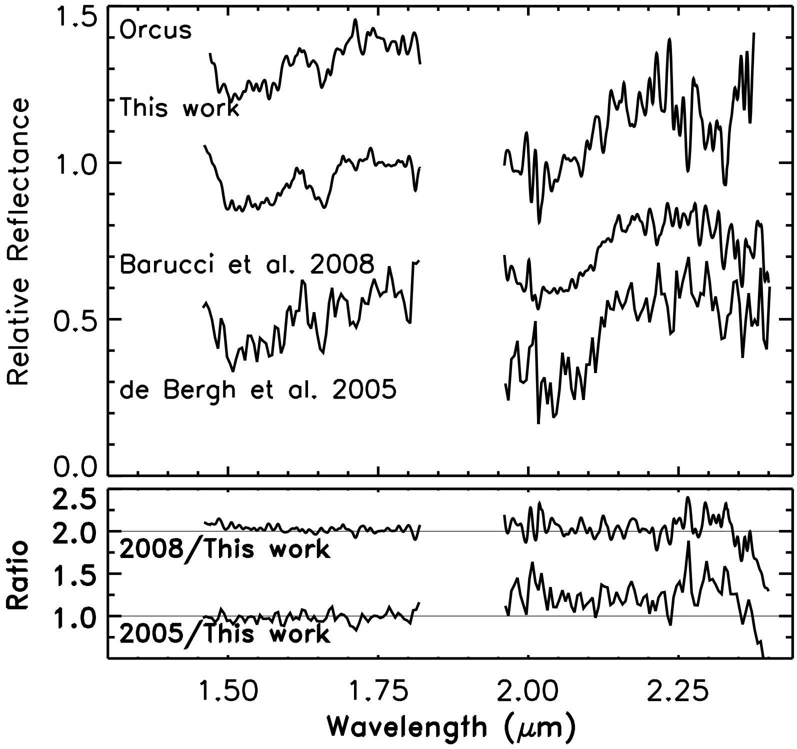

Figure 6.5: **Top:** The near-infrared spectra of Orcus from this and previous work. The data are from de Bergh et al. (2005), Barucci et al. (2008b), and this work from bottom to top. The spectra are normalized to 1 at 1.75 μm, a fairly flat region of the spectrum, and are shifted vertically by 0.4 for clarity. **Bottom:** The ratio of these previously published spectra to this work.

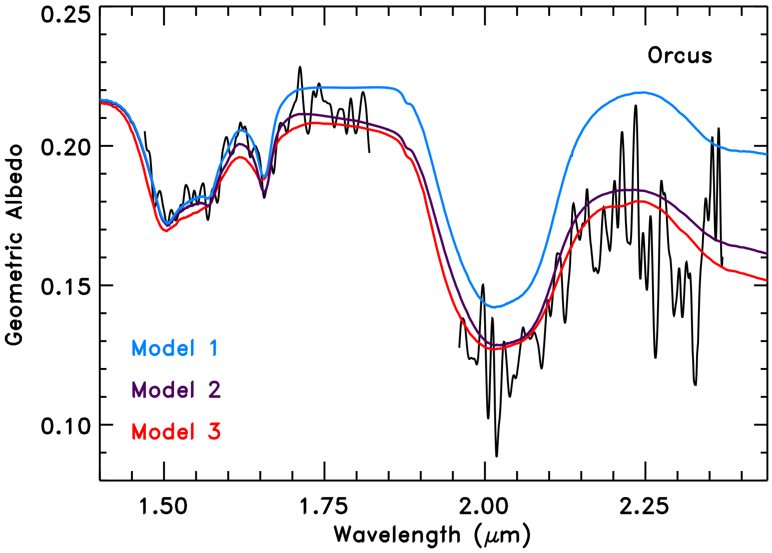

Figure 6.6: Three models compared to Orcus' spectrum at reduced resolution. Model 1 (blue) has no blue component and cannot adequately match the spectrum past 2 microns. Model 2 (red) contains only pure crystalline and amorphous forms of H_2O ice, while Model 3 (blue) includes 100 μm grains of 7% hydrated ammonia in H_2O. See Table 6.4 for the quantities of each component in each model and the χ^2 value indicating goodness-of-fit.

in the model's albedo. Model 2 provides a better fit; this model is shown over the entire wavelength range in Fig. 6.4. It includes an artificially created absorbing blue component to account for the lower albedo at longer wavelengths. A similar blue component was used in models by Barucci et al. (2008b). These first two models (Model 1 and 2) include about 50% crystalline H_2O and 23% amorphous H_2O. Small amounts of Tholins were used to reproduce the red slope in the visible wavelengths. Model 3 includes 7% ammonia hydrate with a grain size of 100 μm. The quality of our data, however, is not great enough to detect the 2.21-micron feature seen by Barucci et al. (2008b). Model 1 is clearly a much poorer fit to the data which is reflected by the larger χ^2 value. Model 2 and 3 have very similar fits and similar χ^2 values. The addition of large-grain NH_3 to the model slightly widens the 2-micron feature, creates a small absorption near 2.2 microns, and reduces the overall albedo. We reduced the grain size of the H_2O grains for this model to compensate for the darkening caused by the large-grain NH_3.

It is evident that we include significantly more H_2O in our models than in previous work. In Fornasier et al. (2004) the albedo was unknown at the time and so they were modeling a much darker surface. The blue component in our models is more heavily absorbing at longer wavelengths than that used by Barucci et al. (2008b), which explains part of the difference between our models and theirs. The choice of modeling parameters could also affect the concentration of each component. If we had chosen a lower cosine asymmetry parameter, we could have recreated Orcus' spectrum just as adequately. This would involve including more absorbing material (carbon or the blue component) and less H_2O ice to lower the albedo and weaken the bands.

6.3.4 Limits on the presence of CH_4 and CO_2 on Orcus

Several atmospheric escape models have been used to explain the loss of volatiles on small bodies in the outer Solar System. Schaller and Brown (2007b) calculate a lower limit to the flux loss by calculating the Jeans escape and ignoring the effects of hydrodynamic escape, which is not as easily constrained. They show that for the size and temperature of Orcus, all volatiles should be lost. Another model was performed by Levi and Podolak (2009) who show that TNO atmospheres can behave in a way analogous to coronal expansion using Parker's theory (Parker, 1963). They use this theory to explain the absence of CH_4 on

Table 6.5: Characteristics of Orcus models including volatiles

Model	**Reduced** $\chi^{2\,a}$	**Depth (%)**[b]
Model 2	72	-
2% CO_2	73	5
5% CO_2	74	11
10% CO_2	76	21
2% CH_4	72	2
5% CH_4	73	5
10% CH_4	80	10

---

[a] The χ^2 is weighted to give greater importance to locations where absorption bands exist (H_2O bands) and lower importance to regions affected by telluric absorption. The value compares the model to the near-infrared data from Barucci et al. (2008b).

[b] The percentage depth of the strongest CO_2 band at 2.012 μm and the CH_4 band at $\sim$2.2 μm relative to the continuum for each model.

smaller TNOs and constrain the maximum temperature for retaining methane to $80 \pm 3 < T < 90^{+32}_{-12}$. A similar model could also be used to predict the presence or absence of other molecules such as N_2, CO, and CO_2 on TNOs based on their density, radius, and surface temperature. These three volatiles could possibly be present on the surface of Orcus (Levi and Podolak, 2009, Levi, personal communication). N_2 and CH_4 have been detected on the largest TNOs (e.g., Owen et al., 1993; Licandro et al., 2006a,b; Tegler et al., 2008a; Merlin et al., 2009). Because of the intermediate size of Orcus determining the presence or lack of volatiles on its surface provides important constraints for volatile retention. The absorption band for N_2 is in a region of H_2O absorption and is easily detectable only for large grain sizes. The main CO band is at a long wavelength where the quality of the data is low. We therefore seek to constrain the abundance of CH_4 and CO_2.

Detecting CO_2 on TNOs is particularly difficult because the three strong absorption bands located at 1.966, 2.012, and 2.071 μm are very narrow. At high resolution, the signal-to-noise ratio of the data is very low, but at low resolution the thin bands would be lost thus preventing detection. Starting with the composition from Model 2, we create models including 2, 5, and 10% CO_2 (reducing the amount of amorphous H_2O accordingly) to compare band strengths with the Barucci et al. (2008b) data that has the highest signal-to-noise ratio and, like the data from this work, was taken with SINFONI simultaneously in the H and K bands with a resolution of 1500. We focus only on the H and K band region where the strongest absorption bands are located. In Fig. 6.7, we can see that by adding CO_2, apart from the three narrow bands, the continuum is not significantly affected. The χ^2 value of the model fits to the Barucci et al. data as well as the band depths of the strongest CO_2 band are given in Table 6.5. The three CO_2 band depths with respect to the continuum when 10% CO_2 is included are 18, 21, and 9%, respectively for the three bands. The noise in the full resolution data in this work at these wavelengths is ±17%, so the data from this work could accommodate nearly 10% CO_2 within the noise. The spectrum from Barucci et al. (2008b) has a higher signal-to-noise ratio, and the noise in the data is ±10% of the median value in this region. In the model with 5% CO_2, the strongest band has a depth of 11%, so their data limit the quantity of CO_2 on the surface to a maximum of about 5%.

CH_4 should be easier to detect because it has wider and stronger bands than CO_2 located at 1.670, 1.724, 1.797, 2.208, 2.324, and 2.379 μm (Quirico and Schmitt, 1997b). While the last two bands are the strongest, it is the 2.208 μm feature that is easiest to identify because it lies in a region relatively free of H_2O absorption. However, this feature is in nearly the same location as NH_3 absorption. While the $\sim$2.21-μm feature seen on Charon is thought to be due to NH_3 due to the lack of other features (Cook et al., 2007b), on Quaoar the presence of other weak features suggests the presence of CH_4 instead (Schaller and Brown, 2007a; Dalle Ore et al., 2009). For models of 5 and 10% methane, we calculate a 2.21-μm band depth of 5 and 10%, respectively. The noise in the data in this region with respect to the median value (calculated from 2.17-2.21 μm) is ±20% and 9% in the full-resolution data from this work and Barucci et al., respectively. Since this feature is much wider than the narrow CO_2 features, however, the feature may be more easily detected when reducing the resolution to increase the signal-to-noise ratio. The noise in the data from Barucci et al. is 3% when the resolution is reduced to 250. The models with varying amounts of pure CH_4 are compared to Barucci et al. (2008b) in Fig. 6.7. The χ^2 value of the fit including 2% methane is nearly identical to that for Model 2 (see Table 6.5), while the values for the

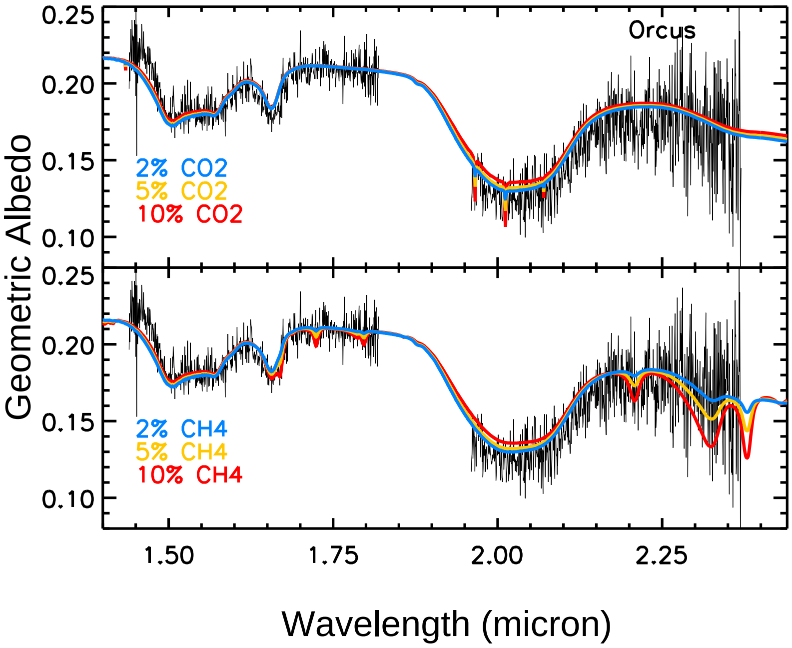

Figure 6.7: Comparison of models containing CH_4 and CO_2 to the full resolution data from Barucci et al. (2008b). Top: Models with 2, 5, and 10% CO_2 (solid blue, purple, red). The three narrow bands are located near 2 μm. Bottom: Models with 2, 5, and 10% CH_4 (solid blue, purple, red).

5 and 10% models become progressively higher. For amounts of around 5% or less of CH_4 the three methane features between 1.6 - 1.8 μm are very weak even though there is a distinct 2.21-μm feature. This raises the possibility that methane could account for the feature seen by Barucci et al. (2008b) even if no other features are seen in the data.

6.4 Conclusion

We model the spectra of three minor bodies in the outer Solar System, (52872) Okyrhoe, (90482) Orcus, and (73480) 2002 PN_{34}, and compare the spectra with those reported in previous work for Okyrhoe and Orcus. Large amounts of amorphous carbon are needed in the model to lower the albedo, although other dark, neutrally absorbing materials could be adequate substitutes. Titan and Triton tholins were important to recreate the red slope of the visible spectrum. Similarly to the carbon, tholins could be replaced with another material that displays red behavior at visible wavelengths.

We find varying amounts of H_2O ice among these bodies, Okyrhoe has no traces in our spectrum, 73480 has small amounts, and Orcus has large quantities. Previously published spectra of Okyrhoe by Dotto et al. (2003) and Barkume et al. (2008) suggest the possibility of trace amounts of H_2O ice which could indicate that this minor component, if present, is unevenly distributed across the surface. Further observations are necessary to constrain the possible presence of H_2O on parts of the surface. The spectrum of Orcus presented here is of lower quality than that presented by Barucci et al. (2008b). While we do clearly see that H_2O ice is in crystalline form from the 1.65-μm feature, we cannot detect the 2.21-μm feature suggested to be due to ammonia hydrate because of the low quality of the data. We also do not see any indication of CH_4 or CO_2 in the spectrum, and limit their presence to no more than about 5%.

Chapter 7

A search for Ethane on Pluto and Triton

We present here a search for solid ethane, C_2H_6, on the surfaces of Pluto and Triton. We model each surface using a radiative transfer model with three basic models: without ethane, with pure ethane, and with ethane diluted in nitrogen. We discuss the presence and absence of features in the spectra of Pluto and Triton that constrain the presence of ethane on their surfaces. Apart from Sections 7.1 and 7.6, this chapter is directly from DeMeo et al. (2010c).

Contents

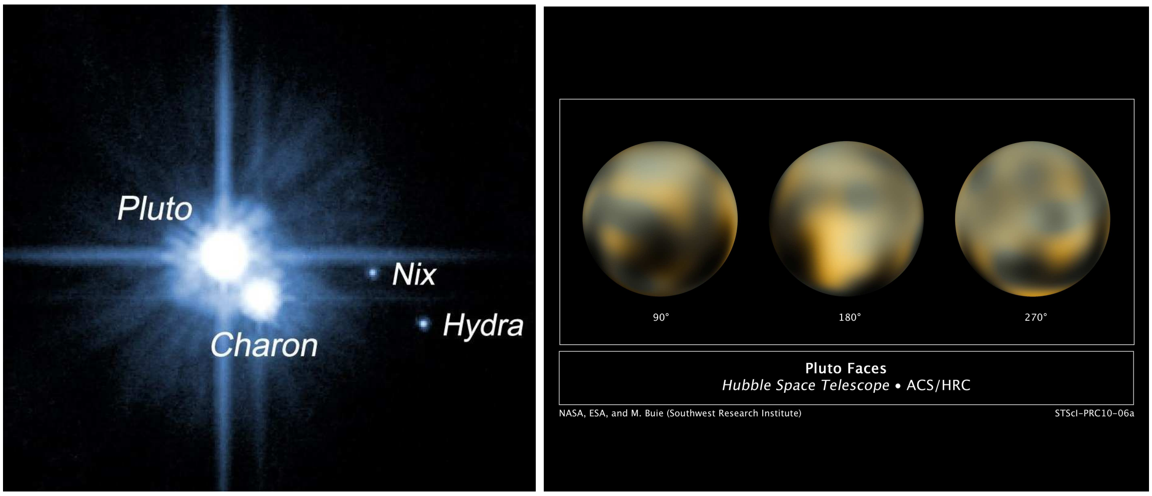

Figure 7.1: **Left:** The first image of the Pluto system that revealed the two new satellites Nyx and Hydra taken with the Hubble Telescope in 2005 by Weaver et al. (2006). **Right:** Albedo map of Pluto by Buie et al. (2010) showing the significant albedo variations across the surface.

7.1 Background on Pluto and Triton

Pluto: Pluto was discovered in 1930 by Percival Lowell. Excitement over this new discovery led to it being named a planet. It's orbit, however, is significantly different than the nearly circular orbits of the eight largest bodies in the solar system, and after the discovery of other objects in the Kuiper Belt Jewitt and Luu (1993) and a body larger than Pluto (Eris, Brown et al., 2005b), it was demoted to "dwarf planet" status. Pluto and Triton are compared to other dwarf planets in Table 7.1. Pluto has a radius of approximately 1200 km, 0.18 that of Earth. Pluto's largest moon, Charon, has a radius of about 600 km, half that of Pluto. Two other small moon's were discovered in 2005 by Weaver et al. (2006) from Hubble Telescope images. These satellites were named Nyx and Hydra and can be seen in Fig. 7.1.

Pluto is the only dwarf planet with a known atmosphere. Its pressure and thermal structure can be measured through stellar occultations, and composition can be studied through high-resolution spectroscopic measurements. The atmosphere is comprised predominantly of N_2 (Owen et al., 1993), but methane (Young et al., 1997) and CO Young et al. (2001b) have also been detected. Pluto's atmosphere has two distinct regions. Above an altitude of about 1210 kilometers the temperature is about 100 K and has remained stable over the past decades (Yelle and Lunine, 1989; Elliot et al., 2007). The region of the atmosphere below 1210 kilometers has changed measurably since its discovery; its pressure increased by a factor of two between 1988 to 2002 (Sicardy et al., 2003; Elliot et al., 2003), and then steadied through 2006 (Elliot et al., 2007). This lower region was characterized by a "kink" (large, sharp drop in flux) in the 1988 occultation lightcurves, which suggested haze and/or a steep thermal gradient (Elliot et al., 1989; Eshleman, 1989). Further study of the abundance of methane in Pluto's atmosphere revealed that the mixing ratio of CH_4/N_2 is orders of magnitude greater than their vapor pressures which is sufficient to explain the thermal gradient, and that haze can justifiably be neglected in models (Lellouch et al., 2009b). The interest in investigating Pluto is especially strong now to prepare for the New Horizons mission that will fly-by in 2015 (see Section 7.6). New albedo maps were recently published by Buie et al. (2010). They find the brighter regions to have minimal color variations, while the darker regions have larger variation suggesting compositional diversity. They also detect brightening and darkening trends at blue wavelengths over the period from 2002 to 2003. New spectroscopic measurements of Pluto have recently extended to the infrared domain out to 5 microns. With data out to 4 microns Olkin et al. (2007) place an upper limit on the abundance of pure nitrogen and find they require tholins for the best-fit model. Protopapa et al. (2008) present data extending to 5 microns and are the first to detect a feature at 4.6 μm that they suggest could be related to the presence of CO and nitriles. More background on the history of spectroscopic measurements of Pluto is provided in Section 7.2.

Table 7.1: Dwarf Planet and Triton Characteristics

Object	Semi-Major Axis (AU)	Diameter[a] (km)	Density[b] (g/cm^3)	Geometric[c] Albedo	Surface[d] Temp (K)	Surface Composition
(1) Ceres	2.77	975	2.08	0.09	165	rocky[e]
(N1) Triton	30.05[f]	2705	2.06	0.76	36 (38±1)	N_2,H_2O,CO_2,CH_4,CO,HCN
(134340) Pluto	39.65	2332	2.03	0.49-0.66	35 (40±2)	N_2,CH_4,CO,C_2H_6?
(136108) Haumea	43.04	1150	2.9	0.84^{+10}_{-20}	27	H_2O
(136472) Makemake	45.35	1500	2	0.80^{+10}_{-20}	28	N_2,CH_4,C_2H_6
(136199) Eris	68.01	2400	2.3	0.70^{+15}_{-20}	25	N_2,CH_4

---

[a] Ceres: Parker et al. (2006); Triton: Davies et al. (1991); Pluto: Young et al. (2007); Haumea and Makemake: Stansberry et al. (2008); Eris: Brown et al. (2006)

[b] Ceres: Li et al. (2006); Triton: Goguen et al. (1989); Pluto: Buie et al. (1997); Haumea, Makemake and Eris: Stansberry et al. (2008)

[c] Ceres: Thomas et al. (2005); Triton: (NASA); Pluto: Buie et al. (2006); Haumea: Brown et al. (2005a); Makemake: assumed value; Eris: Brown et al. (2006)

[d] Calculated as: $T = [\frac{L_\odot(1-p_V)}{16\pi\sigma D^2}]^{\frac{1}{4}}$ where $L_\odot$ is the luminosity of the Sun ($3.939*10^{26}$W), p_V is the albedo, σ is the Stefan-Boltzman constant ($5.67*10^{-8}W/m^2K^4$), and D is the distance from the Sun. The temperature on these bodies could be significantly warmer if they have an atmosphere. The values in parentheses for Pluto and Triton are from measurements of N_2 ice by Tryka et al. (1994).

[e] Ceres is considered carbonaceous chondrite-like and has contains hydrated minerals, carbonates, and iron-rich clay

[f] Neptune's semi-major axis is listed in this table. Triton's semi-major axis in its orbit around Neptune is ~355,000 km.

Triton: Triton, Neptune's largest moon, was discovered in 1846 by William Lassell. It is the only large satellite in retrograde orbit and is suspected to be a captured Transneptunian Object (TNO) (Agnor and Hamilton, 2006). Triton's radius is about 1300 km, larger than Puto's, and its semi-major axis is over 300,000 km from Neptune. Triton was visited by the Voyager 2 spacecraft in 1989. About 40% of the surface was imaged, which was found to be fairly flat and a young surface due to the scarcity of craters (Strom et al., 1990). Triton's surface was found to be geologically active (McEwen, 1990); evidence of cryovolcanism is apparent on the surface and geysers and plumes have been observed (Soderblom et al., 1990; Hansen et al., 1990). The crust is thought to be primarily water ice with a layer of nitrogen frost (CO, CH_4 and CO_2 have also been detected) and organic material. Triton's surface has varying structure including plains, regions of ridges and valleys, and the "canteloupe terrain" full of smooth depressions and thought to be the oldest part of the surface.

The tenuous atmosphere is dominated by N_2 (Broadfoot et al., 1989), and CO was very recently detected (Lellouch et al., 2009a). The atmospheric pressure was measured to be ~14 μbar at the time of the Voyager encounter in 1989 Tyler et al. (1989); Gurrola (1995), and was found to increase over the next decade (Elliot et al., 1998, 2000). Present on Triton's surface, detected by spectroscopic measurements, are N_2, CH_4, H_2O, CO_2, and CO.

7.2 Introduction

Very few minor bodies discovered so far are large enough to retain ices more volatile than H_2O. Of these additional ices, methane is the most spectrally dominant (although not the most volatile) and is therefore readily detectable. Among these larger objects, Pluto (Cruikshank et al., 1976) and Triton (Cruikshank and Silvaggio, 1979), Neptune's largest moon, which has long been suspected to be a captured Transneptunian Object (TNO) (e.g., McCord, 1966; McKinnon, 1984; Agnor and Hamilton, 2006), are the brightest and allow us to perform the most detailed surface studies of all volatile-rich minor bodies.

Nitrogen and CO ice have also been detected on both Pluto and Triton, in addition to CO_2 and H_2O ice on Triton (Owen et al., 1993; Cruikshank et al., 1993, 2000). The heterogeneity of Pluto's surface established by its rotational lightcurve has been confirmed through albedo maps by Young et al. (2001a) and Stern et al. (1997). The strong CH_4 absorption bands correlate with the visible lightcurve, however, N_2, CO and weak CH_4 bands do not, suggesting that independent CH_4 reservoirs account for the different behavior of the strong versus weak CH_4 bands (Grundy and Buie, 2001). Variations of albedo, texture,

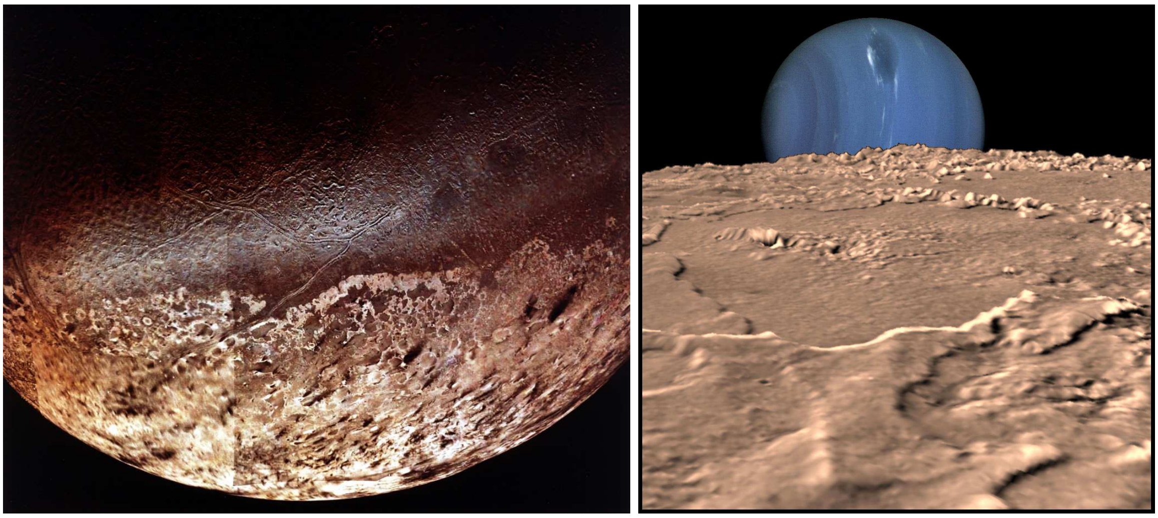

Figure 7.2: **Left:** Image of Triton's surface taken in 1989 during the Voyager 2 mission originally published by McEwen (1990) (Source: NASA). **Right:** View of Neptune from Triton created from a composite of Voyager images (Source: NASA).

and structure across Triton's surface revealed in Voyager images (McEwen, 1990) may be related to an uneven distribution of N_2, the dominant surface component. A global spectral study of Triton's surface by Grundy and Young (2004) and Grundy et al. (2010) shows that absorption due to N_2 ice varies in strength with Triton's rotation and is deepest on the Neptune-facing hemisphere. CO and N_2 display the same rotational variability indicating that they co-occur, while the longitudinal variation of CH_4 bands does not match this behavior (Grundy et al., 2010).

In their paper on a detailed modeling of a near-IR spectrum of Triton, Quirico et al. (1999) mention three unidentified features (at 1.749, 1.683 and 1.543 μm). Based on laboratory measurements of ethane (C_2H_6), they assert that, although one of them (the band at 1.683 μm) could be due to ethane isolated in solid N_2, the lack of features at other wavelengths ruled out this assignment. Quirico et al. (1999) also tentatively identify a feature near 2.40 μm as ^{13}CO.

Nakamura et al. (2000) suggested that ethane could be present on Pluto to explain weak absorptions at 2.28, 2.32 and 2.40 μm that were not well reproduced by surface models including only N_2, CH_4, and CO. They found that by adding a small amount of solid ethane in the pure state in the models they could account for the features at 2.28 and 2.32 μm, but they also noticed that the feature at 2.40 μm in the model was then deeper than observed.

Later, Sasaki et al. (2005) analyzed spectra of Pluto at longer wavelengths (2.9 - 3.9 μm) and showed that the addition of non-methane hydrocarbons could improve the model fits to the data, but there was no clear identification. The best agreement with the data was obtained with a ternary mixture of C_2H_2:C_2H_6 and CH_4 with mass ratios 1:1:10, but the narrow absorption feature of C_2H_6 at 3.65 μm is not present in the data. Olkin et al. (2007) reported observations of Pluto from 1.0 - 4.2 μm and did not find any evidence of non-methane hydrocarbons although their spectrum differed from that of Sasaki et al. (2005). Differences in the spectra by Olkin et al. and Sasaki et al. may be explained by the fact that the central meridian longitudes represented by their observations differ by 145 degrees. Olkin et al. also constrained the amount of pure N_2 to no more than 6% of the surface due to the low albedo over the region from 3.1 to 3.6 μm.

More recently, in a meeting presentation, Cruikshank et al. (2006) revisited the search for ethane on Pluto and Triton using new spectra of Pluto acquired with the Gemini South telescope, and some new laboratory data on the ^{13}CO ice band, but they came to no firm conclusion concerning the presence of ethane. A new spectrum of Pluto (resolution 300) was since obtained by Verbiscer et al. (2007), using a visiting spectrometer at the Magellan telescope in Chile, in which they see possible absorption features at 2.405 and 2.461 μm that could be due to ethane, but no absorption at 2.314 μm.

It is important to note that some of the unidentified features quoted above appear in some data but

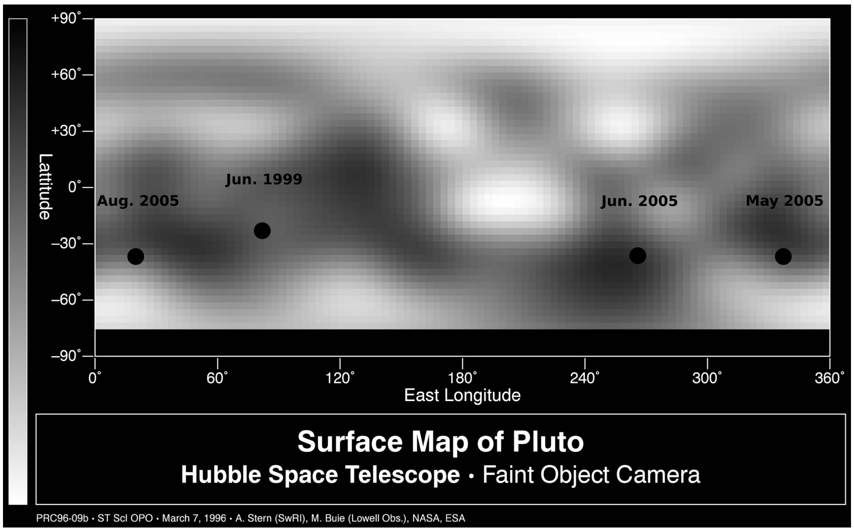

Figure 7.3: The dark circles mark the central longitude and latitude on Pluto's surface for each observation. The figure is shown in a similar format to that in Olkin et al. (2007), with the albedo map from Stern et al. (1997). The rotational north pole is +90 degrees latitude, and longitudes are plotted as 360 minus the IAU definition values reported elsewhere in this article. The longitudes plotted here are 21, 80, 267, and 340 degrees, from left to right.

not in others, even for spectra of comparable spectral resolution, which suggests that this could be due to heterogeneities over the surface of these bodies. Complicating the issue, many of these weak features fall in regions of moderate to poor atmospheric transmission, and thus ratioed spectra are susceptible to spectral artifacts due to incomplete removal of telluric absorption lines.

Other TNOs on which methane has been detected include (136199) Eris (Brown et al., 2005b), (136472) Makemake (Licandro et al., 2006b), (90377) Sedna (Barucci et al., 2005a), and (50000) Quaoar (Schaller and Brown, 2007a). For Eris and Makemake, the presence of nitrogen is also suggested, because the wavelengths of several of the methane absorptions are shifted compared to those for pure methane (Licandro et al., 2006a,b; Tegler et al., 2008b; Merlin et al., 2009). Nitrogen is expected to be much less abundant on Makemake than on Pluto and Triton, because of the large CH_4 grain size and smaller wavelength shifts of the CH_4 bands (Brown et al., 2007a; Tegler et al., 2008b). A detection of ethane ice at the surface of Makemake from weak absorption features around 2.3 μm at the bottom of very strong bands due to methane ice has been published by Brown et al. (2007a). Because ethane is an irradiation by-product of methane (Barata et al., 2003), it has been surprising that no clear signs of ethane have been detected on methane-rich Pluto and Triton. Brown et al. (2007a) argue that the apparent absence on Pluto could be due to the fact that abundant nitrogen on Pluto would prevent the formation of ethane by irradiation of methane. Evidence of ethane was also seen on Quaoar by Schaller and Brown (2007a), who first suggested that a weak feature at 2.21 μm was due to methane rather than ammonia hydrate, which was previously suggested by Jewitt and Luu (2004). Dalle Ore et al. (2009) also found that small amounts of ethane improved model fits of Quaoar's spectrum.

In this paper, we present new spectra of Pluto acquired at the European Southern Observatory (ESO) Very Large Telescope (VLT) in the H and K bands with the instrument SINFONI on three different occasions in 2005, one new spectrum of Triton in 2008 with the same instrument, and unpublished United Kingdom InfraRed Telescope (UKIRT) data of Pluto from 1999. We use these data in particular to search for still unidentified absorption features, especially features that would be present only at certain rotational phases, and attempt to identify them. Our focus is a search for ethane. We seek to understand the effects of irradiation in the outer Solar System, hence the formation of ethane or other non-methane hydrocarbons.

Observational conditions and circumstances are given in Table 7.2. Fig. 7.3 shows the location on Pluto's surface observed for each run overlaid on an albedo map from Stern et al. (1997). The spectra are

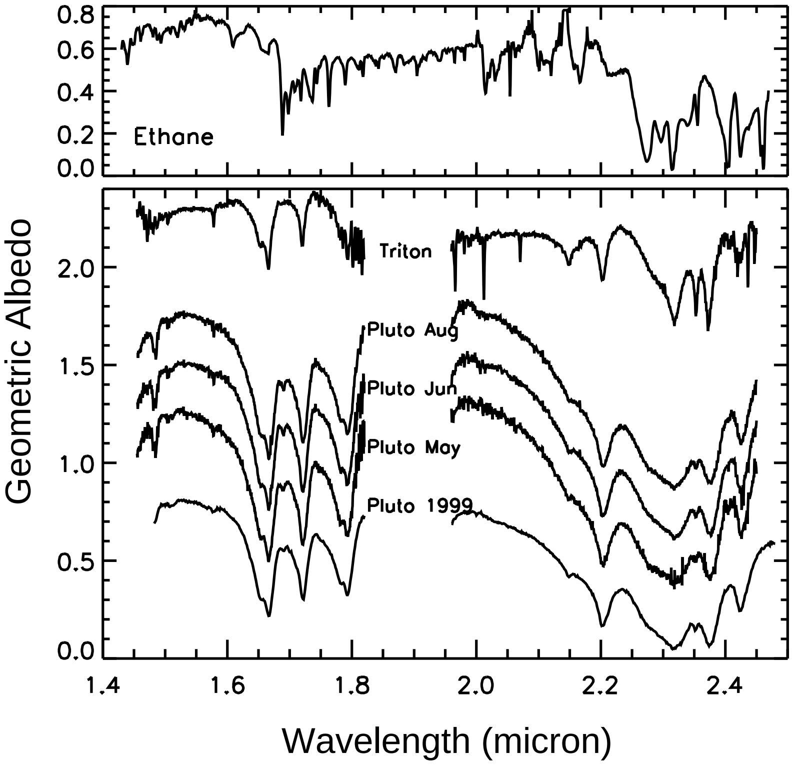

Figure 7.4: Spectra of Triton from Nov. 2008, and Pluto from Aug., Jun., and May, 2005 and Jun. 1999. The June, 1999 spectrum has overall flux differences from the 2005 spectra, likely due to the >10% error in flux in that data. The spectra are shifted vertically by -0.2, +0.25, +0.5, and +0.75 from bottom to top, and are normalized to unity at 1.55 microns. The top portion of the figure displays a synthetic spectrum of ethane to compare band locations with the data.

Table 7.2: Observational Circumstances

Obj	Date	Time (UT)	Sub-E Long	Sub-E Lat	Phase Angle	Airm	Comparison Star
Pluto	1999 Jun 07	08:05 - 09:25 (H)	277	-24	0.5	1.33-1.16	HR 6060
Pluto	1999 Jun 07	10:13 - 12:18 (K)	283	-24	0.5	1.15-1.145	HR 6060
Pluto	2005 May 13	06:23 - 06:27	20	-36	1.0	1.02	HD 154901
Pluto	2005 Jun 09	02:57 - 03:02	93	-35	0.3	1.12-1.13	HD 175773
Pluto	2005 Aug 09	22:55 - 23:00	338	-34	1.5	1.12-1.13	HD 164000
Triton	2008 Nov 22	23:26 - 23:32	93	-48	1.9	1.22-1.15	SA93 101

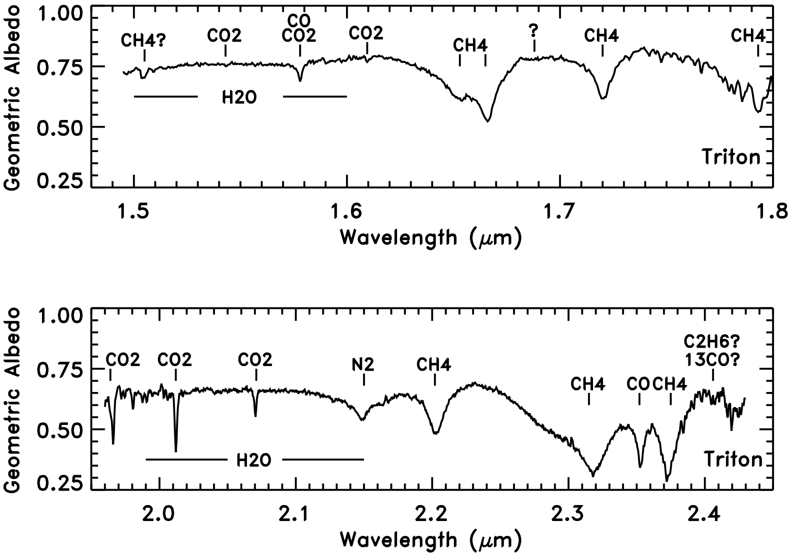

Figure 7.5: Triton: Spectrum of Triton from this work (Nov., 2008). Here we label absorption bands present in the spectrum.

presented in Fig. 7.4, and the features on Triton are labeled in Fig. 7.5. In Section 7.3 we show models of Pluto and Triton with and without the inclusion of ethane, and in Section 7.4 we discuss the implications of these models and the presence and absence of particular features on each body's surface.

7.3 Modeling

We apply a radiative transfer model based on the Hapke theory described in Hapke (1993) to calculate synthetic geometric albedo spectra for comparison with the observational data of Pluto and Triton, with the goal to retrieve information about the surface composition of the analyzed targets. The effects of anisotropic scattering, shadow-hiding opposition geometry, and macroscopic roughness are included in the model. As was done in Olkin et al. (2007) and Protopapa et al. (2008) we approximate Pluto and Triton's surfaces as a 30×30 grid and calculate the incident and emission angle for each surface element in the grid. Because of the similarities between the surfaces of Pluto and Triton, we assumed for both targets the same values for the compaction parameter (h=0.5) and the mean roughness slope (θ=14°). The free parameters in the model are the grain size and the contribution of each surface terrain to the mixture. For the general model for each object, these free parameters are iteratively modified by means of a chi-squared minimization algorithm (Levenberg-Marquardt least-squares minimization) until a best-fit to the observations is achieved. A detailed description of the routine developed for the modeling analysis is given in Protopapa et al. (2008) and Protopapa (2008). In the present work, all models were computed using areal combinations of pure ices and molecular mixtures, meaning the surface components are spatially isolated one from the other.

Table 7.3: Optical Constants used for Modeling

Material	**phase**	**Temp (K)**	**Reference**
CH_4	-	40	Quirico and Schmitt (1997b)
Titan tholin	-	-	Khare et al. (1984, 1993)
H_2O	crystalline	40	Grundy and Schmitt (1998)
N_2	β-N_2	36.5	Quirico and Schmitt (1997b)
N_2:CH_4	β-N_2	36.5	Quirico and Schmitt (1997b)
N_2:CO	β-N_2	36.5	Quirico and Schmitt (1997b)
C_2H_6	amorphous[a]	21	Quirico and Schmitt (1997b)
N_2:C_2H_6	α-N_2, amorphous	21	Quirico and Schmitt (1997b)
CO_2	-	30	Quirico and Schmitt (1997b)

---

[a] Quirico and Schmitt (1997b) do not mention the state of ethane for their measurements, however, it is likely that it is amorphous at 21 K.

Although Hapke's model is generally able to describe the spectral properties of the objects quite well, it is only indicative of grain sizes, abundances, and surface scattering properties for most applications to Solar System bodies and does not give unique solutions. Mixtures with different grain sizes or different mixing ratios of the constituents can give very similar fits to the data. Therefore, the accurate and realistic determination of the surface composition may be difficult. In the case of mixtures, concentration and grain size are linked. Indeed, very similar model results can often be obtained for a large grain size with a low concentration and a small grain size with a high concentration. This is because the grain size directly affects the optical depth of the radiation. A larger grain has a greater internal path where photons may be absorbed. This contributes to the attenuation of the reflectance. Thus, the reflectance and consequently the geometric albedo, decrease with increasing depth (or grain size). For mixtures, the geometric albedo is a linear function of the spatial coverage of each component. We stress, however, that although models of different grain sizes and concentrations may give equally good fits, the presence of a material that exhibits distinct features and the relative strengths of its bands should not be affected by the assumptions made and parameters chosen.

In our case, the concentration and grain size of each component in the mixture are determined once the compaction parameter, mean roughness slope and cosine asymmetry factor are fixed. These parameters affect the continuum level of the spectral modeling. Hence different initial conditions will affect the final values of concentration and grain size, although similar fits to the data can be obtained. This explains why it is important to assume values for the compaction parameter, mean roughness slope and cosine asymmetry factor as close as possible to values determined by other measurements, such as photometric measurements of the different terrains of Triton's surface from resolved Voyager images from (Hillier et al., 1994).

The near-IR spectra of Pluto and Triton have been modeled thoroughly in previous work. Many of these models, such as from Douté et al. (1999), Olkin et al. (2007) and Quirico et al. (1999), use different surface and observational parameters and optical constants for modeling, and thus concentrations are not easily comparable. The goals of the modeling in this work are to show the effects of the presence of ethane on the reflectance spectrum and to constrain ethane's abundance and the environment in which it may be located on Pluto and Triton, not to derive abundances and constraints of other surface constituents and compare them with previous work.

Pluto Modeling

Pluto's hemispherically averaged visible geometric albedo ranges from 0.49 to 0.66 (Buie et al., 1997). As our near-infrared data do not readily provide measurements of the albedo, to use the albedo as a constraint we scale our spectra to that of Olkin et al. (2007). Olkin et al. calibrate their flux levels using spectrophotometry data at 2.9 μm from Spencer et al. (1990). We multiplied our spectra by scaling factors so that the albedo of each was 0.65 at 1.55 μm, which corresponds approximately to the value in the data from Olkin et al. (2007). For modeling Pluto, we used optical constants for pure methane ice at 40 K from Quirico and Schmitt (1997b), Titan Tholin from Khare et al. (1984, 1993), and an artificially

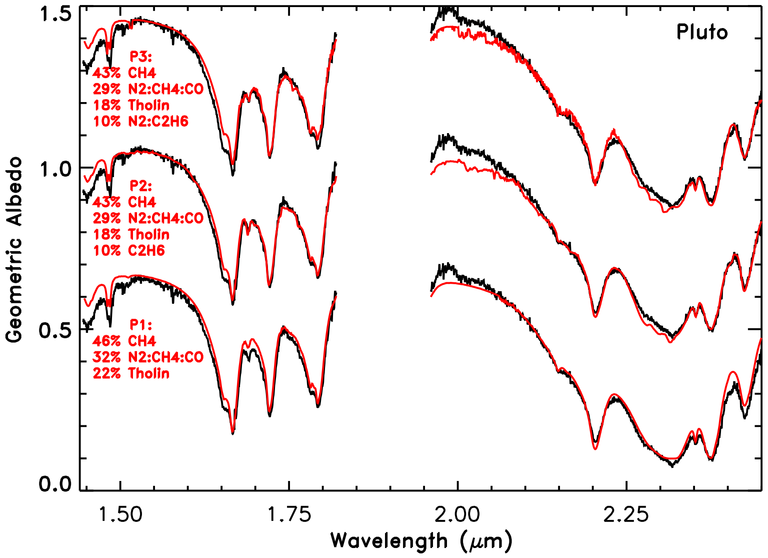

Figure 7.6: Pluto: Models (red) compared to the August, 2005 Pluto spectrum (black). The models are the basic model without ethane (bottom), a model including ethane (middle), and a model including ethane diluted in nitrogen (top). The models are shifted vertically by 0.4 for clarity.

created molecular mixture of 0.36% CH_4 and 0.1% CO in N_2. Following the method described in Douté et al. (1999), this molecular mixture was created from a linear combination of the real and imaginary indices of refraction of each component weighted by the concentration. We used the optical constants of pure N_2, CH_4 diluted in N_2 and CO diluted in N_2 each at 36.5 K from Quirico and Schmitt (1997b). The weak CO features at 1.578 and 2.405 μm cannot be modeled because only the 2.352-μm feature is calculated in the CO optical constants. As in the work of Olkin et al. (2007) and Protopapa et al. (2008), for Pluto we use -0.33 for the cosine asymmetry parameter because it is near the global value found for Triton by Voyager measurements (Hillier et al., 1994). Douté et al. (1999) chose to set this parameter to zero. For solid ethane we used optical constants measured at 21 K for pure ethane and ethane diluted in nitrogen (C_2H_6:N_2 = 1:100) from Quirico and Schmitt (1997b). For details for the optical constants (phase, temperature, and reference), see Table 7.3.

We note that nitrogen is known to be in the warmer β phase for both bodies because of the shape of the 2.15-μm feature. However, we use ethane diluted in nitrogen in the α phase because no laboratory measurements in the β phase have been performed. The band shifts for ethane diluted in β-N_2 might not be uniformly in the same direction as for α-N_2. For example, according to Quirico et al. (1999), if ethane were diluted in β-N_2, the 1.6820 feature would likely shift to about 1.6825 μm, while the 1.755-μm band might shift in the opposite direction by 0.0001 to 0.001 μm, based on the behavior of CH_4 diluted in α- versus β-N_2 seen in Quirico and Schmitt (1997b).

For Pluto, we start with a basic model (P1) of 46% pure CH_4, 32% N_2:CH_4:CO, and 22% Titan tholin, with grain sizes of 500, 95,000, and 15 μm, respectively. In Douté et al.'s models, tholins were not necessary, but when modeling with a cosine asymmetry parameter of -0.33 and a compaction parameter of 0.5 such as in Olkin et al. (2007) and Protopapa et al. (2008), the tholin is important to lower the albedo to match that of Pluto. Olkin et al. also show that tholin or a similar-type material is needed for the model to simultaneously reproduce the shorter wavelength methane bands and the 3-μm band. Our second model (P2) has similar concentrations, but we include 10% pure ethane, and for the third (P3) we include 10% diluted ethane. Table 7.4 lists the quantities of each component used for each model. The models are shown in Fig. 7.6, plotted with the August 2005 spectral data. Figs. 7.7 and 7.8 show an enlarged view of the models in the 1.6 - 1.8 μm and 2.2 - 2.45 μm regions. In these figures, as well as similar ones for Triton, we include a synthetic spectrum of pure ethane created using the optical constants from Quirico and Schmitt (1997b) with a grain size of 100 μm, to aid the comparison of the data with

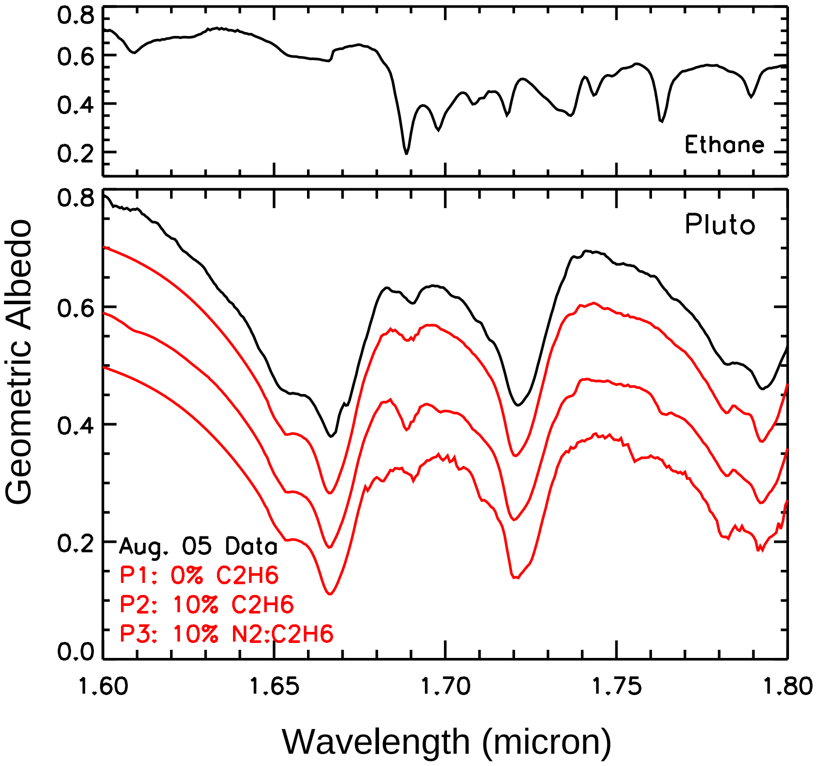

Figure 7.7: Pluto: Models (red) compared to the smoothed August, 2005 Pluto spectrum (black) as in Fig. 7.6 with an enlarged view from 1.6 - 1.8 μm. From top to bottom it shows the data from August, 2005, the model without ethane, with 10% pure ethane, and with 10% ethane diluted in nitrogen. We see here that ethane can be added to the model without increasing significantly the band near 1.69 μm if the amount of pure methane is reduced slightly. The band, however, is slightly shifted to shorter wavelengths than the data. The spectra are shifted by -0.1, 0.0, +0.1, and +0.2, for clarity. For comparison, at the top of this figure (and the next figure) we include a synthetic spectrum of 100% pure ethane created from optical constants from Quirico and Schmitt (1997b) with a grain size of 100 μm.

features of ethane. This ethane spectrum is shown in Fig. 7.4 along with the astronomical spectra.

The model reproduces the many prominent absorption bands characteristic of CH_4 as well as N_2 at 2.15 μm and CO at 2.352 μm that are present in our spectra of Pluto. While the models generally reproduce the data well, there is a mismatch shortward of ~1.55 μm where the albedo in the model is too high. A detailed comparison of the models is presented in Section 7.4. We also detect weak features at ~2.27, 2.317, and 2.405 μm in both the VLT and UKIRT data, and two small features near ~2.46 μm in the UKIRT data that extends to longer wavelengths (presented in Fig. 7.4 and discussed in detail in Section 7.4). The components responsible for creating these features have not yet been unambiguously identified. In Section 7.4 we present a thorough analysis of each strong band of ethane compared to the data.

Triton Modeling

Triton's visible albedo is 0.76 (Goguen et al., 1989). The geometric albedo near-infrared spectrum from Quirico et al. (1999) was obtained by using an expression from Smith and Gottlieb (1974) based on the incoming solar flux and Triton's radius and distance. We normalize our spectrum at 1.55 μm to 0.8, which is approximately the same albedo value as in Quirico et al. (1999). We set the cosine asymmetry parameter to -0.5. Although this value is slightly larger than the average range of -0.35 to -0.45 found on the surface of Triton from Voyager measurements (Hillier et al., 1994), our attempts with lower cosine asymmetry

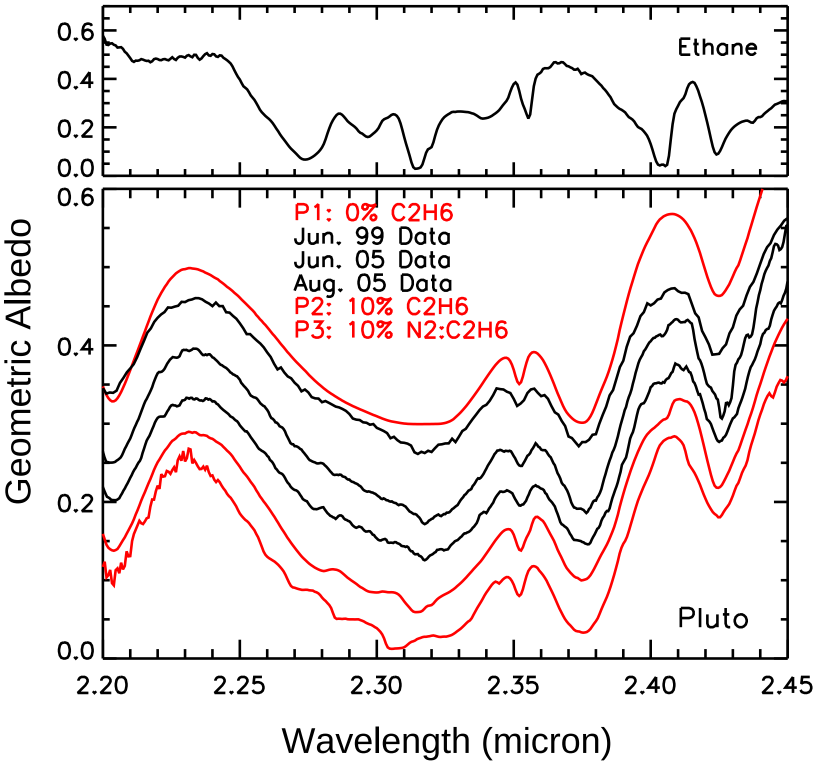

Figure 7.8: Pluto: Models (red) compared to three smoothed Pluto spectra (black) from 2.2 - 2.45 μm. From top to bottom it shows a model with no ethane, the June 1999 data, the June 2005 data, the August, 2005 data, the model with 10% ethane, and the model with 10% ethane diluted in nitrogen. Including 10% ethane in the model improves the fit of the weak feature at ~2.4 μm. However, between 2.27 and 2.32 μm the flux level and the three features are not well matched by the data. The spectra are shifted by -0.05, 0.0, +0.05, +0.1, +0.1, and +0.2 for clarity (recall the 1999 spectrum had a large overall flux error, hence the irregular vertical shift).

Table 7.4: Model Compositions

Pluto					
Model	**CH_4 (500 μm)**	**N_2:CH_4:CO[a] (95000 μm)**	**Titan Tholin (15, 50 μm)[b]**	**C_2H_6 (100 μm)**	**N_2:C_2H_6 (100 μm)**
P1: general	46	32	22	-	-
P2: 10% C_2H_6	43	29	18	10	-
P3: 10% N_2:C_2H_6	43	29	18	-	10
Triton					
Model	**N_2:CH_4:CO[c] (90000 μm)**	**H_2O (380 μm)**	**CO_2 (480 μm)**	**C_2H_6 (100 μm)**	**N_2:C_2H_6 (100 μm)**
T1: general	50	23	27	-	-
T2: 10% C_2H_6	47	20	22	10	-
T3: 10% N_2:C_2H_6	47	20	22	-	10

---

[a] molecular mixture with 0.36% CH_4 and 0.1% CO

[b] The Titan Tholin grain size is 15 μm for the general model and 50 μm for the ethane models.

[c] molecular mixture with 0.11% CH_4 and 0.05% CO

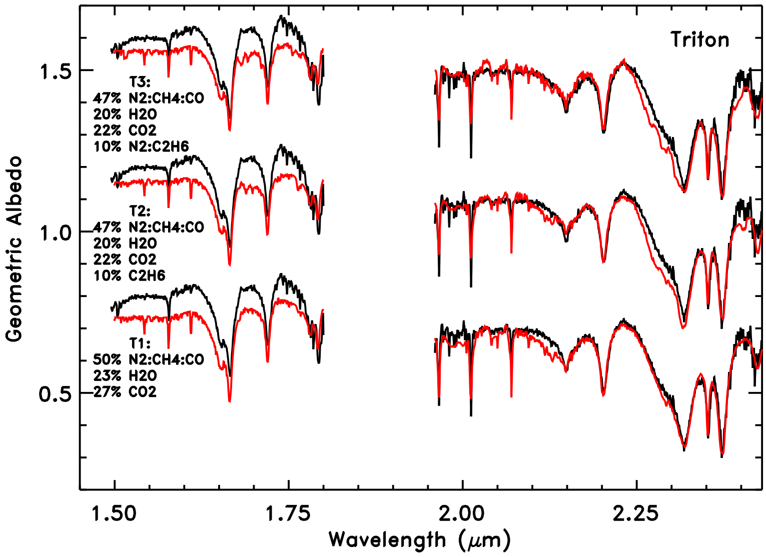

Figure 7.9: Triton: Models (red) compared to spectral data (black) of Triton from this work (Nov. 2008). The models are the basic model without ethane (bottom), a model including ethane (middle), and a model including ethane diluted in nitrogen (top). The models are shifted vertically by 0.4 for clarity. The noise and small "features" of the model in the 2 - 2.1-μm range are due to the large uncertainty in the CO_2 optical constants in the transparent regions. A spurious "kink" is also introduced by CO_2 optical constants in the model at 2.292 μm. The large reflectance difference between the H and K bands made it impossible to adequately fit them simultaneously. This has been a problem for all models shown in previous work as well.

parameters resulted in significantly poorer models, with a lower overall albedo. The continuum level of the model can vary significantly when certain parameters are changed, for example, when varying the cosine asymmetry parameter. We are more concerned about the effect on the spectrum of absorption bands created by adding ethane, so rather than focus on the exact percentages of each component in the model or overall flux levels, we focus on the positions of the absorption bands introduced when including ethane. The optical constants for modeling Triton include crystalline H_2O at 40 K from Grundy and Schmitt (1998), pure CO_2 at 30 K from Quirico and Schmitt (1997b), and a N_2:CH_4:CO molecular mixture with 0.11% CH_4 and 0.05% CO created in the same manner as for Pluto.

Models by Quirico et al. (1999) showed that intimate mixtures of H_2O and CO_2 provided better fits than geographic mixtures. Bernstein et al. (2005) later present laboratory ice mixtures of H_2O and CO_2 at multiple temperatures and show that the spectrum is not equal to the sum of the pure solid components. The CO_2 bands are much broader and are shifted to longer wavelengths and the forbidden $2\nu_3$ overtone is present at 2.138 μm in the H_2O and CO_2 mixture. Grundy et al. (2010) show that these two species are likely to co-exist because of their negligible longitudinal variation in band depth and band area. The positions and shapes of the bands in the spectra suggest that they are not intimately mixed. In our models, H_2O and CO_2 are geographically (spatially) mixed, as are all other components.

For Triton, our basic model (T1) includes 50% N_2:CH_4:CO, 23% crystalline H_2O, and 27% CO_2 with grain sizes of 90,000, 380, and 480 μm, respectively. As for Pluto, we create three Triton models: without ethane (T1), with 10% pure ethane (T2), and with 10% ethane diluted in nitrogen (T3), see Table 7.4). A comparison of each model with respect to the data is shown in Fig. 7.9. In Fig. 7.10 and 7.11 the 1.6 - 1.8 and 2.2 - 2.43 μm regions are plotted, providing a more detailed view of spectral features.

The basic model represents the spectrum fairly well; however, we see some important discrepancies. The continuum level is slightly low in the 1.5 to 1.75-μm region. The model does not reproduce the significant observed difference in the albedo between the H and the K bands, which was seen by both Quirico et al. (1999) and Cruikshank et al. (2000). The relative intensities of the three principal CO_2

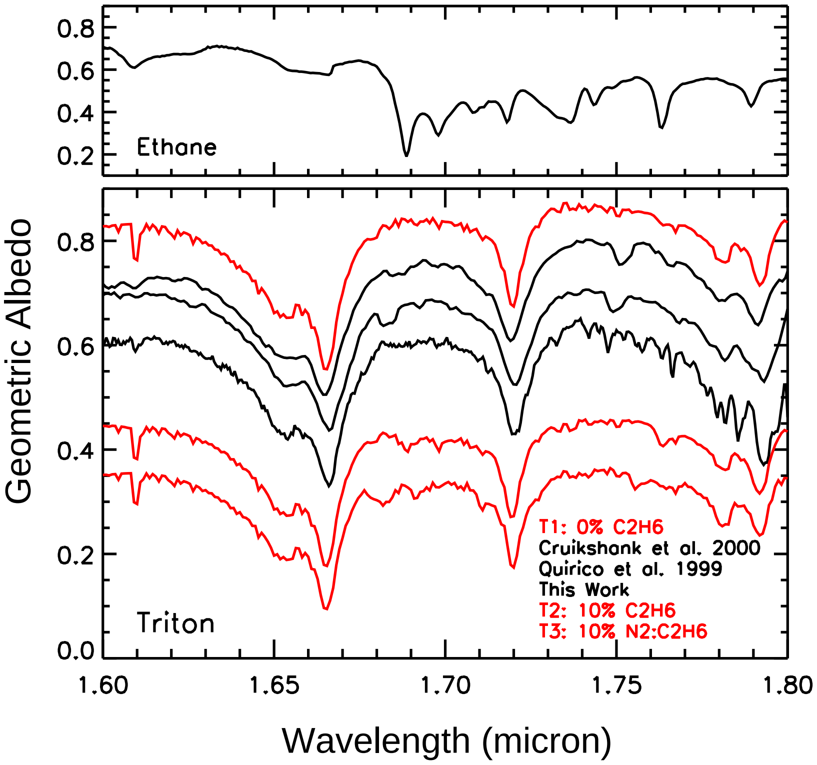

Figure 7.10: Triton: Models (red) compared to spectral data (black) of Triton. From top to bottom it shows the model without ethane, data from Cruikshank et al. (2000) (May, 1995), Quirico et al. (1999) (Sep., 1995), and this work (Nov., 2008), the model with 10% pure ethane, and the model with 10% diluted ethane in the 1.6-1.8-μm range. Interestingly, the features near 1.69 and 1.75 μm are not at the same position among the data. It is clear that these weak features do not match the models, however, laboratory data show that ethane bands can shift as much as 0.007 μm between the pure and diluted forms, which raises the possibility that other amounts of dilution could match the data. The spectra are shifted by -0.42, -0.32, -0.22, -0.12, -0.12, and 0.08 for clarity. For comparison, at the top of this figure (and the next figure) we include a synthetic spectrum of 100% pure ethane created from optical constants from Quirico and Schmitt (1997b) with a grain size of 100 μm.

bands do not match the data, as noted by Quirico et al. (1999). When the 1.966- and 2.012-μm bands are well reproduced by the models, the 2.071-μm band is overestimated in the models, as well as the two weaker bands at 1.543 and 1.609 μm. CO and CO_2 both contribute to the band at 1.578 μm in the data, although this CO absorption is not modeled.

7.4 Discussion

At low temperatures, pure ethane ice can exist in three forms: amorphous (T $<$ 30 K), metastable (30 $<$ T $<$ 55 K), and crystalline (T $>$ 50 K; Hudson et al., 2009). However, heating the amorphous phase to 40 K, or the metastable phase to 65 K, irreversibly changes the ethane to the crystalline form (Hudson et al., 2009). The band centers shift slightly depending on the phase; these band locations for each phase are given in Hudson et al. (2009), and are listed in Table 7.5 for wavelengths relevant for this work.

At 21 K, Quirico and Schmitt (1997b) measure pure ethane's most prominent absorption bands to be located at 1.689, 1.698, 1.764, 2.015, 2.274, 2.297, 2.314, 2.403, and 2.405 μm for the wavelength range presented in this data (see Table 7.5). Quirico and Schmitt (1997b) note that the absorptions at 2.403 and 2.405 μm are a split band very sensitive to the sample thickness. For their original deposition

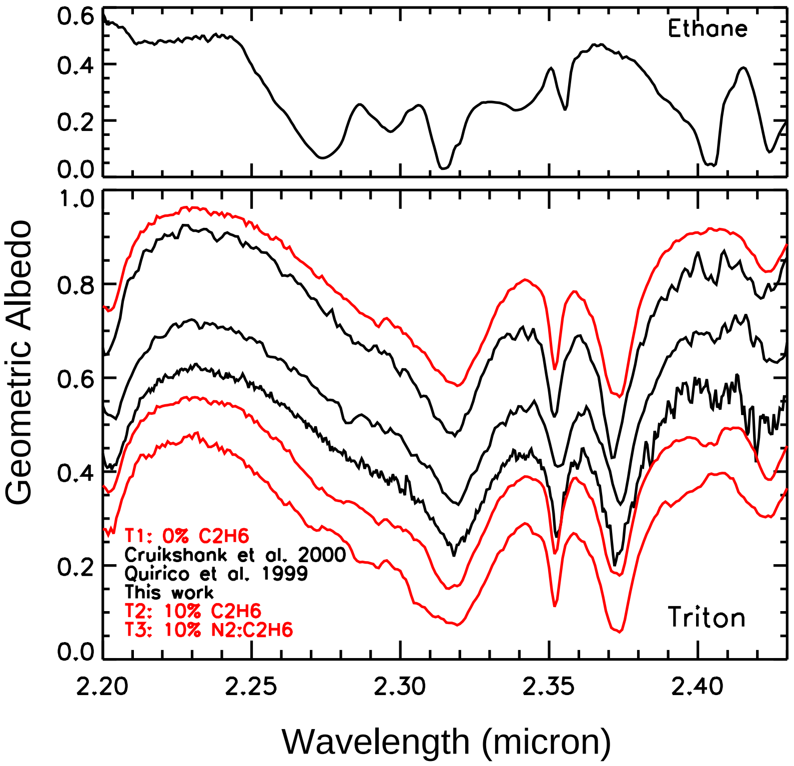

Figure 7.11: Triton: Models (red) compared to spectral data (black) of Triton. From top to bottom it shows the model without ethane, data from Cruikshank et al. (2000) (May, 1995), Quirico et al. (1999) (Sep., 1995), and this work (Nov., 2008), the model with 10% pure ethane, and the model with 10% diluted ethane from 2.2 to 2.43 μm. We see differences in band centers among the data for the ~2.405 μm feature. The *diluted* ethane model is clearly a poor match, because three distinct features are seen in the model between 2.27 and 2.32 μm that are not present in the data. This trio of features is much more subtle in the *pure* ethane model since the 2.314 μm feature overlaps with the diluted methane feature. The 2.405 μm feature of our data is well matched by the pure ethane model, however, other features in the data are weaker than the model. The spectra are shifted by -0.25, -0.15, -0.1, 0.05, 0.1, and 0.25 for clarity.

Table 7.5: Position of selected bands of C_2H_6 and N_2:C_2H_6

Pure C_2H_6[a] **(μm)**	**Diluted C_2H_6 (μm)**	**Absorption Coefficient**[b] **(cm^{-1})**
1.689	1.682	41
1.698	1.691	18
1.764	1.755	15
2.015	[c]	8
-	**2.260**	-
2.274	**2.269**	138
(2.272, 2.274, 2.274)		
2.297	2.285	53
2.298		53
2.314	2.305	333
(2.312, 2.314, 2.315)		
2.403	**-**	209
2.405	**2.392**	228
(2.402, 2.404, 2.406)		
2.424	2.414	103
-	2.445	-
2.457	**2.449**	103
2.461	**-**	315
(2.459, 2.461, 2.461)		

---

[a] These bands' locations and strengths are from Quirico and Schmitt (1997b). In bold are split bands, and dashes signify no band is present. The positions for specific bands in parentheses are measured by Hudson et al. (2009) for amorphous, metastable, and crystalline forms, respectively.

[b] For pure C_2H_6

[c] No information was given for this band in Quirico and Schmitt (1997b)

thickness, only the first band was observed. As the depth increased, the second was eventually seen, and for the thickest samples, only the second band remained. Hudson et al. (2009) measure the 2.4-μm feature at each of the three phases and find it to be centered at 2.402, 2.404, and 2.406 μm for amorphous, metastable, and crystalline ethane, respectively, with increasing relative band area as the band shifts to longer wavelengths.

When ethane is diluted in α-N_2 (mixing ratio 1:100), the bands shift to shorter wavelengths (Quirico and Schmitt, 1997b). The two bands at 2.403 and 2.405 μm measured in pure ethane by Quirico and Schmitt (1997b) combine into one asymmetric band. All dilution experiments were performed with α-phase N_2, although nitrogen is present in the warmer β phase on both Pluto and Triton. For ethane diluted in β- versus α-N_2, the band shifts might not be uniformly in the same direction (Quirico et al., 1999). Pure ethane would likely be in the metastable or possibly crystalline phase at the temperatures found on the surfaces of Pluto and Triton. Optical constants are not yet available for ethane in the metastable state. Thus, for our models we use optical constants of pure ethane at 21 K, so the ethane is likely in the amorphous state (Quirico and Schmitt, 1997b, do not explicitly mention the state of their sample).

Barata et al. (2003) show that when CH_4 is exposed to ion irradiation, the molecular bonds break and form ethane and other hydrocarbons, such as propane (C_3H_8), ethylene (C_2H_4), and acetylene (C_2H_2). In the outer Solar System, sources of irradiation include energetic particles from cosmic rays and solar wind. Ethane could also be deposited to the surface by precipitation from the atmosphere (e.g., Krasnopolsky and Cruikshank, 1995, 1999).

To investigate the presence of ethane on Pluto and Triton, we now discuss the presence or absence of each ethane band in our spectra, as well as in previous work, in order of increasing wavelength.

Pluto

On Pluto, the 1.69-μm band should deepen when adding ethane (see the synthetic spectrum of C_2H_6 and a comparison of the models in Fig. 7.7), but amounts of less than 10% do not greatly affect the strength of the band and could easily be accounted for by a variation in the amount of pure methane in the model.

Based on the strength and location of this feature alone for ethane versus the data, *pure* ethane on Pluto should be constrained to less than 10%. There should be less than a few percent of *diluted* ethane on Pluto, if at all, because this feature shifts to 1.682 μm when the ethane is diluted and it is not detected in the data. The ethane interpretation, however, must be consistent with other ethane bands. We do not detect the slightly weaker pure ethane features at 1.698 and 1.764 μm in the data, nor the feature of diluted ethane at 1.755 μm.

The 2.015-μm ethane band (see the synthetic spectrum of C_2H_6 compared to the data in this region in Fig. 7.4) has never been seen on Pluto's surface, however analyzing this region is difficult because of strong telluric bands that must be carefully corrected. The spectra from 2005 presented in this work have poorly corrected telluric features and thus we cannot confirm or rule-out the presence of this feature, although from a comparison with previous data and the 1999 data from this work, it seems unlikely that this band is present in spectra of Pluto's surface. This feature is also weaker than other prominent features of ethane (i.e. at 1.698, 1.764, 2.274, 2.297, 2.314, and 2.405 μm), and thus in small quantities on the surface the feature may not be detected. Brown et al. (2007a) did not detect the 2-μm feature on Makemake, while they did detect stronger ethane features between 2.27 and 2.32 μm.

Near 2.27 μm there is a change of slope in the spectrum that is likely caused by a broad absorption feature centered at approximately that wavelength. This feature was first suggested by Douté et al. (1999) to be CH_4 (who report it at 2.28 μm). Nakamura et al. (2000) attributed it to ethane along with the 2.40-μm feature seen in their spectra. In our spectra, shown in Fig. 7.8, the 2.27-μm feature is similar to that of Douté et al., and not the Nakamura et al. data. Cruikshank et al. (2006) modeled this feature by removing the methane (CH_4:N_2) contribution and inspecting the residual absorption. They show that this feature could be well explained by C_2H_6. Ethane also has a feature at 2.297 μm which we do not detect, although it is weaker than the 2.27- and 2.314-μm features.

Quirico and Schmitt (1997b) measured a feature at 2.314 μm for pure ethane. In our spectra (seen in Fig. 7.8), a feature is centered near 2.317 μm and is about 0.005-μm wide in both the VLT and UKIRT data. The feature has a narrow, defined minimum at 2.317 μm in the VLT data (the wavelength calibration is accurate to 0.0005 μm or better), while in the UKIRT data it has no clear minimum, but instead it has fairly constant absorption between 2.315 and 2.320 μm. Hudson et al. (2009) reported that the feature for ethane shifts between 2.312 and 2.315 μm, depending on the phase. At 2.317 μm, telluric methane has a strong absorption which should be removed when dividing by the standard star. However, the width of this telluric feature is about 0.002 - 0.003 μm, and the feature in the spectrum is broader (about 0.005 μm). We are, therefore, confident that the feature is due to Pluto's surface, however, we can offer no explanation as to why it would be shifted by at least 0.002 μm if it is due to ethane.

In Fig. 7.8, it is clear that the absorptions in the model with 10% pure ethane are much stronger than what we see in the data at 2.274, 2.297, and 2.314 μm. Also, the overall albedo in the 2.27 - 2.32-μm region in the models with ethane is significantly lower than the data, as seen in Fig. 7.6. Based on this spectral region, pure ethane is limited to only a few percent and diluted ethane to undetectable amounts, which is consistent with the lack of strong features in the H band.

The 2.405-μm feature on Pluto stands out clearly in our data because it is not in a region of strong methane absorption. The presence or absence of this feature in high quality spectroscopic data for both Pluto and Triton are listed in Table 7.6. Nakamura et al. (2000) found a feature near 2.4 μm that appeared related to an absorption at 2.27 μm, both of which were much stronger in their data compared to the Douté et al. (1999) spectrum. Nakamura et al. found that models including ethane produced a much stronger band at 2.4 μm than seen in the spectrum when adequately fitting the 2.27-μm feature. For a comparison of our spectra with that of Nakamura et al. taken in May 1999 and of Douté et al. (1999), see Fig. 7.12. In three of our spectra (Aug. and Jun., 2005 and Jun., 1999), we see a small feature at 2.405 μm, but it is much more subtle than that reported by Nakamura et al. (2000). The feature we detect is shallower and not as broad. Furthermore, the 1999 spectrum was taken one month later at the same location on the surface as the Nakamura et al. spectrum. The quality of the May 2005 spectrum is too low to be confident in a small feature in the 2.4-μm region.

While a similar feature near 2.405 μm on Triton was originally suggested to be due to ^{13}CO (Cruikshank et al., 1993), Cruikshank et al. (2006) note that it is unlikely that this feature is entirely due to CO because laboratory spectra show it is very weak compared to the 2.352-μm feature of the common isotope of CO. Therefore Cruikshank et al. (2006) and Verbiscer et al. (2007) tentatively attributed the

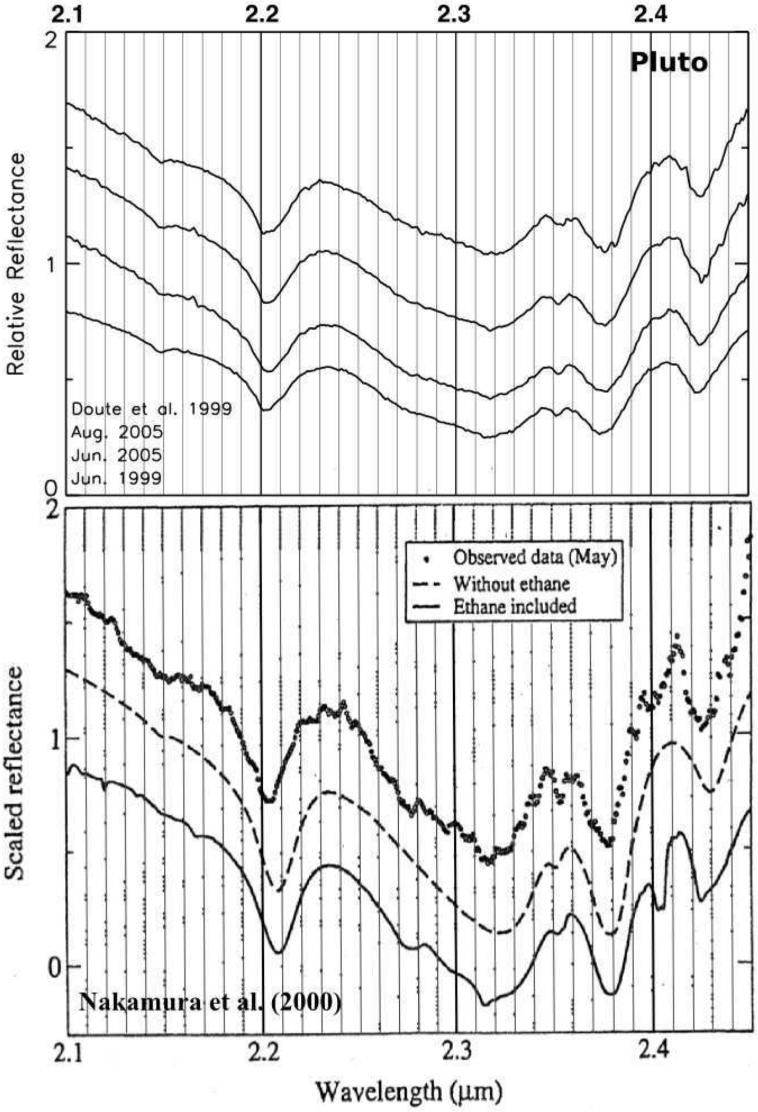

Figure 7.12: Pluto: Comparison of spectra of Pluto from Nakamura et al. (2000) taken on May 6, 1999 with Douté et al. (1999) and this work. The bottom half of the figure is taken from Nakamura et al. (2000), and shows, from top to bottom, the data, a model without ethane, and a model with pure ethane. The top half of the figure shows, from top to bottom, the spectrum from Douté et al. (1999), and our data (smoothed in this case) from August, 2005, June, 2005, and June, 1999. The feature at 2.4 μm is much more subtle in the spectra from this work compared to the Nakamura spectrum. The spectrum from June, 1999 was taken one month after the Nakamura spectrum at the same location on Pluto's surface.

Table 7.6: Detections of features near 2.4 microns

Reference	**Obs Date**	**Sub-E Long**[a]	**Sub-E Lat**	**Feature Present?**	**Instrument**
Pluto					
Douté et al. (1999)	1995 May 11	290	-16	No	UKIRT/CGS4
Douté et al. (1999)	1995 May 13	40	-16	No	UKIRT/CGS4
Douté et al. (1999)	1995 May 15	155	-16	No	UKIRT/CGS4
Nakamura et al. (2000)	1999 May 6	288	-24	Yes (∼2.4 μm)	Subaru/CISCO
Nakamura et al. (2000)	1999 Jun 10	96	-23	Yes (∼2.4 μm)	Subaru/CISCO
Cruikshank et al. (2006)	2005	-	-	Yes (2.405 μm)	Gemini/GNIRS
Verbiscer et al. (2007)	2005 May	123	-36	Yes (2.405 μm)	Magellan/CorMASS
This work	1999 Jun 7	283	-24	weak (∼2.405 μm)	UKIRT/CGS4
This work	2005 May 13	20	-36	low SNR	VLT/SINFONI
This work	2005 Jun 09	93	-35	weak (∼2.405 μm)	VLT/SINFONI
This work	2005 Aug 09	338	-34	weak (∼2.405 μm)	VLT/SINFONI
Triton					
Cruikshank et al. (1993)	1991/1992	-	-	Yes (2.404 μm)	UKIRT
Quirico et al. (1999)	1995 Sep 7	3	-49	Yes (2.406 μm)	UKIRT/CGS4
Cruikshank et al. (2000)	1995 May 13	57	-49	Yes (2.405 μm)	UKIRT/CGS4
Cruikshank et al. (2000)	1998 Oct 28	69	-50	Yes (2.405 μm)	UKIRT/CGS4
Grundy et al. (2010)	2000-2009[b]	-	-	Yes	SpeX/IRTF
This work	2008 Nov 22	93	-48	Yes (2.406 μm)	VLT/SINFONI

---

[a] For consistency, all sub-Earth longitudes presented were taken from HORIZONS (http://ssd.jpl.nasa.gov/horizons.cgi), using the IAU definition of the north pole, based on the date, time, and location of observations reported by the authors in their articles, except for Verbiscer et al. (2007) who report the longitude but not the date of observation in their abstract. These do not correspond to the sub-Earth longitudes reported in the articles by Quirico et al. (1999), Douté et al. (1999), and Nakamura et al. (2000). The date and time of observations were not published for Cruikshank et al. (1993) and Cruikshank et al. (2006) and so sub-Earth longitudes and latitudes could not be determined. These are marked with a "-".

[b] The ∼2.405-μm feature was detected in the global average spectrum of Grundy et al. (2010), which was created from 53 spectra taken from 2000 to 2009.

2.405-μm feature to ethane in Pluto's spectrum.

At 2.457 and 2.461 μm, ethane also has clear and strong bands. This wavelength range is covered only in the 1999 UKIRT Pluto data. In Fig. 7.13 the 2.30 - 2.48 μm portion of the UKIRT spectrum is shown, along with the model including 10% ethane (see figure caption for details). There are many strong telluric water vapor lines near these wavelengths (particularly noticeable in our data is the telluric feature at 2.472 μm), but the transmission between the 2.455 and 2.463 μm atmospheric H_2O lines is close to 100%, which increases our confidence that the 2.457- and 2.461-μm features are real. These two features are comprised of one and four points, respectively, in the smoothed spectrum (in the unsmoothed spectrum, the 2.457-μm feature is made of two points). The noise level is approximately 0.008 of the smoothed continuum, indicating that each of the two absorptions is detected at the 2-3 sigma level.

This region is covered in the Gemini spectrum of Pluto from Cruikshank et al. (2006), and they do not see a feature at this wavelength, although the low quality of their data in this region could affect detection. Verbiscer et al. (2007)'s spectrum also extends to this region, and they do see a weak band at about 2.461 μm. The two features seen in our spectrum at these wavelengths are significantly weaker and narrower than the feature seen by Verbiscer et al. (2007). Perhaps Verbiscer et al. (2007) see only one broad feature because of the lower resolution (∼300) of their data. Because the 2.405-, 2.457- and 2.461- μm bands are so weak in our data it is difficult to tell if their relative strengths are consistent with laboratory data for ethane, particularly because the 2.405 μm feature is weakest in the 1999 data. However, it appears that the two bands at 2.457 and 2.461 μm should be stronger if the 2.405- μm feature is entirely due to pure ethane. This suggests there is some contribution of ^{13}CO to the 2.405- μm band.

To further refine the search for ethane on Pluto, we plot the difference between the data (from August 2005) and the best-fit general model (with no ethane) in Fig. 7.14. While the 2.352-μm feature could be at least partially due to inadequate fitting of the ^{12}CO band, from this plot we see more clearly the absorptions at 2.27, 2.317, 2.352 and 2.405 μm that were not accounted for in the model. Much of the detail of the band shapes is strikingly similar to the spectrum of ethane also plotted. This makes the presence of a few percent of ethane on the surface of Pluto more convincing.

Triton

We see an interesting effect of adding pure ethane in our models of Triton seen in Figs. 7.10 and 7.11. When 10% *pure* ethane is included in the models, the trio of features in the K band at 2.274, 2.297

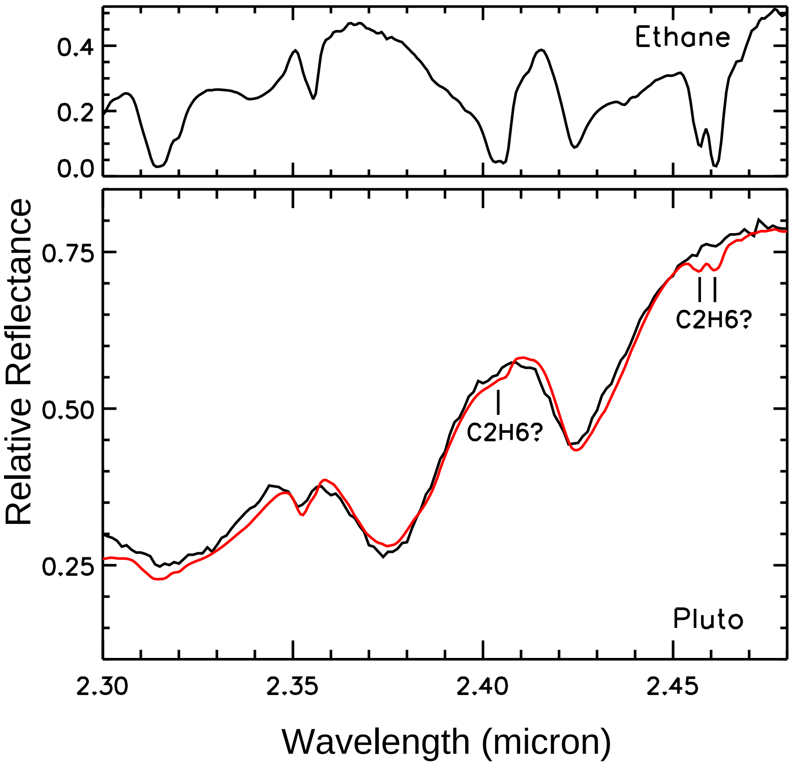

Figure 7.13: Pluto: Here we present the relative reflectance of the 1999 UKIRT spectrum plotted to longer wavelengths that were not measured by SINFONI. The data (black) is normalized to unity at 1.55 μm. A modified version of the model (red) of the August, 2005 spectrum including 10 % ethane is overlaid. Because of the flux issue with the 1999 data we scale and shift the model to generally match the methane bands. We thus cannot make any inferences about the albedo of the data versus the model, however, we can inspect the relative strengths of the ethane bands when 10 % is included in the model. A spectrum of pure ethane with 100 μm grains is included at the top of the figure as a reference. Two faint features (at 2.457 and 2.461 μm) in the data are located at the same position of two strong features of ethane.

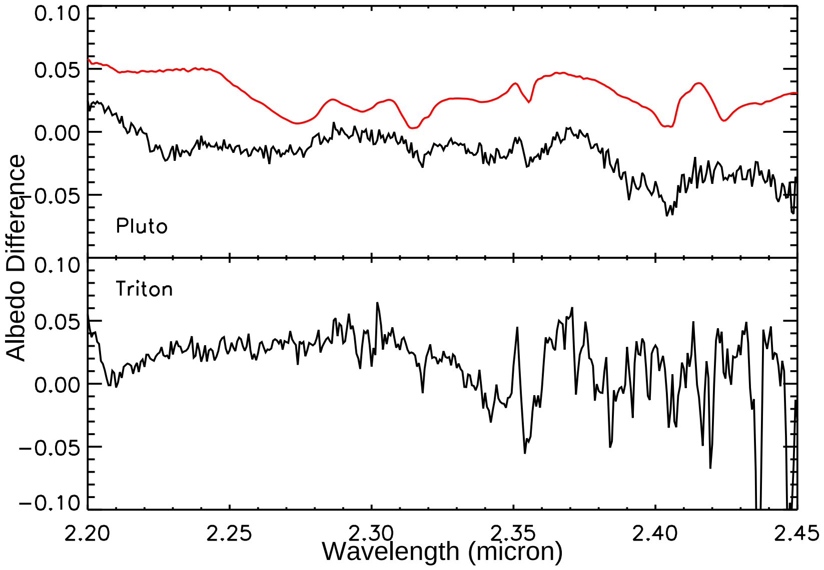

Figure 7.14: Top: The difference between the August, 2005 VLT data for Pluto and the best-fit model that did not include ethane. The spectrum of ethane in red is included in the plot with Pluto residuals and is multiplied by 0.1 to fit the scale of the plot. Many of the residual absorptions match or nearly match the locations of the absorptions of ethane. Bottom: The difference between the Triton spectrum with the best-fit model that did not include ethane. Here we see no distinct match to the ethane features, however, the resulting difference is a bit noisier for Triton than Pluto.

and 2.314 μm is not very distinct. The broad feature created at 2.274 is recognizable, but the 2.314-μm feature appears to overlap entirely with the diluted-methane minimum. This implies that *pure* ethane may be present in small quantities even though the individual features are not distinctly seen. This must be kept in mind as we attempt to identify features in the data. When adding *diluted* ethane, however, the absorption features are clearly seen in the models at 1.682, 1.691, 1.755, 2.260, 2.269, and 2.305 μm. The feature at 2.392 μm is not particularly distinct because it overlaps with strong methane absorption.

Quirico et al. (1999) noted that in their Triton data from September 1995 there are features at 1.683 and 1.749 μm (see Fig. 7.10). These two bands are shifted to longer wavelengths in the May, 1995 spectrum from Cruikshank et al. (2000). In our spectrum, only a very weak, broader absorption at ∼1.69 μm is seen. Poor telluric correction makes identifying a weak feature at 1.75 μm impossible. The wavelength shifts among different observations suggests that some component is diluted in nitrogen in varying concentrations across the surface. Quirico et al. (1999) modeled ethane, by including diluted ethane in the molecular mixture of N_2:CH_4:CO with an abundance of about 0.005% in the mixture. They found that the 1.683-μm feature was matched particularly well, and other features in that region appeared only slightly above the noise level of the spectrum, but that there was no evidence of features in the data at 2.392 and 2.449 μm that were clear in the models.

While it appears that there is a slight, broad feature in the 2.27-μm region in our Triton data, detecting a pure ethane feature at 2.314 μm is complicated by the fact that it is aligned with the feature of methane diluted in nitrogen. No clear signature of ethane is seen in Fig. 7.14, which plots the difference between Triton's spectrum and the model without ethane, although the low quality of the data particularly past 2.35 μm makes any residual band identification difficult.

As seen by Quirico et al. (1999), our models with *diluted* ethane show distinct features that are not seen in the data. It is clear that the positions of ethane bands are very sensitive to dilution (shifting up to 0.008 μm with 1% diluted in α-N_2), and even to the form (metastable versus crystalline). It is possible that the weaker features in the H band are formed at different depths than the stronger K band features, and that vertical stratification of composition causes a mismatch between the two regions. Vertical stratification of methane was detected on the surface of Eris by Licandro et al. (2006a) and Merlin et al.

(2009), who find that the weaker methane bands in the data have smaller wavelength shifts than stronger bands compared to pure methane ice. The possibility still remains, as well, that the features on Triton in the H band are due to another or multiple other materials.

In our Triton spectrum there exists a band located at 2.406 μm which is seen in all previous data, although the band center location varies between 2.404 and 2.406 μm among observations (see Table 7.6). Both C_2H_6 and ^{13}CO display bands near this wavelength. The band is located between 2.402 and 2.406 μm for pure ethane depending on whether it is in the amorphous, metastable or crystalline form (Hudson et al., 2009), and at 2.405 μm for ^{13}CO (Quirico and Schmitt, 1997b). The feature seen in the data is stronger than the model that includes 10% pure ethane. Since no other features in the data are as strong as the model, the 2.405-μm feature cannot be accounted for by pure ethane alone. ^{13}CO also has a feature at 2.404 μm and the common isotope ^{12}CO is much more abundant on Triton than Pluto as seen by the strength of the 1.578- and 2.532 -μm features, we investigate the possibility that ^{13}CO is a significant contributor to the 2.405 -μm feature.

Quirico and Schmitt (1997a) performed laboratory measurements of pure CO and CO diluted in N_2. They found that the 0-2 band of CO when diluted in N_2 was significantly wider than pure CO and that the width, wavelength and intensity were independent of the concentration. They also found that the width and peak intensity were temperature dependent for diluted CO, although the wavelength did not change. These laboratory spectra show that absorption at 1.578 μm is nearly as strong as at 2.405 μm, having absorption coefficients of 2.5 and 5 cm^{-1}, respectively (Quirico and Schmitt, 1997b). For Triton, we perform a rough estimation of the band areas for these two features by calculating the area of a triangle that approximates each band. We find the areas to be nearly the same, with the area of the 1.578-μm feature being slightly smaller. Both features on Triton, however, could have contributions from other materials (CO_2 at 1.578-μm and C_2H_6 at 2.405 μm), making band strength comparisons difficult.

Cruikshank et al. (2006) note that new laboratory measurements of CO verified the expectation that the absorption per molecule is the same for the ^{12}C and ^{13}C isotopes, signifying that the band strengths are proportional to their isotopic abundance. Since the terrestrial ratio of $^{13}C/^{12}C$ is about 0.011 and the ratio is expected to be similar in the outer Solar System, the measurements show that the band they see on Triton is too strong to be due to ^{13}CO alone. With respect to a continuum of methane diluted in nitrogen with no CO, we calculate a band depth of 37.1% ± 1.7% for the 2.352-μm observed feature with respect to the surrounding continuum level. The band depth for the 2.406-μm observed feature is 5.6% ± 2.8%. The second band is much stronger than the $\sim$1% that should be expected from ^{13}CO. Even assuming the largest plausible 2.352-μm band depth and correspondingly smallest 2.406-μm depth within the errors the 2.406-μm band is still 7% of the depth of the 2.352-μm band. Since neither ^{13}CO nor pure ethane could be solely responsible for the depth of 2.406-μm band on Triton, it appears convincing that they both contribute.

7.5 Conclusion

We have presented near-infrared spectral observations in the H and K bands (1.4 - 2.45 μm) of Pluto over four regions of the surface and Triton for one observation. We have searched for the presence of ethane on these bodies by looking for its strongest spectral signatures. To aid the investigation we have modeled each surface with three basic models: a general model (no ethane), a 10% pure ethane model, and a 10% diluted ethane model. Our main conclusions are as follows:

- On Pluto, we identify four features that match generally well with pure ethane at 2.274 and 2.405 μm for all data, and at 2.457 and 2.461 μm for the UKIRT data. The position and strengths of these features suggest that a few percent of *pure* ethane is present on the surface of Pluto. The model with *diluted* ethane is not a good match to the data.

- The 2.317-μm feature on Pluto does not match the exact position of pure ethane in any of its forms, the closest form being crystalline ethane at 2.315 μm. The feature has a narrow minimum centered at 2.317 μm in the VLT data, while it has a nearly constant absorption between approximately 2.315 - 2.320 μm for the UKIRT data.

- On Triton, the bands near 1.68-1.69 μm and 1.75 μm are seen to shift when comparing their locations in this and previous work (Quirico et al., 1999; Cruikshank et al., 2000; Grundy et al., 2010). This suggests that some component diluted in N_2 is present in different concentrations throughout the surface. These bands could potentially be matched by ethane diluted in nitrogen. However, the lack of diluted ethane features in the K band makes its presence unlikely (also noted by Quirico et al., 1999).
- Models of Triton including pure ethane show that the 2.314-μm feature of ethane is in the same location as the CH_4 diluted in N_2 band. The model shows that pure ethane features in the 2.27- to 2.32-μm region would not be very distinct if pure ethane were present in small quantities.
- Based on models including ethane and relative band depths of ^{12}CO and ^{13}CO, the 2.405-2.406-μm feature is too strong to be due entirely to either ethane or ^{13}CO alone on both Pluto and Triton, implying that the feature is a combination of these two components.

Ethane has been sought on Pluto or Triton in several investigations. It is intriguing that it has not been easily detectable especially since it has been found on the surface of other large bodies in the Kuiper Belt such as Makemake and possibly Quaoar. Brown et al. (2007a) discuss how the dominant component on Pluto and Triton is nitrogen with grain sizes close to 1 cm, while on Makemake methane is the dominant, large-grain component. They argue that the large nitrogen grains could inhibit the irradiation of methane particles thus preventing ethane production. Our data show that it is likely that we see a few percent of ethane on the surface of Pluto, which indicates that while large nitrogen grains may inhibit ethane production, it is not entirely prevented. Perhaps the existence of pure methane makes this possible. While small amounts of pure ethane are needed on both Pluto and Triton to account for the depth of the 2.405-μm feature, the contribution of ^{13}CO to this feature complicates constraining ethane's abundance.

Future work needed to improve our understanding of minor constituents on the surface of Pluto and Triton includes more detailed laboratory studies of C_2H_6, C_2H_6 diluted in N_2, and CO in conditions similar to what is expected for the surfaces of large minor bodies in the outer Solar System. Particularly, experiments at temperatures and phases expected on Pluto and Triton are crucial since we were limited to colder temperatures and unlikely phases for C_2H_6 diluted in N_2. Further analysis and modeling of spectra that include high quality, high-resolution data extending to the 2.461-μm-band region should also provide further constraints on the abundances of ethane versus ^{13}CO.

The New Horizons mission will arrive at Pluto in 2015, and the Ralph infrared spectrometer will measure the surface from 1.25 - 2.5 μm with a spectral resolution of 300 over the entire range and 600 over the 2.1 - 2.25-μm range. While this resolution does not exceed the capabilities of current ground-based telescopes, hopefully higher signal-to-noise data, and more localized measurements will shed more light on the presence of ethane on Pluto's surface.

7.6 Mission to Pluto: New Horizons

New Horizons launched in January 2006. In February 2007, it underwent a gravity assist with Jupiter. It will finally reach and fly by Pluto and its moons, Charon, Nyx and Hydra, in July 2015. The spacecraft will then visit a second Kuiper Belt object which has yet to be chosen (and yet to be discovered!). New Horizons is the farthest mission ever launched and the first to explore distant, icy bodies. It will provide insight on large, icy worlds similar to Pluto, and possibly smaller less-understood TNOs.

New Horizons Mission Objectives (Source: JHU APL):

- Map the surface composition of Pluto and Charon
- Characterize the geology and morphology of Pluto and Charon
- Characterize Pluto's atmosphere
- Search for an atmosphere around Charon
- Map the surface temperatures on Pluto and Charon

- Search for rings and satellites around Pluto
- Explore one or more additional TNOs

The New Horizons spacecraft is equipped with 7 instruments. *Ralph* will obtain high resolution color maps and surface composition maps of Pluto and Charon. *Alice* will measure Pluto's atmospheric composition. *REX* is part of the radio communications system. *LORRI* will take high-resolution images of Pluto's surface. *SWAP* will measure solar wind in Pluto's vicinity to investigate the atmospheric escape rate and the possible presence of a magnetosphere. *PEPSSI* also measures solar wind, examining neutral atmospheric atoms as they interact with the charged solar wind. And *SDC* measures dust particles sizes en route to Pluto.

Part IV

Synthesis of Research and Conclusions

Chapter 8

The surface variation of small bodies across the solar system

In this chapter the trends of surface variation of small bodies across the Solar System is explored. First, the expected compositional trend in the early Solar System is summarized. Then, the variation in taxonomy, albedo, slopes, and composition are described. Finally, a review of the presence and state of H_2O throughout the Solar System is presented. The intent of this global view is to provide a unifying picture and new perspective for our understanding small bodies.

Contents

8.1 The Early Solar System

During the formation of the Solar System, the temperature gradient across the protoplanetary disk naturally caused a corresponding compositional gradient. At high temperatures close to the Sun only refractory materials could condense, metals at highest temperatures and silicates at lower temperatures. At further distances, hydrated minerals condensed, then water, and finally more volatile species such as ammonia, methane, nitrogen, carbon monoxide, carbon dioxide, and nitrogen. Figure 8.1 shows the condensation temperatures of materials in the disk compared to the location of the planets and asteroids as a simple explanation of the compositional differences correlated with distance. Figure 8.2 is a simple cartoon of the separation between rocky, silicate-rich bodies and ice-rich bodies past the ice line at the time of planetesimal formation.

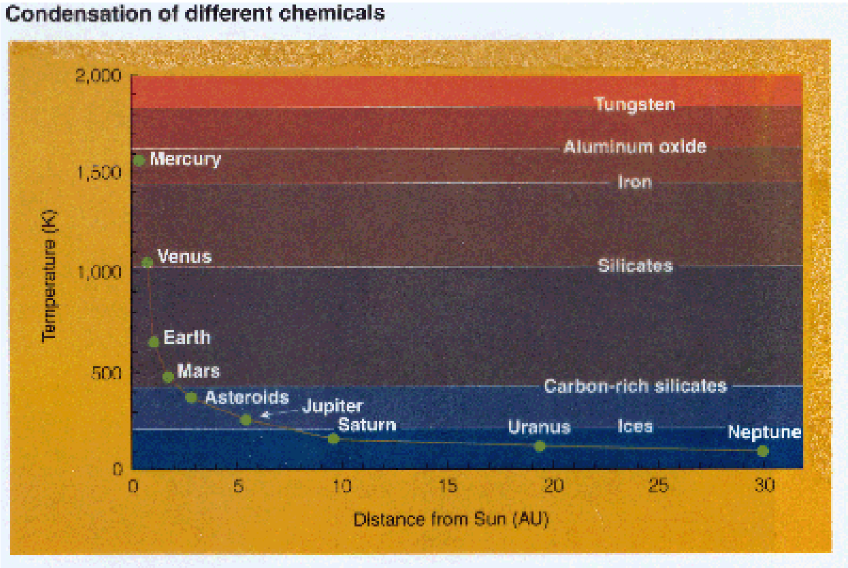

Figure 8.1: Plot of condensation temperatures for various materials with the temperatures and heliocentric distances of the planets and asteroids. At high temperatures, metals such as tungsten, aluminum oxide, and iron can condense. Further from the Sun silicates can form, and at greater distances and low temperatures ices condense (Figure Source).

8.2 Compositional trends in the Solar System today

Remnants of the compositional gradient from the Solar System formation are still observed today, despite significant mixing. The strong temperature gradient as a function of distance from the Sun currently preserves some of the original characteristics. Discovering the breaks from this trend, however, are just as significant as the trend itself because they reveal a rich history of planetary encounters, collisions, planet migration, sweeping resonances, and many other processes that have disturbed the original distribution. Here the trends that are seen today are explored.

8.2.1 Variation across the Main Asteroid Belt

The most basic trend across the Main Asteroid Belt is the distribution of silicate-rich (S- complex) versus carbon-rich (C-, X- complexes) asteroids across the belt. The inner belt is dominated by S- complex objects, the middle to outer belt is dominated by C- and X- complexes (particularly the low albedo X-types, labeled P-types in the Tholen system), and the farthest parts of outer belt and Jupiter Trojans are overwhelmingly very red, D-type asteroids. Vilas and Smith (1985) found that their sample separated into four distinct groups with increasing slope as a function of increasing heliocentric distance. Figure 8.3,

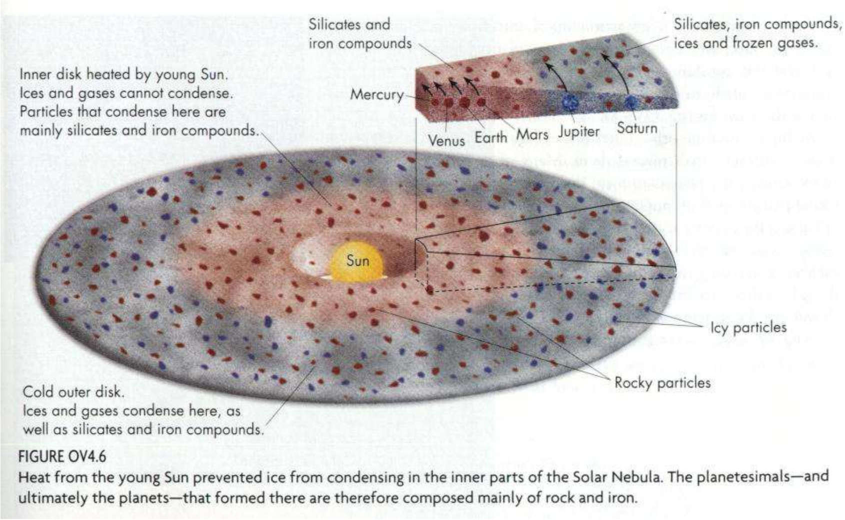

Figure 8.2: Cartoon of the division in the protoplanetary disk between regions at high temperatures where only silicates and metals could condense, and low temperatures where ices could condense as well (Figure Source).

is a cartoon depicting the general abundance of the main asteroid classes as a function of semi-major axis.

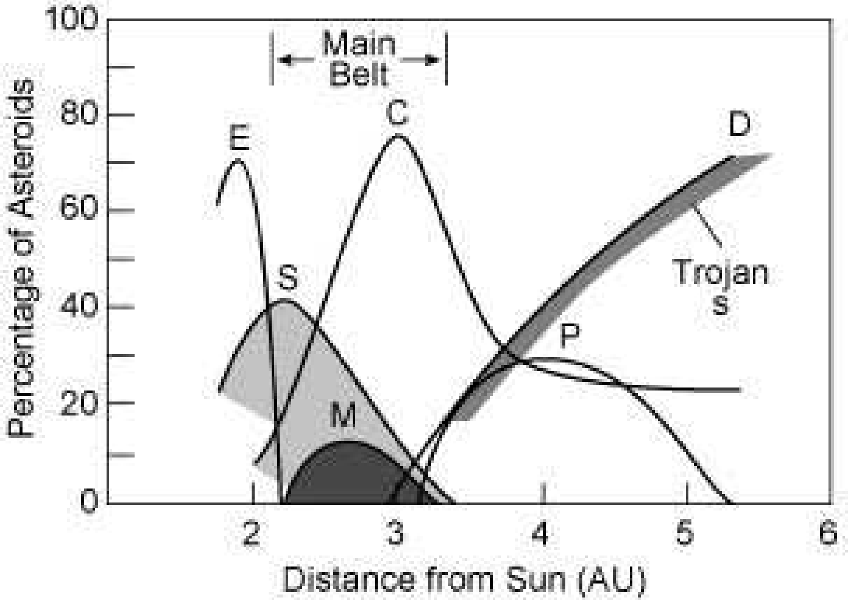

Figure 8.3: Taxonomic distribution of asteroids in the Main Belt. S-types dominate the inner belt, C-types dominate the outer belt, and D-and P-types are abundant in the outer edge of the belt and past the belt up to the Trojan region. E-, M-, and P-types all fall under the X-type spectral category and are distinguished by their albedo; E is high, M is medium, and P is low (Source: NASA Cosmos).

A few explanations have been proposed for the change in slope from C- to X- to D- types. Vilas and Smith (1985) propose that the slope difference could be related to a change in the complexity of hydrocarbons as a function of heliocentric distance. They also suggest that the change in temperature

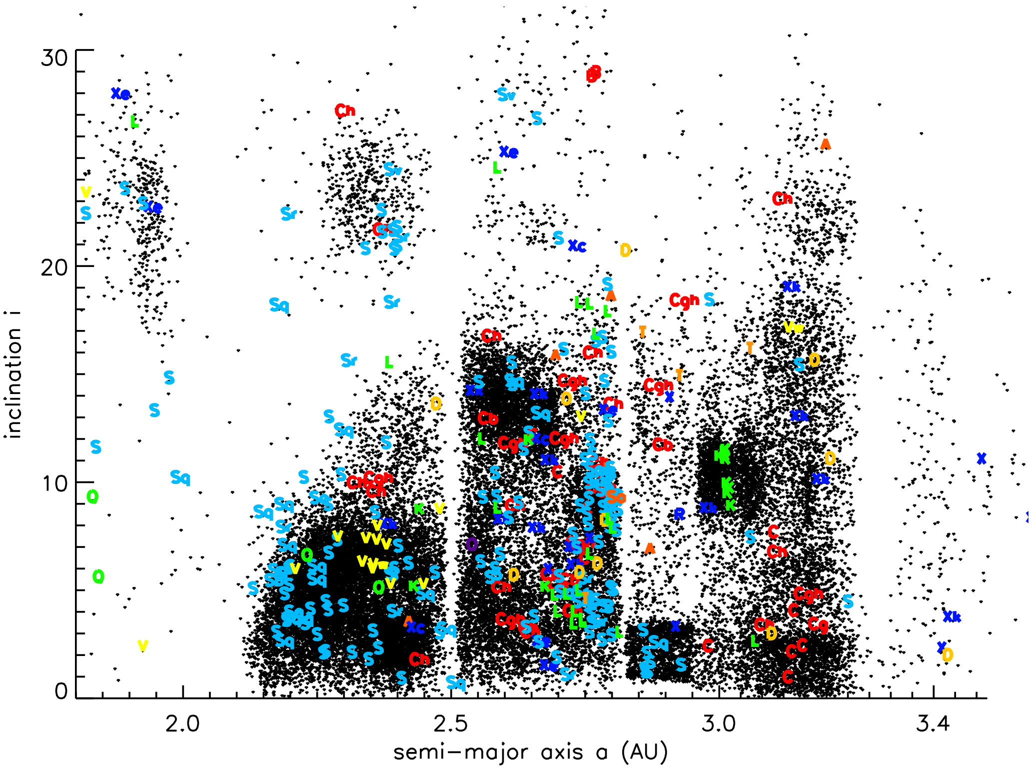

Figure 8.4: Plotted here are a large sample of known asteroids (black dots) according to their semi-major axis and inclination and the asteroids classified in Chapter 4 of this thesis (labeled in color according to their type). Here we see S-types in the outer part of the belt are confined to the small low inclination clump shortward of 2.9 AU which is the Koronis family. Even C-types in the outer belt seem to be confined to low inclinations. The Eos K-type family can be seen near 3 AU at inclinations near 10 degrees. Vestoids are present in the inner belt at fairly low inclinations. Also in the inner belt there appears to be a small clump of Ch and Cgh-type objects at an inclination of about 10 degrees.

could cause changes in the color of the hydrocarbons. It is now also expected that irradiation due to space weathering contributes to the steep slope of D-types in addition to compositional differences between D-types and the C- and X-complexes.

Using the taxonomy presented in DeMeo et al. (2009a) and this thesis, Figures 8.4, 8.5, and 8.6 show the distribution of taxonomic classes as a function of heliocentric distance for selected classes. Figure 8.4 plot the objects according to their inclination along with dots representing a sample of known asteroids to reveal the general structure of the belt. In the inner belt we see that S-types dominate, vestoids are present at fairly low inclinations, and there appears to be a small clump of Ch and Cgh-type objects at an inclination of about 10 degrees. In the outer belt S-types are confined to the small low inclination clump shortward of 2.9 AU, the Koronis family. Even C-types in the outer belt seem to be confined to low inclinations. The Eos K-type family is evident near 3 AU at inclinations near 10 degrees.

In Fig. 8.5 the general trend of S- to C- and X- to D-type is clearly seen. In Fig. 8.6 we search for trends within the S-complex for which this taxonomy is well suited because of the distinct near-infrared features in this complex. It appears that Sq-types, with the widest 1-μm absorption bands (and presumably the most olivine-rich), are more prevalent in the inner belt with its frequency decreasing at increasing heliocentric distances. Sr-types, with more narrow 1-μm absorption bands (and presumably less olivine-rich and more pyroxene-rich) are slightly more abundant at greater distances. Because S-types make up the largest part of the sample and their olivine content is less defined than for Sq- and Sr-types, a more rigorous mineralogic analysis of the 1- and 2- μm bands is necessary. Also, de-biasing for families

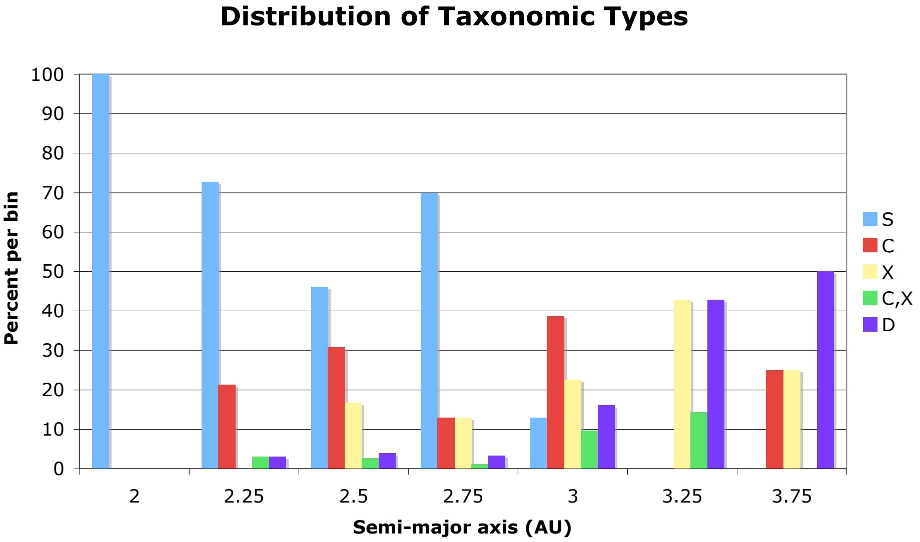

Figure 8.5: The distribution of selected taxonomic types in the Main Belt as a function of heliocentric distance. In this plot, the columns represent the percent of each type per bin. For example, a value of 100 for S-types at 2 AU indicates that of all the asteroids in the sample with semi-major axes between 2 and 2.25 AU, 100% of them are S-types. No correction for detection biases for certain classes is performed. 275 asteroids were included in this sample from Bus and Binzel (2002a), DeMeo et al. (2009a), and unpublished spectra from `smass.mit.edu`.

(such as the Flora family in the inner belt which is olivine rich) and size effects is required to make any claims about olivine and pyroxene trends across the belt to determine if there is any remnant structure or if it has been entirely erased by radial mixing.

Albedo trends have also been noted throughout the belt. Cellino (2000), in a review of the compositional distribution of the Main Belt, shows that albedo trends from higher to lower across the Main Belt (Fig. 8.7). This also seems logical given that S-type asteroids which dominate the inner belt have a much higher albedo than the average for C-, X- and D-type asteroids. At the time of Cellino's work, however, there was not enough data on TNOs and Centaurs to make any significant conclusions about the population of small bodies in the outer Solar System. In the next section, we overview these more recently discovered populations past Jupiter and Neptune.

8.2.2 Variation among Centaurs, in the Kuiper Belt and beyond

Probing further, past the Main Belt and Trojans, the Centaurs and TNOs are markers of the formation and subsequent evolution of the outer Solar System.

The most striking feature of the Centaur population is its bimodality: its B-R colors separate into two different groups, gray and red, with 99.5% confidence (Peixinho et al., 2003; Tegler and Romanishin, 2003). The gray Centaurs have a slightly lower average albedo than red Centaurs, but there is no significant differences between the two populations and their orbital elements (Tegler et al., 2008a).

Color distributions have also been searched for among TNOs. The most significant correlation is between redness of objects and orbit in the classical belt. It has been found that red objects are more

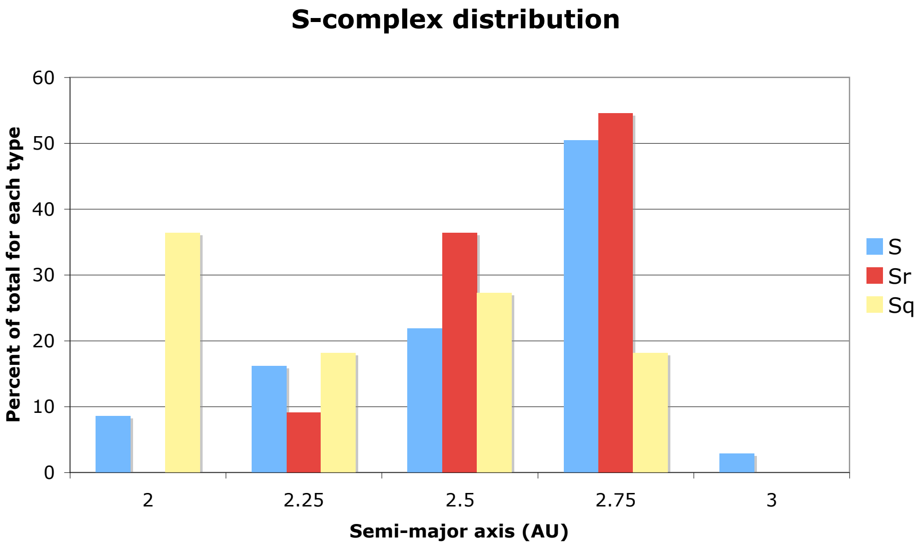

Figure 8.6: The distribution of S-complex types in the Main Belt as a function of heliocentric distance. Sa- and Sv-types are excluded because of their rarity. 127 objects were included in this sample for which there exists both visible and near-infrared data available (from DeMeo et al. (2009a), and unpublished spectra from `smass.mit.edu`).

frequent in orbits with low ($e < 0.05$) eccentricities and low ($i < 5°$) inclinations (e.g., Tegler and Romanishin, 2000; Doressoundiram et al., 2002). There is a color versus perihelion correlation for the TNO population, however, it is at the threshold of statistical significance (Doressoundiram et al., 2008).

The reddest objects in the entire Solar System are found in the outer regions. The reason for their extreme redness is still unknown. Even laboratory-created irradiated organics can't simulate the high slopes of these bodies' spectra. It has also been suggested that colorless ice is responsible, since the slope behavior exists only in cold regions of the Solar System (Grundy, 2009). Increased redness could be achieved if a colorless ice has a mean optical path length and absorption coefficient that vary with wavelength in such a way that the reflectance is greater at longer wavelengths and less at shorter wavelengths (Grundy, 2009). While colorless ice is not a unique solution, it offers an explanation for the higher average albedo of TNOs and Centaurs with respect to Jupiter Family Comets which are thought to originate from those populations, and could also explain why the supposedly less evolved cold classical belt has a much higher frequency of very red objects than the hot population or Centaurs (Grundy, 2009).

There is a stark spectral difference between the reddest bodies at or inside Jupiter's orbit, and the reddest bodies in the Centaur and TNO populations. D-type asteroids (as well as X- and T-types) have steep slopes that have insignificant slope changes between the visible and near-infrared. Their slope is fairly constant, resulting in a smooth straight line spectrum. The reddest TNOs, however, have very steep visible slopes, often much steeper than the inner Solar System bodies, but the slope levels to nearly neutral in the near-infrared (see Fig. 8.10 for a comparison). There is a sharp kink around 1 μm in the spectra distinguishing the visible and near-infrared slope differences. This strongly suggests that the red material on the inner Solar System bodies is not the same as the outer Solar System. On TNOs, either the red material is only red at visible wavelengths, or less likely there is an additional strong blue component offsetting the slope in the near-infrared.

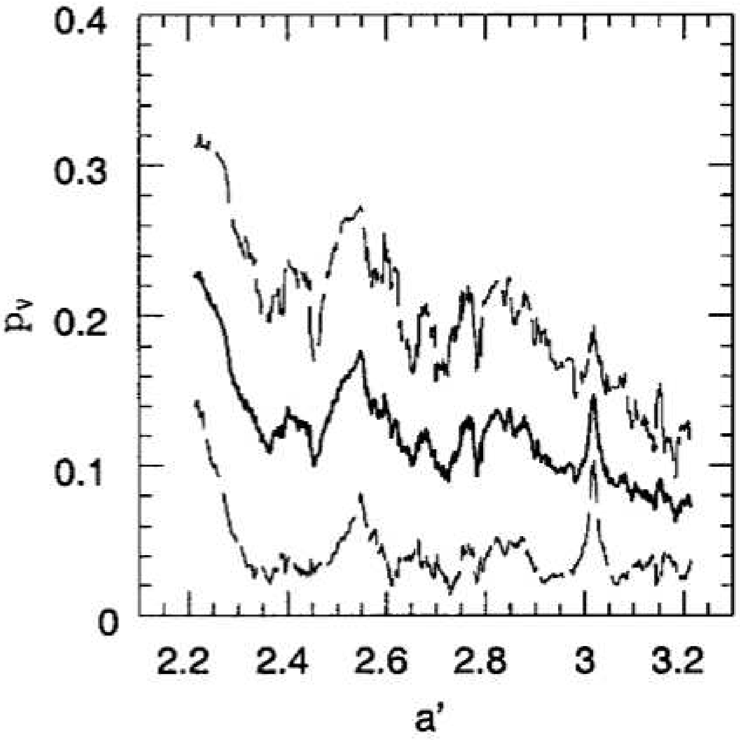

Figure 8.7: The running box plot is based on data from the IMPS radiometric survey, and considering boxes formed by 50 objects. The albedo spike due to the presence of the Eos family at about 3 A.U. is well visible in the plot, where the two dashed lines show the 1σ curves (Figure and Caption from Cellino, 2000). It is evident that the average albedo at the inner edge of the belt is highest and trends to lower albedos at larger distances.

Despite the existence of very red objects in the outer Solar System the average slope trend stops at the Jupiter Trojans. Among featureless objects in the outer Solar System there is a wide range of visible wavelength spectral slopes from neutral to very red (Alvarez-Candal et al., 2008; Fornasier et al., 2009). The near-infrared slopes also vary, but not as markedly as in the visible. The near-infrared is also affected by absorptions due to H_2O ice and sometimes other more volatile species. No trend has been noticed, however, of slope as a function of distance from the Sun among Centaurs and TNOs. Either the material causing the reddening is prevalent over this entire distance, or there has been significant mixing of objects that has erased the evidence. Barkume et al. (2008) searched for compositional trends, but found no correlation between the abundance of H_2O and taxonomic type, albedo, or visible slope (once removing the Haumea collisional family from the statistics). Composition in the Kuiper Belt appear to be less dependent on heliocentric distance and more dependent on the size of the body.

8.3 Water throughout the solar system

Water is considered one of the most fundamental components to life, however it is not unique to Earth. An important question in planetary science is where did all of Earth's water come from? Water is found on comets, and in solid form on the surfaces of satellites and small bodies in the outer Solar System. Strong evidence has been found that liquid water once ran on the surface of Mars. It has been hypothesized that liquid water could be present in the form of subsurface oceans on Jupiter's satellite Europa and Saturn's satellite Enceladus. Evidence of water has been inferred to be present on some asteroids at some point

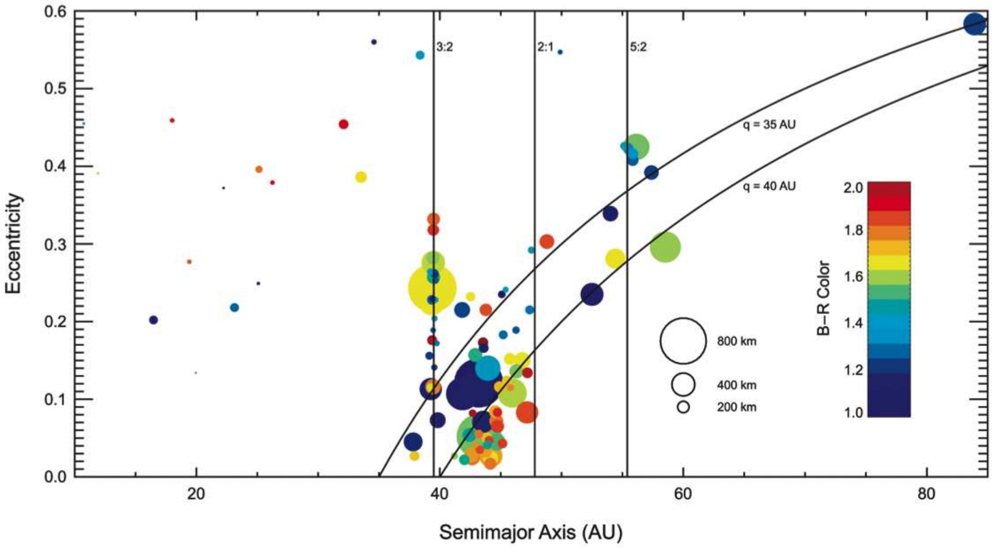

Figure 8.8: Colors of TNOs and Centaurs (more than 100 objects) in the orbital eccentricity vs. semimajor axis plane. A wide color diversity characterizes the outer solar system objects. Interesting patterns clearly emerge from this color map. For instance, objects with perihelion distances around and beyond 40 AU are mostly very red. Classical objects (mostly between the 2:3 and 1:2 resonances) with high eccentricity (and also inclination) are preferentially neutral/slightly red. In contrast, no clear trend is obvious for SDOs ($a > 50$ AU), nor for the Plutinos, which appear to lack any trends in their surface colors. (Figure and Caption from Doressoundiram et al., 2008)

during their lifetimes because of the presence absorption bands due to aqueous alteration or adsorbed water and even the discovery of outgassing seen on activated asteroids (or Main Belt Comets). There have also been very recent discoveries of water in unexpected places such as the Moon. Here the presence and evidence of water on small bodies throughout the Solar System is explored.

After half a century of detailed study including many spacecraft missions, evidence of water was just discovered in 2009 on a body that was previously expected to be completely anhydrous: the Moon. Analysis of data from the Chandrayaan-1 and Deep Impact missions as well as reanalyzed Cassini data from 1999 (Clark, 2009; Pieters et al., 2009; Sunshine et al., 2009), revealed a feature at 3-μm due to OH and H_2O pervasive throughout the surface including the sunlit side. The signature is strongest at the poles and exists only on the upper few millimeters to centimeters of the surface. Because ice is not stable on the Moon, the favored explanation for the water is continuous solar wind interactions with the oxygen-rich surface (Clark, 2009). The strongest 3 μm absorption is seen at the terminator which suggests a diurnal cycle (Sunshine et al., 2009).

A thorough review of hydrated minerals on asteroids on which this paragraph is based is presented in Rivkin et al. (2002). For many decades it has been known that some asteroids are aqueously altered. The most convincing evidence comes from meteorites on which hydrated minerals are found. CI and CM meteorites contain 5 - 10 wt % H_2O/OH (Salisbury et al., 1991). CI meteorites are predominantly composed of phyllosilicates, clay minerals, which are formed in conditions where rock and water are both present (Browning et al., 1996). For asteroid spectra, a handful of features in the UV, visible, and near-infrared wavelengths have been attributed to aqueous alteration, hydroxyls, or water (for a review see Rivkin et al., 2002). The most diagnostic features, found primarily on low albedo (mostly C-complex) bodies, are the 0.7 μm feature typically indicating the presence of phyllosilicates (Vilas and Gaffey, 1989), and the 3.0 μm feature attributed to OH and adsorbed H_2O (Lebofsky, 1978, 1980). The distinct features of solid H_2O on Centaurs and TNOs at 1.5 and 2.0 μm is conspicuously absent from any asteroid or meteorite spectra. Clark (1981) show through laboratory spectra that in the presence of opaque minerals these features are concealed much more easily than the 3-μm feature.

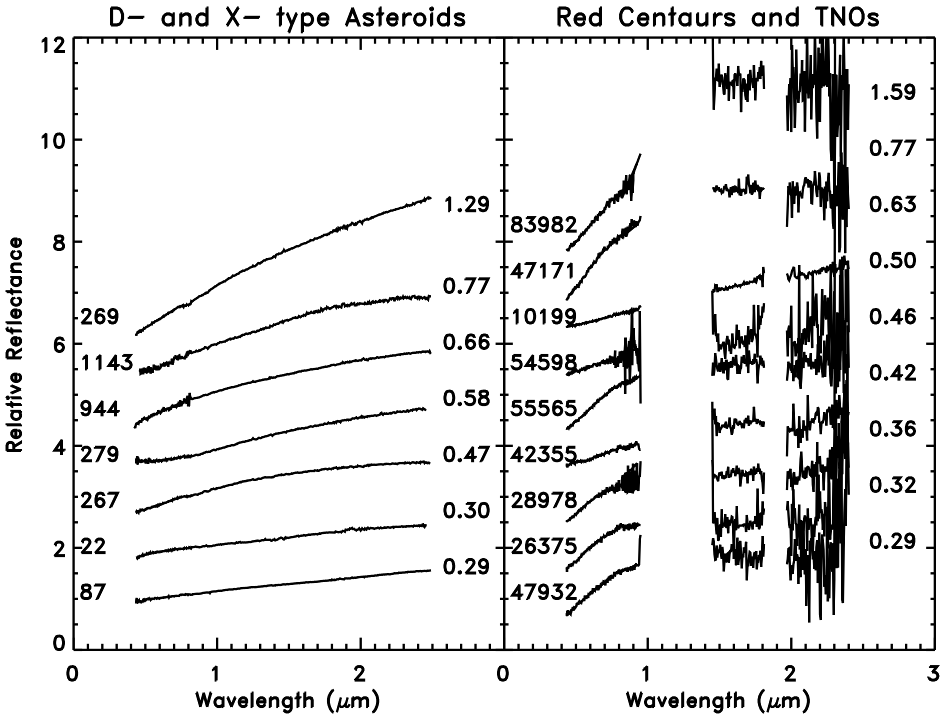

Figure 8.9: Comparison of D- and X-type asteroid spectra with Centaur and TNO spectra with the highest slopes. The object number is labeled on the left, and the overall visible and near-infrared slope is labeled on the right. In general, the TNOs have much steeper visible slopes, but flatten out in the near-infrared.

Water has been detected on "activated asteroids", bodies that have asteroidal orbits in the Main Belt, but exhibit comas indicating outgassing of volatile material (Hsieh and Jewitt, 2006). Two of these bodies belonged to the Themis family and all were in the outer belt, until the recent discovery of P/2010 A2 (Minor Planet Electronic Circular 2010-A32), that resides in the middle belt with a semi-major axis of 2.73 AU. This object's orbit is consistent with the Flora family (Zappala et al., 1995) which is a silicate-rich (S-type) family where water is unexpected. Subsequent Hubble Telescope images by D. Jewitt reveal a complex debris structure suggesting that they observe dust ejection from two recently collided bodies rather than outgassing of volatile material Source: Hubble Website.

Rivkin and Emery (2010) detected a 3-μm band on Themis that is distinctly different from that seen on carbonaceous chondrite meteorites and other low albedo asteroids, and Campins et al. (2010) observed its presence throughout the entire surface. Rivkin and Emery (2010) and Campins et al. (2010) propose that the feature is due to a fine-grained layer of water ice frost. Searches for activated asteroids or the 3-μm feature will certainly play an important role in the years to come for asteroid science and our understanding of the role water plays in the inner Solar System.

Since the first near-infrared spectral data of TNOs have been available it has been apparent that solid H_2O is common on outer Solar System small bodies (detected clearly as broad absorptions at 1.5 and 2.0 μm). Barkume et al. (2008) detected water ice on 4 of 12 Centaurs and 12 of 33 TNOs at the 3σ level or higher in their survey. H_2O ice is detected in the crystalline form on many bodies because of the presence of the 1.65 μm-feature (e.g. Charon, Haumea, Quaoar, Orcus). The ice on smaller TNOs appears to be in amorphous form, although higher signal-to-noise data may reveal otherwise. Cometary activity has been discovered on four Centaurs (2060 Chiron, 166P/NEAT, 167P/CINEOS, and 60558 Echeclus). Temporal or spatial variations in the water ice signature has been detected on these bodies as well as other Centaurs that do not exhibit cometary activity. No trend has been discovered on the presence or properties of water on the surfaces of Centaurs and TNOs as a function of heliocentric distance.

Water discovered in unexpected locations by unexpected means forces us to reconsider the prevalence of water on airless bodies in the inner solar system. An investigation similar to that for the Moon will likely be performed for Vesta's and Ceres' surfaces when the Dawn mission reaches them in 2011 and 2015, respectively. Water could potentially be significantly more pervasive throughout the inner Solar System than has ever been predicted.

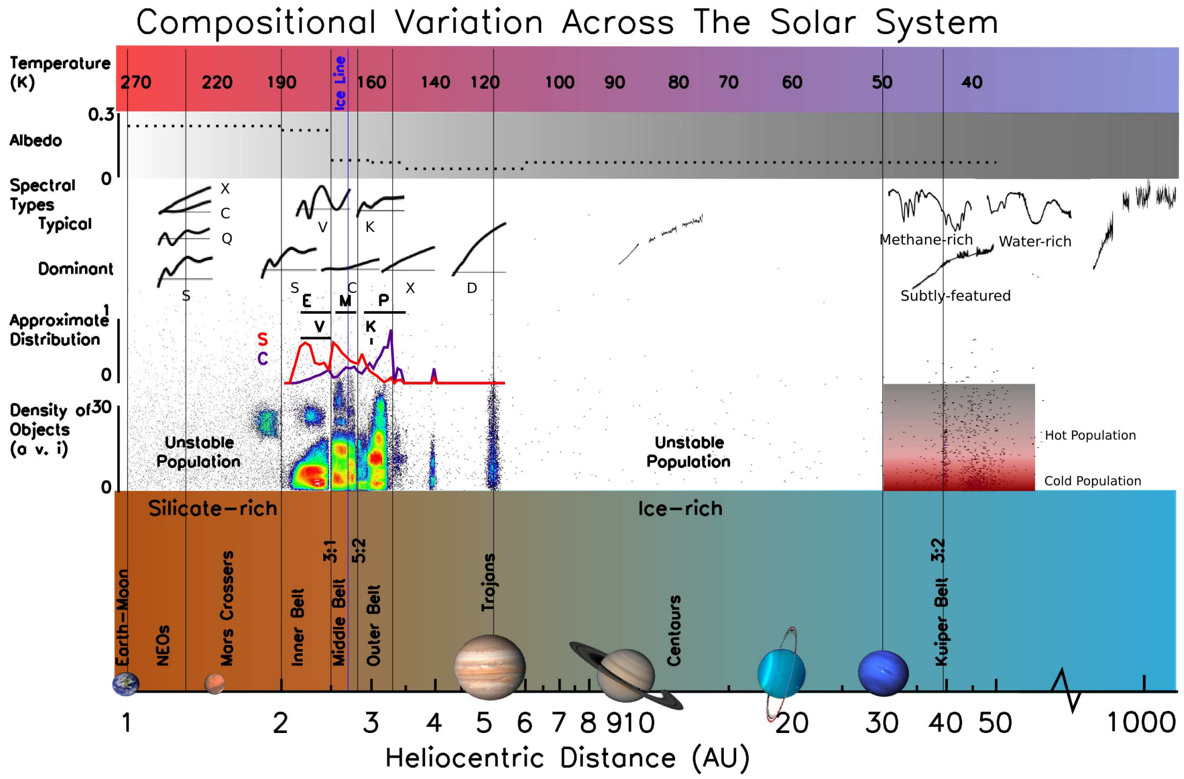

Figure 8.10: This cartoon summarizes and simplifies the distribution of material across the Solar System. The planets are pictured at the bottom and the location of different small body populations are labeled. The bottom panel shows the gradient from the predominantly "silicate-rich" material (brown) toward the predominantly "ice-rich" material (blue). The ice line is labeled at 2.7 AU, which is believed to be the approximate location past which water ice is stable, although this is a rough location and is debatable (Kennedy and Kenyon, 2008). The next panel shows the density of small bodies as a function of heliocentric distance plotted as semi-major axis versus inclination with color showing the density of bodies (red indicates highest density). In the classical Kuiper Belt region, the approximate hot and cold populations are indicated (cold population has $i < 5\,^{\circ}$). The approximate distribution of taxonomic type is displayed for the inner Solar System in the next panel. The lines mark the distribution of certain taxonomic types according to their frequency among SDSS colors, we show the frequency of S and C-types, and the generally location of a few other types. The general locations of less prominent spectral types are also marked. Above that is a model spectrum of the dominant spectral type per region and then the typical spectral types per region which are present, but not the most frequent. The gray bar shows the average albedo. In the inner Solar System the albedo marked is the average albedo for the dominant spectral type from the sample from DeMeo et al. (2009a). The Trojan albedo is from Fernández et al. (2003), and the Centaur and TNO albedos are averages from the data presented in Stansberry et al. (2008), however, only objects NOT dominated by water and other volatiles were included (Orcus, Quaoar, dwarf planets, etc. were excluded). The top panel displays the approximate effective temperature based on a black body calculation as a function of distance from the Sun with an assumed albedo of 0.1.

Chapter 9

Comparison of systems around solar-like stars

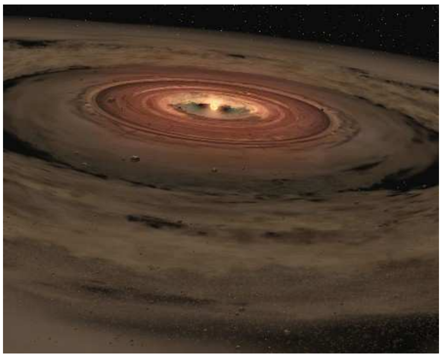

Circumstellar disks are rings of matter composed of dust, gas, and for older systems, minor bodies that orbit around other stars. By studying their structure and composition, particularly as a function of age and distance to the star, researchers have sought to find analogues of our own Solar System that could reveal more information about its general structure, its past, and its future. Finding Solar System analogues is also an important step in the search for Earth-like planets. Presented here are three stars with circumstellar disks that share important characteristics of our Solar System, an overview of the current knowledge of debris disk evolution, and an example of the composition of the dust in disks.

Contents

9.1 Evolution of Debris Disks

Our understanding of the evolution of debris disks comes from infrared photometry of hundreds of disks of different ages as well as from dynamical models. Disks are discovered around stars by an excess thermal emission that cannot be accounted for by the star that is due to the surrounding dust. The first thermal excess was discovered around Vega (Aumann et al., 1984). It appears that most, if not all, stars originally have protoplanetary disks surrounding them which form from the collapsed nebula. Over time this dust should be cleared away from stellar winds. Debris disks that are older than their expected life time of 10^7 years must be replenished. Planetesimal collisions are thought to be the primary source of dust in these systems, just as in our Solar System. 15% of all nearby stars have debris disks (Backman and Paresce, 1993). Many of these older disks are considered comparable to the Kuiper Belt in our Solar System, although our current technology only permits the discovery of belts much more massive than our own (Wyatt, 2008).

Protoplanetary disks are dominated by gas, and by mass about 1% sub-micron dust particles. Around solar-like stars they do no vary with age while the protoplanetary disk exists except for mass loss at distances less than 1 AU, presumably because material is being accreted by the star. By about 6 My, the frequency of protoplanetary disks around stars drops to zero, and the time scale is shorter for more massive stars. Much is yet to be understood about the transition from protoplanetary to evolved disk as well as the timescales and mechanisms for forming larger planetesimals up to kilometers in size. In the older disks, destructive collisional evolution is the primary source of replenishment. There are several evolutional models that have been suggested for debris disk evolution. These include (reviewed in Wyatt, 2008) steady state collisions, stochastic collisions, delayed stirring, planetary shake-down (the effects of planet migration toward steady states on the planetesimal population), comet sublimation, and external processes (such as stellar encounters). (The previous paragraph is summarized from Wyatt, 2008, and references therein).

For younger A stars the frequency and intensity of the fraction excess is greater than for older stars. For all ages, one third of stars exhibit excess at 24 and/or 70 μm. For solar-like (FGK) stars the frequency of 24 μm excess is 20 to 40% for young stars and declines to a few percent after 100 My. The large number of young disks with 24 μm emission suggest that planetesimal growth close to sun-like stars is common and one third of them could have belts at distances less than 30 AU. Excess at 70 μm can persist around sun-like stars for up to 10 Gy. (The previous information is summarized from Wyatt, 2008, and references therein). Isella et al. (2009) find that disk surface densities seem correlated with the stellar ages, and that the disk radius increases from 20 AU to 100 AU over about 5 Myr. They note, however, that this is an overall trend and does not necessarily apply to individual systems. It is also not known if all circumstellar disks develop into planetary systems. Our Solar System is expected to have a tenuous debris disk, seen as the zodiacal cloud, extending past the Kuiper Belt.

In an analysis of sun-like (FGK) stars, Greaves et al. (2009) find that the 70 μm dust excess forms a smooth distribution suggesting a single population of small bodies, such as the Kuiper Belt. Systems with gas giants, such as our own appear to make up only a few percent of sun-like stars suggesting that the configuration of the Solar System is relatively rare.

Studying debris disks gives us context for our own Solar System. They provide information on the structure and gradients across the system, as well as give a general overall view that could tell us if they are parallel to our system or even if there are components to other systems that have not yet been discovered in ours. Here I describe three of the most well-known debris disk systems, Formalhaut, Epsilon Eridani, and Beta Pictoris, and specify how they compare to the Solar System.

9.2 Formalhaut

Formalhaut is a young (100-200 Myr), bright (m_v=1.2) A3V star 7.7 parsecs (25 light-years) from Earth. It has a dust ring 25 AU wide, with an inner edge at 133 AU; the belt's geometric center is 15 AU from Formalhaut (Kalas, 2005). The center displacement and sharp inner edge of the belt suggested the presence of a planet in the system which was discovered by Kalas et al. (2008). This exoplanet, named Formalhaut b and the first ever to be detected in optical images, has a semi-major axis of ~115 AU and at most a few Jupiter masses (Kalas et al., 2008). Figure 9.1 is an image of the disk and the planets. The disk is approximately the same width as our Kuiper Belt, although it is located farther from the star.

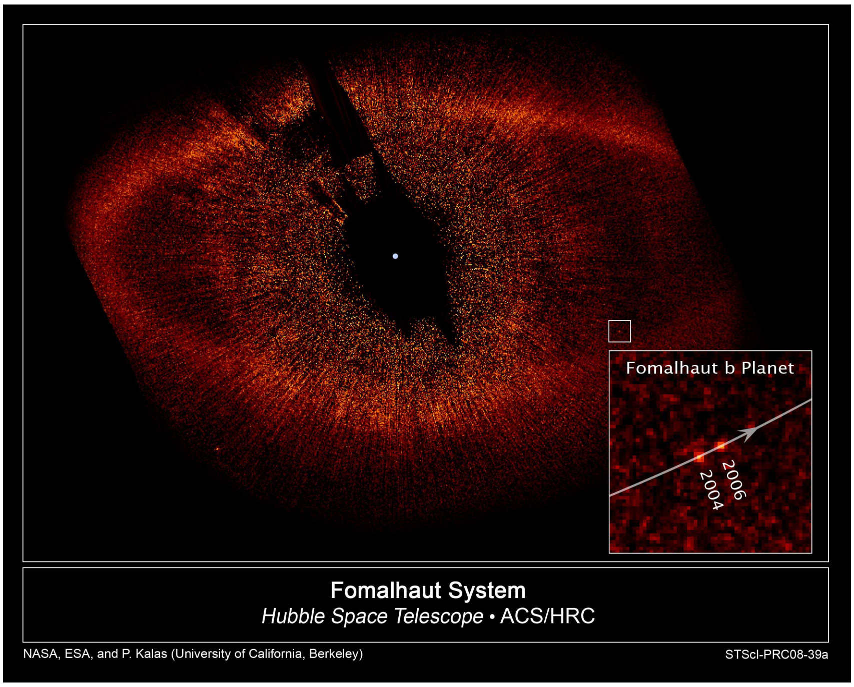

Figure 9.1: A visible wavelength image with the Hubble Space Telescope of the Formalhaut disk. The large Kuiper Belt-like ring 25 AU wide with an inner edge of 133 AU is clearly seen. A planet as discovered at the inner edge of the ring, called Formalhaut b. (Image from Kalas et al., 2008)

9.3 Epsilon Eridani

Epsilon Eridani appears to be the closest analogue to our Solar System yet discovered. It is a particularly interesting target because its proximity allows higher resolution imaging and thus more detail than was previously possible. It is older than many other resolved disks (such as Formalhaut and Beta Pictoris), and has a disk that lies at a similar distance from the star as our Kuiper Belt to the Sun as well as asteroidal belts closer to the star. Figure 9.2 compares an image of Epsilon Eridani at 850 μm to a simulation of what the Solar System would look like at the same distance at the same resolution and a dynamical model of our Solar System.

Epsilon Eridani is a K2V star of 0.8 Solar masses with an age of 0.5-1.0 Gyr, only 3.2 parsecs from Earth. It is a complex system with three known dust rings. The outer ring has a peak emission between 35-75 AU with a mass between 0.01 and 0.4 Earth masses and is considered to be a young analog to the Kuiper Belt (Greaves et al., 1998). The dust opacity index from submillimeter data suggests the ring is comprised of large grains (Pollack et al., 1994; Greaves et al., 1998) at around 30K (Backman and Paresce, 1993). Inside the distance of Neptune's orbit the dust has been cleared suggesting that planetesimals have formed in this region (Greaves et al., 1998). Backman et al. (2009) detect two warm belts in the inner part of the system, one at 20 AU and a second, narrow one, at 3 AU with small ($\sim$8, and $\sim$3 μm, respectively) grain sizes. The planet Epsilon Eridani b was discovered by Hatzes et al. (2000) in the inner exosystem. It has a highly inclined and eccentric orbit (i=30°, e=0.7, a= 3.3 AU) with a period of 6.85 Earth years (Benedict et al., 2006). Two other planets are expected to shape the middle and outer belts (see Figure 9.3 for a diagram and comparison with the Solar System).

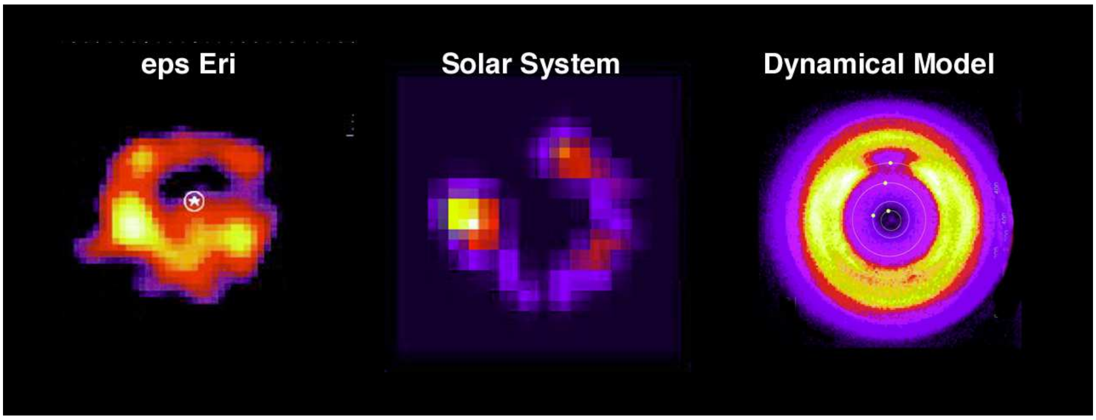

Figure 9.2: Image of Epsilon Eridani debris disk (left) at 850 μm from Greaves et al. (1998) compared to a simulated image (middle) of the Solar System under the same conditions (Source: The Circumstellar Disk Learning Site) and a dynamical model (right) of the Solar System from (Liou and Zook, 1999).

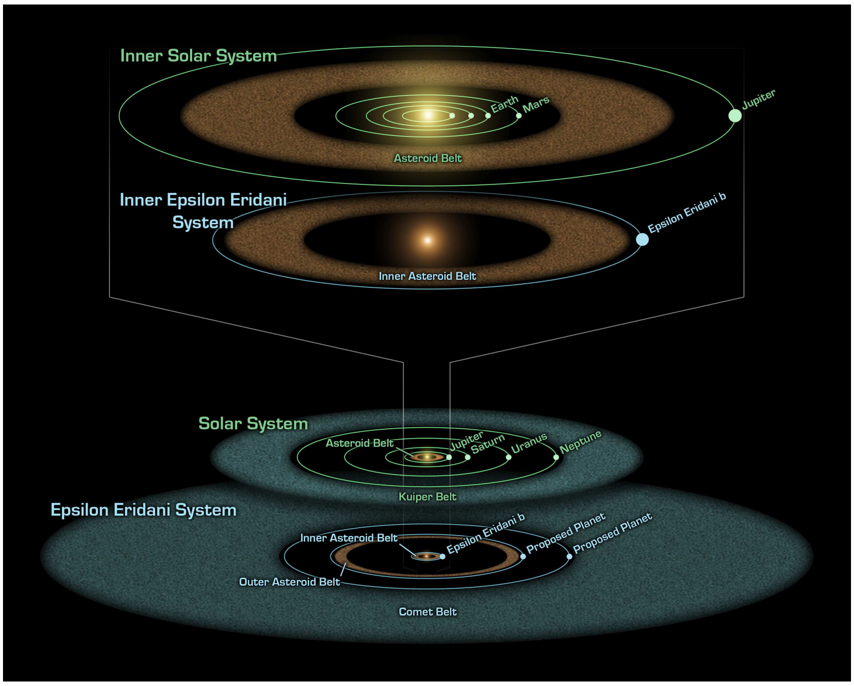

Figure 9.3: An artists diagram of the Epsilon Eridani system compared to our own Solar System. The sizes of the two systems are comparable, although the structure is different. Epsilon Eridani has two inner belts. (Source: NASA)

9.4 Beta Pictoris

Beta Pictoris is the first (Smith and Terrile, 1984) and best studied main-sequence star with a second-generation (not primordial and continuously replenished) circumstellar disk; hundreds of papers have been written on this system alone. It is consistent with a young Solar System ($\lesssim$ 100 Myr). The star is type A5V and is 19.4 parsecs away. The disk is comprised of grains larger than one micron and at a temperature of 100K (Artymowicz, 1997).

The Beta Pictoris system is much larger than our own Solar System. The dust extends to 1300 AU with dust depletion inside 100 AU, although the disk is detected as close as 15 AU from the star (Heap et al., 2000). The disk is seen nearly edge on and asymmetries (Kalas and Jewitt, 1995) along the plane and a warp in the inner disk (Burrows et al., 1995) are detected. A coronagraphic image of the disk is shown in Fig. 9.4. Recently, a close-orbiting giant planet was discovered at 8 AU (Lagrange et al., 2009). Both imaging and spectroscopy (through peaks in the distribution of amorphous silicate grains) have suggested that there are planetesimal belts at approximately 6, 15, 30, 50, and 80 AU (Wahhaj et al., 2003; Okamoto et al., 2004).

Spectral observations of the disk have repeatedly found time-varying, redshifted absorption bands that are attributed to active kilometer-size comets near the star (several hundred per year Lagrange-Henri et al., 1992), termed Falling Evaporating Bodies (FEBs), star-grazers, and infalling comets (Vidal-Madjar et al., 1994). While the amount of material seen appears consistent with what would be expected for our own Solar System at that age, the mechanism for an infall of this magnitude is not entirely understood. A few scenarios that have been suggested include the Kozai mechanism, secular resonances, and mean motion resonances with a potential massive planet in the disk (Bailey et al., 1992; Levison et al., 1994; Beust and Morbidelli, 1996, 2000).

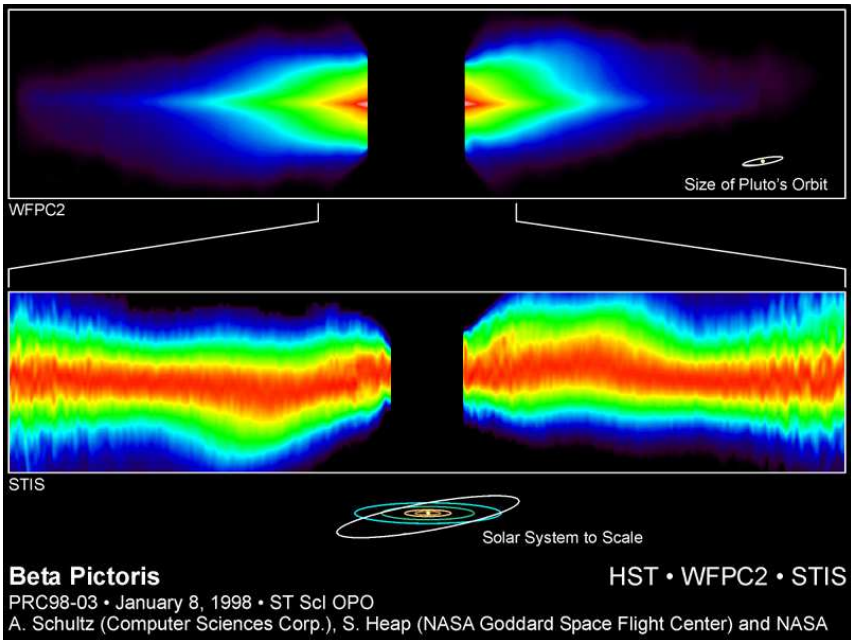

Figure 9.4: A coronagraphic image of the Beta Pictoris disk from Heap et al. (2000). The disk, extending as far as 1300 AU, is much larger than our own Solar System. Asymmetries and a warp are evident due to our edge-on view of the disk.

9.5 Composition of Dust Excess Emission

The interstellar medium contains primarily amorphous rather than crystalline silicate grains. In the Solar System, however, the abundance of crystalline silicates is significant. Observations by van Boekel et al. (2004) of the composition of protoplanetary disks within 2 AU of the host star reveal that the dust is highly crystallized. They also find that the inner regions of the disk are dominated by olivine, while the outer regions had equal amounts of pyroxene and olivine. This work suggests that crystallization of silicates occurs before the formation of large bodies and could provide clues to the original composition within our own Solar System.

Spectra of 152 nearby solar-like stars were observed spectrally with Spitzer in the infrared by (Lawler et al., 2009). All excess emissions were found to be featureless except for two stars (HD 40136 and HD

10647). Compositional models of these two stars suggest the presence of crystalline olivine and pyroxene and some water ice.

Beichman et al. (2005) measured the excess emission spectrum of HD 69830 and detected strong crystalline silicate features. Because the excess exists between 8 and 35 μm but not at 70 μm they conclude that the disk is warm (400K) and close to the star (<1 AU); HD 69830 is unique among main-sequence stars in this respect. Beichman et al. (2005) note the similarity of the spectrum to emission from comet Hale-Bop measured by Crovisier et al. (1996) (see Fig. 9.5). Through spectral modeling of the same data, Lisse et al. (2007) determine that the composition of the excess emission is likely analogous to D- and P-type asteroids.

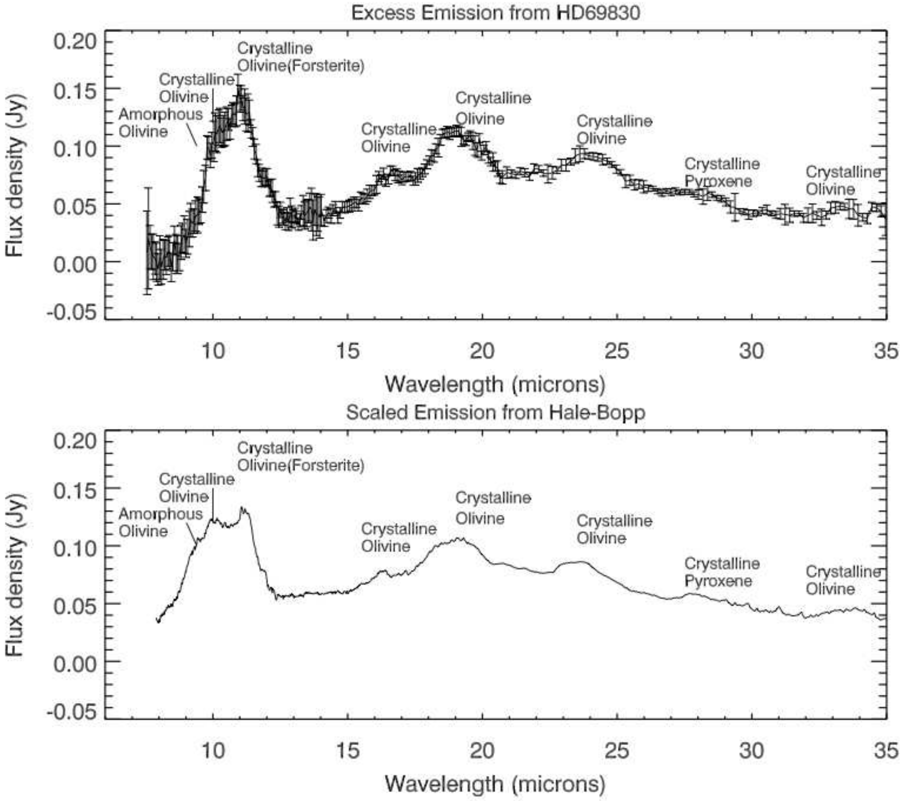

Figure 9.5: This image, from Beichman et al. (2005), compares an excess emission spectrum from HD 69830 to comet Hale-Bopp (Crovisier et al., 1996) normalized to 400K. There is a striking resemblance between the two signatures.

Lisse et al. (2008) observe the excess emission spectrum of HD 113766. Using a model originally intended for the Temple 1 Deep Impact encounter, they find the composition to be primarily Mg-rich olivine, crystalline pyroxenes, amorphous silicates, Fe-rich sulfides, amorphous carbon, and water ice. They suggest that apart from the water ice, the composition is analogous to S-type asteroids in our Solar System.

Chapter 10

Conclusions and Perspectives

This thesis has involved remote observations on the IRTF in Hawaii, a few trips to Chile for observations and a few months of research at ESO in Santiago, and a handful of international conferences: DPS 2007-2009, ACM in 2008, and Marco Polo in 2009, and two week winter school (Physics and Astrophysics of Planetary Systems) at Les Houches in 2008. Throughout this thesis, my research focused on the study of the surface properties of small bodies using spectroscopy and photometry. A summary of the work follows.

I take hundreds of individual spectra and organize them in a fashion that provides clarity on compositions of small inner Solar System bodies and provides the first look at the efficiency and effectiveness of interpreting composition for all known spectral types based on near-infrared data. From the creation of this taxonomy we learn that with only visible wavelength data there is uncertainty in shape of the 1-μm band. While the indication of an absorption past $\sim$0.75 μm corresponded with the existence of a 1-μm band, the behavior in the visible does not always indicate the depth and width of the band in the near-infrared. The near-infrared wavelength ranges are excellent for interpreting data containing diagnostic 1- and 2-μm bands, however, the more subtly featured C- and X-complexes appear to be largely degenerate in this wavelength regime.

I analyze the photometric colors of 23 TNOs and Centaurs, nine of which have never been previously observed, and assign them taxonomic classifications. Three objects that had been previously observed and classified, and changed classes most likely due to surface variation: 26375 (1999 DE9), 28978 (Ixion), and 32532 (Thereus). Two objects, 47932 (2000 GN171) and 54598 (Bienor) had absolute magnitude values that were significantly different from previously published results, attributed to extreme lightcurve amplitudes.

I interpret the surface composition of three outer Solar System small bodies, Jupiter-coupled object (52872) Okyrhoe, and TNOs (90482) Orcus and (73480) 2002 PN$_{34}$, by modeling spectroscopic measurements in the visible and near-infrared wavelength ranges. The spectra reveal varying amounts of H_2O ice among these bodies. I discuss differences between this data and previous observations that could suggest surface heterogeneity. For Orcus I provide rough constraints for the presence of materials more volatile than water and the ratio of crystalline to amorphous ice on the surface.

I present a search for solid ethane, C_2H_6, on the surfaces of Pluto and Triton, based on near-infrared spectral observations. Each surface is modeled using a radiative transfer model based on Hapke theory (Hapke, 1993) with three basic models: without ethane, with pure ethane, and with ethane diluted in nitrogen. While the presence of less than a few percent of ethane cannot be excluded on both bodies, there is no strong detection on either.

Finally, I review the current understanding of the compositional distribution of material in our Solar System, particularly focusing on the presence of water in all its phases which is especially important for our understanding of our own planet, Earth, and the life on it. I briefly compare the general structure of our Solar System to other imaged debris disks to put into perspective the detailed, though narrow, view of our own Solar System with the broad, low resolution view of others.

I have been involved in many other research projects throughout this thesis. There are two long term programs that have contributed significantly to our understanding of small bodies: SMASS and the second

ESO Large Program. In collaboration with researchers at MIT, I participate in the Small Main-Belt Asteroid Spectroscopic Survey (SMASS, smass.mit.edu). In visible wavlengths, over 1,000 spectra were published (Bus and Binzel, 2002b) and are publicly available on the website. The program was extended to survey near-Earth objects under the "MIT-UH-IRTF Joint Campaign for NEO Reconnaissance" which aims to publicly release near-infrared spectral data shortly after observation (e.g., Binzel et al., 2006b).

There have been many scientific results from this program. We constrained the quantity of active and dormant comets to 8±5% of the NEO population based on spectral, physical, and dynamical parameters (DeMeo and Binzel, 2008). We found that the most common near-Earth asteroids do not match the composition of the most common meteorite fall (Vernazza et al., 2008), suggesting that processes dependent on size and heliocentric distance such as the Yarkovsky effect may be responsible for our apparent observational mismatch. Members of the group have linked meteorites to their probable source regions, finding that while the ν_6 resonance is the dominant source for H, L, LL and HED chondrites, the 3:1 resonance is also a significant source of H chondrites (Thomas and Binzel, 2010). We categorized the infamous PHA 99942 Apophis (Binzel et al., 2009) and assess the potential amount of energy it would release in the case of an impact. In the article by Binzel et al. (2010), we proposed a solution to the "ordinary chondrite problem." All asteroids with young surfaces that match the most common meteorite (ordinary chondrites) all have a high probability of a recent close encounter with Earth, revealing that the close approach (∼16 Earth radii) freshens their surface.

I have been fortunate, as well, to be a part of a team with ample access to some of the largest telescopes in the world. This second Large Program (PI M. A. Barucci) is dedicated to investigating the surface properties of Centaurs and Transneptunian objects. The observations were carried out between 2006 and 2008 using the European Southern Observatory (ESO) Very Large Telescope (VLT). Observational methods were primarily spectroscopy and photometry. 45 objects were observed within this program, which constitutes a huge percentage of the total spectroscopic sample of TNOs available today.

An analysis of the final sample of photometric colors of 45 objects was performed by Perna et al. (2010). In this work we identified possible surface heterogeneity, confirmed the bimodality of the centaur population, and confirmed that IR class objects are confined to the classical and resonant populations, the result of Fulchignoni et al. (2008). Visible spectra for 43 TNOs and Centaurs were measured in Alvarez-Candal et al. (2008) and Fornasier et al. (2009), and 22 of these had no previously published spectra. They find most spectra to be featureless, although a few have a broad, shallow feature centered at 0.65 μm similar to that due to aqueously altered minerals on asteroids. 21 near-infrared spectra were presented in Guilbert et al. (2009a). Of this sample, 4 are featureless, 6 show clear signatures of H_2O ice, 7 show more uncertain signatures of H_2O ice, 1 (Eris) has methane, and the signal-to-noise ratio of the last three is too low to analyze. Protopapa et al. (2009), Alvarez-Candal et al. (2010) and Merlin et al. (2010) model visible and near-infrared TNO spectra and find most surfaces are well fit with varying amounts of H_2O ice, tholins, and a dark material. Heterogeneity is seen on Centaur 10199 Chariklo that was previously ice-rich, but is now featureless (Guilbert et al., 2009b). The larger TNOs (90482) Orcus, (50000) Quaoar, and (136199) Eris were thoroughly modeled to characterize their surfaces for the presence of NH_3, CH_4, and N_2 (Barucci et al., 2008b; Dalle Ore et al., 2009; Merlin et al., 2009).

Part of my research during this thesis has also included a spectroscopic study of the planet Mercury. We scan 70% of Mercury's surface in the near-infrared wavelength range and find the spectra to be very similar. We also confirm the presence of a shallow 1-μm feature likely due to calcium-rich clinopyroxene (Vernazza et al., 2010). I also contributed to the search for a parent body for 2008 TC_3 (Jenniskens et al., 2010), Almahata Sitta, the asteroid that was observed days before it impacted the Earth and was subsequently recovered in the desert of Sudan. We find that the Polana family is the best dynamical match for the meteorite, although spectral measurements of the primary are not a direct match. Observations of other family members will reveal if 2008 TC_3 is compositionally consistent. Within the SMASS spectral database, I identified 6 NEOs with unique spectral characteristics that are similar to that of Almahata Sitta.

There are many ongoing and upcoming projects that I will be undertaking, both short and long term projects. One project underway includes spectral measurements of 379 Huenna's binary. The binary is on a highly elliptic orbit suggesting it is a captured fragment or a captured body of different composition. I will also soon be performing an analysis of the surface of Charon. Charon is known to have H_2O and NH_3 on its surface. With high resolution spectral measurements in the H and K bands, I will search for hints of other surface components. In collaboration with planetary scientists within LESIA, we will attempt to constrain the temperature and mixing of CO ice on Triton's surface and search for CO in Pluto's atmosphere. In collaboration with a group at MIT, we will characterize the NEO population based on near-infrared spectra of hundreds of NEOs, and continue surveys of the population. Pierre Vernazza, Benoit Carry, and I have submitted an application to NASA to work on Dawn data following its arrival at Vesta in 2011.

Besides the constant technological advancements that improve ground-based observations, there are a few space missions that will be delivering results soon. Rosetta will fly by asteroid 21 Lutetia on July 10, 2010 and will land on comet 67P/Churyumov-Gerasimenko in 2014 to characterize the coma and nucleus as it reaches perihelion. Dawn will arrive at Vesta in July 2011 and Ceres in February 2015. It will make detailed topographic and spectral maps of the surfaces. New Horizons will encounter the Pluto system in July 2015 and will pass by one or more TNOs in the years to follow. This mission will give us a first close look at "the last planet" and will provide ample information about dwarf planets and transneptunian objects.

The time to synthesize our knowledge and stitch together the story of the Solar System is here. Much of our understanding of small bodies until recently has come from studying individual populations, patches, in isolation. We are now learning how interconnected all these populations are. NEOs are a jumble of bodies from a wide span of source regions, Centaurs likely originated in the Kuiper Belt, and long-period comets may be our only peek at the Oort Cloud extending far beyond our current observational capabilities. Understanding the original locations of all these populations and comparing them to the current distribution teaches us the relation all the small bodies and the joint role they had with the planets in forming and shaping the Solar System we see today. This thesis is a small attempt in the greater scheme to unify what were individual units and pockets of material into the complex whole that is our Solar System.

Acknowledgments

This thesis has been quite an adventure. I've had ample opportunity to travel both for work and pleasure and have learned two languages and about two cultures, and have met and worked with many amazing and inspiring people throughout the process. The path as a PhD was not easy, and here I'd like to give the huge thanks I owe to the many people that have helped me get where I am today.

First of all, thanks to my advisors Rick and Antonella. Rick, you have helped me transform from the lost little undergraduate to the "grown up" researcher that I am today. I appreciate all the patience and support you've given me over the years. Without your help I would not have had so many of the opportunities throughout the past years, including studying here in Paris.

Antonella, when I arrived in Paris for a stage in 2005, I never would have expected that I would have the opportunity to spend 3 years studying here with you. I can't thank you enough for all the help and guidance you have given me, and especially for the important role you played in my first year here, which was a challenging transition for me. You have always given me great advice and have been very attentive to any questions, problems, or needs throughout my time here in Paris whether it be work or life related.

I also have many thanks to give to two people who have also acted as thesis advisors for me: Catherine de Bergh and Christophe Dumas. Thank you Catherine for all the help and support throughout the Pluto and Triton project. I started with little knowlege, and struggled to explain myself scientifically in French, but with your dedication and attention to detail I made great progress. Thank you for all the time you spent helping with the analysis and editing draft after draft.

Thank you Christophe for giving me the opportunity for me to travel to Chile for research. You provided me with an exciting project, great data, and pushed me to learn tools that will serve me well for my research well into the future. Chile was an incredible experience for me both in and outside of work. I had close contact with other students and post-docs working in a wide variety of topics. I had an amazing time living at "la casa", learning spanish and Chilean culture, having fun practically every night with Ben, both Pedros, Bene, Olivia and Thomas.

Thank you to my thesis committee, to Bruno Sicardy the jury president, Hermann Boehnhardt and Alberto Cellino the reviewers, Daniel Hestroffer, Beth Clark, and Humberto Campins the examiners, and of course, my two thesis advisors for all the time you've spent reading and evaluating my work.

I thank the Fulbright Program for funding the first two years of my PhD. Thanks Amy Tondu for your help getting me settled here in Paris and Arnaud Roujou de Boubée. And thanks Morby for recommending my Fulbright acceptance. I thank the Eiffel Grant and Egide for funding my third year, and Christiane Adam for all your help preparing the application.

To the students and researchers of batiment 17, Alvaro, Sonia, Audrey, Fred, Davide, Cédric, Vladimir, Sandrine, Erwan, Aurélie, Marcello, Irina, Dominique, Alain, Emmanuel, and Thierry, its been wonderful working with you all. Thank you to Alvaro, Sonia, Audrey, and Fred for always taking time to answer my questions particularly in my first year. Pierre, you have always been a dear colleague, danke shön. Silvia, thanks for all the help you've given me for modeling, your openness is so appreciated, and I had a great time visiting you in Lindau. Mirel, thank you for always being so kind and supportive, for always congratulating me on my work, for the fun times observing in CODAM, and for the interesting opportunities such as talking to the reporter from the Nouvel Observateur.

Thanks to all the researchers I have been fortunate to work and collaborate with, for all the important discussions and insight they provided, including Andy Rivkin, Bobby Bus, Steve Slivan, Dale Cruikshank, Tom Geballe, Beth Clark, Maureen Bell, Peter Jenniskens, Franck Marchis, and Pascal Descamps.

Thanks to the past and present 4th floor MIT crew, Jim Elliot, Jack Wisdom, Andy Rivkin, Cristina Thomas, Elisabeth Adams, Jenny Meyer, Alessondra Springman, Shaye Storm, Mike Person, Susan Benecchi, and Amanda Gulbis. They were all there at the start of my graduate work, and always welcomed me warmly when I was back to visit.

Thank you to everyone who made my transition to living in France easier. Thanks Fred and Dimitra for the dinners. Thank you Alvaro for always inviting me out and for all the fun. Thank you Antonella and Marcello for always thinking of me and for having me over for so many of your wonderful dinner parties. Thanks to the Binzel family for making me feel like I was part of the family. It was so refreshing having you here during your sabbatical year, and it was great to feel so included.

Rosario, thank you for so many things: good times at the apartment, cooking and Italian lessons, advice ranging from all areas of life to work. You were so important to my first year in Paris and how could I have adjusted to being so far from home so easily without having you there?

Adeline, coming to the office is always more fun when you're there. You've taught me so many things about France, the culture, the language. I certainly wouldn't be able to speak half as well as I do now if it weren't for you. Thank you for all the fun trips we've been on. Most of all, thanks for being such a great friend.

Ben, from pisco and dancing in Chile to officemates in Paris, you know I can't thank you enough for everything, from being such an important friend to always being willing to help with work and computer questions. It's been wonderful having Clara here and I'm so glad I was here to watch Anaël grow in her first year. The only thing that could have made things better, is if we managed to overlap in the same country more often!

Thank you Fredo for your love and support over the past three years. The distance has not been ideal, and I am amazed at how well we've managed to cope with it. Thank you for always being there and for continually challenging me to learn and grow. Thanks to my family, Mom, Dad, and Dante for always supporting what I do, even when it involved moving so far away for so long. I'm so glad you've been able to come visit, so I could show you my life here and give you a taste of the culture I've been living in. I've missed you all very much and I look forward to being back in Boston again soon.

Appendix A

Bus-DeMeo Taxonomy

A.1 Table of Observations[a] and Designations

Obj	Name	Tholen	Bus	This Work	Date
1	Ceres	G	C	C	19-May-05
2	Pallas	B	B	B	29-Mar-01
3	Juno	S	Sk	Sq	17-Mar-03
4	Vesta	V	V	V	09-Oct-00
5	Astraea	S	S	S	20-Feb-04
7	Iris	S	S	S	20-Feb-04
8	Flora	S		Sw	16-Sep-02 [b]
10	Hygiea	C	C	C	19-Feb-04
11	Parthenope	S	Sk	Sq	13-Nov-05
13	Egeria	G	Ch	Ch	19-May-05
14	Irene	S	S	S	17-May-01
15	Eunomia	S	S	K	19-Feb-04
16	Psyche	M	X	Xk	09-Oct-00
17	Thetis	S	Sl	S	15-Aug-01
18	Melpomene	S	S	S	22-Jun-01
19	Fortuna	G	Ch	Ch	29-Jan-06
20	Massalia	S	S	S	22-Jun-01
21	Lutetia	M	Xk	Xc	22-Sep-04
22	Kalliope	M	X	X	25-Oct-06
24	Themis	C	B	C	08-Oct-05
25	Phocaea	S	S	S	30-Jan-01
26	Proserpina	S	S	S	24-Aug-01
27	Euterpe	S	S	S	22-Sep-04
28	Bellona	S	S	S	13-Jan-02
29	Amphitrite	S	S	S	29-Jan-01
30	Urania	S	Sl	S	08-Oct-00
32	Pomona	S	S	Sw	30-Jan-01
33	Polyhymnia	S	Sq	S	06-Mar-02
34	Circe	C	Ch	Ch	20-Feb-04
37	Fides	S	S	S	15-Aug-01
38	Leda	C	Cgh	Cgh	05-Jul-03
39	Laetitia	S	S	Sqw	14-Aug-01
40	Harmonia	S	S	S	16-Oct-04
41	Daphne	C	Ch	Ch	10-May-08
42	Isis	S	L	K	21-Jun-01
43	Ariadne	S	Sk	Sq	22-Nov-05
48	Doris	CG	Ch	Ch	08-Oct-05
49	Pales	CG	Ch	Ch	02-Aug-03
50	Virginia	X	Ch	Ch	05-Jul-03
51	Nemausa	CU	Ch	Cgh	15-Jun-04
52	Europa	CF	C	C	28-Jun-06
54	Alexandra	C	C	Cgh	27-Oct-02
55	Pandora	M	X	Xk	29-Jan-06
56	Melete	P	Xk	Xk	22-Sep-04
57	Mnemosyne	S	S	S	01-Jun-02
58	Concordia	C	Ch	Ch	02-Aug-03
61	Danae	S	S	S	08-Oct-00
63	Ausonia	S	Sa	Sw	30-Sep-03
64	Angelina	E	Xe	Xe	30-Jan-01
65	Cybele	P	Xc	Xk	30-Sep-03
66	Maja	C	Ch	Ch	22-Nov-05
67	Asia	S	S	S	16-Jun-04
69	Hesperia	M	X	Xk	11-May-05
70	Panopaea	C	Ch	Cgh	29-Sep-02
73	Klytia	S		S	16-Oct-03 [b,c]
76	Freia	P	X	C	05-Sep-05
77	Frigga	MU	Xe	Xe	25-Oct-06
78	Diana	C	Ch	Ch	31-Oct-05
82	Alkmene	S	Sq	S	24-Aug-01
84	Klio	G	Ch	Ch	02-Aug-03
85	Io	FC	B	C	02-Aug-03
87	Sylvia	P	X	X	04-Sep-05
90	Antiope	C	C	C	05-Sep-05
92	Undina	X	Xc	Xk	08-Oct-00
93	Minerva	CU	C	C	27-Apr-03
96	Aegle	T	T	T	28-Jan-06
97	Klotho	M	X	Xc	08-Oct-05
99	Dike	C	Xk	Xk	13-Nov-05
101	Helena	S	S	S	22-Dec-06
103	Hera	S	S	S	14-Aug-01
105	Artemis	C	Ch	Ch	02-Aug-03
106	Dione	G	Cgh	Cgh	02-Aug-03
108	Hecuba	S	Sl	Sw	06-Mar-02
110	Lydia	M	X	Xk	29-Jan-01
111	Ate	C	Ch	Ch	22-Sep-04
114	Kassandra	T	Xk	K	28-Jun-06
115	Thyra	S	S	S	06-Mar-02
119	Althaea	S	Sl	S	21-Jun-01
128	Nemesis	C	C	C	02-Aug-03
130	Elektra	G	Ch	Ch	29-Mar-01

Observations and Designations (cont.)

Obj	**Name**	**Tholen**	**Bus**	**This Work**	**Date**	**Obj**	**Name**	**Tholen**	**Bus**	**This Work**	**Date**
131	Vala	SU	Xc	K	20-Jul-06	289	Nenetta	A	A	A	04-Sep-00
132	Aethra	M	Xe	Xe	05-Sep-05	295	Theresia	S	S	Sw	28-Sep-02
133	Cyrene	SR	S	S	22-Jun-01	308	Polyxo	T	T	T	18-Apr-05
147	Protogeneia	C	C	C	02-Aug-03	322	Phaeo	X	X	D	29-Sep-02
150	Nuwa	CX	Cb	C	02-Aug-03	337	Devosa	X	X	Xk	28-Sep-02
151	Abundantia	S	Sl	Sw	13-Nov-05	345	Tercidina	C	Ch	Ch	08-Oct-05
153	Hilda	P	X	X	10-May-05	346	Hermentaria	S	S	S	31-May-02
158	Koronis	S	S	S	16-Mar-03	349	Dembowska	R	R	R	22-Jun-01
160	Una	CX	C	Xk	5-Jul-03	352	Gisela	S	Sl	Sw	22-Jun-01
170	Maria	S	S	S	22-Jun-01	354	Eleonora	S	Sl	A	15-Apr-02
175	Andromache	C	Cg	Cg	13-Nov-05	359	Georgia	CX	X	Xk	30-Jan-01
180	Garumna	S	Sq	Sr	28-Sep-02	371	Bohemia	QSV	S	S	14-Aug-01
181	Eucharis	S	Xk	Xk	30-Sep-03	378	Holmia	S	S	S	14-Apr-02
188	Menippe	S	S	S	15-Apr-02	387	Aquitania	S	L	L	27-Apr-03
191	Kolga	XC:	Cb	Cb	12-Apr-05	389	Industria	S	S	S	24-Aug-01
192	Nausikaa	S	Sl	Sw	30-Apr-06	402	Chloe	S	K	L	19-Feb-01
199	Byblis		X	D	17-Mar-03	403	Cyane	S	S	S	27-Apr-03
201	Penelope	M	X	Xk	19-Feb-04	433	Eros	S	S	Sw	17-Aug-02
205	Martha	C	Ch	Ch	02-Aug-03	434	Hungaria	E	Xe	Xe	23-Aug-01
210	Isabella	CF	Cb	Cb	13-Nov-05	444	Gyptis	C	C	C	15-Aug-01
214	Aschera	E	Xc	Cgh	24-Oct-04	446	Aeternitas	A	A	A	14-Aug-01
216	Kleopatra	M	Xe	Xe	17-Jun-02	453	Tea	S	S	Sw	15-Aug-01
221	Eos	S	K	K	08-Oct-00	456	Abnoba		S	S	17-Jun-02
226	Weringia		S	S	06-Mar-02	460	Scania		K	L	17-Jun-02
233	Asterope	T	K	Xk	29-Sep-02	485	Genua		S	S	06-Mar-02
234	Barbara	S	Ld	L	22-Dec-06	512	Taurinensis	S	S	Sqw	16-Oct-04
236	Honoria	S	L	L	01-May-06	513	Centesima	S	K	K	29-Mar-01
237	Coelestina	S	S	Sr	15-Apr-02	532	Herculina	S	S	S	21-Jun-01
243	Ida	S	S	Sw	17-Mar-03	570	Kythera	ST	T	D	20-Feb-04
244	Sita		Sa	Sw	29-Mar-01	579	Sidonia	S	K	K	20-Feb-01
246	Asporina	A	A	A	09-Mar-05	596	Scheila	PCD	T	T	01-Jun-02
250	Bettina	M	Xk	Xk	16-Oct-03	599	Luisa	S	K	L	19-Feb-01
258	Tyche	S	S	S	24-Aug-01	606	Brangane	TSD	K	L	29-Sep-02
264	Libussa	S	S	S	19-May-05	625	Xenia		Sa	Sw	20-Feb-01
266	Aline	C	Ch	Ch	05-Sep-05	631	Philippina	S	S	S	29-Sep-02
267	Tirza	DU	D	D	02-Aug-03	653	Berenike	S	K	K	17-Mar-03
269	Justitia		Ld	D	11-May-05	661	Cloelia	S	K	K	16-Mar-03
278	Paulina		S	S	31-May-02	670	Ottegebe		S	S	29-Sep-02
279	Thule	D	X	D	08-Jan-05	673	Edda	S	S	L	21-Jun-01
288	Glauke	S	S	S	29-Sep-02	675	Ludmilla	S	S	Sw	15-Apr-02

Observations and Designations (cont.)

Obj	Name	Tholen	Bus	This Work	Date	Obj	Name	Tholen	Bus	This Work	Date
679	Pax	I	K	L	19-Feb-01	1204	Renzia		S	Sw	10-Mar-05
688	Melanie		C	C	28-Sep-02	1228	Scabiosa		S	Sr	16-Mar-03
699	Hela	S	Sq	S	08-Jan-05	1300	Marcelle		Cg	Cgh	25-Oct-06
706	Hirundo		Cgh	Cgh	30-Jan-06	1329	Eliane	S	S	Sqw	17-Aug-02
716	Berkeley	S	S	S	24-Aug-01	1332	Marconia		Ld	L	10-Jun-05
719	Albert			S	23-Aug-01 [d]	1350	Rosselia	S	Sa	S	21-Jun-01
720	Bohlinia	S	Sq	Sq	09-Oct-00	1374	Isora		Sq	Sq	20-Feb-04
729	Watsonia	STGD	L	L	14-Aug-01	1433	Geramtina		S	S	17-Aug-02
739	Mandeville	X	X	Xc	28-Sep-02	1459	Magnya			Vw	20-Feb-01 [b]
742	Edisona	S	K	K	16-Mar-03	1471	Tornio		T	D	08-Oct-05
773	Irmintraud	D	T	T	22-Sep-04	1494	Savo		Sa	Sqw	25-Oct-06
776	Berbericia	C	Cgh	Cgh	12-Apr-05	1508	Kemi	BCF	C	B	19-Feb-04
782	Montefiore	S	Sl	Sw	22-Jun-01	1542	Schalen		D	D	18-Apr-05
785	Zwetana	M	Cb	Cb	19-May-05	1565	Lemaitre		Sq	S	03-Mar-05
789	Lena		X	Xk	17-Aug-02	1620	Geographos	S	S	S	29-Jan-01
793	Arizona	DU:	S	S	28-Sep-02	1640	Nemo		S	S	08-Mar-05
808	Merxia		Sq	Sr	14-Aug-01	1642	Hill		S	S	15-Aug-01
824	Anastasia	S	L	L	14-Aug-01	1658	Innes	AS		Sw	30-Jan-01 [c]
832	Karin			S	05-Jul-03 [e]	1659	Punkaharju		S	S	15-Mar-02
847	Agnia	S	S	S	19-Feb-01	1660	Wood		S	S	08-Mar-05
863	Benkoela	A	A	A	14-Jan-02	1662	Hoffmann		Sr	Sr	17-Mar-03
908	Buda		L	D	20-Jul-06	1667	Pels		Sa	Sw	28-Oct-02
913	Otila		Sa	Sw	15-Aug-01	1685	Toro	S	S	Sq	08-May-02 [h]
925	Alphonsina	S	S	S	28-Sep-02	1751	Herget		S	S	22-Jun-01
929	Algunde		S	S	21-Jun-01	1807	Slovakia		S	Sqw	15-Sep-04
944	Hidalgo	D		D	22-Sep-04 [e]	1839	Ragazza		S	S	29-Mar-01
984	Gretia		Sr	Sa	29-Sep-02	1848	Delvaux		S	S	15-Aug-01
985	Rosina		S	S	11-May-05	1858	Lobachevskij		L	S	14-Apr-02
1011	Laodamia	S	Sr	Sw	12-Jan-02	1862	Apollo	Q	Q	Q	13-Nov-05
1020	Arcadia		S	Sr	17-Mar-03	1864	Daedalus	SQ	Sr	Sq	29-Mar-01
1036	Ganymed	S	S	S	09-Mar-05	1866	Sisyphus		S	Sw	21-Nov-06
1065	Amundsenia		S	S	08-Mar-05	1903	Adzhimushkaj		K	K	17-Mar-03
1094	Siberia		Xk	Xk	16-Mar-03	1904	Massevitch		R	V	04-Sep-00
1126	Otero		A	Sw	20-Feb-01	1916	Boreas	S		Sw	14-Aug-01 [d]
1131	Porzia		S	S	11-May-05	1929	Kollaa		V	V	19-Feb-01
1139	Atami	S	S	Sw	05-Sep-05	1943	Anteros	S		Sw	12-Jan-02 [g,h]
1143	Odysseus	D		D	10-Jun-05 [b]	1980	Tezcatlipoca	SU	Sl	Sw	25-Oct-06
1147	Stavropolis		S	Sw	15-Aug-01	2035	Stearns	E	Xe	Xe	28-Oct-02
1148	Rarahu	S	K	K	29-Mar-01	2042	Sitarski		Sq	Sr	23-Aug-01
1198	Atlantis			Sw	28-Oct-02 [b]	2045	Peking		V	V	14-Jan-02

Observations and Designations (cont.)

Obj	**Name**	**Tholen**	**Bus**	**This Work**	**Date**	**Obj**	**Name**	**Tholen**	**Bus**	**This Work**	**Date**
2063	Bacchus		Sq	Sq	19-May-05	3248	Farinella		D	D	18-Apr-05
2064	Thomsen		S	Sqw	29-Jun-06	3255	Tholen		S	S	16-Sep-02
2074	Shoemaker			Sw	30-Sep-03 [b]	3317	Paris		T	D	01-May-06
2085	Henan		L	L	14-Apr-02	3363	Bowen		Sq	Sr	15-Apr-02
2099	Opik	S	Ch	Ch	08-Oct-05	3395	Jitka		Sr	S	19-Feb-01
2107	Ilmari		S	Sw	29-Jan-06	3402	Wisdom			S	30-Sep-03 [e]
2157	Ashbrook		S	S	16-Mar-03	3430	Bradfield		Sq	S	17-Jun-02
2246	Bowell	D	D	D	17-Apr-05	3491	Fridolin		Sq	S	17-Jun-02
2335	James			S	30-Oct-05	3511	Tsvetaeva		S	Srw	15-Apr-02
2353	Alva		S	S	31-May-02	3628	Boznemcova		O	O	30-Apr-06
2354	Lavrov		L	L	17-Mar-03	3635	Kreutz		S	Srw	12-Nov-05
2378	Pannekoek		Cgh	Cgh	11-May-05	3701	Purkyne		S	S	14-Aug-01
2386	Nikonov		S	S	17-Jun-02	3734	Waland		Ld	L	24-Aug-01
2396	Kochi		Sa	S	15-Aug-01	3753	Cruithne		Q	Q	08-Oct-05
2401	Aehlita		S	S	17-Aug-02	3788	Steyaert		S	S	17-Mar-03
2442	Corbett			V	15-Sep-02 [c]	3844	Lujiaxi		L	L	27-Apr-03
2448	Sholokhov		L	L	16-Mar-03	3858	Dorchester		Sa	Srw	20-Feb-04
2501	Lohja	A	A	A	12-Jan-02	3873	Roddy		S	Sw	28-Oct-02
2504	Gaviola		Sq	Sr	27-Apr-03	3903	Kliment Ohridski		Sq	S	16-Sep-02
2521	Heidi		S	S	13-Jan-02	3908	Nyx	V		V	15-Sep-04
2566	Kirghizia		V	V	16-Sep-02	3910	Liszt		S	S	17-Aug-02
2579	Spartacus		V	V	10-Oct-00	3920	Aubignan		Sa	Sqw	16-Sep-02
2715	Mielikki		A	Sw	15-Aug-01	3949	Mach		Sq	Sq	24-Aug-01
2732	Witt		A	L	15-Aug-01	4038	Kristina			Vw	28-Oct-02 [d]
2851	Harbin		V	V	24-Aug-01	4055	Magellan	V		V	11-Apr-05 [d]
2873	Binzel		Sq	Sq	13-Jan-02	4179	Toutatis		Sk	Sq	15-Sep-04
2875	Lagerkvist		S	S	16-Mar-02	4188	Kitezh		V	V	14-Aug-01
2911	Miahelena		S	Sw	17-Mar-03	4197	1982 TA		Sq	Sq	30-Sep-03
2912	Lapalma		V	V	20-Feb-01	4352	Kyoto		S	S	17-Jun-02
2957	Tatsuo		K	K	16-Mar-03	4407	Taihaku		Sa	Sqw	24-Aug-01
2965	Surikov			Sv	10-May-05 [b]	4417	Lecar		S	Sw	24-Aug-01
2977	Chivilikhin		S	S	28-Sep-02	4451	Grieve			Svw	14-Jan-02 [d]
3028	Zangguoxi		K	K	16-Sep-02	4558	Janesick		S	Sr	15-Jun-04
3102	Krok	S		Sqw	09-Oct-00 [d]	4570	Runcorn		Sa	Sw	21-Jun-01
3103	Eger		Xe	Xe	21-Jun-01 [i]	4688	1980 WF	QU		Q	29-Jan-01 [d]
3122	Florence		S	Sqw	26-Jan-04	4713	Steel		A	Sw	14-Apr-02
3155	Lee		V	V	22-Jun-01	4737	Kiladze		L	L	17-Jun-02
3198	Wallonia		S	Sqw	10-May-05	4995	Griffin		S	S	28-Oct-02
3199	Nefertiti	S	Sq	K	03-Mar-05	5013	Suzhousanzhong		Sl	Sw	14-Jan-02
3200	Phaethon	F	B	B	10-Dec-04	5111	Jacliff		R	V	05-Sep-05

Observations and Designations (cont.)

Obj	Name	Tholen	Bus	This Work	Date
5143	Heracles		O	Q	25-Oct-06
5230	Asahina		S	S	5-Sep-05
5261	Eureka		Sr	Sa	19-May-05
5379	Abehiroshi		V	Sr	3-Jun-06
5401	Minamioda		S	Sw	16-Mar-03
5407	1992 AX		Sk	S	13-Jan-02
5587	1990 SB		Sq	Sr	28-Mar-01
5604	1992 FE			V	29-Mar-01 [f]
5641	McCleese		A	Sw	12-Apr-05
5660	1974 MA		Q	Q	22-Aug-93
5685	Sanenobufukui		S	S	29-Mar-01
5817	Robertfrazer		S	Sr	22-Sep-04
5840	Raybrown		Ld	L	24-Aug-01
6047	1991 TB1		S	S	8-Oct-05
6239	Minos			Sqw	26-Jan-04 [e]
6386	Keithnoll		S	S	3-Mar-05
6411	Tamaga			B	20-Feb-04 [e]
6455	1992 HE		S	Srw	28-Oct-02
6585	O'Keefe		Sk	S	25-Oct-06
7341	1991 VK		Sq	Q	16-Mar-02
7763	Crabeels		L	L	1-Jun-02
8334	1984 CF		S	S	17-Mar-03
8444	Popovich			S	30-Sep-03 [e]
17274	2000 LC16			D	10-Oct-00 [d]
18736	1998 NU			Sw	30-Jan-01 [d]
19127	Olegefremov			Srw	30-Sep-03 [e]
19356	1997 GH3		S	Sq	30-Jan-01
20786	2000 RG62			Sq:	1-Sep-03 [d]
20790	2000 SE45			S	29-Jan-01 [d]
22771	1999 CU3			S	16-Oct-03 [d]
24475	2000 VN2			Sw	29-Mar-01 [d]
25330	1999 KV4			Xk	27-Oct-02 [d]
35107	1991 VH		Sk	Sq	27-Dec-02
36284	2000 DM8			K	16-Mar-02 [d]
53435	1999 VM40			Srw	25-Oct-06 [g]
54690	2001 EB			S	28-Mar-01 [d]
66146	1998 TU3			Q	1-Sep-03 [e]
86450	2000 CK33			L	29-Jan-01 [d]
86819	2000 GK137			Sq	9-Oct-00 [d]
89355	2001 VS78			Sr	16-Mar-02
98943	2001 CC21			Sw	24-Oct-04 [f]
99907	1989 VA		Sq	Sr	27-Oct-02
137062	1998 WM		Sq	Sr	27-Oct-02
138258	2000 GD2			Sq	16-Oct-03 [d]
162058	1997 AE12			Q	15-Mar-02
162781	2000 XL44			S	29-Jan-01 [d]
2000PG3				D	4-Sep-00 [d]
2001TX16				X	15-Mar-02 [d]
2001XN254				S	14-Apr-02 [d]
2002AA				S	13-Jan-02 [d]
2002AV				S	13-Jan-02 [d]

[a] All visible data are from Bus (1999), Bus and Binzel (2002a) and Bus and Binzel (2002b) unless marked by a footnote. [b] Visible data: Xu (1994); Xu et al. (1995). [c] Visible data: Burbine (2000); Burbine and Binzel (2002). [d] Binzel et al. (2004c) [e] Visible data: This Work. 832, 03-Mar-05; 944, 14-June-01; 3402, 01-Sep-03; 6239 29-Dec-03; 6411, 29-Dec-03; 8444, 28-Dec-03; 19127 28-Dec-03; 66146, 3-Sep-03. All these observations were taken on telescope KPNO 4m except 944 on Magellan 6.5m. [f] Visible data: Binzel et al. (2004b). [g] Visible data: Binzel et al. (2001). [h] Near-IR data: Binzel et al. (2004a). [i] Near-IR data: Rivkin et al. (2005).

A.2 371 Asteroid Spectra from Bus-DeMeo Taxonomy

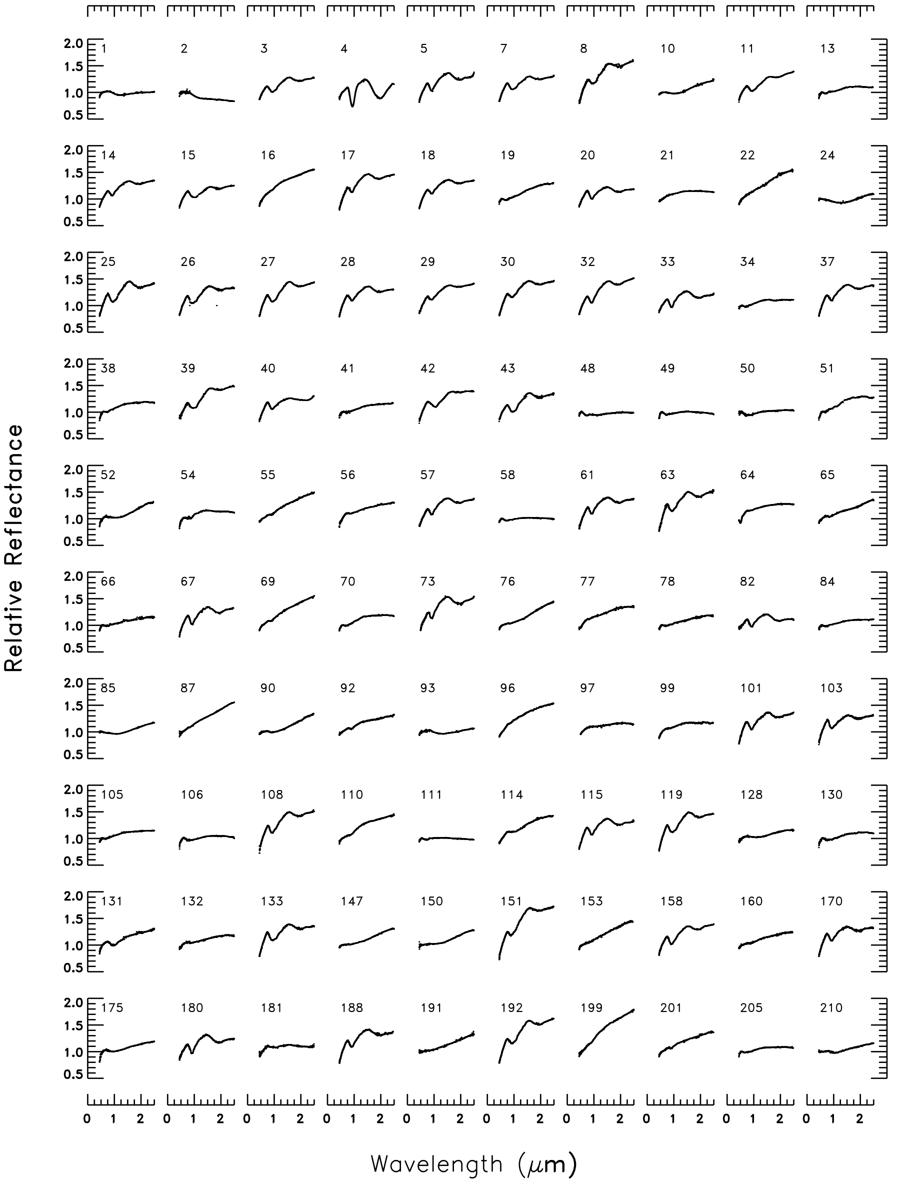

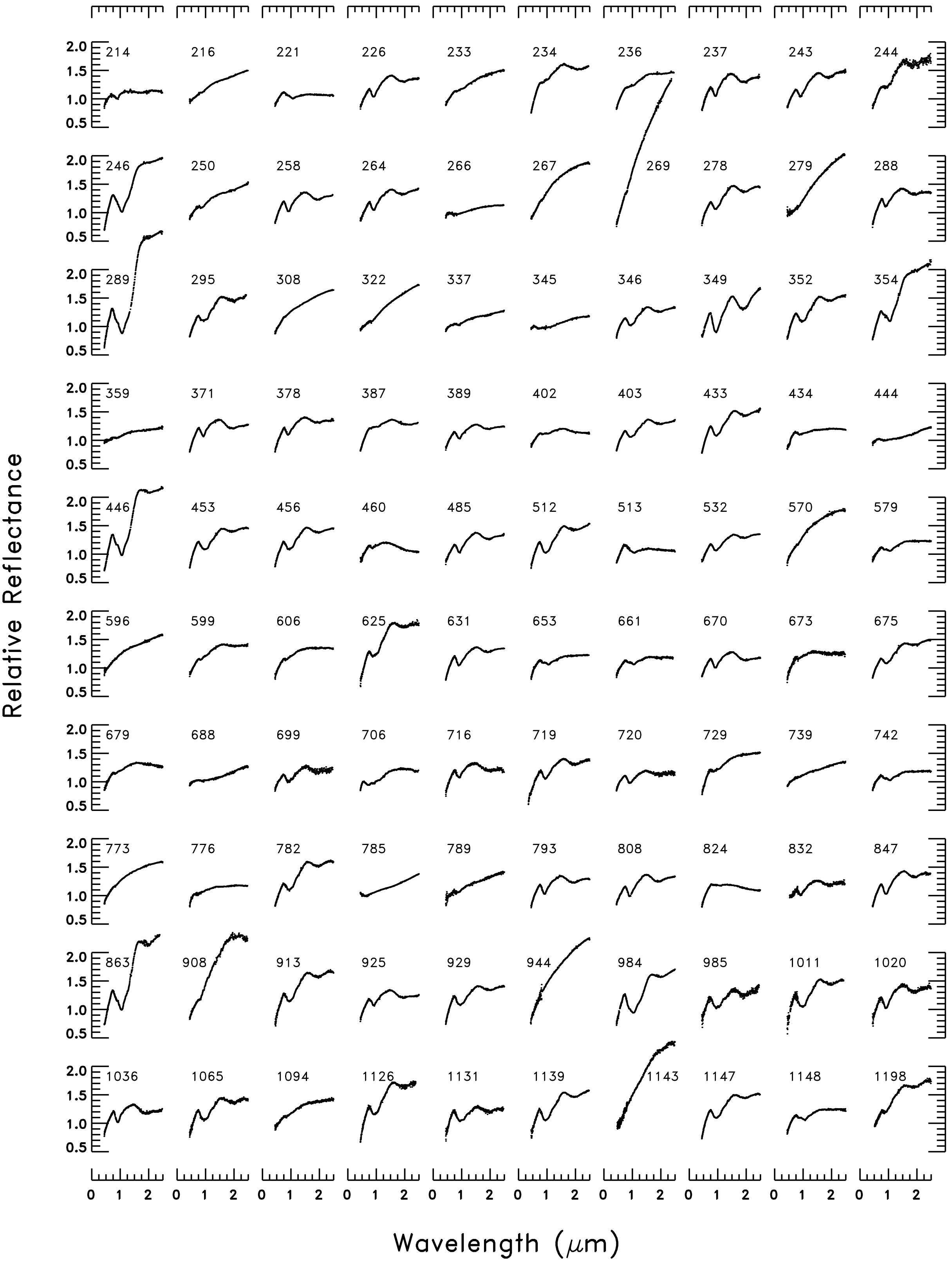
Relative Reflectance
Wavelength (μm)
2.0
1.5
1.0
0.5
0 1 2
214 216 221 226 233 234 236 237 243 244
246 250 258 264 266 267 269 278 279 288
289 295 308 322 337 345 346 349 352 354
359 371 378 387 389 402 403 433 434 444
446 453 456 460 485 512 513 532 570 579
596 599 606 625 631 653 661 670 673 675
679 688 699 706 716 719 720 729 739 742
773 776 782 785 789 793 808 824 832 847
863 908 913 925 929 944 984 985 1011 1020
1036 1065 1094 1126 1131 1139 1143 1147 1148 1198

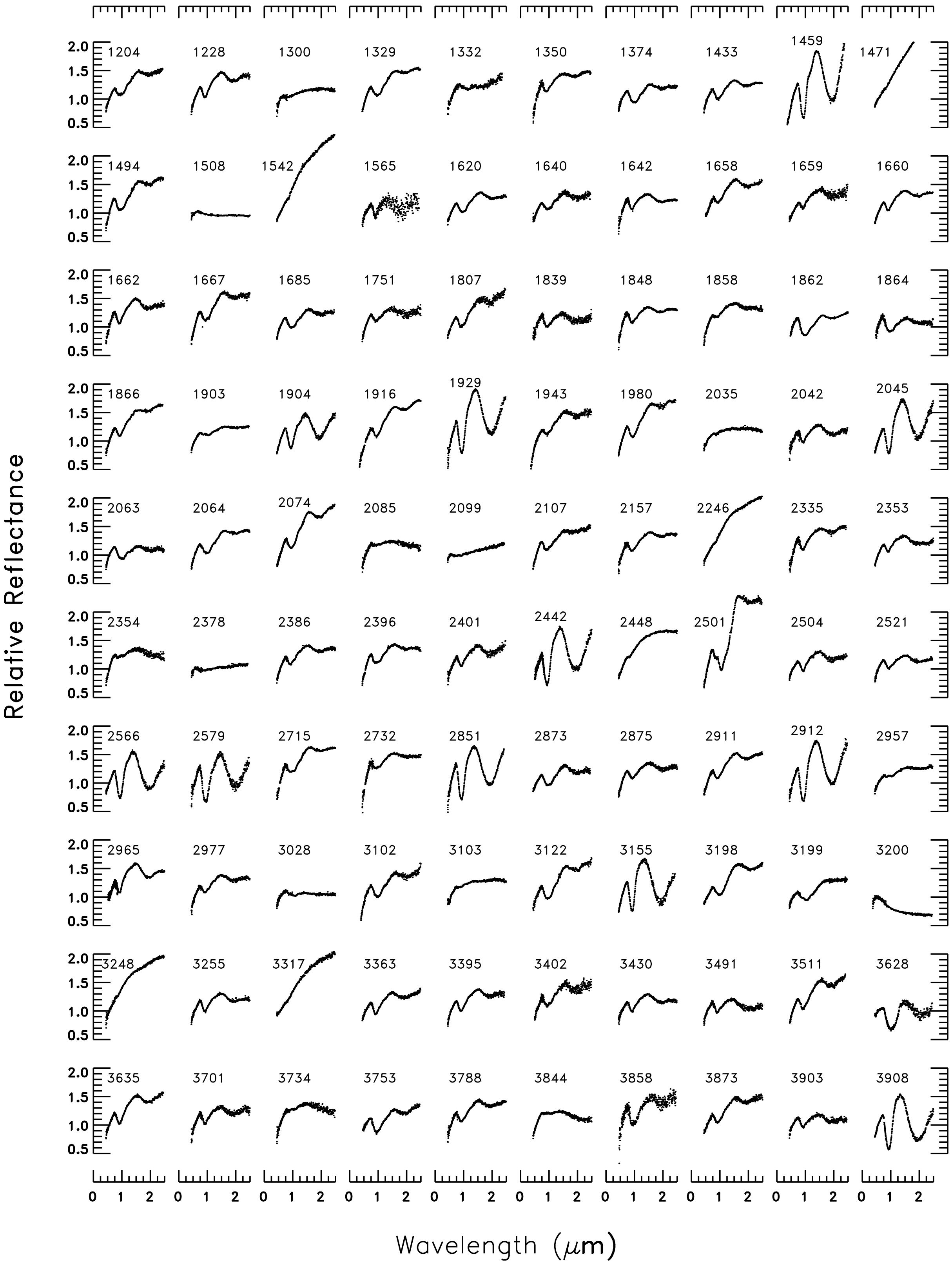
Relative Reflectance
2.0
1.5
1.0
0.5
1204
1228
1300
1329
1332
1350
1374
1433
1459
1471
1494
1508
1542
1565
1620
1640
1642
1658
1659
1660
1662
1667
1685
1751
1807
1839
1848
1858
1862
1864
1866
1903
1904
1916
1929
1943
1980
2035
2042
2045
2063
2064
2074
2085
2099
2107
2157
2246
2335
2353
2354
2378
2386
2396
2401
2442
2448
2501
2504
2521
2566
2579
2715
2732
2851
2873
2875
2911
2912
2957
2965
2977
3028
3102
3103
3122
3155
3198
3199
3200
3248
3255
3317
3363
3395
3402
3430
3491
3511
3628
3635
3701
3734
3753
3788
3844
3858
3873
3903
3908
0
1
2
Wavelength (μm)

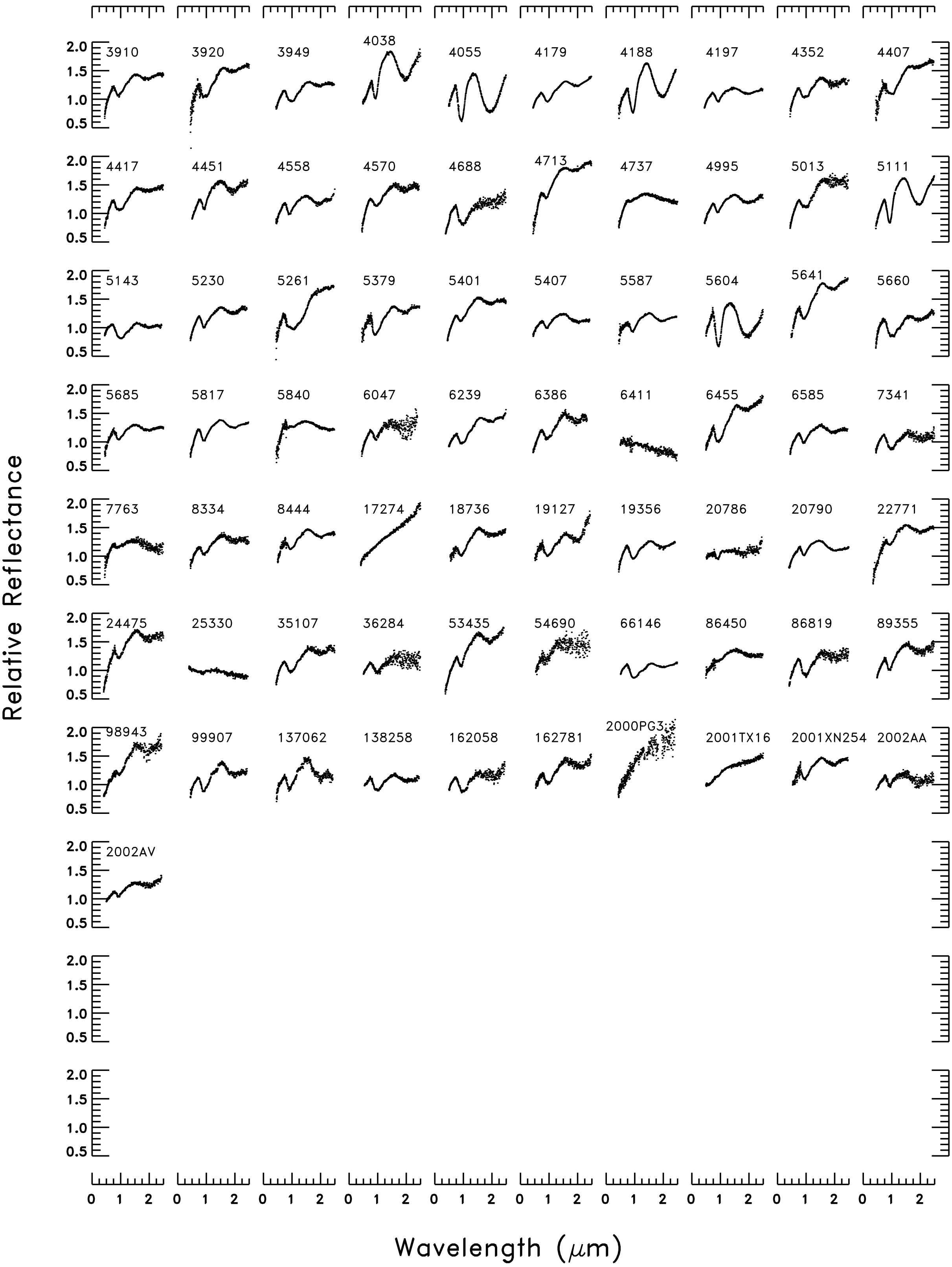
3910
3920
3949
4038
4055
4179
4188
4197
4352
4407
4417
4451
4558
4570
4688
4713
4737
4995
5013
5111
5143
5230
5261
5379
5401
5407
5587
5604
5641
5660
5685
5817
5840
6047
6239
6386
6411
6455
6585
7341
7763
8334
8444
17274
18736
19127
19356
20786
20790
22771
24475
25330
35107
36284
53435
54690
66146
86450
86819
89355
98943
99907
137062
138258
162058
162781
2000PG3
2001TX16
2001XN254
2002AA
2002AV
2.0
1.5
1.0
0.5
0
1
2
Relative Reflectance
Wavelength (μm)

Appendix B

TNO Photometry

B.1 Observational Circumstances

Object[a]	**Name**	**Dynamical Class**[b]	**Date**	**Δ (AU)**[c]	**r (AU)**	**α (deg)**
10199	Chariklo	Centaur	20 Mar 2007	12.496	13.276	2.7
26375	1999 DE9	Resonant(5:2)	22 Jan 2007	34.764	35.435	1.2
28978	Ixion	Resonant(3:2)	15 Jul 2007	41.242	42.019	0.9
32532	Thereus	Centaur	19 Sep 2007	10.341	11.006	4.0
42355	Typhon	Scattered	24 Jan 2007	16.710	17.542	1.8
47171	1999 TC36	Resonant(3:2)	9 Nov 2006	30.086	30.920	1.1
47932	2000 GN171	Resonant(3:2)	23 Jan 2007	28.373	28.352	2.0
47932	2000 GN171	Resonant(3:2)	24 Jan 2007	28.356	28.352	2.0
47932	2000 GN171	Resonant(3:2)	24 Mar 2007	27.519	28.346	1.1
50000	Quaoar	Classical	15 Jul 2007	42.450	43.267	0.8
54598	Bienor	Centaur	18 Sep 2007	17.127	18.116	0.6
55565	2002 AW197	Classical	23 Jan 2007	45.859	46.796	0.4
55637	2002 UX25	Classical	18 Sep 2007	41.185	42.004	0.8
60558	Echeclus	JFC	14 May 2007	11.239	12.124	2.4
83982	Crantor	Centaur	14 Jul 2007	14.008	14.739	2.8
83982	Crantor	Centaur	16 Jul 2007	14.032	14.741	2.9
90568	2004 GV9	Classical	13 May 2007	38.142	39.069	0.6
119951	2002 KX14	Classical	13 Jul 2007	38.856	39.535	1.1
120132	2003 FY128	Detached	22 Jan 2007	37.930	38.297	1.4
136199	Eris	Detached	19 Sep 2007	95.921	96.803	0.3
136199	Eris	Detached	20 Oct 2006	95.890	96.849	0.2
145451	2005 RM43		19 Sep 2007	34.665	35.183	1.4
145452	2005 RN43		19 Sep 2007	39.838	40.714	0.7
145453	2005 RR43		18 Sep 2007	37.977	38.492	1.3
2003 AZ84		Resonant(3:2)	24 Jan 2007	44.654	45.604	0.3
2003 QW90		Classical	9 Nov 2006	43.516	44.227	0.9
2003 UZ117		Classical	25 Dec 2006	38.858	39.512	1.1

[a] All objects in bold have their colors reported for the first time ever.

[b] Dynamical classes are from Gladman et al. (2008).

[c] Δ, r, and α are the topocentric and heliocentric distances and the phase angle, respectively.

B.2 Observed Magnitudes using the V, J, H, and K$_s$ Filters

Object	**Date**	**t1**[a]	**t2**[b]	**V**[c]	**J**	**H**	**K**$_s$	**H**$_v$**(1,1,0)**[d]
10199	20 Mar 2007	5:32	3:22	18.49 ± 0.05	17.00 ± 0.05	16.51 ± 0.06	16.30 ± 0.06	7.09 ± 0.05
26375	22 Jan 2007	6:49	5:48	20.75 ± 0.04	19.22 ± 0.06	18.93 ± 0.07	18.87 ± 0.07	5.13 ± 0.05
28978	15 Jul 2007	2:47	3:51	20.22 ± 0.05	18.63 ± 0.04	18.37 ± 0.05	18.38 ± 0.05	3.90 ± 0.06
32532	19 Sep 2007	6:44	6:55	19.90 ± 0.03	18.55 ± 0.04	18.15 ± 0.06	18.04 ± 0.06	9.18 ± 0.03
42355	24 Jan 2007	5:33	6:20	20.34 ± 0.02	18.78 ± 0.04	18.33 ± 0.05	18.17 ± 0.05	7.75 ± 0.04
42355	24 Jan 2007	5:46		20.36 ± 0.02				7.77 ± 0.04
47171	09 Nov 2006	0:58	0:58	20.25 ± 0.03	18.17 ± 0.07	17.85 ± 0.07	17.79 ± 0.08	5.25 ± 0.04
47171	09 Nov 2006	1:09		20.26 ± 0.03				5.26 ± 0.04
47932	23 Jan 2007	7:06	6:45	21.01 ± 0.03	19.43 ± 0.08	19.09 ± 0.09		6.20 ± 0.04
47932	23 Jan 2007	7:15		21.04 ± 0.03				6.23 ± 0.04
47932	24 Jan 2007	7:17	7:45	21.11 ± 0.03	19.42 ± 0.06	19.04 ± 0.07	18.98 ± 0.07	6.30 ± 0.04
47932	24 Jan 2007	7:26		21.12 ± 0.03				6.31 ± 0.04
47932	24 Mar 2007	5:12	5:57	21.30 ± 0.06				6.69 ± 0.07
50000	15 Jul 2007	1:33	2:17	19.25 ± 0.05	17.07 ± 0.03	16.71 ± 0.04	16.68 ± 0.04	2.82 ± 0.06
54598	18 Sep 2007	4:51	4:05	19.98 ± 0.03	18.46 ± 0.05	18.09 ± 0.05		7.46 ± 0.03
55565	23 Jan 2007	5:13	5:28	20.36 ± 0.02	18.62 ± 0.05	18.28 ± 0.06	18.21 ± 0.06	3.65 ± 0.04
55565	23 Jan 2007	5:25		20.37 ± 0.02				3.66 ± 0.04
55637	18 Sep 2007	6:50		20.28 ± 0.06				3.98 ± 0.07
60558	14 May 2007	1:10	0:51	20.61 ± 0.06	19.13 ± 0.04	18.76 ± 0.06	18.42 ± 0.09	9.67 ± 0.06
83982	14 Jul 2007	1:32		21.00 ± 0.07				9.12 ± 0.07
83982	16 Jul 2007	1:03		20.91 ± 0.02				9.01 ± 0.02
90568	13 May 2007	2:44	2:14	20.20 ± 0.03	18.63 ± 0.05	18.29 ± 0.08	18.15 ± 0.05	4.25 ± 0.04
119951	13 Jul 2007	1:29		20.95 ± 0.08				4.86 ± 0.09
120132	22 Jan 2007	6:49	7:13	21.06 ± 0.03	19.42 ± 0.05	19.06 ± 0.06	18.95 ± 0.06	5.05 ± 0.04
120132	22 Jan 2007	7:01		21.06 ± 0.03				5.05 ± 0.04
136199	19 Sep 2007	5:24	9:03	18.74 ± 0.04	17.96 ± 0.04	17.88 ± 0.06	18.16 ± 0.06	-1.14 ± 0.05
136199	20 Oct 2006	5:40	4:24	18.74 ± 0.02	17.79 ± 0.08			-1.13 ± 0.04
136199	20 Oct 2006	5:49		18.75 ± 0.02				-1.12 ± 0.04
145451	19 Sep 2007	9:17	9:23	20.18 ± 0.03	19.27 ± 0.06	19.07 ± 0.06	18.79 ± 0.07	4.55 ± 0.04
145452	19 Sep 2007	4:07	3:23	20.02 ± 0.03	18.47 ± 0.05	18.16 ± 0.05	17.97 ± 0.05	3.87 ± 0.04
145452	19 Sep 2007		4:04		18.39 ± 0.05			
145453	18 Sep 2007	7:57	6:50	20.08 ± 0.03	19.06 ± 0.06			4.07 ± 0.04
145453	18 Sep 2007		7:33		19.12 ± 0.06			
2003 AZ84	24 Jan 2007	3:38	4:13	20.33 ± 0.02	19.12 ± 0.05	18.81 ± 0.05	18.75 ± 0.05	3.74 ± 0.04
2003 AZ84	24 Jan 2007	3:47		20.33 ± 0.02				3.74 ± 0.04
2003 QW90	09 Nov 2006	2:37	2:19	21.80 ± 0.06	19.87 ± 0.15			5.25 ± 0.07
2003 QW90	09 Nov 2006	2:45		21.82 ± 0.06				5.27 ± 0.07
2003 UZ117	25 Dec 2006	2:01	1:02	21.25 ± 0.04				5.16 ± 0.05
2003 UZ117	25 Dec 2006	2:18		21.26 ± 0.04				5.17 ± 0.05

[a] UT start time for visible data

[b] UT start time for IR data

[c] For some objects, the visible magnitude was observed more than once in a night. Both magnitudes are reported and the observational start times are shown in column 3.

[d] H$_v$(1,1,0) is the absolute magnitude calculated using visible magnitudes reported in this table as well as helio- and topocentric distances and the phase angle reported in Table 1. The calculation is shown as Equation 1.

B.3 Mean TNO Colors

Object	**Prev**[a]	**New**[b]	**Total**[c]	**B-V**	**V-R**	**V-I**	**V-J**	**V-H**	**V-K$_s$**
Sun[d]				0.67	0.36	0.69	1.08	1.37	1.43
10199	BR	BR,BB	4		0.45 ± 0.07		1.49 ± 0.07	1.98 ± 0.08	2.19 ± 0.08
26375	IR	*	5		0.62 ± 0.02	1.12 ± 0.02	1.53 ± 0.07	1.82 ± 0.08	1.88 ± 0.08
28978	IR	BB	4		0.55 ± 0.06		1.59 ± 0.06	1.85 ± 0.07	1.84 ± 0.07
32532	BR	BB	5	0.81 ± 0.05		0.9 ± 0.13	1.35 ± 0.05	1.75 ± 0.06	1.86 ± 0.06
42355	BR	BR	5		0.48 ± 0.04	0.94 ± 0.03	1.56 ± 0.04	2.01 ± 0.05	2.17 ± 0.05
47171	RR	RR	4			1.26 ± 0.04	2.08 ± 0.08	2.4 ± 0.08	2.46 ± 0.09
47932	IR	BR,IR	5		0.59 ± 0.09	1.12 ± 0.04	1.65 ± 0.05	2.01 ± 0.06	2.13 ± 0.08
50000		RR	4		0.6 ± 0.05		2.18 ± 0.06	2.54 ± 0.06	2.57 ± 0.06
54598	BR	BR	4	0.73 ± 0.05		0.93 ± 0.16	1.52 ± 0.06	1.89 ± 0.06	
55565	IR	IR,RR	5		0.61 ± 0.03	1.16 ± 0.03	1.74 ± 0.05	2.08 ± 0.06	2.15 ± 0.06
55637	IR	RR,IR	2	1.03 ± 0.23		1.16 ± 0.34			
60558	BR	BR,BB	4		0.49 ± 0.07		1.48 ± 0.07	1.85 ± 0.08	2.19 ± 0.11
83982	RR				0.74 ± 0.09				
90568		BR	4		0.56 ± 0.03		1.57 ± 0.06	1.91 ± 0.09	2.05 ± 0.06
119951					0.61 ± 0.04				
120132		BR	5		0.59 ± 0.03	1.15 ± 0.03	1.64 ± 0.06	2 ± 0.07	2.11 ± 0.07
136199	BB	BB	5	0.85 ± 0.06		0.74 ± 0.12	0.83 ± 0.05	0.86 ± 0.07	0.58 ± 0.07
145451		BB	5	0.7 ± 0.06		0.7 ± 0.18	0.91 ± 0.06	1.11 ± 0.07	1.39 ± 0.07
145452		*	5	1.03 ± 0.07		1.13 ± 0.21	1.59 ± 0.05	1.86 ± 0.06	2.05 ± 0.06
145453		BB	3	0.71 ± 0.12		0.76 ± 0.16	0.99 ± 0.05		
2003 AZ84	BB	BB	5		0.4 ± 0.03	0.73 ± 0.03	1.21 ± 0.05	1.52 ± 0.05	1.58 ± 0.05
2003 QW90		IR,RR,BR	2			1.16 ± 0.07	1.98 ± 0.16		
2003 UZ117						0.67 ± 0.05			

[a] Previous classifications reported in Fulchignoni et al. (2008).

[b] Objects that fall within more than one class range have types listed in order of probability. Objects marked with a * did not fall within the parameters of any taxonomic class.

[c] The total number of colors used to determine the taxonomic class. Objects with more colors have a higher quality class determination.

[d] Solar Colors are taken from Hardorp (1980) and Campins et al. (1985).

Appendix C

List of Publications

C.1 Published Articles: First Author

6. **DeMeo F. E.**, Barucci M. A., Merlin F., Guilbert-Lepoutre A., Alvarez-Candal A., Delsanti A. Fornasier S., & de Bergh C.,
A spectroscopic analysis of Jupiter-coupled object (52872) Okyrhoe, and TNOs (90482) Orcus and (73480) 2002 PN$_3$*4*,
Submitted to A&A

5. **DeMeo F. E.**, Barucci M. A., Alvarez-Candal A., de Bergh C., Fornasier S., Merlin F., Perna D., & Belskaya I.,
Surface properties of icy transneptunian objects from the second ESO large program,
Icy Bodies of the Solar System, Proceedings of the International Astronomical Union, IAU Symposium, 263:186-191

4. **DeMeo F. E.**, Dumas C., deBergh C., Protopapa S., Cruikshank D., Geballe T., Alvarez-Candal A., Merlin F., & Baruci M. A.,
A search for ethane on Pluto and Triton,
Icarus, Accepted

3. **DeMeo F. E.**, Binzel R. P., Slivan S. M., & Bus S. J.,
An extension of the Bus asteroid taxonomy in the near-infrared.,
Icarus, 202:160-180, July 2009

2. **DeMeo F. E.**, Fornasier S., Barucci M. A., Perna D., Protopapa S., Alvarez-Candal A., Delsanti A., Doressoundiram A., Merlin F., & de Bergh C.,
Visible and near-infrared colors of TNOs and Centaurs from the second ESO large program,
A&A, 493:283-290, January 2009

1. **DeMeo F. E.**, & Binzel R. P.,
Comets in the near-Earth Object Population,
Icarus, 194:436-449, April 2008

C.2 Published Articles: Co-Author

12. Merlin F., Barucci, .M. A., de Bergh C., **DeMeo F. E.**, Alvarez-Candal, A., Dumas, C., & Cruikshank, D. P.
Chemical and physical properties of the variegated Pluto and Charon surfaces Astronomical Journal,

Submitted

11. Jenniskens P., Vaubaillon J., Binzel R. P., **DeMeo F. E.**, Nesvorny D., Fitzsimmons A., Hiroi T., Marchis F., Bishop J., Zolensky M., Herrin J.,& Shaddad M.,
2008 TC3 and the Search For the Ureilite Parent Body,
M&PS, Submitted

10. Perna D., Barucci M. A., Fornasier S., **DeMeo F. E.**, Alvarez-Candal A., Merlin F., Dotto E., Doressoundiram A., & de Bergh C.,
Colors and taxonomy of Centaurs and Trans-Neptunian Objects,
A&A, 510:A53

9. Binzel R. P., Morbidelli A., Merouane S., **DeMeo F. E.**, Birlan M., Vernazza P., Thomas C. A., Rivkin A. S, Bus S. J., & Tokunaga A.
Earth encounters as the origin of fresh asteroid surfaces,
Nature, 7279:331-334

8.Clark B. E., Ziffer J., Nesvorny D., Campins H., Rivkin A. S., Hiroi T., Barucci M. A., Fulchignoni M., Binzel R. P., Fornasier S., **DeMeo F. E.**, Ockert-Bell M. E., Licandro J., & Moth-Diniz T.,
Spectroscopy of B-Type Asteroids: Subgroups and Meteorite Analogs.
JGR, accepted

7. Fornasier S., Barucci M. A., de Bergh C., Alvarez-Candal A. **DeMeo F.**, Merlin F., Perna D., Guilbert A., Deslanti A., Dotto E., & Doressoundiram A.
Visible spectroscopy of the new ESO Large Program on Trans-Neptunian Objects and Centaurs: final results,
A&A 508:457-465 December 2009

6. Vernazza P., **DeMeo F. E.**, Nedelcu A., Birlan M., Doressoundiram A., Erard S., & Volquardsen E.
Resolved spectroscopy of Mercury in the Near-IR with SpeX/IRTF,
Icarus, Accepted

5. Binzel R. P., Rivkin A. S., Thomas C. A., Vernazza P., Burbine T. H., **DeMeo F. E.**, Bus S. J., Tokunaga A. T., Birlan M.
Spectral Properties and Composition of Potentially Hazardous Asteroid (99942) Apophis,
Icarus, 200:480-485, April 2009

4. Merlin F., Alvarex-Candal A., Delsanti A., Fornasier S., Barucci M. A., **DeMeo F. E**., de Bergh C., & Doressoundiram A.
Stratification of methane ice on Eris surface,
A&A, 137:315-328, January 2009

3. Vernazza P., Binzel R. P., Thomas C. A., **DeMeo F. E.**, Bus S. J., Rivkin A. S, & Tokunaga A.
Compositional differences between meteorites and near-Earth asteroids,
Nature, 7206:858-860, August 2008

2. Ockert-Bell M. E. Clark B. E. Shepard M. K., Rivkin A. S., Binzel R. P., Thomas C. A., **DeMeo F. E.**, Bus S. J., & Shah S.
Observations of X/M asteroids across multiple wavelengths,
Icarus, 195:206-219, May 2008

1. Rivkin A. S., Trilling D. E., Thomas C. A., **DeMeo F. E.**, Spahr T. B., Binzel R. P.,
Composition of the L5 Mars Trojans: Neighbors, Not Siblings,
Icarus, 192:431-441, December 2007

C.3 Conference Proceedings

DeMeo F. E., Dumas C., deBergh C., Protopapa S., Cruikshank D., Geballe T., Alvarez-Candal A., Merlin F., & Baruci M. A.,
A Search for Ethane on Pluto and Triton,
41th AAS Division for Planetary Science Meeting, October 4-9, 2009

Binzel R. P., Merouane S., **DeMeo F.**, Birlan M., Vernazza P., Morbidelli A., Thomas C. A., Rivkin A. S., Bus S. J., Tokunaga A.,
Planetary Encounters as the Cause of Fresh Asteroid Surfaces,
41th AAS Division for Planetary Science Meeting, October 4-9, 2009

Perna D., Fornasier S., Barucci M. A., **DeMeo F.**, Merlin F., Alvarez-Candal A., Guilbert A., Deslanti A., Protopapa S., Dotto E., Doressoundiram A., & de Bergh C.,
Colors and taxonomy of TNOs and Centaurs,
41th AAS Division for Planetary Science Meeting, October 4-9, 2009

Merlin F., Barucci M. A., de Bergh C., Alvarez-Candal A., **DeMeo F.**, & Dumas C.,
Chemical and physical properties of the heterogeneous Pluto and Charon surfaces,
41th AAS Division for Planetary Science Meeting, October 4-9, 2009

Barucci M. A., Fornasier S., Alvarez-Candal A., de Bergh C., Merlin F., **DeMeo F. E.**, Perna D., & Dumas C.,
Surface Properties of TNOs: preliminary statistical analysis,
41th AAS Division for Planetary Science Meeting, October 4-9, 2009

Clark B. E., Ziffer J., Nesvorny D., Campins H., Rivkin A. S., Hiroi T., Barucci M. A., Fulchignoni M., Binzel R. P., Fornasier S., **DeMeo F. E.**, Ockert-Bell M. E.,
Spectroscopy of B-Type Asteroids: Subgroups and Meteorite Analogs,
41th AAS Division for Planetary Science Meeting, October 4-9, 2009

Thomas C. A., **DeMeo F. E.**, Binzel R. P., Birlan M., Bus S. J., Tokunaga A., Vernazza P., Rivkin A. S.,
Spectral Gallery of Low Delta V Mission Targets,
Marco Polo Symposium, May 18-20, 2009

Clark B. E., Ziffer J., Nesvorny D., Campins H., Rivkin A. S., Hiroi T., Barucci M. A., Fulchignoni M., Binzel R. P., Fornasier S., **DeMeo F. E.**, Ockert-Bell M. E.,
B-Type Asteroids,
Marco Polo Symposium, May 18-20, 2009

DeMeo F. E., Fornasier S., Barucci M. A., Protopapa S., Perna D., Alvarez-Candal A., Delsanti A., Doressoundiram A., Merlin F., & de Bergh C.,
Colors of Centaurs and TNOs from the ESO Large Program,
40th AAS Division for Planetary Science Meeting, #47.05, October 10-15, 2008

Bus S. J., **DeMeo F. E.**, Binzel R. P., & Slivan S. M.,
A New Taxonomy of Visible and Near-IR Spectral Data,
40th AAS Division for Planetary Science Meeting, #28.22, October 10-15, 2008

Binzel R. P., Vernazza P., Thomas C. A., **DeMeo F. E.**, Bus S. J., Rivkin A. S., & Tokunaga A. T.,
Meteorite Associations and Source Regions for Potentially Hazardous Near-Earth Objects,

40th AAS Division for Planetary Science Meeting, #25.02, October 10-15, 2008

Binzel R. P., Thomas C. A., Tokunaga A., Bus S. J., **DeMeo F E.**, Rivkin A. S., Burbine T. H., Vernazza P., Birlan M., Storm S. P., Springmann A., & Masterman M.,
Spectral Properties of Near-Earth Object Mission Targets,
Asteroids, Comets, Meteors 2008, #8228, July 14-18, 2008

DeMeo F. E., Fornasier S., Barucci M. A., Protopapa S., Perna D., Alvarez-Candal A., Delsanti A., Doressoundiram A., Merlin F., & de Bergh C.,
Visible and Near-Infrared Colors of KBOs and Centaurs from the Second ESO Large Program,
Asteroids, Comets, Meteors 2008, #8189, July 14-18, 2008

DeMeo F. E., Binzel R. P., Slivan S. M., & Bus S. J.,
Bus-DeMeo Taxonomy: Extending Asteroid Taxonomy into the Near-Infrared,
Asteroids, Comets, Meteors 2008, #8186, July 14-18, 2008

Merlin F., Alvarez-Candal A., Delsanti A., Quirico E., Schmitt B., Fornasier S., Barucci M. A., **DeMeo F. E.**, de Bergh C., & Doressoundiram, A.,
Icy Surface Properties of the Dwarf Planet Eris,
Asteroids, Comets, Meteors 2008, #8141, July 14-18, 2008

DeMeo F. E., Binzel R. P., & Bus S. J.
A New Taxonomy of Asteroids Based on Visible and Near-Infrared Spectral Properties.
39th AAS Division for Planetary Science Meeting, #35.02, October 7-12, 2007

Vernazza P., Binzel R. P., **DeMeo F. E.**, &Thomas C. A.,
Mineralogical Characterization Of 150 S-type Asteroids And Comparison With OC Meteorites,
39th AAS Division for Planetary Science Meeting, #33.05, October 7-12, 2007

Bell M., Clark B. E., Shepard M. K., Rivkin A. S., Binzel R. P., Thomas C. A., **DeMeo F. E.**, Bus S J., & Shah S.,
Observations of X/M Asteroids Across Multiple Wavelengths
39th AAS Division for Planetary Science Meeting, #33.02, October 7-12, 2007

Binzel R. P., Rivkin A. S., Thomas C. A., Vernazza P., Burbine T. H., DeMeo F. E., Bus S. J., Tokunaga A. T., & Birlan M.,
Spectral Properties and Composition of Potentially Hazardous Asteroid (99942) Apophis,
39th AAS Division for Planetary Science Meeting, #13.04, October 7-12, 2007

Binzel R. P., Masi G., Foglia S., Vernazza P., Burbine T. H., Thomas C. A., **DeMeo F. E.**, Nesvorny D., Birlan M., & Fulchignoni M.,
Searching for V-type and Q-type Main-Belt Asteroids Based on SDSS Colors,
38th Lunar and Planetary Science Conference, # 1338, p.1851, March 12-16, 2007

Tokunaga A., Bus S. J., Binzel R. P., Thomas C. A., **DeMeo F. E.**, & Rivkin A. S.
MIT-Hawaii-IRTF Joint Program for Characterization of Near-Earth Objects,
38th AAS Division for Planetary Science Meeting, #59.07, October 8-13, 2006

DeMeo F. E., & Binzel R. P.,
Comets in the Near-Earth Object Population,
38th AAS Division for Planetary Science Meeting, #53.03, October 8-13, 2006

Binzel R. P., Thomas C. A., **DeMeo F. E.**, Tokunaga A., Rivkin A. S., & Bus S. J.,

The MIT-Hawaii-IRTF Joint Campaign for NEO Spectral Reconnaissance,
37th Lunar and Planetary Science Conference, # 1491, March 13-17, 2006

DeMeo F. E., & Binzel R. P.,
Comets in the Near-Earth Object Population,
Asteroids, Comets, Meteors, August 7-12, 2005

Binzel R. P., Rivkin A. S., Thomas C. A.,**DeMeo F. E.**, Tokunaga A., & Bus S. J.,
The MIT-Hawaii-IRTF Joint Campaign for NEO Spectral Reconnaissance,
36th Lunar and Planetary Science Conference, # 1817, March 14-18, 2005

C.4 IAU Circulars

Binzel R. P., Birlan M., & **DeMeo F. E.**,
2009 DD45,
IAU Circular 9024, 2009

C.5 Invited Talks

A search for ethane on Pluto and Triton
New Horizons Science Team Meeting Jan 19-20, 2010

C.6 Public Outreach

Discubriendo el Sistema Solar (Discovering the Solar System)
Elementary School in Aroyo, Puerto Rico
Highschool in Patillas, Puerto Rico, October 13, 2009

IYA Public Astronomy Talks in Spanish
National Astronomy and Ionosphere Center, Arecibo Observatory Newsletter, December 2009, N.46
NAIC Newsletter

Interviewed with Mirel Birlan about the Potential Hazardous Asteroid 2009 DD45 by journalist Fabien Gruhier
“Un astŕoide frôlè la Terre...Danger, météorite!” Le Nouvel Observateur March 26, 2009 N2316 p.84
Le Nouvel Observateur

Interviewed for the 80th anniversary of the discovery of Pluto by journalist Catherine de Coppet of La Marche des Sciences (France Culture)
“L’histoire de Pluton” France Culture (radio) March 11, 2010 2-3pm

Bibliography

Adams, J. B., McCord, T. B., 1971a. Alteration of Lunar Optical Properties: Age and Composition Effects. Science 171, 567–571.

Adams, J. B., McCord, T. B., 1971b. Optical properties of mineral separates, glass, and anorthositic fragments from Apollo mare samples. In: Lunar and Planetary Science Conference Proceedings. Vol. 2 of Lunar and Planetary Science Conference Proceedings. p. 2183.

Agnor, C. B., Hamilton, D. P., 2006. Neptune's capture of its moon Triton in a binary-planet gravitational encounter. Nature 441, 192–194.

Allen, R. L., Bernstein, G. M., Malhotra, R., 2001. The Edge of the Solar System. Astrophysical Journal 549, L241–L244.

Alvarez-Candal, A., Barucci, M. A., Merlin, F., de Bergh, C., Fornasier, S., Guilbert, A., Protopapa, S., 2010. The trans-Neptunian object (42355) Typhon: composition and dynamical evolution. Astronomy and Astrophysics 511, A35.

Alvarez-Candal, A., Fornasier, S., Barucci, M. A., de Bergh, C., Merlin, F., 2008. Visible spectroscopy of the new ESO large program on trans-Neptunian objects and Centaurs. Part 1. Astronomy and Astrophysics 487, 741–748.

Artymowicz, P., 1997. Beta Pictoris: an Early Solar System? Annual Review of Earth and Planetary Sciences 25, 175–219.

Aumann, H. H., Beichman, C. A., Gillett, F. C., de Jong, T., Houck, J. R., Low, F. J., Neugebauer, G., Walker, R. G., Wesselius, P. R., 1984. Discovery of a shell around Alpha Lyrae. Astrophysical Journal 278, L23–L27.

Backman, D., Marengo, M., Stapelfeldt, K., Su, K., Wilner, D., Dowell, C. D., Watson, D., Stansberry, J., Rieke, G., Megeath, T., Fazio, G., Werner, M., 2009. Epsilon Eridani's Planetary Debris Disk: Structure and Dynamics Based on Spitzer and Caltech Submillimeter Observatory Observations. Astrophysical Journal 690, 1522–1538.

Backman, D. E., Paresce, F., 1993. Main-sequence stars with circumstellar solid material - The VEGA phenomenon. In: E. H. Levy & J. I. Lunine (Ed.), Protostars and Planets III. Univ. of Arizona Press, Tucson, AZ, USA, pp. 1253–1304.

Bailey, M. E., Chambers, J. E., Hahn, G., 1992. Origin of sungrazers - A frequent cometary end-state. Astronomy and Astrophysics 257, 315–322.

Barata, G. A., Domingo, M., Ferini, G., Leto, G., Palumbo, M. E., Satorre, M. A., Strazzulla, G., 2003. Ion irradiation of ch_4-containing icy mixtures. Nucl. Instrum. Methods Phys. Res. B 209, 283–287.

Barkume, K. M., Brown, M. E., Schaller, E. L., 2008. Near-Infrared Spectra of Centaurs and Kuiper Belt Objects. Astronomical Journal 135, 55–67.

Barucci, M. A., Belskaya, I. N., Fulchignoni, M., Birlan, M., 2005a. Taxonomy of Centaurs and Trans-Neptunian Objects. Astronomical Journal 130, 1291–1298.

Barucci, M. A., Boehnhardt, H., Dotto, E., Doressoundiram, A., Romon, J., Lazzarin, M., Fornasier, S., de Bergh, C., Tozzi, G. P., Delsanti, A., Hainaut, O., Barrera, L., Birkle, K., Meech, K., Ortiz, J. L., Sekiguchi, T., Thomas, N., Watanabe, J., West, R. M., Davies, J. K., 2002. Visible and near-infrared spectroscopy of the Centaur 32532 (2001 PT_{13}). ESO Large Program on TNOs and Centaurs: First spectroscopy results. Astronomy and Astrophysics 392, 335–339.

Barucci, M. A., Brown, M. E., Emery, J. P., Merlin, F., 2008a. Composition and Surface Properties of Transneptunian Objects and Centaurs. In: Barucci, M. A., Boehnhardt, H., Cruikshank, D. P., Morbidelli, A. (Eds.), The Solar System Beyond Neptune. Univ. of Arizona Press, Tucson, AZ, USA, pp. 143–160.

Barucci, M. A., Capria, M. T., Coradini, A., Fulchignoni, M., 1987. Classification of asteroids using G-mode analysis. Icarus 72, 304–324.

Barucci, M. A., Cruikshank, D. P., Dotto, E., Merlin, F., Poulet, F., Dalle Ore, C., Fornasier, S., de Bergh, C., 2005b. Is Sedna another Triton? Astronomy and Astrophysics 439, L1–L4.

Barucci, M. A., Fulchignoni, M., Birlan, M., Doressoundiram, A., Romon, J., Boehnhardt, H., 2001. Analysis of Trans-Neptunian and Centaur colours: continuous trend or grouping? Astronomy and Astrophysics 371, 1150–1154.

Barucci, M. A., Merlin, F., Dotto, E., Doressoundiram, A., de Bergh, C., 2006. TNO surface ices. Observations of the TNO 55638 (2002 VE_{95}). Astronomy and Astrophysics 455, 725–730.

Barucci, M. A., Merlin, F., Guilbert, A., de Bergh, C., Alvarez-Candal, A., Hainaut, O., Doressoundiram, A., Dumas, C., Owen, T., Coradini, A., 2008b. Surface composition and temperature of the TNO Orcus. Astronomy and Astrophysics 479, L13–L16.

Bauer, J. M., Meech, K. J., Fernández, Y. R., Pittichova, J., Hainaut, O. R., Boehnhardt, H., Delsanti, A. C., 2003. Physical survey of 24 Centaurs with visible photometry. Icarus 166, 195–211.

Beichman, C. A., Bryden, G., Gautier, T. N., Stapelfeldt, K. R., Werner, M. W., Misselt, K., Rieke, G., Stansberry, J., Trilling, D., 2005. An Excess Due to Small Grains around the Nearby K0 V Star HD 69830: Asteroid or Cometary Debris? Astrophysical Journal 626, 1061–1069.

Benedict, G. F., McArthur, B. E., Gatewood, G., Nelan, E., Cochran, W. D., Hatzes, A., Endl, M., Wittenmyer, R., Baliunas, S. L., Walker, G. A. H., Yang, S., Kürster, M., Els, S., Paulson, D. B., 2006. The Extrasolar Planet ϵ Eridani b: Orbit and Mass. Astronomical Journal 132, 2206–2218.

Bernstein, G. M., Trilling, D. E., Allen, R. L., Brown, M. E., Holman, M., Malhotra, R., 2004. The Size Distribution of Trans-Neptunian Bodies. Astronomical Journal 128, 1364–1390.

Bernstein, M. P., Cruikshank, D. P., Sandford, S. A., 2005. Near-infrared laboratory spectra of solid H_2O/CO_2 and CH_3OH/CO_2 ice mixtures. Icarus 179, 527–534.

Beust, H., Morbidelli, A., 1996. Mean-Motion Resonances as a Source for Infalling Comets toward beta Pictoris. Icarus 120, 358–370.

Beust, H., Morbidelli, A., 2000. Falling Evaporating Bodies as a Clue to Outline the Structure of the β Pictoris Young Planetary System. Icarus 143, 170–188.

Binzel, R. P., 2003. Planetary science: Spin control for asteroids. Nature 425, 131–132.

Binzel, R. P., Masi, G., Foglia, S., 2006a. Prediction and Confirmation of V-type Asteroids Beyond 2.5 AU Based on SDSS Colors. In: Bulletin of the American Astronomical Society. Vol. 38 of Bulletin of the American Astronomical Society. p. 627.

Binzel, R. P., Masi, G., Foglia, S., Vernazza, P., Burbine, T. H., Thomas, C. A., Demeo, F. E., Nesvorny, D., Birlan, M., Fulchignoni, M., 2007. Searching for V-type and Q-type Main-Belt Asteroids Based on SDSS Colors. In: Lunar and Planetary Institute Conference Abstracts. Vol. 38 of Lunar and Planetary Inst. Technical Report. p. 1851.

Binzel, R. P., Morbidelli, A., Merouane, S., DeMeo, F. E., Birlan, M., Vernazza, P., Thomas, C. A., Rivkin, A. S., Bus, S. J., Tokunaga, A. T., 2010. Earth encounters as the origin of fresh surfaces on near-Earth asteroids. Nature 463, 331–334.

Binzel, R. P., Rivkin, A. S., Stuart, J. S., Harris, A. W., Bus, S. J., Burbine, T. H., 2004. Observed spectral properties of near-Earth objects: results for population distribution, source regions, and space weathering processes. Icarus 170, 259–294.

Binzel, R. P., Rivkin, A. S., Thomas, C. A., Vernazza, P., Burbine, T. H., DeMeo, F. E., Bus, S. J., Tokunaga, A. T., Birlan, M., 2009. Spectral properties and composition of potentially hazardous Asteroid (99942) Apophis. Icarus 200, 480–485.

Binzel, R. P., Thomas, C. A., DeMeo, F. E., Tokunaga, A., Rivkin, A. S., Bus, S. J., 2006b. The MIT-Hawaii-IRTF Joint Campaign for NEO Spectral Reconnaissance. In: S. Mackwell & E. Stansbery (Ed.), 37th Annual Lunar and Planetary Science Conference. Vol. 37 of Lunar and Planetary Institute Science Conference Abstracts. p. 1491.

Binzel, R. P., Xu, S., 1993. Chips off of asteroid 4 Vesta - Evidence for the parent body of basaltic achondrite meteorites. Science 260, 186–191.

Binzel, R. P., Xu, S., Bus, S. J., Skrutskie, M. F., Meyer, M. R., Knezek, P., Barker, E. S., 1993. Discovery of a Main-Belt Asteroid Resembling Ordinary Chondrite Meteorites. Science 262, 1541–1542.

Boehnhardt, H., Delsanti, A., Barucci, A., Hainaut, O., Doressoundiram, A., Lazzarin, M., Barrera, L., de Bergh, C., Birkle, K., Dotto, E., Meech, K., Ortiz, J. E., Romon, J., Sekiguchi, T., Thomas, N., Tozzi, G. P., Watanabe, J., West, R. M., 2002. ESO large program on physical studies of Transneptunian Objects and Centaurs: Visible photometry - First results. Astronomy and Astrophysics 395, 297–303.

Bonnet, H., Abuter, R., Baker, A., Bornemann, W., Brown, A., Castillo, R., Conzelmann, R., Damster, R., Davies, R., Delabre, B., Donaldson, R., Dumas, C., Eisenhauer, F., Elswijk, E., Fedrigo, E., Finger, G., Gemperlein, H., Genzel, R., Gilbert, A., Gillet, G., Goldbrunner, A., Horrobin, M., Ter Horst, R., Huber, S., Hubin, N., Iserlohe, C., Kaufer, A., Kissler-Patig, M., Kragt, J., Kroes, G., Lehnert, M., Lieb, W., Liske, J., Lizon, J., Lutz, D., Modigliani, A., Monnet, G., Nesvadba, N., Patig, J., Pragt, J., Reunanen, J., Röhrle, C., Rossi, S., Schmutzer, R., Schoenmaker, T., Schreiber, J., Stroebele, S., Szeifert, T., Tacconi, L., Tecza, M., Thatte, N., Tordo, S., van der Werf, P., Weisz, H., 2004. First light of SINFONI at the VLT. The Messenger 117, 17–24.

Bottke, W. F., 2007. Asteroids: Spun in the sun. Nature 446, 382–383.

Bottke, W. F., Levison, H. F., Nesvorný, D., Dones, L., 2007. Can planetesimals left over from terrestrial planet formation produce the lunar Late Heavy Bombardment? Icarus 190, 203–223.

Bottke, W. F., Morbidelli, A., Jedicke, R., Petit, J., Levison, H. F., Michel, P., Metcalfe, T. S., 2002. Debiased Orbital and Absolute Magnitude Distribution of the Near-Earth Objects. Icarus 156, 399–433.

Bottke, Jr., W. F., Vokrouhlický, D., Rubincam, D. P., Nesvorný, D., 2006. The Yarkovsky and Yorp Effects: Implications for Asteroid Dynamics. Annual Review of Earth and Planetary Sciences 34, 157–191.

Bowell, E., Chapman, C. R., Gradie, J. C., Morrison, D., Zellner, B., 1978. Taxonomy of asteroids. Icarus 35, 313–335.

Broadfoot, A. L., Atreya, S. K., Bertaux, J. L., Blamont, J. E., Dessler, A. J., Donahue, T. M., Forrester, W. T., Hall, D. T., Herbert, F., Holberg, J. B., Hunten, D. M., Krasnopolsky, V. A., Linick, S., Lunine, J. I., Mcconnell, J. C., Moos, H. W., Sandel, B. R., Schneider, N. M., Shemansky, D. E., Smith, G. R., Strobel, D. F., Yelle, R. V., 1989. Ultraviolet spectrometer observations of Neptune and Triton. Science 246, 1459–1466.

Brown, M. E., 2001. The Inclination Distribution of the Kuiper Belt. Astronomical Journal 121, 2804–2814.

Brown, M. E., Barkume, K. M., Blake, G. A., Schaller, E. L., Rabinowitz, D. L., Roe, H. G., Trujillo, C. A., 2007a. Methane and Ethane on the Bright Kuiper Belt Object 2005 FY_9. Astronomical Journal 133, 284–289.

Brown, M. E., Barkume, K. M., Ragozzine, D., Schaller, E. L., 2007b. A collisional family of icy objects in the Kuiper belt. Nature 446, 294–296.

Brown, M. E., Bouchez, A. H., Rabinowitz, D., Sari, R., Trujillo, C. A., van Dam, M., Campbell, R., Chin, J., Hartman, S., Johansson, E., Lafon, R., Le Mignant, D., Stomski, P., Summers, D., Wizinowich, P., 2005a. Keck Observatory Laser Guide Star Adaptive Optics Discovery and Characterization of a Satellite to the Large Kuiper Belt Object 2003 EL_{61}. Astrophysical Journal 632, L45–L48.

Brown, M. E., Calvin, W. M., 2000. Evidence for Crystalline Water and Ammonia Ices on Pluto's Satellite Charon. Science 287, 107–109.

Brown, M. E., Schaller, E. L., Roe, H. G., Rabinowitz, D. L., Trujillo, C. A., 2006. Direct Measurement of the Size of 2003 UB_{313} from the Hubble Space Telescope. Astrophysical Journal 643, L61–L63.

Brown, M. E., Trujillo, C. A., Rabinowitz, D. L., 2005b. Discovery of a Planetary-sized Object in the Scattered Kuiper Belt. Astrophysical Journal 635, L97–L100.

Browning, L. B., McSween, Jr., H. Y., Zolensky, M. E., 1996. Correlated alteration effects in CM carbonaceous chondrites. Geochimica et Cosmochimica Acta 60, 2621–2633.

Brunetto, R., Barucci, M. A., Dotto, E., Strazzulla, G., 2006a. Ion Irradiation of Frozen Methanol, Methane, and Benzene: Linking to the Colors of Centaurs and Trans-Neptunian Objects. Astrophysical Journal 644, 646–650.

Brunetto, R., Fulvio, D., Blanco, C., Strazzulla, G., 2006b. Laboratory Simulations of Planetary Surfaces Space Weathering Induced by Solar Wind and Cosmic Ions. In: SOHO-17. 10 Years of SOHO and Beyond. Vol. 617 of ESA Special Publication. p. 146.

Brunetto, R., Vernazza, P., Marchi, S., Birlan, M., Fulchignoni, M., Orofino, V., Strazzulla, G., 2006c. Modeling asteroid surfaces from observations and irradiation experiments: The case of 832 Karin. Icarus 184, 327–337.

Brunini, A., Melita, M. D., 2002. The Existence of a Planet beyond 50 AU and the Orbital Distribution of the Classical Edgeworth-Kuiper-Belt Objects. Icarus 160, 32–43.

Buie, M. W., Grundy, W. M., 2000. The Distribution and Physical State of H_2O on Charon. Icarus 148, 324–339.

Buie, M. W., Grundy, W. M., Young, E. F., Young, L. A., Stern, S. A., 2006. Orbits and Photometry of Pluto's Satellites: Charon, S/2005 P1, and S/2005 P2. Astronomical Journal 132, 290–298.

Buie, M. W., Grundy, W. M., Young, E. F., Young, L. A., Stern, S. A., 2010. Pluto and Charon with the Hubble Space Telescope. II. Resolving Changes on Pluto's Surface and a Map for Charon. Astronomical Journal 139, 1128–1143.

Buie, M. W., Tholen, D. J., Wasserman, L. H., 1997. Separate Lightcurves of Pluto and Charon. Icarus 125, 233–244.

Burbine, T. H., 2000. Forging asteroid-meteorite relationships through reflectance spectroscopy. Ph.D. thesis, Massachusetts Institute of Technology.

Burbine, T. H., Binzel, R. P., 2002. Small Main-Belt Asteroid Spectroscopic Survey in the Near-Infrared. Icarus 159, 468–499.

Burbine, T. H., Binzel, R. P., Bus, S. J., Clark, B. E., 2001. K asteroids and CO3/CV3 chondrites. Meteoritics and Planetary Science 36, 245–253.

Burrows, C. J., Krist, J. E., Stapelfeldt, K. R., WFPC2 Investigation Definition Team, 1995. HST Observations of the Beta Pictoris Circumstellar Disk. In: Bulletin of the American Astronomical Society. Vol. 27 of Bulletin of the American Astronomical Society. p. 1329.

Bus, S. J., 1999. Compositional structure in the asteroid belt: Results of a spectroscopic survey. Ph.D. thesis, Massachusetts Institute of Technology.

Bus, S. J., Binzel, R. P., 2002a. Phase II of the Small Main-Belt Asteroid Spectroscopic Survey, A Feature-Based Taxonomy. Icarus 158, 146–177.

Bus, S. J., Binzel, R. P., 2002b. Phase II of the Small Main-Belt Asteroid Spectroscopic Survey, The Observations. Icarus 158, 106–145.

Campins, H., Hargrove, K., Pinilla-Alonso, N., Howell, E. S., Kelley, M. S., Licandro, J., Mothé-Diniz, T., Fernández, Y., Ziffer, J., 2010. Water ice and organics on the surface of the asteroid 24 Themis. Nature 464, 1320–1321.

Campins, H., Rieke, G. H., Lebofsky, M. J., 1985. Absolute calibration of photometry at 1 through 5 microns. Astronomical Journal 90, 896–899.

Carry, B., 2009. études des propriétés physiques des astéroïdes par imagerie à haute résolution angulaire. Ph.D. thesis, Universit̀de Paris 7.

Cellino, A., 2000. Minor Bodies: Spectral Gradients and Relationships with Meteorites. Space Science Reviews 92, 397–412.

Chandrasekhar, S., 1960. Radiative transfer. Dover Publications Inc.

Chapman, C. R., Cohen, B. A., Grinspoon, D. H., 2007. What are the real constraints on the existence and magnitude of the late heavy bombardment? Icarus 189, 233–245.

Chapman, C. R., Johnson, T. V., McCord, T. B., 1971. A Review of Spectrophotometric Studies of Asteroids. In: Gehrels, T. (Ed.), IAU Colloq. 12: Physical Studies of Minor Planets. pp. 51–65.

Chapman, C. R., Morrison, D., Zellner, B., 1975. Surface properties of asteroids - A synthesis of polarimetry, radiometry, and spectrophotometry. Icarus 25, 104–130.

Chesley, S. R., 2005. Potential impact detection for near-Earth asteroids: The case of 99942 Apophis (2004 MN4). In: IAU Symposium. Vol. 229. pp. 215–228.

Clark, B. E., Hapke, B., Pieters, C., Britt, D., 2002. Asteroid Space Weathering and Regolith Evolution. Asteroids III, 585–599.

Clark, B. E., Ockert-Bell, M. E., Cloutis, E. A., Nesvorny, D., Mothé-Diniz, T., Bus, S. J., 2009. Spectroscopy of K-complex asteroids: Parent bodies of carbonaceous meteorites? Icarus 202, 119–133.

Clark, R. N., 1981. The spectral reflectance of water-mineral mixtures at low temperatures. Journal of Geophysical Research 86, 3074–3086.

Clark, R. N., Oct. 2009. Detection of Adsorbed Water and Hydroxyl on the Moon. Science 326, 562–564.

Cohen, B. A., Swindle, T. D., Kring, D. A., 2000. Support for the Lunar Cataclysm Hypothesis from Lunar Meteorite Impact Melt Ages. Science 290, 1754–1756.

Cohen, M., Walker, R. G., Barlow, M. J., Deacon, J. R., 1992. Spectral irradiance calibration in the infrared. I - Ground-based and IRAS broadband calibrations. Astronomical Journal 104, 1650–1657.

Collander-Brown, S., Maran, M., Williams, I. P., 2000. The effect on the Edgeworth-Kuiper Belt of a large distant tenth planet. Monthly Notices of the Royal Astronomical Society 318, 101–108.

Conel, J. E., Nash, D. B., 1970. Spectral reflectance and albedo of Apollo 11 lunar samples: Effects of irradiation and vitrification and comparison with telescopic observations. Geochimica et Cosmochimica Acta Supplement 1, 2013.

Consulmagno, G. J., Drake, M. J., 1977. Composition and evolution of the eucrite parent body - Evidence from rare earth elements. Geochimica et Cosmochimica Acta. 41 (9), 1271–1282.

Cook, J. C., Desch, S. J., Roush, T. L., 2007a. Near Infreared Spectroscopy of Kuiper Belt Objects: More than Just Water Ice. In: Bulletin of the American Astronomical Society. Vol. 38 of Bulletin of the American Astronomical Society. p. 510.

Cook, J. C., Desch, S. J., Roush, T. L., Trujillo, C. A., Geballe, T. R., 2007b. Near-Infrared Spectroscopy of Charon: Possible Evidence for Cryovolcanism on Kuiper Belt Objects. Astrophysical Journal 663, 1406–1419.

Cooper, J. F., Christian, E. R., Richardson, J. D., Wang, C., 2003. Proton Irradiation of Centaur, Kuiper Belt, and Oort Cloud Objects at Plasma to Cosmic Ray Energy. Earth Moon and Planets 92, 261–277.

Coradini, A., Fulchignoni, M., Fanucci, O., Gavrishin, A. I., 1977. A fortran v program for a new classification technique: The g-mode central method. Computational Geosciences 3, 85–105.

Crovisier, J., Brooke, T. Y., Hanner, M. S., Keller, H. U., Lamy, P. L., Altieri, B., Bockelee-Morvan, D., Jorda, L., Leech, K., Lellouch, E., 1996. The infrared spectrum of comet C/1995 O1 (Hale-Bopp) at 4.6 AU from the Sun. Astronomy and Astrophysics 315, L385–L388.

Cruikshank, D. P., Mason, R. E., Dalle Ore, C. M., Bernstein, M. P., Quirico, E., Mastrapa, R. M., Emery, J. P., Owen, T. C., Sep. 2006. Ethane on Pluto and Triton. In: Bulletin of the American Astronomical Society. Vol. 38 of Bulletin of the American Astronomical Society. p. 518.

Cruikshank, D. P., Pilcher, C. B., Morrison, D., 1976. Pluto - Evidence for methane frost. Science 194, 835–837.

Cruikshank, D. P., Roush, T. L., Bartholomew, M. J., Geballe, T. R., Pendleton, Y. J., White, S. M., Bell, J. F., Davies, J. K., Owen, T. C., de Bergh, C., Tholen, D. J., Bernstein, M. P., Brown, R. H., Tryka, K. A., Dalle Ore, C. M., 1998. The Composition of Centaur 5145 Pholus. Icarus 135, 389–407.

Cruikshank, D. P., Roush, T. L., Owen, T. C., Geballe, T. R., de Bergh, C., Schmitt, B., Brown, R. H., Bartholomew, M. J., 1993. Ices on the surface of Triton. Science 261, 742–745.

Cruikshank, D. P., Schmitt, B., Roush, T. L., Owen, T. C., Quirico, E., Geballe, T. R., de Bergh, C., Bartholomew, M. J., Dalle Ore, C. M., Douté, S., Meier, R., 2000. Water Ice on Triton. Icarus 147, 309–316.

Cruikshank, D. P., Silvaggio, P. M., 1979. Triton - A satellite with an atmosphere. Astrophysical Journal 233, 1016–1020.

Cuzzi, J. N., Hogan, R. C., Shariff, K., 2008. Toward Planetesimals: Dense Chondrule Clumps in the Protoplanetary Nebula. Astrophysical Journal 687, 1432–1447.

Dalle Ore, C. M., Barucci, M. A., Emery, J. P., Cruikshank, D. P., Dalle Ore, L. V., Merlin, F., Alvarez-Candal, A., de Bergh, C., Trilling, D. E., Perna, D., Fornasier, S., Mastrapa, R. M. E., Dotto, E., 2009. Composition of KBO (50000) Quaoar. Astronomy and Astrophysics 501, 349–357.

Davies, M. E., Rogers, P. G., Colvin, T. R., 1991. A control network of Triton. Journal of Geophysical Research 96, 15675.

de Bergh, C., Delsanti, A., Tozzi, G. P., Dotto, E., Doressoundiram, A., Barucci, M. A., 2005. The surface of the transneptunian object 90482 Orcus. Astronomy and Astrophysics 437, 1115–1120.

Delsanti, A., Hainaut, O., Jourdeuil, E., Meech, K. J., Boehnhardt, H., Barrera, L., 2004. Simultaneous visible-near IR photometric study of Kuiper Belt Object surfaces with the ESO/Very Large Telescopes. Astronomy and Astrophysics 417, 1145–1158.

Delsanti, A., Peixinho, N., Boehnhardt, H., Barucci, A., Merlin, F., Doressoundiram, A., Davies, J. K., 2006. Near-Infrared Color Properties of Kuiper Belt Objects and Centaurs: Final Results from the ESO Large Program. Astronomical Journal 131, 1851–1863.

DeMeo, F., Binzel, R. P., 2008. Comets in the near-Earth object population. Icarus 194, 436–449.

DeMeo, F. E., 2007. DeMeo Taxonomy: Categorization of Asteroids in the Near-Infrared. Master's thesis, Massachusetts Institute of Technology.

DeMeo, F. E., Barucci, M. A., Alvarez-Candal, A., de Bergh, C., Fornasier, S., Merlin, F., Perna, D., Belskaya, I., 2010a. Surface properties of icy transneptunian objects from the second ESO large program. In: J. A. Fernández, D. Lazzaro, D. Prialnik, & R. Schulz (Ed.), IAU Symposium. Vol. 263 of IAU Symposium. pp. 186–191.

DeMeo, F. E., Barucci, M. A., Merlin, F., Guilbert-Lepoutre, A., Alvarez-Candal, A., Delsanti, A., Fornasier, S., de Bergh, C., 2010b. A spectroscopic analysis of Jupiter-coupled object (52872) Okyrhoe, and TNOs (90482) Orcus and (73480) 2002 PN$_{34}$. Astronomy and Astrophysics, submitted.

DeMeo, F. E., Binzel, R. P., Slivan, S. M., Bus, S. J., 2009a. An extension of the Bus asteroid taxonomy into the near-infrared. Icarus 202, 160–180.

DeMeo, F. E., Dumas, C., de Bergh, C., Protopapa, S., Cruikshank, D. P., Geballe, T. R., Alvarez-Candal, A., Merlin, F., Barucci, M. A., 2010c. A search for ethane on pluto and triton. Icarus.

DeMeo, F. E., Fornasier, S., Barucci, M. A., Perna, D., Protopapa, S., Alvarez-Candal, A., Delsanti, A., Doressoundiram, A., Merlin, F., de Bergh, C., 2009b. Visible and near-infrared colors of Transneptunian objects and Centaurs from the second ESO large program. Astronomy and Astrophysics 493, 283–290.

Doressoundiram, A., Boehnhardt, H., Tegler, S. C., Trujillo, C., 2008. Color Properties and Trends of the Transneptunian Objects. In: Barucci, M. A., Boehnhardt, H., Cruikshank, D. P., Morbidelli, A. (Eds.), The Solar System Beyond Neptune. Univ. of Arizona Press, Tucson, AZ, USA, pp. 91–104.

Doressoundiram, A., Peixinho, N., de Bergh, C., Fornasier, S., Thébault, P., Barucci, M. A., Veillet, C., 2002. The Color Distribution in the Edgeworth-Kuiper Belt. Astronomical Journal 124, 2279–2296.

Doressoundiram, A., Peixinho, N., Doucet, C., Mousis, O., Barucci, M. A., Petit, J. M., Veillet, C., 2005. The Meudon Multicolor Survey (2MS) of Centaurs and trans-neptunian objects: extended dataset and status on the correlations reported. Icarus 174, 90–104.

Doressoundiram, A., Peixinho, N., Moullet, A., Fornasier, S., Barucci, M. A., Beuzit, J.-L., Veillet, C., 2007. The Meudon Multicolor Survey (2MS) of Centaurs and Trans-Neptunian Objects: From Visible to Infrared Colors. Astronomical Journal 134, 2186–2199.

Doressoundiram, A., Tozzi, G. P., Barucci, M. A., Boehnhardt, H., Fornasier, S., Romon, J., 2003. ESO Large Programme on Trans-Neptunian Objects and Centaurs: Spectroscopic Investigation of Centaur 2001 BL$_{41}$ and TNOs (26181) 1996 GQ$_{21}$ and (26375) 1999 DE$_{9}$. Astronomical Journal 125, 2721–2727.

Dotto, E., Barucci, M. A., Boehnhardt, H., Romon, J., Doressoundiram, A., Peixinho, N., de Bergh, C., Lazzarin, M., 2003. Searching for water ice on 47171 1999 TC$_{36}$, 1998 SG$_{35}$, and 2000 QC$_{243}$: ESO large program on TNOs and centaurs*. Icarus 162, 408–414.

Douté, S., Schmitt, B., Quirico, E., Owen, T. C., Cruikshank, D. P., de Bergh, C., Geballe, T. R., Roush, T. L., 1999. Evidence for Methane Segregation at the Surface of Pluto. Icarus 142, 421–444.

Drake, M. J., 2001. The eucrite/Vesta story. Meteoritics and Planetary Science 36, 501–513.

Eisenhauer, F., Abuter, R., Bickert, K., Biancat-Marchet, F., Bonnet, H., Brynnel, J., Conzelmann, R. D., Delabre, B., Donaldson, R., Farinato, J., Fedrigo, E., Genzel, R., Hubin, N. N., Iserlohe, C., Kasper, M. E., Kissler-Patig, M., Monnet, G. J., Roehrle, C., Schreiber, J., Stroebele, S., Tecza, M., Thatte, N. A., Weisz, H., 2003. SINFONI - Integral field spectroscopy at 50 milli-arcsecond resolution with the ESO VLT. In: M. Iye & A. F. M. Moorwood (Ed.), Society of Photo-Optical Instrumentation Engineers (SPIE) Conference Series. Vol. 4841 of Society of Photo-Optical Instrumentation Engineers (SPIE) Conference Series. pp. 1548–1561.

Elliot, J. L., Ates, A., Babcock, B. A., Bosh, A. S., Buie, M. W., Clancy, K. B., Dunham, E. W., Eikenberry, S. S., Hall, D. T., Kern, S. D., Leggett, S. K., Levine, S. E., Moon, D., Olkin, C. B., Osip, D. J., Pasachoff, J. M., Penprase, B. E., Person, M. J., Qu, S., Rayner, J. T., Roberts, L. C., Salyk, C. V., Souza, S. P., Stone, R. C., Taylor, B. W., Tholen, D. J., Thomas-Osip, J. E., Ticehurst, D. R., Wasserman, L. H., 2003. The recent expansion of Pluto's atmosphere. Nature 424, 165–168.

Elliot, J. L., Dunham, E. W., Bosh, A. S., Slivan, S. M., Young, L. A., Wasserman, L. H., Millis, R. L., 1989. Pluto's atmosphere. Icarus 77, 148–170.

Elliot, J. L., Hammel, H. B., Wasserman, L. H., Franz, O. G., McDonald, S. W., Person, M. J., Olkin, C. B., Dunham, E. W., Spencer, J. R., Stansberry, J. A., Buie, M. W., Pasachoff, J. M., Babcock, B. A., McConnochie, T. H., 1998. Global warming on Triton. Nature 393, 765–767.

Elliot, J. L., Kern, S. D., Clancy, K. B., Gulbis, A. A. S., Millis, R. L., Buie, M. W., Wasserman, L. H., Chiang, E. I., Jordan, A. B., Trilling, D. E., Meech, K. J., 2005. The Deep Ecliptic Survey: A Search for Kuiper Belt Objects and Centaurs. II. Dynamical Classification, the Kuiper Belt Plane, and the Core Population. Astronomical Journal 129, 1117–1162.

Elliot, J. L., Person, M. J., Gulbis, A. A. S., Souza, S. P., Adams, E. R., Babcock, B. A., Gangestad, J. W., Jaskot, A. E., Kramer, E. A., Pasachoff, J. M., Pike, R. E., Zuluaga, C. A., Bosh, A. S., Dieters, S. W., Francis, P. J., Giles, A. B., Greenhill, J. G., Lade, B., Lucas, R., Ramm, D. J., 2007. Changes in Pluto's Atmosphere: 1988-2006. Astronomical Journal 134, 1–13.

Elliot, J. L., Strobel, D. F., Zhu, X., Stansberry, J. A., Wasserman, L. H., Franz, O. G., 2000. NOTE: The Thermal Structure of Triton's Middle Atmosphere. Icarus 143, 425–428.

Eshleman, V. R., 1989. Pluto's atmosphere - Models based on refraction, inversion, and vapor-pressure equilibrium. Icarus 80, 439–443.

Farnham, T. L., Davies, J. K., 2003. The rotational and physical properties of the Centaur (32532) 2001 PT_{13}. Icarus 164, 418–427.

Fernandez, J. A., Ip, W.-H., 1984. Some dynamical aspects of the accretion of Uranus and Neptune - The exchange of orbital angular momentum with planetesimals. Icarus 58, 109–120.

Fernández, Y. R., Sheppard, S. S., Jewitt, D. C., 2003. The Albedo Distribution of Jovian Trojan Asteroids. Astronomical Journal 126, 1563–1574.

Fornasier, S., Barucci, M. A., de Bergh, C., Alvarez-Candal, A., DeMeo, F., Merlin, F., Perna, D., Guilbert, A., Delsanti, A., Dotto, E., Doressoundiram, A., 2009. Visible spectroscopy of the new ESO large programme on trans-Neptunian objects and Centaurs: final results. Astronomy and Astrophysics 508, 457–465.

Fornasier, S., Dotto, E., Barucci, M. A., Barbieri, C., 2004. Water ice on the surface of the large TNO 2004 DW. Astronomy and Astrophysics 422, L43–L46.

Fulchignoni, M., Belskaya, I., Barucci, M. A., de Sanctis, M. C., Doressoundiram, A., 2008. Transneptunian Object Taxonomy. In: Barucci, M. A., Boehnhardt, H., Cruikshank, D. P., Morbidelli, A. (Eds.), The Solar System Beyond Neptune. Univ. of Arizona Press, Tucson, AZ, USA, pp. 181–192.

Fulchignoni, M., Birlan, M., Antonietta Barucci, M., 2000. The Extension of the G-Mode Asteroid Taxonomy. Icarus 146, 204–212.

Gaffey, M. J., Burbine, T. H., Piatek, J. L., Reed, K. L., Chaky, D. A., Bell, J. F., Brown, R. H., 1993. Mineralogical variations within the S-type asteroid class. Icarus 106, 573–602.

Gil-Hutton, R., Licandro, J., Pinilla-Alonso, N., Brunetto, R., Jun. 2009. The trans-Neptunian object size distribution at small sizes. Astronomy and Astrophysics 500, 909–916.

Gladman, B., Kavelaars, J. J., Petit, J.-M., Morbidelli, A., Holman, M. J., Loredo, T., 2001. The Structure of the Kuiper Belt: Size Distribution and Radial Extent. Astronomical Journal 122, 1051–1066.

Gladman, B., Marsden, B. G., Vanlaerhoven, C., 2008. Nomenclature in the Outer Solar System. In: Barucci, M. A., Boehnhardt, H., Cruikshank, D. P., Morbidelli, A. (Eds.), The Solar System Beyond Neptune. Univ. of Arizona Press, Tucson, AZ, USA, pp. 43–57.

Gladman, B., Michel, P., Froeschlé, C., 2000. The Near-Earth Object Population. Icarus 146, 176–189.

Goguen, J. D., Hammel, H. B., Brown, R. H., 1989. V photometry of Titania, Oberon, and Triton. Icarus 77, 239–247.

Gomes, R., 2003a. Planetary science: Conveyed to the Kuiper belt. Nature 426, 393–395.

Gomes, R., Levison, H. F., Tsiganis, K., Morbidelli, A., 2005. Origin of the cataclysmic Late Heavy Bombardment period of the terrestrial planets. Nature 435, 466–469.

Gomes, R. D. S., 2009. On the origin of the Kuiper belt. Celestial Mechanics and Dynamical Astronomy 104, 39–51.

Gomes, R. S., 2003b. The origin of the Kuiper Belt high-inclination population. Icarus 161, 404–418.

Gomes, R. S., Matese, J. J., Lissauer, J. J., 2006. A distant planetary-mass solar companion may have produced distant detached objects. Icarus 184, 589–601.

Gomes, R. S., Morbidelli, A., Levison, H. F., 2004. Planetary migration in a planetesimal disk: why did Neptune stop at 30 AU? Icarus 170, 492–507.

Gradie, J., Veverka, J., 1980. The composition of the Trojan asteroids. Nature 283, 840–842.

Greaves, J. S., Holland, W. S., Moriarty-Schieven, G., Jenness, T., Dent, W. R. F., Zuckerman, B., McCarthy, C., Webb, R. A., Butner, H. M., Gear, W. K., Walker, H. J., 1998. A Dust Ring around epsilon Eridani: Analog to the Young Solar System. Astrophysical Journal 506, L133–L137.

Greaves, J. S., Wyatt, M. C., Bryden, G., 2009. Debris discs around nearby solar analogues. Monthly Notices of the Royal Astronomical Society 397, 757–762.

Grundy, W. M., 2009. Is the missing ultra-red material colorless ice? Icarus 199, 560–563.

Grundy, W. M., Buie, M. W., 2001. Distribution and Evolution of CH_4, N_2, and CO Ices on Pluto's Surface: 1995 to 1998. Icarus 153, 248–263.

Grundy, W. M., Schmitt, B., 1998. The temperature-dependent near-infrared absorption spectrum of hexagonal H_2O ice. Journal of Geophysical Research 103, 25809–25822.

Grundy, W. M., Young, L. A., 2004. Near-infrared spectral monitoring of Triton with IRTF/SpeX I: establishing a baseline for rotational variability. Icarus 172, 455–465.

Grundy, W. M., Young, L. A., Stansberry, J. A., Buie, M. W., Olkin, C. B., Young, E. F., 2010. Near-infrared spectral monitoring of Triton with IRTF/SpeX II: Spatial distribution and evolution of ices. Icarus 205, 594–604.

Guilbert, A., Alvarez-Candal, A., Merlin, F., Barucci, M. A., Dumas, C., de Bergh, C., Delsanti, A., 2009a. ESO-Large Program on TNOs: Near-infrared spectroscopy with SINFONI. Icarus 201, 272–283.

Guilbert, A., Barucci, M. A., Brunetto, R., Delsanti, A., Merlin, F., Alvarez-Candal, A., Fornasier, S., de Bergh, C., Sarid, G., 2009b. A portrait of Centaur 10199 Chariklo. Astronomy and Astrophysics 501, 777–784.

Gulbis, A. A. S., Elliot, J. L., Kane, J. F., 2006. The color of the Kuiper belt Core. Icarus 183, 168–178.

Gurrola, E. M., 1995. Interpretation of radar data from the icy galilean satellites and triton. Ph.D. thesis, Stanford University.

Hansen, C. J., Terrile, R. J., McEwen, A., Ingersoll, A., 1990. Surface and airborne evidence for plumes and winds on Triton. Science 250, 421–424.

Hapke, B., 1981. Bidirectional reflectance spectroscopy. I - Theory. Journal of Geophysical Research 86, 3039–3054.

Hapke, B., 1993. Theory of reflectance and emittance spectroscopy. Topics in Remote Sensing, Cambridge, UK: Cambridge University Press.

Hapke, B., 2001. Space weathering from Mercury to the asteroid belt. Journal of Geophysical Research 106, 10039–10074.

Hardorp, J., 1980. The sun among the stars. III - Energy distributions of 16 northern G-type stars and the solar flux calibration. Astronomy and Astrophysics 91, 221–232.

Hatzes, A. P., Cochran, W. D., McArthur, B., Baliunas, S. L., Walker, G. A. H., Campbell, B., Irwin, A. W., Yang, S., Kürster, M., Endl, M., Els, S., Butler, R. P., Marcy, G. W., 2000. Evidence for a Long-Period Planet Orbiting ϵ Eridani. Astrophysical Journal 544, L145–L148.

Heap, S. R., Lindler, D. J., Lanz, T. M., Cornett, R. H., Hubeny, I., Maran, S. P., Woodgate, B., 2000. Space Telescope Imaging Spectrograph Coronagraphic Observations of β Pictoris. Astrophysical Journal 539, 435–444.

Henyey, L. G., Greenstein, J. L., 1941. Diffuse radiation in th galaxy. Astrophysical Journal 93, 70.

Hillier, J., Veverka, J., Helfenstein, P., Lee, P., 1994. Photometric diversity of terrains on Triton. Icarus 109, 296–312.

Hirayama, K., 1918. Groups of asteroids probably of common origin. Annales de l'Observatoire astronomique de Tokyo 6, 185–188.

Hiroi, T., Ohashi, H., Otake, H., 1999. Simulation of space weathering of planet-forming materials: Nanosecond pulse laser irradiation and proton implantation on olivine and pyroxene samples. Earth, Planets, and Space 51, 1255–1265.

Hiroi, T., Sasaki, S., 2001. Importance of space weathering simulation products in compositional modeling of asteroids: 349 Dembowska and 446 Aeternitas as examples. Meteoritics and Planetary Science 36, 1587–1596.

Hiroi, T., Zolensky, M. E., Pieters, C. M., 2001. The Tagish Lake Meteorite: A Possible Sample from a D-Type Asteroid. Science 293, 2234–2236.

Howell, E. S., Merenyi, E., Lebofsky, L. A., 1994. Classification of asteroid spectra using a neural network. Journal of Geophysical Research 99, 10847–10865.

Howell, S. B., 2006. Handbook of CCD astronomy. Cambridge Univ. Press.

Hsieh, H. H., Jewitt, D., 2006. A Population of Comets in the Main Asteroid Belt. Science 312, 561–563.

Hudson, R. L., Moore, M. H., Raines, L. L., 2009. Ethane ices in the outer Solar System: Spectroscopy and chemistry. Icarus 203, 677–680.

Ida, S., Bryden, G., Lin, D. N. C., Tanaka, H., 2000. Orbital Migration of Neptune and Orbital Distribution of Trans-Neptunian Objects. Astrophysical Journal 534, 428–445.

Isella, A., Carpenter, J. M., Sargent, A. I., 2009. Structure and Evolution of Pre-main-sequence Circumstellar Disks. Astrophysical Journal 701, 260–282.

Jenniskens, P., Shaddad, M. H., Numan, D., Elsir, S., Kudoda, A. M., Zolensky, M. E., Le, L., Robinson, G. A., Friedrich, J. M., Rumble, D., Steele, A., Chesley, S. R., Fitzsimmons, A., Duddy, S., Hsieh, H. H., Ramsay, G., Brown, P. G., Edwards, W. N., Tagliaferri, E., Boslough, M. B., Spalding, R. E., Dantowitz, R., Kozubal, M., Pravec, P., Borovicka, J., Charvat, Z., Vaubaillon, J., Kuiper, J., Albers, J., Bishop, J. L., Mancinelli, R. L., Sandford, S. A., Milam, S. N., Nuevo, M., Worden, S. P., 2009. The impact and recovery of asteroid 2008 tc_3. Nature 458, 485–488.

Jenniskens, P., Vaubaillon, J., Binzel, R. P., DeMeo, F. E., Nesvorný, D., Fitzsimmons, A., Hiroi, T., Marchis, F., Bishop, J. L., Zolensky, M. E., Shaddad, M. H., 2010. 2008 tc3 and the search for the ureilite parent body. Meteoritics and Planetary Science.

Jewitt, D., Luu, J., 1993. Discovery of the candidate Kuiper belt object 1992 QB1. Nature 362, 730–732.

Jewitt, D. C., Luu, J., 2004. Crystalline water ice on the Kuiper belt object (50000) Quaoar. Nature 432, 731–733.

Jewitt, D. C., Luu, J. X., 2001. Colors and Spectra of Kuiper Belt Objects. Astronomical Journal 122, 2099–2114.

Jewitt, D. C., Trujillo, C. A., Luu, J. X., 2000. Population and Size Distribution of Small Jovian Trojan Asteroids. Astronomical Journal 120, 1140–1147.

Johansen, A., Oishi, J. S., Low, M., Klahr, H., Henning, T., Youdin, A., 2007. Rapid planetesimal formation in turbulent circumstellar disks. Nature 448, 1022–1025.

Kalas, P., 2005. First Optical Images of Circumstellar Dust Surrounding the Debris Disk Candidate HD 32297. Astrophysical Journal 635, L169–L172.

Kalas, P., Graham, J. R., Chiang, E., Fitzgerald, M. P., Clampin, M., Kite, E. S., Stapelfeldt, K., Marois, C., Krist, J., 2008. Optical Images of an Exosolar Planet 25 Light-Years from Earth. Science 322, 1345–1348.

Kalas, P., Jewitt, D., 1995. Asymmetries in the Beta Pictoris Dust Disk. Astronomical Journal 110, 794–804.

Kennedy, G. M., Kenyon, S. J., 2008. Planet formation around stars of various masses: Hot Super-Earths. Astrophysical Journal 682, 1264–1276.

Kenyon, S. J., Bromley, B. C., 2006. Terrestrial Planet Formation. I. The Transition from Oligarchic Growth to Chaotic Growth. Astronomical Journal 131, 1837–1850.

Khare, B. N., Sagan, C., Arakawa, E. T., Suits, F., Callcott, T. A., Williams, M. W., 1984. Optical constants of organic tholins produced in a simulated Titanian atmosphere - From soft X-ray to microwave frequencies. Icarus 60, 127–137.

Khare, B. N., Thompson, W. R., Cheng, L., Chyba, C., Sagan, C., Arakawa, E. T., Meisse, C., Tuminello, P. S., 1993. Production and optical constraints of ice tholin from charged particle irradiation of (1:6) C_2H_6/H_2O at 77 K. Icarus 103, 290–300.

Kouchi, A., Kuroda, T., 1990. Amorphization of cubic ice by ultraviolet irradiation. Nature 344, 134–135.

Krasnopolsky, V. A., Cruikshank, D. P., 1995. Photochemistry of Triton's Atmosphere and Ionosphere. Journal of Geophysical Research 100, 11271.

Krasnopolsky, V. A., Cruikshank, D. P., 1999. Photochemistry of Pluto's atmosphere and ionosphere near perihelion. Journal of Geophysical Research 104, 21979–21996.

Lacerda, P., Luu, J., 2006. Analysis of the Rotational Properties of Kuiper Belt Objects. Astronomical Journal 131, 2314–2326.

Lagrange, A., Gratadour, D., Chauvin, G., Fusco, T., Ehrenreich, D., Mouillet, D., Rousset, G., Rouan, D., Allard, F., Gendron, É., Charton, J., Mugnier, L., Rabou, P., Montri, J., Lacombe, F., 2009. A probable giant planet imaged in the β Pictoris disk. VLT/NaCo deep L'-band imaging. Astronomy and Astrophysics 493, L21–L25.

Lagrange-Henri, A. M., Gosset, E., Beust, H., Ferlet, R., Vidal-Madjar, A., 1992. The Beta Pictoris circumstellar disk. XIII - Survey of the variable CA II lines. Astronomy and Astrophysics 264, 637–653.

Landolt, A. U., 1992. UBVRI photometric standard stars in the magnitude range 11.5-16.0 around the celestial equator. Astronomical Journal 104, 340–371.

Lawler, S. M., Beichman, C. A., Bryden, G., Ciardi, D. R., Tanner, A. M., Su, K. Y. L., Stapelfeldt, K. R., Lisse, C. M., Harker, D. E., 2009. Explorations Beyond the Snow Line: Spitzer/IRS Spectra of Debris Disks Around Solar-type Stars. Astrophysical Journal 705, 89–111.

Lazzarin, M., Barucci, M. A., Boehnhardt, H., Tozzi, G. P., de Bergh, C., Dotto, E., 2003. ESO Large Programme on Physical Studies of Trans-Neptunian Objects and Centaurs: Visible Spectroscopy. Astronomical Journal 125, 1554–1558.

Lazzaro, D., Michtchenko, T., Carvano, J. M., Binzel, R. P., Bus, S. J., Burbine, T. H., Mothé-Diniz, T., Florczak, M., Angeli, C. A., Harris, A. W., 2000. Discovery of a Basaltic Asteroid in the Outer Main Belt. Science 288, 2033–2035.

Lebofsky, L. A., 1978. Asteroid 1 Ceres - Evidence for water of hydration. Monthly Notices of the Royal Astronomical Society 182, 17P–21P.

Lebofsky, L. A., 1980. Infrared reflectance spectra of asteroids - A search for water of hydration. Astronomical Journal 85, 573–585.

Lebofsky, L. A., Sykes, M. V., Tedesco, E. F., Veeder, G. J., Matson, D. L., Brown, R. H., Gradie, J. C., Feierberg, M. A., Rudy, R. J., 1986. A refined 'standard' thermal model for asteroids based on observations of 1 Ceres and 2 Pallas. Icarus 68, 239–251.

Lellouch, E., De Bergh, C., Moreno, R., Sicardy, B., Käufl, H., Sep. 2009a. Search for CO in Pluto's and Triton's Atmospheres. In: AAS/Division for Planetary Sciences Meeting Abstracts. Vol. 41 of AAS/Division for Planetary Sciences Meeting Abstracts. p. 06.08.

Lellouch, E., Sicardy, B., de Bergh, C., Käufl, H., Kassi, S., Campargue, A., 2009b. Pluto's lower atmosphere structure and methane abundance from high-resolution spectroscopy and stellar occultations. Astronomy and Astrophysics 495, L17–L21.

Levi, A., Podolak, M., 2009. Corona-like atmospheric escape from KBOs. I. Gas dynamics. Icarus 202, 681–693.

Levison, H. F., Duncan, M. J., Wetherill, G. W., 1994. Secular resonances and cometary orbits in the β Pictoris system. Nature 372, 441–444.

Levison, H. F., Morbidelli, A., Vanlaerhoven, C., Gomes, R., Tsiganis, K., 2008. Origin of the structure of the Kuiper belt during a dynamical instability in the orbits of Uranus and Neptune. Icarus 196, 258–273.

Levison, H. F., Stern, S. A., 2001. On the Size Dependence of the Inclination Distribution of the Main Kuiper Belt. Astronomical Journal 121, 1730–1735.

Li, J., McFadden, L. A., Parker, J. W., Young, E. F., Stern, S. A., Thomas, P. C., Russell, C. T., Sykes, M. V., 2006. Photometric analysis of 1 Ceres and surface mapping from HST observations. Icarus 182, 143–160.

Licandro, J., Ghinassi, F., Testi, L., 2002. Infrared spectroscopy of the largest known trans-Neptunian object 2001 KX_{75}. Astronomy and Astrophysics 388, L9–L12.

Licandro, J., Grundy, W. M., Pinilla-Alonso, N., Leisy, P., 2006a. Visible spectroscopy of 2003 UB_{313}: evidence for N_2 ice on the surface of the largest TNO? Astronomy and Astrophysics 458, L5–L8.

Licandro, J., Pinilla-Alonso, N., Pedani, M., Oliva, E., Tozzi, G. P., Grundy, W. M., 2006b. The methane ice rich surface of large TNO 2005 FY_9: a Pluto-twin in the trans-neptunian belt? Astronomy and Astrophysics 445, L35–L38.

Liou, J., Zook, H. A., 1999. Signatures of the Giant Planets Imprinted on the Edgeworth-Kuiper Belt Dust Disk. Astronomical Journal 118, 580–590.

Lisse, C. M., Beichman, C. A., Bryden, G., Wyatt, M. C., 2007. On the Nature of the Dust in the Debris Disk around HD 69830. Astrophysical Journal 658, 584–592.

Lisse, C. M., Chen, C. H., Wyatt, M. C., Morlok, A., 2008. Circumstellar Dust Created by Terrestrial Planet Formation in HD 113766. Astrophysical Journal 673, 1106–1122.

Lord, S. D., 1992. A new software tool for computing earth's atmospheric transmission of near- and far-infrared radiation. NASA Tech. Mem. 1 (103957).

Lykawka, P. S., Mukai, T., 2008. An Outer Planet Beyond Pluto and the Origin of the Trans-Neptunian Belt Architecture. Astronomical Journal 135, 1161–1200.

Malhotra, R., 1993. The origin of Pluto's peculiar orbit. Nature 365, 819–821.

Malhotra, R., 1995. The Origin of Pluto's Orbit: Implications for the Solar System Beyond Neptune. Astronomical Journal 110, 420–429.

Mastrapa, R. M., Bernstein, M. P., Sandford, S. A., 2006. Near Infrared Spectra of H_2O/HCN Mixtures. In: Mackwell, S., Stansbery, E. (Eds.), 37th Annual Lunar and Planetary Science Conference. Vol. 37 of Lunar and Planetary Institute Conference Abstracts. p. 1378.

Matese, J. J., Whitmire, D. P., Lissauer, J. J., 2005. A Widebinary Solar Companion as a Possible Origin of Sedna-like Objects. Earth Moon and Planets 97, 459–470.

McBride, N., Green, S. F., Davies, J. K., Tholen, D. J., Sheppard, S. S., Whiteley, R. J., Hillier, J. K., 2003. Visible and infrared photometry of Kuiper Belt objects: searching for evidence of trends. Icarus 161, 501–510.

McCord, T. B., 1966. Dynamical evolution of the Neptunian system. Astronomical Journal 71, 585.

McCord, T. B., Adams, J. B., 1973. Progress in remote optical analysis of lunar surface composition. Moon 7, 453–474.

McCord, T. B., Johnson, T. V., 1970. Lunar Spectral Reflectivity (0.30 to 2.50 Microns) and Implications for Remote Mineralogical Analysis. Science 169, 855–858.

McEwen, A. S., 1990. Global color and albedo variations on Triton. Geophysical Research Letters 17, 1765–1768.

McKinnon, W. B., 1984. On the origin of Triton and Pluto. Nature 311, 355–358.

Merlin, F., Alvarez-Candal, A., Delsanti, A., Fornasier, S., Barucci, M. A., DeMeo, F. E., de Bergh, C., Doressoundiram, A., Quirico, E., Schmitt, B., 2009. Stratification of Methane Ice on Eris' Surface. Astronomical Journal 137, 315–328.

Merlin, F., Barucci, M. A., de Bergh, C., Fornasier, S., Doressoundiram, A., Perna, D., Protopapa, S., 2010. Surface composition and physical properties of several trans-neptunian objects from the hapke scattering theory and shkuratov model. Astronomical Journal, submitted.

Merlin, F., Guilbert, A., Dumas, C., Barucci, M. A., de Bergh, C., Vernazza, P., 2007. Properties of the icy surface of the TNO 136108 (2003 EL_{61}). Astronomy and Astrophysics 466, 1185–1188.

Moorwood, A., Cuby, J., Biereichel, P., Brynnel, J., Delabre, B., Devillard, N., van Dijsseldonk, A., Finger, G., Gemperlein, H., Gilmozzi, R., Herlin, T., Huster, G., Knudstrup, J., Lidman, C., Lizon, J., Mehrgan, H., Meyer, M., Nicolini, G., Petr, M., Spyromilio, J., Stegmeier, J., 1998. ISAAC sees first light at the VLT. The Messenger 94, 7–9.

Morbidelli, A., Bottke, W. F., Nesvorný, D., Levison, H. F., 2009a. Asteroids were born big. Icarus 204, 558–573.

Morbidelli, A., Brasser, R., Tsiganis, K., Gomes, R., Levison, H., 2009b. Asteroid Belt Constraints on Giant Planets Evolution. In: AAS/Division for Planetary Sciences Meeting Abstracts. Vol. 41 of AAS/Division for Planetary Sciences Meeting Abstracts. p. 55.03.

Morbidelli, A., Brown, M. E., 2004. The kuiper belt and the primordial evolution of the solar system. In: Festou, M. C., Keller, H. U., Weaver, H. A. (Eds.), Comets II. Univ. of Arizona Press, Tucson, AZ, USA, pp. 175–191.

Morbidelli, A., Levison, H. F., 2003. Planetary science: Kuiper-belt interlopers. Nature 422, 30–31.

Morbidelli, A., Levison, H. F., Gomes, R., 2008. The Dynamical Structure of the Kuiper Belt and Its Primordial Origin. In: Barucci, M. A., Boehnhardt, H., Cruikshank, D. P., Morbidelli, A. (Eds.), The Solar System Beyond Neptune. Univ. of Arizona Press, Tucson, AZ, USA, pp. 275–292.

Morbidelli, A., Levison, H. F., Tsiganis, K., Gomes, R., 2005. Chaotic capture of Jupiter's Trojan asteroids in the early Solar System. Nature 435, 462–465.

Moroz, L., Baratta, G., Strazzulla, G., Starukhina, L., Dotto, E., Barucci, M. A., Arnold, G., Distefano, E., 2004. Optical alteration of complex organics induced by ion irradiation: 1. Laboratory experiments suggest unusual space weathering trend. Icarus 170, 214–228.

Moskovitz, N. A., Jedicke, R., Gaidos, E., Willman, M., Nesvorný, D., Fevig, R., Ivezić, Ž., 2008. The distribution of basaltic asteroids in the Main Belt. Icarus 198, 77–90.

Murchie, S., Robinson, M., Clark, B., Li, H., Thomas, P., Joseph, J., Bussey, B., Domingue, D., Veverka, J., Izenberg, N., Chapman, C., 2002. Color Variations on Eros from NEAR Multispectral Imaging. Icarus 155, 145–168.

Murray, C. D., Dermott, S. F., 1999. Solar System Dynamics. Cambridge Univ. Press.

Nakamura, R., Sumikawa, S., Ishiguro, M., Mukai, T., Iwamuro, F., Terada, H., Motohara, K., Goto, M., Hata, R., Taguchi, T., Harashima, T., Kaifu, N., Hayashi, M., Maihara, T., 2000. Subaru Infrared Spectroscopy of the Pluto-Charon System. PASJ 52, 551–556.

Noll, K. S., Grundy, W. M., Stephens, D. C., Levison, H. F., Kern, S. D., 2008. Evidence for two populations of classical transneptunian objects: The strong inclination dependence of classical binaries. Icarus 194, 758–768.

Norman, M. D., Duncan, R. A., Huard, J. J., 2006. Identifying impact events within the lunar cataclysm from ^{40}Ar ^{39}Ar ages and compositions of Apollo 16 impact melt rocks. Geochimica et Cosmochimica Acta 70, 6032–6049.

Okamoto, Y. K., Kataza, H., Honda, M., Yamashita, T., Onaka, T., Watanabe, J., Miyata, T., Sako, S., Fujiyoshi, T., Sakon, I., 2004. An early extrasolar planetary system revealed by planetesimal belts in β Pictoris. Nature 431, 660–663.

Olkin, C. B., Young, E. F., Young, L. A., Grundy, W., Schmitt, B., Tokunaga, A., Owen, T., Roush, T., Terada, H., 2007. Pluto's Spectrum from 1.0 to 4.2 μm: Implications for Surface Properties. Astronomical Journal 133, 420–431.

Öpik, E. J., 1963. The stray bodies in the solar system. part i. survival of comet nuclei and the asteroids. Advances in Astronomical Astrophysics 2, 219–262.

Ortiz, J. L., Baumont, S., Gutiérrez, P. J., Roos-Serote, M., 2002. Lightcurves of Centaurs 2000 QC_{243} and 2001 PT_{13}. Astronomy and Astrophysics 388, 661–666.

Ortiz, J. L., Gutiérrez, P. J., Casanova, V., Sota, A., 2003a. A study of short term rotational variability in TNOs and Centaurs from Sierra Nevada Observatory. Astronomy and Astrophysics 407, 1149–1155.

Ortiz, J. L., Gutiérrez, P. J., Santos-Sanz, P., Casanova, V., Sota, A., 2006. Short-term rotational variability of eight KBOs from Sierra Nevada Observatory. Astronomy and Astrophysics 447, 1131–1144.

Ortiz, J. L., Gutiérrez, P. J., Sota, A., Casanova, V., Teixeira, V. R., 2003b. Rotational brightness variations in Trans-Neptunian Object 50000 Quaoar. Astronomy and Astrophysics 409, L13–L16.

Owen, T. C., Roush, T. L., Cruikshank, D. P., Elliot, J. L., Young, L. A., de Bergh, C., Schmitt, B., Geballe, T. R., Brown, R. H., Bartholomew, M. J., 1993. Surface ices and the atmospheric composition of Pluto. Science 261, 745–748.

Parker, E. N., 1963. Interplanetary dynamical processes. New York, Interscience Publishers.

Parker, J. W., McFadden, L. A., Russell, C. T., Stern, S. A., Sykes, M. V., Thomas, P. C., Young, E. F., 2006. Ceres: High-resolution imaging with HST and the determination of physical properties. Advances in Space Research 38, 2039–2042.

Peixinho, N., Boehnhardt, H., Belskaya, I., Doressoundiram, A., Barucci, M. A., Delsanti, A., 2004. ESO large program on Centaurs and TNOs: visible colors-final results. Icarus 170, 153–166.

Peixinho, N., Doressoundiram, A., Delsanti, A., Boehnhardt, H., Barucci, M. A., Belskaya, I., 2003. Reopening the TNOs color controversy: Centaurs bimodality and TNOs unimodality. Astronomy and Astrophysics 410, L29–L32.

Peixinho, N., Lacerda, P., Jewitt, D., 2008. Color-Inclination Relation of the Classical Kuiper Belt Objects. Astronomical Journal 136, 1837–1845.

Perna, D., Barucci, M. A., Fornasier, S., DeMeo, F. E., Alvarez-Candal, A., Merlin, F., Dotto, E., Doressoundiram, A., de Bergh, C., 2010. Colors and taxonomy of Centaurs and trans-Neptunian objects. Astronomy and Astrophysics 510 (26), A53.

Persson, S. E., Murphy, D. C., Krzeminski, W., Roth, M., Rieke, M. J., 1998. A New System of Faint Near-Infrared Standard Stars. Astronomical Journal 116, 2475–2488.

Pieters, C. M., Goswami, J. N., Clark, R. N., Annadurai, M., Boardman, J., Buratti, B., Combe, J., Dyar, M. D., Green, R., Head, J. W., Hibbitts, C., Hicks, M., Isaacson, P., Klima, R., Kramer, G., Kumar, S., Livo, E., Lundeen, S., Malaret, E., McCord, T., Mustard, J., Nettles, J., Petro, N., Runyon, C., Staid, M., Sunshine, J., Taylor, L. A., Tompkins, S., Varanasi, P., 2009. Character and Spatial Distribution of OH/H_2O on the Surface of the Moon Seen by M^3 on Chandrayaan-1. Science 326, 568–572.

Pieters, C. M., Taylor, L. A., Noble, S. K., Keller, L. P., Hapke, B., Morris, R. V., Allen, C. C., McKay, D. S., Wentworth, S., 2000. Space weathering on airless bodies: Resolving a mystery with lunar samples. Meteoritics and Planetary Science 35, 1101–1107.

Pinilla-Alonso, N., Brunetto, R., Licandro, J., Gil-Hutton, R., Roush, T. L., Strazzulla, G., 2009. The surface of (136108) Haumea (2003 EL_{61}), the largest carbon-depleted object in the trans-Neptunian belt. Astronomy and Astrophysics 496, 547–556.

Pollack, J. B., Hollenbach, D., Beckwith, S., Simonelli, D. P., Roush, T., Fong, W., 1994. Composition and radiative properties of grains in molecular clouds and accretion disks. Astrophysical Journal 421, 615–639.

Poulet, F., Cuzzi, J. N., Cruikshank, D. P., Roush, T., Dalle Ore, C. M., 2002. Comparison between the Shkuratov and Hapke Scattering Theories for Solid Planetary Surfaces: Application to the Surface Composition of Two Centaurs. Icarus 160, 313–324.

Protopapa, S., 2008. Surface characterization of Pluto, Charon, and (47171) 1999 TC36. Max Planck Institute for Solar System Research. Doctoral Thesis. Lindau, Germany.

Protopapa, S., Alvarez-Candal, A., Barucci, M. A., Tozzi, G. P., Fornasier, S., Delsanti, A., Merlin, F., 2009. ESO large program about transneptunian objects: surface variations on (47171) 1999 TC_{36}. Astronomy and Astrophysics 501, 375–380.

Protopapa, S., Boehnhardt, H., Herbst, T. M., Cruikshank, D. P., Grundy, W. M., Merlin, F., Olkin, C. B., 2008. Surface characterization of Pluto and Charon by L and M band spectra. Astronomy and Astrophysics 490, 365–375.

Quirico, E., Doute, S., Schmitt, B., de Bergh, C., Cruikshank, D. P., Owen, T. C., Geballe, T. R., Roush, T. L., 1999. Composition, Physical State, and Distribution of Ices at the Surface of Triton. Icarus 139, 159–178.

Quirico, E., Schmitt, B., 1997a. A Spectroscopic Study of CO Diluted in N_2 Ice: Applications for Triton and Pluto. Icarus 128, 181–188.

Quirico, E., Schmitt, B., 1997b. Near-Infrared Spectroscopy of Simple Hydrocarbons and Carbon Oxides Diluted in Solid N_2 and as Pure Ices: Implications for Triton and Pluto. Icarus 127, 354–378.

Ragozzine, D., Brown, M. E., 2007. Candidate Members and Age Estimate of the Family of Kuiper Belt Object 2003 EL61. Astronomical Journal 134, 2160–2167.

Rayner, J. T., Toomey, D. W., Onaka, P. M., Denault, A. J., Stahlberger, W. E., Vacca, W. E., Cushing, M. C., Wang, S., 2003. Spex: A medium-resolution 0.8-5.5 micron spectrograph and imager for the nasa infrared telescope facility. Astron. Soc. of the Pacific 115, 362–382.

Richardson, J. E., Melosh, H. J., Greenberg, R. J., O'Brien, D. P., 2005. The global effects of impact-induced seismic activity on fractured asteroid surface morphology. Icarus 179, 325–349.

Rivkin, A. S., Binzel, R. P., Bus, S. J., 2005. Constraining near-Earth object albedos using near-infrared spectroscopy. Icarus 175, 175–180.

Rivkin, A. S., Emery, J. P., 2010. Detection of ice and organics on an asteroidal surface. Nature 464, 1322–1323.

Rivkin, A. S., Howell, E. S., Vilas, F., Lebofsky, L. A., 2002. Hydrated Minerals on Asteroids: The Astronomical Record. Asteroids III, 235–253.

Rousselot, P., Petit, J.-M., Poulet, F., Sergeev, A., 2005. Photometric study of Centaur (60558) 2000 EC_{98} and trans-neptunian object (55637) 2002 UX_{25} at different phase angles. Icarus 176, 478–491.

Rubincam, D. P., 2000. Radiative Spin-up and Spin-down of Small Asteroids. Icarus 148, 2–11.

Saito, J., Miyamoto, H., Nakamura, R., Ishiguro, M., Michikami, T., Nakamura, A. M., Demura, H., Sasaki, S., Hirata, N., Honda, C., Yamamoto, A., Yokota, Y., Fuse, T., Yoshida, F., Tholen, D. J., Gaskell, R. W., Hashimoto, T., Kubota, T., Higuchi, Y., Nakamura, T., Smith, P., Hiraoka, K., Honda, T., Kobayashi, S., Furuya, M., Matsumoto, N., Nemoto, E., Yukishita, A., Kitazato, K., Dermawan, B., Sogame, A., Terazono, J., Shinohara, C., Akiyama, H., 2006. Detailed Images of Asteroid 25143 Itokawa from Hayabusa. Science 312, 1341–1344.

Salisbury, J. W., D'Aria, D. M., Jarosewich, E., 1991. Midinfrared (2.5-13.5 microns) reflectance spectra of powdered stony meteorites. Icarus 92, 280–297.

Sasaki, S., Nakamura, K., Hamabe, Y., Kurahashi, E., Hiroi, T., 2001. Production of iron nanoparticles by laser irradiation in a simulation of lunar-like space weathering. Nature 410, 555–557.

Sasaki, T., Kanno, A., Ishiguro, M., Kinoshita, D., Nakamura, R., 2005. Search for Nonmethane Hydrocarbons on Pluto. The Astrophysical Journal Letters 618, L57–L60.

Schaller, E. L., Brown, M. E., 2007a. Detection of Methane on Kuiper Belt Object (50000) Quaoar. Astrophysical Journal 670, L49–L51.

Schaller, E. L., Brown, M. E., 2007b. Volatile Loss and Retention on Kuiper Belt Objects. Astrophysical Journal 659, L61–L64.

Schlichting, H. E., Ofek, E. O., Wenz, M., Sari, R., Gal-Yam, A., Livio, M., Nelan, E., Zucker, S., 2009. A single sub-kilometre Kuiper belt object from a stellar occultation in archival data. Nature 462, 895–897.

Schmitt, B., Quirico, E., Trotta, F., Grundy, W. M., 1998. Optical Properties of Ices from UV to Infrared. In: Schmitt, B., de Bergh, C., Festou, M. (Eds.), Solar System Ices. Vol. 227. Kluwer Academic Publishers, pp. 199–240.

Schwamb, M. E., Brown, M. E., Rabinowitz, D. L., 2009. A Search for Distant Solar System Bodies in the Region of Sedna. Astrophysical Journal 694, L45–L48.

Sheppard, S. S., 2007. Light Curves of Dwarf Plutonian Planets and other Large Kuiper Belt Objects: Their Rotations, Phase Functions, and Absolute Magnitudes. Astronomical Journal 134, 787–798.

Sheppard, S. S., Jewitt, D. C., 2002. Time-resolved Photometry of Kuiper Belt Objects: Rotations, Shapes, and Phase Functions. Astronomical Journal 124, 1757–1775.

Sheppard, S. S., Jewitt, D. C., 2003. Hawaii Kuiper Belt Variability Project: An Update. Earth Moon and Planets 92, 207–219.

Sheppard, S. S., Lacerda, P., Ortiz, J. L., 2008. Photometric Lightcurves of Transneptunian Objects and Centaurs: Rotations, Shapes, and Densities. In: The Solar System Beyond Neptune. Univ. of Arizona Press, Tucson, AZ, USA, pp. 129–142.

Shkuratov, Y., Starukhina, L., Hoffmann, H., Arnold, G., 1999. A Model of Spectral Albedo of Particulate Surfaces: Implications for Optical Properties of the Moon. Icarus 137, 235–246.

Shlens, J., 2009. A tutorial on principal component analysis.
URL `www.snl.salk.edu/~shlens/pub/notes/pca.pdf`

Sicardy, B., Widemann, T., Lellouch, E., Veillet, C., Cuillandre, J., Colas, F., Roques, F., Beisker, W., Kretlow, M., Lagrange, A., Gendron, E., Lacombe, F., Lecacheux, J., Birnbaum, C., Fienga, A., Leyrat, C., Maury, A., Raynaud, E., Renner, S., Schultheis, M., Brooks, K., Delsanti, A., Hainaut, O. R., Gilmozzi, R., Lidman, C., Spyromilio, J., Rapaport, M., Rosenzweig, P., Naranjo, O., Porras, L., Díaz, F., Calderón, H., Carrillo, S., Carvajal, A., Recalde, E., Cavero, L. G., Montalvo, C., Barría, D., Campos, R., Duffard, R., Levato, H., 2003. Large changes in Pluto's atmosphere as revealed by recent stellar occultations. Nature 424, 168–170.

Smith, B. A., Terrile, R. J., 1984. A circumstellar disk around Beta Pictoris. Science 226, 1421–1424.

Smith, E. V. P., Gottlieb, D. M., 1974. Solar flux and its variations. Space Science Reviews 16, 771–802.

Smith, L. I., 2002. A tutorial on principal components analysis.
URL `www.cs.otago.ac.nz/cosc453/student_tutorials/principal_components.pdf`

Soderblom, L. A., Becker, T. L., Kieffer, S. W., Brown, R. H., Hansen, C. J., Johnson, T. V., 1990. Triton's geyser-like plumes - Discovery and basic characterization. Science 250, 410–415.

Spencer, J. R., Buie, M. W., Bjoraker, G. L., 1990. Solid methane on Triton and Pluto - 3- to 4-micron spectrophotometry. Icarus 88, 491–496.

Stansberry, J., Grundy, W., Brown, M., Cruikshank, D., Spencer, J., Trilling, D., Margot, J.-L., 2008. Physical Properties of Kuiper Belt and Centaur Objects: Constraints from the Spitzer Space Telescope. In: Barucci, M. A., Boehnhardt, H., Cruikshank, D. P., Morbidelli, A. (Eds.), The Solar System Beyond Neptune. Univ. of Arizona Press, Tucson, AZ, USA, pp. 161–179.

Stern, S. A., Buie, M. W., Trafton, L. M., 1997. HST High-Resolution Images and Maps of Pluto. Astronomical Journal 113, 827.

Strazzulla, G., Leto, G., Gomis, O., Satorre, M. A., 2003. Implantation of carbon and nitrogen ions in water ice. Icarus 164, 163–169.

Strazzulla, G., Palumbo, M. E., 1998. Evolution of icy surfaces : an experimental approach. Planetary and Space Science 46, 1339–1348.

Strazzulla, G., Palumbo, M. E., 2001. Organics produced by ion irradiation of ices: some recent results. Advances in Space Research 27, 237–243.

Strom, R. G., Croft, S. K., Boyce, J. M., 1990. The impact cratering record on Triton. Science 250, 437–439.

Stuart, J. S., Binzel, R. P., 2004. Bias-corrected population, size distribution, and impact hazard for the near-Earth objects. Icarus 170, 295–311.

Sunshine, J. M., Bus, S. J., Corrigan, C. M., McCoy, T. J., Burbine, T. H., 2007. Olivine-dominated asteroids and meteorites: Distinguishing nebular and igneous histories. Meteoritics and Planetary Science 42.

Sunshine, J. M., Farnham, T. L., Feaga, L. M., Groussin, O., Merlin, F., Milliken, R. E., A'Hearn, M. F., 2009. Temporal and Spatial Variability of Lunar Hydration As Observed by the Deep Impact Spacecraft. Science 326, 565–568.

Tedesco, E. F., Noah, P. V., Noah, M., Price, S. D., 2002. The Supplemental IRAS Minor Planet Survey. Astronomical Journal 123, 1056–1085.

Tegler, S. C., Bauer, J. M., Romanishin, W., Peixinho, N., 2008a. Colors of Centaurs. In: Barucci, M. A., Boehnhardt, H., Cruikshank, D. P., Morbidelli, A. (Eds.), The Solar System Beyond Neptune. Univ. of Arizona Press, Tucson, AZ, USA, pp. 105–114.

Tegler, S. C., Grundy, W. M., Vilas, F., Romanishin, W., Cornelison, D. M., Consolmagno, G. J., 2008b. Evidence of N_2-ice on the surface of the icy dwarf Planet 136472 (2005 FY_9). Icarus 195, 844–850.

Tegler, S. C., Romanishin, W., 2000. Extremely red Kuiper-belt objects in near-circular orbits beyond 40 AU. Nature 407, 979–981.

Tegler, S. C., Romanishin, W., 2003. Resolution of the kuiper belt object color controversy: two distinct color populations. Icarus 161, 181–191.

Tholen, D. J., 1984. Asteroid taxonomy from cluster analysis of photometry. Ph.D. thesis, University of Arizona.

Tholen, D. J., Barucci, M. A., 1989. Asteroid taxonomy. In: Binzel, R. P., Gehrels, T., Matthews, M. S. (Eds.), Asteroids II. pp. 298–315.

Thomas, C. A., Binzel, R. P., 2010. Identifying meteorite source regions through near-Earth object spectroscopy. Icarus 205, 419–429.

Thomas, P. C., Parker, J. W., McFadden, L. A., Russell, C. T., Stern, S. A., Sykes, M. V., Young, E. F., 2005. Differentiation of the asteroid Ceres as revealed by its shape. Nature 437, 224–226.

Tody, D., 1993. Iraf in the nineties. in astronomical data. In Astronomical Data Analysis Software and Systems II.

Tosi, F., Coradini, A., Gavrishin, A. I., Adriani, A., Capaccioni, F., Cerroni, P., Filacchione, G., Brown, R. H., 2005. G-Mode Classification of Spectroscopic Data. Earth Moon and Planets 96, 165–197.

Trujillo, C. A., Brown, M. E., 2002. A Correlation between Inclination and Color in the Classical Kuiper Belt. Astrophysical Journal 566, L125–L128.

Trujillo, C. A., Brown, M. E., Rabinowitz, D. L., Geballe, T. R., 2005. Near-Infrared Surface Properties of the Two Intrinsically Brightest Minor Planets: (90377) Sedna and (90482) Orcus. Astrophysical Journal 627, 1057–1065.

Tryka, K. A., Brown, R. H., Chruikshank, D. P., Owen, T. C., Geballe, T. R., de Bergh, C., 1994. Temperature of nitrogen ice on Pluto and its implications for flux measurements. Icarus 112, 513–527.

Tsiganis, K., Gomes, R., Morbidelli, A., Levison, H. F., 2005. Origin of the orbital architecture of the giant planets of the Solar System. Nature 435, 459–461.

Tyler, G. L., Sweetnam, D. N., Anderson, J. D., Borutzki, S. E., Campbell, J. K., Kursinski, E. R., Levy, G. S., Lindal, G. F., Lyons, J. R., Wood, G. E., 1989. Voyager radio science observations of Neptune and Triton. Science 246, 1466–1473.

van Boekel, R., Min, M., Leinert, C., Waters, L. B. F. M., Richichi, A., Chesneau, O., Dominik, C., Jaffe, W., Dutrey, A., Graser, U., Henning, T., de Jong, J., Köhler, R., de Koter, A., Lopez, B., Malbet, F., Morel, S., Paresce, F., Perrin, G., Preibisch, T., Przygodda, F., Schöller, M., Wittkowski, M., 2004. The building blocks of planets within the 'terrestrial' region of protoplanetary disks. Nature 432, 479–482.

Verbiscer, A., Helfenstein, P., 1998. Reflectance spectroscopy of icy surfaces. In: B. Schmitt, C. de Bergh, & M. Festou (Ed.), Solar System Ices. Vol. 227. Kluwer Academic Publishers, pp. 157–198.

Verbiscer, A. J., Peterson, D. E., Skrutskie, M. F., Cushing, M., Nelson, M. J., Smith, J. D., Wilson, J. C., 2007. Simultaneous Spatially-resolved Near-Infrared Spectra of Pluto and Charon. In: Lunar and Planetary Institute Science Conference Abstracts. Vol. 38 of Lunar and Planetary Inst. Technical Report. p. 2318.

Vernazza, P., Binzel, R. P., Thomas, C. A., DeMeo, F. E., Bus, S. J., Rivkin, A. S., Tokunaga, A. T., 2008. Compositional differences between meteorites and near-Earth asteroids. Nature 454, 858–860.

Vernazza, P., DeMeo, F. E., Nedelcu, A., Birlan, M., Doressoundiram, A., Erard, S., Volquardsen, E., 2010. Resolved spectroscopy of mercury in the near-ir with spex/irtf. Icarus, accepted.

Veverka, J., Thomas, P. C., Bell, III, J. F., Bell, M., Carcich, B., Clark, B., Harch, A., Joseph, J., Martin, P., Robinson, M., Murchie, S., Izenberg, N., Hawkins, E., Warren, J., Farquhar, R., Cheng, A., Dunham, D., Chapman, C., Merline, W. J., McFadden, L., Wellnitz, D., Malin, M., Owen, Jr., W. M., Miller, J. K., Williams, B. G., Yeomans, D. K., 1999. Imaging of asteroid 433 Eros during NEAR's flyby reconnaissance. Science 285, 562–564.

Vidal-Madjar, A., Lagrange-Henri, A., Feldman, P. D., Beust, H., Lissauer, J. J., Deleuil, M., Ferlet, R., Gry, C., Hobbs, L. M., McGrath, M. A., McPhate, J. B., Moos, H. W., 1994. HST-GHRS observations of β Pictoris: additional evidence for infalling comets. Astronomy and Astrophysics 290, 245–258.

Vilas, F., Gaffey, M. J., 1989. Phyllosilicate absorption features in main-belt and outer-belt asteroid reflectance spectra. Science 246, 790–792.

Vilas, F., Smith, B. A., 1985. Reflectance spectrophotometry (about 0.5-1.0 micron) of outer-belt asteroids - Implications for primitive, organic solar system material. Icarus 64, 503–516.

Wahhaj, Z., Koerner, D. W., Ressler, M. E., Werner, M. W., Backman, D. E., Sargent, A. I., 2003. The Inner Rings of β Pictoris. Astrophysical Journal 584, L27–L31.

Walsh, K. J., Richardson, D. C., Michel, P., 2008. Rotational breakup as the origin of small binary asteroids. Nature 454, 188–191.

Weaver, H. A., Stern, S. A., Mutchler, M. J., Steffl, A. J., Buie, M. W., Merline, W. J., Spencer, J. R., Young, E. F., Young, L. A., 2006. Discovery of two new satellites of Pluto. Nature 439, 943–945.

Weidenschilling, S. J., 2000. Formation of Planetesimals and Accretion of the Terrestrial Planets. Space Science Reviews 92, 295–310.

Weidenschilling, S. J., Cuzzi, J. N., 1993. Formation of planetesimals in the solar nebula. In: Protostars and Planets III. Univ. of Arizona Press, Tucson, AZ, USA, pp. 1031–1060.

Wetherill, G. W., 1976. Where do the meteorites come from - A re-evaluation of the earth-crossing Apollo objects as sources of chondritic meteorites. Geochimica et Cosmochimica Acta 40, 1297–1317.

Wetherill, G. W., 1979. Steady state populations of Apollo-Amor objects. Icarus 37, 96–112.

Wisdom, J., 1985. Meteorites may follow a chaotic route to earth. Nature 315, 731–733.

Wood, X. H. J., Kuiper, G. P., 1963. Photometric Studies of Asteroids. Astrophysical Journal 137, 1279–1285.

Wyatt, M. C., 2008. Evolution of Debris Disks. Annual Review of Astronomy and Astrophysics 46, 339–383.

Yelle, R. V., Lunine, J. I., 1989. Evidence for a molecule heavier than methane in the atmosphere of Pluto. Nature 339, 288–290.

Yin, Q., Jacobsen, S. B., Yamashita, K., Blichert-Toft, J., Télouk, P., Albarède, F., 2002. A short timescale for terrestrial planet formation from Hf-W chronometry of meteorites. Nature 418, 949–952.

Young, E. F., Binzel, R. P., Crane, K., 2001a. A Two-Color Map of Pluto's Sub-Charon Hemisphere. Astronomical Journal 121, 552–561.

Young, E. F., Young, L. A., Buie, M., 2007. Pluto's Radius. In: Bulletin of the American Astronomical Society. Vol. 38 of Bulletin of the American Astronomical Society. p. 541.

Young, L. A., Cook, J. C., Yelle, R. V., Young, E. F., 2001b. Upper Limits on Gaseous CO at Pluto and Triton from High-Resolution Near-IR Spectroscopy. Icarus 153, 148–156.

Young, L. A., Elliot, J. L., Tokunaga, A., de Bergh, C., Owen, T., May 1997. Detection of Gaseous Methane on Pluto. Icarus 127, 258–262.

Zappala, V., Bendjoya, P., Cellino, A., Farinella, P., Froeschle, C., 1995. Asteroid families: Search of a 12,487-asteroid sample using two different clustering techniques. Icarus 116, 291–314.

Zellner, B., Tholen, D. J., Tedesco, E. F., 1985. The eight-color asteroid survey: Results for 589 minor planets. Icarus 61, 335–416.

Zheng, W., Jewitt, D., Kaiser, R. I., 2008. Amorphization of Crystalline Water Ice. ArXiv e-prints. URL `http://adsabs.harvard.edu/abs/2008arXiv0801.2805Z`

Zubko, V. G., Mennella, V., Colangeli, L., Bussoletti, E., 1996. Optical constants of cosmic carbon analogue grains - I. Simulation of clustering by a modified continuous distribution of ellipsoids. Monthly Notices of the Royal Astronomical Society 282, 1321–1329.

List of Figures

List of Tables

Index

Glossary

Adaptive Optics A technology for minimizing atmospheric aberrations by creating real-time deformations of a mirror to compensate for the wavefront distortions. 34

airmass A measurement of the amount of atmosphere passed through by the light from an object. The measurement goes from 1 at zenith to infinity and is calculated by $1/\cos(z)$ where z is the angle between the the direction of observation and the zenith direction. 35

albedo Albedo is the measurement of the brightness, or reflectivity, of a surface on a 0 to 1 scale where 0 is perfectly absorbing and 1 is perfectly reflecting. There are three different ways of measuring albedo, which include the normal, geometric (physical), and bond (spherical) albedos. 14–17, 24

astronomical unit A unit of measurement corresponding to the Earth-Sun distance. One astronomical unit is equivalent to 149,598,000 kilometers. 14, 15

Autospex A software tool to streamline reduction procedures that writes macros containing a set of IRAF command files that are then executed by the image processing package. 56

Kuiper Belt The belt of Transneptunian objects between roughly 30 to 55 AU. 14, 17

LHB A short period about 4 billion years ago when the inner Solar System is thought to have experienced a large influx of small bodies, many of which impacted the bodies still existing today. 22

Magnitude Measurement of the intensity of brightness of a celestial object. 0 corresponds to the magnitude of Vega, the brightest star in the sky. It is based on a logarithmic scale and higher values correspond to dimmer objects. 21

Main Belt The belt of asteroids in the inner Solar System located roughly between 2-3.3 AU. 14

MOID The minimum distance at which the orbit of one body passes by another, such as the Earth. 16

NEO Small bodies that have orbits that have a semi-major axis of less than or equal to 1.3 AU. They pass within near-Earth space, and some cross Earth's orbit. 15, 16, 27, 28

Pan-STARRS A wide-field imaging facility under development that will discover and characterize small moving objects in the Solar System. Four 2.2-meter telescopes will be built on Mauna Kea. PS1, the first telescope, is already functioning. More information is available on the Pan-STARRS website. 16

perihelion The location in an orbit where the object is at its closest distance to the Sun. 16

PHA Any asteroid that has an orbit that passes within 0.05 AU of Earth's orbit. 16

phase angle The Sun-Object-Earth angle. 46

resolution Spectral resolution (R) is the resolving power of an instrument and is related to the smallest difference in wavelength (λ) that can be distinguished ($\Delta\lambda$). $R = \frac{\Delta\lambda}{\lambda}$. 23, 32

Seeing A measurement of the effect of atmospheric turbulence. It is the corresponding size of a point source and is measured in arcsecond. 35

standard star A solar-like star (usually G type, specifically G2V) used to correct an objects spectrum for solar features and telluric absorptions. 31, 35

Transneptunian Object Any object that resides past 30 AU, the orbit of Neptune. These objects are within the Edgeworth-Kuiper Belt and are also known as Kuiper Belt Objects (KBOs), Edgeworth-Kuiper Belt Objects (EKOs). 17, 18, 24, 25

Yarkovsky Non gravitational effect due to thermal radiation that can change the orbit of an asteroid over long periods of time. 22

YORP Non gravitational effect due to thermal radiation that can change the rotational properties of asteroids as well as their orbits. 22, 23

Acronyms

ATRAN	Atmospheric Transmission Model
CCD	Charge-Coupled Device
ESA	European Space Agency
ESO	European Southern Observatory
FORS1	Focal Reducer Spectrograph 1
FORS2	Focal Reducer Spectrograph 2
IDL	Interactive Data Language
IRAF	Image Reduction and Analysis Facility
IRTF	InfraRed Telescope Facility
ISAAC	Infrared Spectrometer and Array Camera
JAXA	Japan Aerospace Exploration Agency
LESIA	Laboratoire d'Étude Spatial et d'Instrumentation en Astrophysique
NASA	National Aeronautics and Space Administration
NOAO	National Optical Astronomy Observatories
SINFONI	Spectrograph for INtegral Field Observations in the Near Infrared
SMASS	Small Main-Belt Asteroid Spectroscopic Survey
UKIRT	United Kingdom InfraRed Telescope
VLT	Very Large Telescope